The Dissertation Committee for Shivam Agrawal Certifies that this is the approved version of the following dissertation:

An Integrated Peridynamics-Finite Volume Based Multi-Phase Flow, Geomechanics and Hydraulic Fracture Model

Committee:

Mukul M. Sharma, Supervisor

John T. Foster, Co-Supervisor

Jon E. Olson

Kishore Mohanty

Hisanao Ouchi

An Integrated Peridynamics-Finite Volume Based Multi-Phase Flow, Geomechanics and Hydraulic Fracture Model

by

Shivam Agrawal

Dissertation

Presented to the Faculty of the Graduate School of
The University of Texas at Austin
in Partial Fulfillment
of the Requirements
for the Degree of

Doctor of Philosophy

The University of Texas at Austin
December 2019

Dedication

To my parents for giving me the first chance, and
to my surgeons and the supreme power for the second.

Acknowledgements

I would like to express my heartfelt gratitude to my advisor Dr Mukul M. Sharma for his guidance, motivation, and patience throughout my education at The University of Texas at Austin. Despite his busy schedule, he always made time for discussing my work and progress. While he was never short of ideas from his immense experience, he allowed me to explore as well. Moreover, I greatly benefitted from the collaborative research atmosphere that he has nurtured over the years. I would also like to thank my committee members for their useful suggestions and helping me broaden my scope of thoughts.

I would sincerely like to acknowledge my co-supervisor Dr John T. Foster whose expertise in the theory of Peridynamics helped me improve my understanding of the subject. Moreover, I learnt a lot in the classes that I studied from him. His keenness to learn and evolve, including the many technologies that he uses in his teaching and profession, inspire me.

I am extremely thankful to Dr Hisanao Ouchi. During his supportive mentorship, I gained the knowledge of developing computational code and more importantly, debugging it. Despite his busy schedule after his graduation and the large difference in time zone with Japan, he was always available for detailed technical discussions and feedback.

I would like to thank the university staff, especially Jin Lee, Amy D. Stewart, and Frankie L. Hart for their support. Jin provided great administrative advices that allowed the graduate studies to be more productive.

My earnest acknowledgements to my co-authors, including Dr. Amit Katiyar, Dr. Murtadha AlTammar, Kaustubh Shrivastava, Ashish Kumar, and Shuang Zheng for undertaking the collaborative projects and the thoughtful discussions. I would like to thank my colleagues, especially, Dr Ripudaman Manchanda, Dr Jongsoo Hwang, Dr Javid Shiriyev, Dr Peng Zhang, Dr Shawn Wu, Dr Shiting Yi, Dr Haotian Wang, Dr Hanyi Wang, Dr Emmanouil Karantinos, Dr Dongkeun Lee, Dr Weiwei Wu, Dr Deepen Gala, Sho Hirose, Puneet Seth, and Min Zhang.

I enjoyed the company of several friends in Austin, including Chandra Shekhar, Hasan Khan, Vivek Ravi, Sai Uppati, Abhishek Bihani, Neha Anand, Harshit Mehta, Praful Gupta, Shiraz Gulraiz, Mujtaba Khan, and Asad ul Haq.

I am grateful to my family, teachers, and surgeons. My parents' sacrifices, love, and patience have been the guiding light. My brother's and sister-in-law's affection, encouragement, and pride have kept me going. The lessons that I learnt from my teachers, both inside the class and outside, have made me what I am. Last but not the least, my profound thanks to Preeti, whose unwavering support, care, sacrifices, and suggestions have motivated me to strive harder and aim higher. Because of her presence, the graduate studies were accomplishing and memorable.

Abstract

An Integrated Peridynamics-Finite Volume Based Multi-Phase Flow, Geomechanics and Hydraulic Fracture Model

Shivam Agrawal, PhD
The University of Texas at Austin, 2019

Supervisor: Mukul M. Sharma
Co-Supervisor: John T. Foster

Hydraulic fracturing in unconventional reservoirs exhibits several interesting phenomena including the interaction of hydraulic fractures with multi-scale heterogeneities such as natural fractures, stress/barrier layers, bedding planes, shale laminations, and mineralogy. Moreover, hydraulic fractures originating from different clusters or stages in a multi-stage, multi-cluster treatment interact among themselves. Mathematical models, with various degrees of numerical complexity, are developed for gaining better insights into the physics governing these phenomena. Peridynamics-based hydraulic fracturing model developed by Ouchi (2016) has been demonstrated to capture all of these phenomena. However, its major drawback is that it is computationally expensive. In this dissertation, we have extended the capabilities of the model to multi-phase flow and made it significantly faster by coupling it with the less expensive Finite Volume Method.

The single-phase peridynamics flow model for slightly compressible, Newtonian fluids has been generalized for multiphase, multicomponent flow of compressible, non-Newtonian fluids. The generalized flow model has been coupled with the fracturing model and compared with laboratory experiments performed under low confining stresses. The extended model is also applied to simulate the growth of fractures from a new (child) well in the presence of depleted regions created by production from the fractures of an old (parent) well under high confining stresses.

The interaction of a hydraulic fracture (HF) with a natural fracture (NF) is investigated. Remote shear failure of the NF due to the pororelastic stress changes caused by the propagating HF are considered. Consistent with the experiments, the remote shear failure is shown to result in the bending of the HF towards the NF before intersecting with it. Accounting for the effects of remote shear failure and poroelasticity, numerical crossing criteria for the HF-NF interaction are developed.

The hydraulic fracturing model based on peridynamics (PD) theory is coupled with the less expensive Finite Volume Method (FVM), following the PD-FEM coupling method proposed by Galvanetto et al. (2016). Significant improvements in computational performance are achieved by the coupled model relative to the pure PD-based model, without compromising the unique original capabilities. By monitoring material damage in remote heterogeneous regions, a workflow for estimating the extent of the Stimulated Reservoir Volume (SRV) around a primary hydraulic fracture is developed. A sensitivity study for the effects of elastic properties of the formation, injection rate, and the reservoir fluid type on SRV extent is presented.

Table of Contents

CHAPTER 5 : EFFECT OF SHEAR SLIPPAGE ON THE INTERACTION OF HYDRAULIC FRACTURES WITH NATURAL FRACTURES **92**

List of Tables

List of Figures

CHAPTER 1: INTRODUCTION

1.1. BACKGROUND AND MOTIVATION

The EIA (2019) reports that in December 2018, 70% of the total US natural gas production and 60% of the total US crude oil production came from the shale gas and tight oil reservoirs respectively (Figure 1.1). The combination of horizontal drilling and multi-stage hydraulic fracturing has made production feasible from these ultra-low permeability unconventional reservoirs. However, the completions decisions in these reservoirs are mostly taken based on market economics and some non-technical factors such as the duration of the lease. Engineering analyses, involving field data and advanced mathematical models, have gained momentum in the past years and can help sustain the upward trend in oil and gas production.

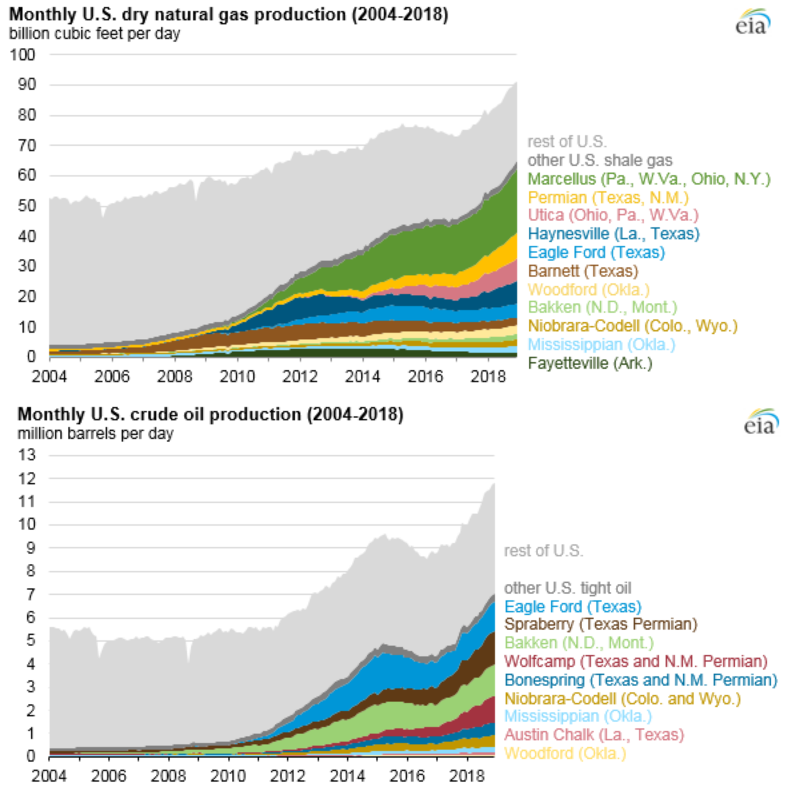

Figure 1.1. US oil and gas production over the past years (EIA, 2019)

Analytical and numerical models have been developed to understand the interesting physics related to hydraulic fracturing. These include interactions with multi-scale reservoir heterogeneities including natural fractures, stress/barrier layers, bedding planes, shale laminations, and mineralogy. Another common phenomenon that is addressed by the numerical models is the stress interference among the fractures. Peridynamics-based hydraulic fracturing model developed by Ouchi (2016) has been demonstrated to capture all of the important physics. However, its major drawback is that it is computationally expensive.

1.2. RESEARCH OBJECTIVES

In this dissertation, we have extended the capabilities of our peridynamics-based hydraulic fracturing model for multi-phase flow and have considerably improved its computational performance by coupling it with a faster, traditional numerical method. The main objectives of this research are as follows:

a) Develop a general peridynamics (PD) model for multiphase transport of non-Newtonian compressible fluids in porous media.
b) Couple the general fluid flow model with the PD-based fracturing model for new reservoir engineering and fracturing applications.
c) Investigate the interaction of a hydraulic fracture with a natural fracture, accounting for remote shear failure of the natural fracture and poroelasticity.
d) Couple the PD-based fracturing model with the Finite Volume Method (FVM) for improved computational performance, while retaining the salient features of the original model.
e) Demonstrate the capability of the coupled PD-FVM model in estimating the Stimulated Reservoir Volume (SRV) around a hydraulic fracture.

1.3. LITERATURE REVIEW OF HYDRAULIC FRACTURING MODELS

Hydraulic fracturing is a multi-physics process. Its modeling requires solution of coupled equations describing rock deformation, flow of reservoir fluids, flow of fracturing fluid including the proppant, and wellbore effects. Numerous fracturing models with varying levels of complexity have been developed, depending on the simplifying assumptions that are made and the potential applications that they are intended for. Analytical models are simplistic but require very less computational resources as they make the most forgiving assumptions. Numerical models are more complex and applicable to a wider variety of reservoir conditions and completion strategies. However, they require significantly more computational resources since they relax some of the assumptions made in the analytical models.

1.3.1. Analytical 2-D models

There are three popular analytical 2-D models, namely the KGD model (Khristianovic and Zheltov, 1955; Geertsma and De Klerk, 1969), the PKN model (Perkins and Kern, 1961; Nordgren, 1972), and the penny-shaped fracture model (Abé et al., 1976).

The KGD model assumes plane strain condition in a horizontal plane and is applicable when the fracture height is greater than the fracture length (Figure 1.2). The other assumptions include elliptic fracture growth and constant injection rate.

The PKN model assumes plane strain condition in a vertical plane, because of which it is applicable when the fracture length is greater than the fracture height (Figure 1.3). It assumes elliptic shape in the vertical direction and a constant injection rate. Fracture toughness is neglected since it is assumed that the energy required to flow the fluid in the fracture is much greater than that required to propagate the fracture.

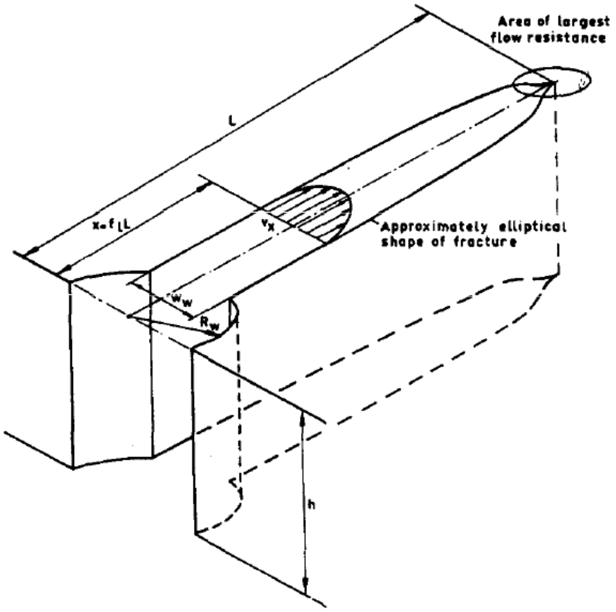

Figure 1.2. Fracture geometry in KGD model (Geertsma and De Klerk, 1969)

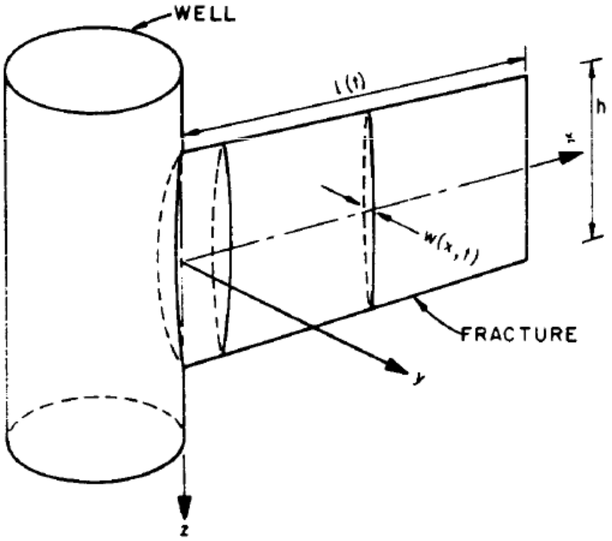

Figure 1.3. Fracture geometry in PKN model (Nordgren, 1972)

The penny-shaped fracture model assumes that the fracture grows radially outward in a plane from an injection source. It was developed for application in geothermal reservoirs where the overburden stress and the minimum horizontal stress are about the same. Injection rate and fluid pressure inside the fracture are assumed to be constant.

These analytical 2-D fracture models are widely used for verifying the more complicated numerical fracturing models. However, since they make restrictive assumptions such as fractures propagating in a homogeneous isotropic formation, they are not used for designing fracturing treatments in the field.

1.3.2. Simplified 3-D models

The next family of fracturing models comprise pseudo 3-D (P3D) and planar 3-D (PL3D) models. These are applicable to fractures spanning multiple layers with some key assumptions, including elastic rock deformation (LEFM), no poroelasticity, transverse isotropic rock and fluid properties, planar fracture geometry, parallel-plate assumption for fluid flow in the fractures, and an analytical expression for fluid leak-off. These assumptions may be valid for some reservoirs or some applications.

Simonson et al. (1978) developed the first P3D model by considering the effects of varying in-situ stresses and varying properties of pay zone and barrier layers on fracture height containment. Several modifications to the P3D model have been proposed (Cleary et al., 1983; Settari and Cleary, 1984; Fung et al., 1987; Meyer, 1989), which are classified into lumped and cell-based approaches (Adachi et al., 2007). In the lumped approach, the fracture is divided into top and bottom half-ellipses and the geometry of both at any given time are calculated (Figure 1.4). In the cell-based approach, the fracture is divided into multiple cells and the geometry of each, assuming PKN model, is calculated (Figure 1.5).

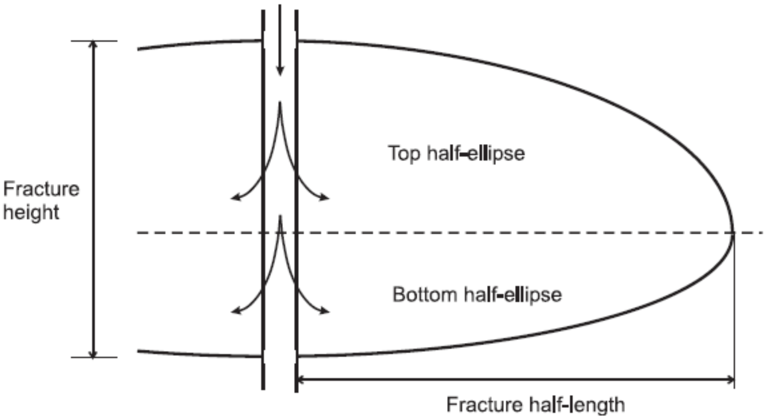

Figure 1.4. Fracture geometry in pseudo 3-D lumped model (Adachi et al., 2007)

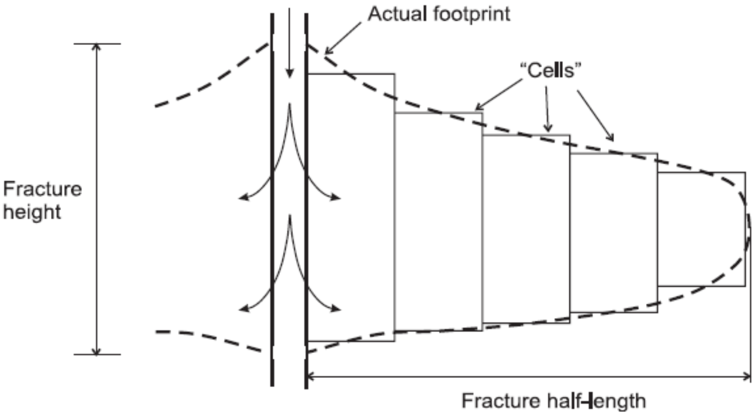

Figure 1.5. Fracture geometry in pseudo 3-D cell-based model (Adachi et al., 2007)

Clifton and Abou-Sayed (1981) proposed the PL3D model by simplifying the elasticity problem into an integral equation that related the fracture pressure to the fracture width, neglecting the fluid leak-off. Several variations of the model have been reported by implementing different meshing schemes and solution strategies for the integral equation (Barree, 1983; Morita et al., 1988; Yew and Weng, 2015).

Due to their applicability to heterogeneous reservoirs and low requirement of computational resources, P3D and PL3D models are used in various commercial simulators (Warpinski et al. 1993).

1.3.3. Non-planar 3-D models

In heterogeneous unconventional reservoirs, many of the assumptions in analytical 2-D and simplified 3-D models are not reasonable. Fractures in such conditions may be non-planar, multi-stranded, and complex due to interactions with reservoir heterogeneities such as layer boundaries, laminations, and natural fractures. Moreover, they may be complex because of the stress shadow effect in some completion designs such as in multi-stage, multi-cluster treatments. Thus, more expensive numerical fracturing models have gained popularity.

Displacement discontinuity based method (DDM) is capable of modeling the interaction of hydraulic fractures with multiple natural fractures using moderate computational resources. Olson (2004) developed a pseudo 3-D DDM model that can simulate multiple propagating fractures accounting for the mechanical stress interaction between them. However, fluid flow in the pore space or in the fracture are not solved, rather a constant pressure boundary condition is assumed in the fractures (Olson, 2008). Subsequently, several authors have presented modifications and improvements of the DDM model (Weng et al., 2011; Sesetty and Ghassemi, 2012; McClure, 2012; Wu and Olson, 2015).

Discrete Element Method (DEM) is another numerical approach of modeling the non-planar growth of hydraulic fractures. The rock is modeled as a group of particles connected with each other through ‘bonds’. When a force exceeding the pre-defined critical strength of a bond is applied, it breaks and initiates a micro-crack. Zhao and Young (2009) developed a 2-D DEM-based hydraulic fracturing model to capture the interactions between a hydraulic fracture and a natural fracture. Using their DEM-based model, Shimizu et al. (2011) showed that the fracture geometry in unconsolidated sands greatly depends on the viscosity of the fracturing fluid. Thallak et al. (1991) concluded from their

DEM simulations that the fractures in unconsolidated sands are influenced more by the stress interactions from each other as compared to the far-field stresses. Although DEM methods can predict complex fracture patterns, they are limited to 2-D plane strain problems at small length scales.

Finite Element Method (FEM) and Finite Volume Method (FVM) coupled with the Cohesive Zone Model (CZM) are also used commonly for simulating hydraulic fractures. Both these methods are implemented in commercial or open-source packages for continuum mechanics and provide a good foundation for further development. By coupling CZM with FEM-based ABAQUS software, Yao et al. (2010) demonstrated that their model predicted the fracture geometry in ductile shales more accurately than the PKN and P3D models. Combining CZM with FVM-based OpenFOAM package, Manchanda (2015) simulated the growth of multiple non-planar fractures both in 2-D and 3-D and presented several applications related to fracturing in unconventional reservoirs.

Extended Finite Element Method (XFEM) have been applied for hydraulic fracture modeling. Dahi-Taleghani and Olson (2011) developed an energy criterion with their XFEM model to predict diversion of a hydraulic fracture upon interaction with a cemented or uncemented natural fracture. Haddad and Sepehrnoori (2016) developed planar CZM and XFEM-based CZM models to simulate the stress interactions between hydraulic fractures originating from three perforation clusters of a single stage.

Damage models based on phase-field theory and peridynamics theory have been recently applied for investigating the growth of complex hydraulic fractures. Mikelić et al. (2015) presented theoretical considerations for the application of the phase-field model in hydraulic fracturing. Wilson and Landis (2016) applied the phase-field model to capture the asymptotic solutions for fracture growth. Ouchi (2016) developed a comprehensive model by generalizing the peridynamics theory, initially proposed for solid mechanics, to simulate the growth of complex interacting fractures in heterogeneous reservoirs.

1.4. REVIEW OF PERIDYNAMICS THEORY

Since this dissertation builds upon the peridynamics (PD) theory, it is imperative to review the related concepts. Peridynamics was introduced by Silling (2000) as a reformulation of the continuum theory for elasticity problems involving discontinuities. Unlike classical continuum theory which requires the computation of gradient/flux terms, PD is an integral formulation and does not involve the calculation of spatial derivatives. Thus, the same formulation is applicable to both continuous and discontinuous media, such as cracks. The PD theory has been applied to various engineering problems including viscoplasticity, transient heat conduction, and crack branching (Foster et al., 2010; Bobaru and Duangpanya, 2010; Ha and Bobaru, 2010).

As illustrated in Figure 1.6, a PD body is supposed to be comprised of material points. A material point at position $\boldsymbol{x} \epsilon \mathcal{B}$ interacts with all the other material points at position $\boldsymbol{x}'$ within a length scale called a horizon, $\mathcal{H}_x$. Force interactions between these nodes happen through the connecting bonds, $\boldsymbol{\xi}$. In 2-D or 3-D problems, the horizon is respectively a circle or sphere of radius δ.

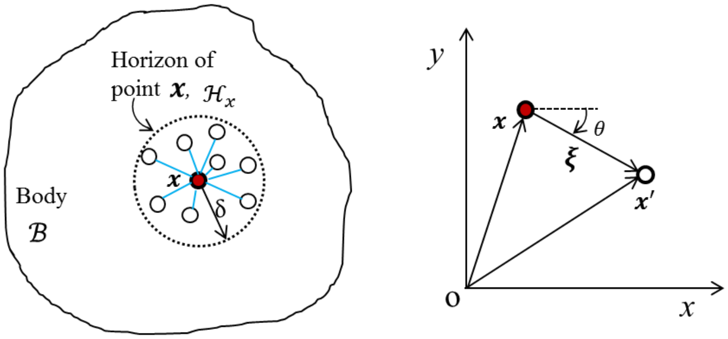

Figure 1.6. (a) Schematic of a peridynamic material point $\boldsymbol{x}$ and connected flow bonds in its horizon. (b) Schematic of a flow bond between a material point $\boldsymbol{x}$ with its non-local neighboring material point $\boldsymbol{x}'$ in 2-D (Katiyar et al., 2014).

PD has three different formulations as shown in Figure 1.7. In the bond-based formulation, pairwise force interaction of the same magnitude is assumed within a bond. This introduces limitations on the model such that it can be used to simulate only an isotropic, linear, micro-elastic material with a Poisson ratio of 0.25. For application to a broader range of materials, Silling et al. (2007) proposed the concept of states, which was used to derive the state-based formulations. PD states are a function of position and time, which are enclosed in square brackets. They operate on a vector connecting two material points, which are written in angled brackets. Depending on whether the result of this operation is a scalar or a vector, the PD state is termed as a "scalar state" or a "vector state". Scalar states are represented by underlined non-bold letters, whereas vector states are represented by underlined bold letters.

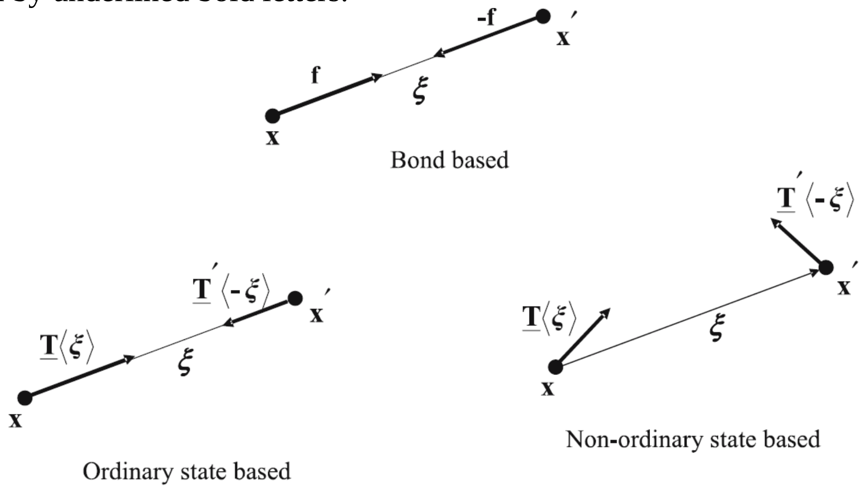

Bond based

Ordinary state based

Non-ordinary state based

Figure 1.7. Schematic of bond-based, ordinary state-based, and non-ordinary state-based peridynamic model (Silling et al., 2007).

Reference and deformed configurations are introduced to track the deformation of the material points upon application of forces. In state-based theory, the relative position of material points $\boldsymbol{x}$ and $\boldsymbol{x}'$ in the reference configuration is defined by the reference position vector state $\underline{\boldsymbol{X}}$.

$$\underline{\boldsymbol{X}}\langle\xi\rangle = \xi = \boldsymbol{x}' - \boldsymbol{x} \tag{1.1}$$

where $\boldsymbol{\xi}$ is a bond vector. The relative position of these points in the deformed configuration is defined by the deformed position vector state $\underline{\boldsymbol{Y}}$.

$$\underline{\boldsymbol{Y}}\langle\xi\rangle = \xi + \boldsymbol{\eta} = \boldsymbol{y}(\boldsymbol{x}') - \boldsymbol{y}(\boldsymbol{x}) \tag{1.2}$$

where $\boldsymbol{y}$ represents the coordinates in the deformed configuration, and $\boldsymbol{\eta}$ is the relative displacement given by:

$$\boldsymbol{\eta} = \boldsymbol{u}(\boldsymbol{x}') - \boldsymbol{u}(\boldsymbol{x}) \tag{1.3}$$

where $\boldsymbol{u}$ is the displacement vector field.

The bond length scalar states $\underline{\boldsymbol{x}}$ and $\underline{\boldsymbol{y}}$ in the reference and deformed configurations respectively are given by:

$$\begin{gathered} \underline{x}\langle\xi\rangle = \|\boldsymbol{\xi}\| \\ \underline{y}\langle\xi\rangle = \|\boldsymbol{\xi} + \boldsymbol{\eta}\| \end{gathered} \tag{1.4}$$

1.5. REVIEW OF PERIDYNAMICS-BASED POROELASTIC MODEL

Peridynamics theory was originally developed by Silling (2000) for applications to elastic materials. Later, it was extended by Katiyar et al. (2014) for modeling poroelastic media that are commonly found in subsurface problems. In this section, we summarize the state-based PD poroelastic governing equations and constitutive relations, with reference to the original equations, wherever necessary.

1.5.1. Momentum conservation for the rock

The governing equation for momentum balance in a PD node at position $\boldsymbol{x} \boldsymbol{\epsilon} \boldsymbol{B}$ (Figure 1.6) and time t is given by the state-based PD theory:

$$\frac{\partial^2}{\partial t^2}(\rho_r \boldsymbol{u}) = \int_{\mathcal{H}_x} (\underline{\boldsymbol{T}}[\boldsymbol{x}, t]\langle\xi\rangle - \underline{\boldsymbol{T}}[\boldsymbol{x}', t]\langle -\xi\rangle)\, dV_{x'} + b[\boldsymbol{x}] \tag{1.5}$$

where ρ_r is rock density, $dV_{\boldsymbol{x}'}$ is the differential volume of material point $\boldsymbol{x}'$, and the PD force vector state $\underline{\boldsymbol{T}}[\boldsymbol{x},t]\langle\xi\rangle$ is computed as:

$$\underline{\boldsymbol{T}}[\boldsymbol{x},t]\langle\xi\rangle = \underline{t}[\boldsymbol{x},t]\langle\xi\rangle\frac{\boldsymbol{\xi}+\boldsymbol{\eta}}{\|\boldsymbol{\xi}+\boldsymbol{\eta}\|} \tag{1.6}$$

where the original constitutive relation for the PD force scalar state $\underline{t}[\boldsymbol{x},t]\langle\boldsymbol{\xi}\rangle$ is modified to account for the poroelastic effects.

$$\begin{aligned}
&\underline{t}[\boldsymbol{x},t]\langle\boldsymbol{\xi}\rangle = \frac{2\big((K_b - G/3)\theta - \alpha P\big)}{m}\underline{\omega}\,\underline{x}\langle\boldsymbol{\xi}\rangle + \frac{8G}{m}\underline{\omega}\,\underline{e^d}\langle\boldsymbol{\xi}\rangle && \text{2-D plane strain}\\
&\underline{t}[\boldsymbol{x},t]\langle\boldsymbol{\xi}\rangle = \frac{3(K_b\theta - \alpha P)}{m}\underline{\omega}\,\underline{x}\langle\boldsymbol{\xi}\rangle + \frac{15G}{m}\underline{\omega}\,\underline{e^d}\langle\boldsymbol{\xi}\rangle && \text{3-D}
\end{aligned} \tag{1.7}$$

where P is fluid pressure, K_b is bulk modulus of the rock grains, K_b is bulk modulus of the rock, and G is shear modulus of the rock. $\underline{\omega}$ is the influence function, discussed in more detail in Chapter 2. Biot coefficient α, weighted volume m, dilatation θ, elongation scalar state $\underline{e}\langle\boldsymbol{\xi}\rangle$, and its deviatoric part $\underline{e^d}\langle\boldsymbol{\xi}\rangle$ are computed as:

$$\alpha = 1 - \frac{K_b}{K_m} \tag{1.8}$$

$$\begin{aligned}
&m = \int_{\mathcal{H}_x}\underline{\omega}\,\underline{x}\langle\xi\rangle.\underline{x}\langle\xi\rangle\,dA_{\boldsymbol{x}'} = \delta^4\pi && \text{2-D}\\
&m = \int_{\mathcal{H}_x}\underline{\omega}\,\underline{x}\langle\xi\rangle.\underline{x}\langle\xi\rangle\,dV_{\boldsymbol{x}'} = 2\delta^3\pi/3 && \text{3-D}
\end{aligned} \tag{1.9}$$

$$\begin{aligned}
\theta &= \frac{2}{m}\int_{\mathcal{H}_x}\underline{\omega}\,\underline{x}\langle\xi\rangle.\underline{e}\langle\xi\rangle\,dA_{\boldsymbol{x}'}\\
\theta &= \frac{3}{m}\int_{\mathcal{H}_x}\underline{\omega}\,\underline{x}\langle\xi\rangle.\underline{e}\langle\xi\rangle\,dV_{\boldsymbol{x}'}
\end{aligned} \tag{1.10}$$

$$\begin{aligned}
\underline{e}\langle\xi\rangle &= \|\boldsymbol{\xi}+\boldsymbol{\eta}\| - \|\boldsymbol{\xi}\|\\
\underline{e^d}\langle\xi\rangle &= \underline{e}\langle\xi\rangle - \frac{\theta}{3}\underline{x}\langle\xi\rangle
\end{aligned} \tag{1.11}$$

1.5.2. Mass conservation for the pore fluid

For a PD material point $\boldsymbol{x}$ interacting with its neighboring material point $\boldsymbol{x}'$, the fluid mass balance is given by:

$$\frac{\partial}{\partial t}(\rho_w[\boldsymbol{x}]\phi[\boldsymbol{x}]) = \int_{\mathcal{H}_x} (\underline{Q}[\boldsymbol{x}]\langle\xi\rangle - \underline{Q}[\boldsymbol{x}']\langle-\xi\rangle)\, dV_{\boldsymbol{x}'} + R[\boldsymbol{x}] \tag{1.12}$$

where ρ_w is fluid density, ϕ is medium porosity, R is a specified mass flow density field, and $\underline{Q}[\boldsymbol{x}]\langle\boldsymbol{\xi}\rangle$ is the PD mass flow scalar state defined as:

$$\underline{Q}[\boldsymbol{x}]\langle\xi\rangle = \frac{\gamma}{2\mu_w}\underline{\omega}\langle\xi\rangle\rho_w \frac{\boldsymbol{\xi}\mathbb{K}[\boldsymbol{x},\boldsymbol{x}']\boldsymbol{\xi}}{||\xi||^4}(\Phi[\boldsymbol{x}'] - \Phi[\boldsymbol{x}]) \tag{1.13}$$

$$-\underline{Q}[\boldsymbol{x}']\langle-\xi\rangle = \frac{\gamma}{2\mu_w}\underline{\omega}\langle\xi\rangle\rho_w \frac{\boldsymbol{\xi}\mathbb{K}[\boldsymbol{x},\boldsymbol{x}']\boldsymbol{\xi}}{||\xi||^4}(\Phi[\boldsymbol{x}'] - \Phi[\boldsymbol{x}]) \tag{1.14}$$

where μ_w is fluid viscosity, and γ is the scaling factor, discussed in more detail in Chapter 2. Φ is the fluid potential given as:

$$\Phi[\boldsymbol{x}] = P[\boldsymbol{x}] + \rho_w[\boldsymbol{x}]gz[\boldsymbol{x}] \tag{1.15}$$

$\mathbb{K}[\boldsymbol{x},\boldsymbol{x}']$ is a symmetric constitutive tensor, such that each of its elements is a symmetric function of $\boldsymbol{x}'$ and $\boldsymbol{x}$:

$$\mathbb{K}[\boldsymbol{x},\boldsymbol{x}'] = \boldsymbol{k}[\boldsymbol{x}] - \frac{1}{2+d}trace(\boldsymbol{k}[\boldsymbol{x}])\boldsymbol{I} \tag{1.16}$$

The effect of poroelasticity on medium porosity ϕ is calculated as:

$$\phi^{(n+1)}[\boldsymbol{x}] = \phi^{(n)}[\boldsymbol{x}](1 - c_r\Delta P) + \alpha\left(1 - \varepsilon_v{}^{(n)}\right)(c_r\Delta P + \Delta\theta_{local}) \tag{1.17}$$

where superscripts $(n+1)$ and (n) represent the values at the current and previous time steps respectively, c_r is rock compressibility, ε_v is volumetric strain, and θ_{local} is local dilatation.

$$
\begin{aligned}
\theta_{local} &= \frac{2}{m}\int_{\mathcal{H}_{x,local}} \underline{\omega}\ \underline{x}\langle\xi\rangle . \underline{e}\langle\xi\rangle dA_{x'}, \quad \text{2-D} \\
\theta_{local} &= \frac{3}{m}\int_{\mathcal{H}_{x,local}} \underline{\omega}\ \underline{x}\langle\xi\rangle . \underline{e}\langle\xi\rangle dV_{x'}, \quad \text{3-D}
\end{aligned}
\tag{1.18}
$$

1.6. Review of Peridynamics-Based Hydraulic Fracturing Model

The peridynamics-based pororelastic model was further developed for hydraulic fracturing applications by Ouchi (2016). Each computational cell could potentially have five primary unknowns corresponding to *x*-, *y*-, and *z*- displacements, matrix pore pressure *P*, and fracturing fluid pressure P_f (Figure 1.8). The three components of displacement and the matrix pore pressure are solved using equations (1.5) and (1.12) respectively. The fracturing fluid pressure is solved using another mass balance equation over the fracturing fluid, which will be reviewed in this section. In addition, some new formulations and modifications to the previous equations will also be reviewed.

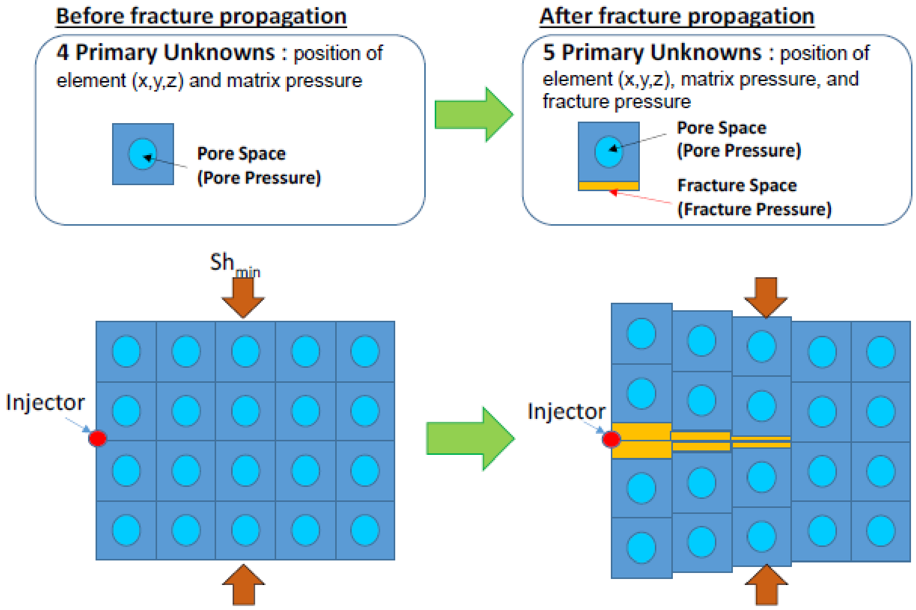

Figure 1.8. Peridynamics-based hydraulic fracturing model (Ouchi, 2016).

1.6.1. Momentum conservation for the rock

The rock displacement equation remains the same as in the poroelastic model (equation (1.5)). However, the force scalar state, $\underline{t}[\boldsymbol{x},t]\langle\xi\rangle$ is modified based on whether a bond is unbroken, broken and not passing through a fracture space, or broken and passing through a fracture space. The force scalar state for the three categories is given by equations (1.7), (1.19), and (1.20) respectively.

$$\underline{t}[\boldsymbol{x},t]\langle\xi\rangle = \frac{2\alpha P}{m}\underline{\omega}\,\underline{x}\langle\xi\rangle \qquad \text{2-D plane strain}$$
$$\underline{t}[\boldsymbol{x},t]\langle\xi\rangle = \frac{3\alpha P}{m}\underline{\omega}\,\underline{x}\langle\xi\rangle \qquad \text{3-D} \tag{1.19}$$

$$\underline{t}[\boldsymbol{x},t]\langle\xi\rangle = \frac{2\alpha P_f}{m}\underline{\omega}\,\underline{x}\langle\xi\rangle \qquad \text{2-D plane strain}$$
$$\underline{t}[\boldsymbol{x},t]\langle\xi\rangle = \frac{3\alpha P_f}{m}\underline{\omega}\,\underline{x}\langle\xi\rangle \qquad \text{3-D} \tag{1.20}$$

1.6.2. Damage model

In the PD theory, material failure is represented by a scalar field referred to as damage d. Damage at a material point is defined as the ratio of the number of broken bonds passing through the point to the total number of bonds passing through the point. Thus, damage ranges between 0 and 1.

$$d[\boldsymbol{x}] = 1 - \frac{\int_{\mathcal{H}_x}\beta\langle\xi\rangle dV_{\boldsymbol{x}'}}{\int_{\mathcal{H}_x} dV_{\boldsymbol{x}'}} \tag{1.21}$$

The state-based PD theory introduced two types of criteria for bond failure – critical stretch and critical energy criteria. Both were implemented by Ouchi (2016) in the PD-based fracturing simulator.

The strain s in a bond is defined as:

$$s = \frac{\underline{e}\langle\xi\rangle}{\underline{x}\langle\xi\rangle} = \frac{\|\boldsymbol{\xi}+\boldsymbol{\eta}\| - \|\boldsymbol{\xi}\|}{\|\boldsymbol{\xi}\|} \tag{1.22}$$

In the critical strain criterion, the force scalar state for a bond vanishes if the strain in the bond exceeds a certain critical strain s_c. This is ensured in the simulator by multiplying a boolean function $\beta\langle\xi\rangle$ as defined below. The critical strain is a material property, which depends on the energy release rate and the length scale under consideration.

$$\beta\langle\xi\rangle = \begin{cases} 0 & (s > s_c) \\ 1 & (otherwise) \end{cases} \tag{1.23}$$

By equating the work required to break all the bonds across a fracture plane to the critical energy release rate of a material, Silling and Askari (2005) derived the critical strain s_c in a bond.

$$G_c = \int_0^{\delta}\int_0^{2\pi}\int_z^{\delta}\int_0^{\cos^{-1}(z/\xi)} \frac{1}{2}(c{s_c}^2\xi)\xi^2 \sin\varphi \, d\varphi \, d\xi \, d\theta \, dz = \frac{\pi c {s_c}^2 \delta^5}{10} \qquad \text{3-D} \tag{1.24}$$

$$s_c = \sqrt{\frac{5G_c}{9K\delta}} \qquad \text{3-D} \tag{1.25}$$

Equating G_c to the energy release rate from LEFM, one can obtain the critical strain s_c in terms of the material properties, as demonstrated in equation (1.30) for the critical energy criterion.

In the critical energy criterion proposed by Foster et al. (2011), the force the force scalar state for a bond vanishes if the energy density stored in the bond (due to relative displacement of the associated material points) exceeds a certain critical energy density ω_c. Equation (1.26) shows that the energy density stored in a bond $\boldsymbol{\xi}$ is calculated by integrating the infinitesimal relative displacement between the concerned material points $\boldsymbol{x}$ and $\boldsymbol{x}'$ caused by the total force vector state acting on the bond. It must be noted that the energy density in a bond is evaluated only when it is under tension (equation (1.27)).

$$\omega_{\xi} = \int_{0}^{\boldsymbol{\eta}(t_{final})} \left(\underline{T}^{*}[\boldsymbol{x}, t]\langle\xi\rangle - \underline{T}^{*}[\boldsymbol{x}', t]\langle-\xi\rangle\right). d\boldsymbol{\eta} \tag{1.26}$$

$$\underline{T}^{*}[\boldsymbol{x}, t]\langle\xi\rangle - \underline{T}^{*}[\boldsymbol{x}', t]\langle-\xi\rangle = \max\left(\underline{t}[\boldsymbol{x}, t]\langle\xi\rangle - \underline{t}[\boldsymbol{x}', t]\langle-\xi\rangle, 0.0\right) \frac{\boldsymbol{\xi} + \boldsymbol{\eta}}{\|\boldsymbol{\xi} + \boldsymbol{\eta}\|} \tag{1.27}$$

where $\boldsymbol{\eta}(t_{final})$ is the final relative displacement.

Using equation (1.28), the PD energy release rate G_c is obtained by integrating the energy required to create a unit fracture as a function of critical energy density, which is equivalent to the energy required to break all the bonds connecting each point A along $0 \le z \le \delta$ to point B in the spherical cap (the green region in Figure 1.9) using the coordinate system centered at A. The PD critical energy density ω_c in each bond is obtained by equating the PD energy release rate to the energy release rate of the fracture given by the classical Linear Elastic Fracture Mechanics (LEFM) theory.

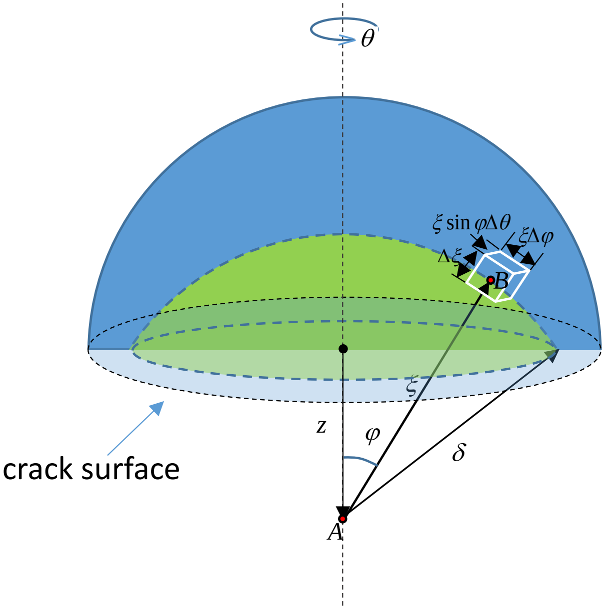

Figure 1.9. Calculation of energy release rate in Peridynamics theory (Ouchi, 2016).

$$G_c = \int_0^\delta \int_z^\delta \int_{\sin^{-1}(z/\xi)}^{\pi-\sin^{-1}(z/\xi)} \omega_c \zeta \, d\zeta \, d\theta \, dz = \frac{4\delta^3}{9}\omega_c \qquad \text{2-D}$$
$$G_c = \int_0^\delta \int_0^{2\pi} \int_z^\delta \int_0^{\cos^{-1}(z/\xi)} \omega_c \xi^2 \sin\varphi \, d\varphi \, d\xi \, d\theta \, dz = \frac{\pi\delta^4}{4}\omega_c \qquad \text{3-D} \tag{1.28}$$

Solving equation (1.28) for the PD critical energy density:

$$\omega_c = \frac{9}{4\delta^3} G_c \qquad \text{2-D}$$
$$\omega_c = \frac{4}{\pi\delta^4} G_c \qquad \text{3-D} \tag{1.29}$$

Equating the energy release rate from PD to that from LEFM according to the dimensionality of the problem:

$$\omega_c = \frac{9}{4\delta^3} G_c = \frac{9}{4\delta^3} \frac{{K_{IC}}^2(1-\nu^2)}{E} \qquad \text{2-D plane strain}$$
$$\omega_c = \frac{4}{\pi\delta^4} G_c = \frac{4}{\pi\delta^4} \frac{{K_{IC}}^2}{E} \qquad \text{3-D} \tag{1.30}$$

where E is the Young's modulus, ν is the Poisson ratio, and K_{IC} is the fracture toughness.

If the energy density stored in a bond $\omega_{\boldsymbol{\xi}}$ exceeds the critical energy density $\boldsymbol{\omega_c}$, the bond is broken and its force scalar state is set to zero by multiplying the following Boolean function:

$$\beta\langle\boldsymbol{\xi}\rangle = \begin{cases} 0 & (\omega_{\boldsymbol{\xi}} > \omega_c) \\ 1 & (otherwise) \end{cases} \tag{1.31}$$

1.6.3. Mass conservation for the pore fluid

To account for the leak-off of the fracturing fluid into the reservoir matrix, a new source term $I[\boldsymbol{x}]$ is added to equation (1.12).

$$\frac{\partial}{\partial t}(\rho_w[\boldsymbol{x}]\phi[\boldsymbol{x}]) = \int_{\mathcal{H}_x} (\underline{Q}[\boldsymbol{x}]\langle\boldsymbol{\xi}\rangle - \underline{Q}[\boldsymbol{x}']\langle-\boldsymbol{\xi}\rangle) \, dV_{x'} + R[\boldsymbol{x}] + I[\boldsymbol{x}] \tag{1.32}$$

The leak-off is modeled as a source term assuming the Darcy flow.

$$I[\boldsymbol{x}] = -\frac{\rho_f[\boldsymbol{x}]k_{leak}A}{V\mu_f}\frac{dP}{dl} = \frac{\rho_f[\boldsymbol{x}]k_{leak}\Delta A_p[\boldsymbol{x}](\Phi_f[\boldsymbol{x}] - \Phi[\boldsymbol{x}])}{\Delta V[\boldsymbol{x}]\mu_f(l_p/2)} \tag{1.33}$$

$$k_{leak} = \boldsymbol{n}_{surf}.\,(\boldsymbol{k}[\boldsymbol{x}]\boldsymbol{n}_{surf}) \tag{1.34}$$

1.6.4. Mass conservation for the fracturing fluid

The flow of fracturing fluid is modeled based on the lubrication theory.

$$\frac{\partial}{\partial t}\big(\rho_f[\boldsymbol{x}]\phi_f[\boldsymbol{x}]\big) = \int_{\mathcal{H}_{x,local}} (\underline{Q}_f[\boldsymbol{x}]\langle\xi\rangle - \underline{Q}_f[\boldsymbol{x}']\langle-\xi\rangle)\, dV_{x'} + R_f[\boldsymbol{x}] - I[\boldsymbol{x}] \tag{1.35}$$

where ρ_f is the fracturing fluid density, ϕ_f is fracture porosity, R_f is a specified fracturing fluid mass flow density field, and $\underline{Q}_f[\boldsymbol{x}]\langle\boldsymbol{\xi}\rangle$ is the PD mass flow scalar state for the fracturing fluid.

$$\underline{Q}_f\langle\xi\rangle = \frac{\gamma}{2\mu_f}\rho_f\frac{k_f[\boldsymbol{x}]}{2||\boldsymbol{\xi}||^2}(\Phi_f[\boldsymbol{x}'] - \Phi_f[\boldsymbol{x}]) \tag{1.36}$$

where μ_w is fluid viscosity, k_f is fracture permeability, and Φ_f is the fracturing fluid potential.

Fracture porosity, which is the fraction of fracture volume to control volume, is given by:

$$\begin{aligned} &\phi_f[\boldsymbol{x}] = 0 && \text{for } d \le d_c \\ &\phi_f[\boldsymbol{x}] = \theta_{local} - \theta_{local}(s_c) && \text{for } d > d_c \end{aligned} \tag{1.37}$$

where $\theta_{local}(s_c)$ at a given point i is the local dilatation evaluated at the critical strain.

$$\begin{aligned}&\theta_{local,i}(s_c)\\&=\sum_{j=1}^{N_{local}}\left\{\frac{\underline{\omega}_i\left\|\boldsymbol{x_j}-\boldsymbol{x_i}\right\|{e_i}^{*(n+1)}dV_{x_j}}{m_{local,i}}\right\}\\&=\sum_{j=1}^{N_{local}}\left\{\frac{\underline{\omega}_i\left\|\boldsymbol{x_j}-\boldsymbol{x_i}\right\|\left(\min\left(\left\|\boldsymbol{y_j}^{(\boldsymbol{n+1})}-\boldsymbol{y_i}^{(\boldsymbol{n+1})}\right\|,s_c\left\|\boldsymbol{x_j}-\boldsymbol{x_i}\right\|\right)-\left\|\boldsymbol{x_j}-\boldsymbol{x_i}\right\|\right)dV_{x_j}}{m_{local,i}}\right\}\end{aligned}\tag{1.38}$$

where $m_{local,i}$ and s_c at a given point i are calculated as:

$$m_{local,i}=\sum_{j=1}^{N_{local}}\underline{\omega}_j\left\{\underline{\omega}_i\left\|\boldsymbol{x_j}-\boldsymbol{x_i}\right\|^2dV_{x_j}\right\}\tag{1.39}$$

$$s_c=\left.\frac{\|\boldsymbol{\xi}+\boldsymbol{\eta}\|-\|\boldsymbol{\xi}\|}{\|\boldsymbol{\xi}\|}\right|_{\omega_\xi=\omega_c}=\left.\frac{\left\|\boldsymbol{y_j}^{(\boldsymbol{n+1})}-\boldsymbol{y_i}^{(\boldsymbol{n+1})}\right\|-\left\|\boldsymbol{x_j}-\boldsymbol{x_i}\right\|}{\left\|\boldsymbol{x_j}-\boldsymbol{x_i}\right\|}\right|_{\omega_\xi=\omega_c}\tag{1.40}$$

The fracture permeability k_f is estimated based on the fracture width w, which in turn is calculated based on the fracture volume.

$$k_f=\frac{w^2}{12}\tag{1.41}$$

$$w=\frac{\Delta V\phi_f}{\Delta A_p}\tag{1.42}$$

1.7. OUTLINE OF THE DISSERTATION

This dissertation is divided into eight chapters. Chapter 2 presents a general peridynamics flow model. Chapter 3 couples the general flow model with the existing hydraulic fracturing simulator. Chapter 4 demonstrates an application of the new fracturing model. Chapter 5 develops the poroelastic crossing criteria. Chapter 6 couples the peridynamics simulator with the Finite Volume Method. Chapter 7 presents applications of the coupled PD-FVM simulator.

Chapter 2 extends the peridynamics-based single-phase flow model for Newtonian, slightly compressible fluids developed by Katiyar et al. (2014) to multiphase, multicomponent flow model for non-Newtonian, compressible fluids. Verification problems involving porous flow are presented, showing the convergence of the non-local model to the classical local model in limiting cases.

Chapter 3 presents the incorporation of the general flow model in the peridynamics-based hydraulic fracturing simulator developed by Ouchi (2016). Validation problems involving comparison with recent laboratory experiments are also demonstrated.

Chapter 4 introduces an application of the extended fracturing simulator for modeling fracture propagation in depleted reservoirs. Peridynamics is shown to capture the attraction of a fracture from a new (child) well towards the depleted region of an old (parent) well.

Chapter 5 investigates the interaction of a hydraulic fracture with a natural fracture. It is identified that a propagating hydraulic fracture causes remote shear failure of a natural fracture, resulting in poroelastic stress relaxation on the natural fracture and bending of the hydraulic fracture before intersection. This makes the turning of the hydraulic fracture along the natural fracture more feasible and significantly modifies the crossing criteria that were derived in the literature using the Linear Elastic Fracture Mechanics theory.

Chapter 6 couples the peridynamics-based poroelastic model with the Finite Volume Method (FVM) for improved computational performance. Verification problems concerning porous flow and poroelastic flow are demonstrated. Two different approaches for matrix assembly are proposed and one is shown to considerably outperform the other, resulting in shorter computational times relative to the pure peridynamics model.

Chapter 7 extends the coupling of Peridynamics-Finite Volume poroelastic model for applications in hydraulic fracturing. A coupled model domain is divided into peridynamic and finite-volume subdomains. A fracture is propagated in either of the two subdomains. Validation of both the types is presented against laboratory experiments.

Stress changes due to a fracture propagating in finite-volume are monitored to capture material damage in remote heterogeneous peridynamics regions. The extent of this material damage away from the fracture face provides an estimate of the Stimulated Reservoir Volume (SRV) created during a fracturing job in unconventional reservoirs.

Chapter 8 summarizes the contributions of the research, presents overall conclusions and makes recommendations for future work.

CHAPTER 2: DEVELOPMENT OF A GENERAL PERIDYNAMICS-BASED FLUID FLOW MODEL*

2.1. INTRODUCTION

In a recent paper by Katiyar et al. (2014), a detailed mathematical formulation to obtain a governing peridynamic equation of transport of a single Newtonian fluid of small and constant compressibility through arbitrary heterogeneous porous media was developed. The adjective "peridynamic" is used here due to the similarity of the formulation to the peridynamic theory developed by Silling (2000) and Silling et al. (2007) within the field of solid mechanics. The peridynamic formulation was verified by simulating the transport of a fluid of uniform properties through a porous medium and comparing the results with those from a corresponding analytical model derived from the classical theory of flow in porous media. The peridynamic porous flow is broadly aimed at simulating the transport of hydrocarbons as well as other complex fluids in fractured heterogeneous reservoirs. Reservoir hydrocarbons can be compressible, non-Newtonian and present in multiple phases. These fluids are also transported through the reservoirs for different applications such as hydraulic fracturing. Therefore, to simulate more realistic scenarios of fluid transport in heterogeneous porous media, the present work extends the previously developed model (Katiyar et al., 2014) to a more general peridynamic model of multiphase transport of a compressible, non-Newtonian fluid in porous media.

In Katiyar et al. (2014), motivations for developing a non-local peridynamic formulation for modeling porous flow were discussed. For completeness, some of the

---

*[1]Katiyar, Amit; [1]Agrawal, Shivam; Ouchi, Hisanao; Seleson, Pablo; Foster, John T; and Sharma, Mukul M. 2020. "A General Peridynamics Model for Multiphase Transport of Non-Newtonian Compressible Fluids in Porous Media." Journal of Computational Physics 402: 109075. Katiyar derived and documented the formulation in consultation with Seleson and Foster, Agrawal coded the general flow model into the peridynamics-based simulator developed by Ouchi, conducted the simulations, performed the convergence study, and documented the numerical sections, and Sharma supervised the research.

advantages are summarized here. Fundamentally, the integral-equation based non-local peridynamic formulation remains valid even when discontinuities in the field variables appear in the domain. The peridynamic formulation also preserves both strong and weak discontinuities across domain boundaries without the need of special interface conditions as required by an equivalent classical model, for example an explicit flux continuity condition. Various complex systems in nature can elucidate diffusion processes due to local as well non-local potential differences. Non-local transport of fluids, observed in geological formations (Koch and Brady, 1988; Cortis and Berkowitz, 2004; Ganti et al., 2010), can be attributed to a reservoir's multi-scale heterogeneity in the form of material properties and/or natural fractures. The integral equation based non-local theory of peridynamics allows modeling of the transport effects of such spatial non-locality without explicitly resolving the multiscale heterogeneities. In addition to capturing this non-local transport, the fluid-flow formulation presented here provides a novel approach for simulating complex fluid-driven cracks when coupling it with the existing fracture mechanics model from peridynamic theory. Thus, it has practical applications in simulating hydraulic fracturing of unconventional hydrocarbon reservoirs.

The theory of Peridynamics was originally developed by Silling (2000) as a reformulation of the classical equation of motion for modeling elasticity and material failure in solid materials and structures. Bobaru and Duangpanya (2010) extended its application for simulating transient heat conduction in bodies with evolving discontinuities. Katiyar et al. (2014) developed and implemented a peridynamics theory for simulating fluid flow in porous media though limiting it only to Newtonian fluids of constant and small compressibility. In the present work, through specializing the constitutive model of Seleson et al. (2013), such limitations are relaxed to simulate compressible and non-Newtonian fluids.

2.2. MATHEMATICAL MODEL

In this chapter, we use both lower-case and upper-case letters for scalars, e.g. ρ, μ, t, A, V, lower case boldface letters and symbols for vectors, e.g., $\boldsymbol{x}$, $\boldsymbol{u}$, $\boldsymbol{\xi}$, upper-case bold face letters for second-order tensors in the local theory, e.g., $\boldsymbol{K}$ and blackboard letters for the corresponding second-order tensors in the non-local theory, e.g., $\mathbb{K}$. Borrowing from the mathematical notation of peridynamic mechanics, mathematical objects called peridynamic states have been introduced for convenience (Silling et al., 2007). In this formulation, we have used vector and scalar valued peridynamic states. Peridynamics states depend on position and time and operate on a vector connecting any two continuum material points. Depending on whether the mapped value of this operation is a scalar or vector, the state is called a scalar-state or a vector-state, respectively. To differentiate, peridynamic scalar states are denoted with underlined letters or symbols and peridynamic vector-states are denoted with underlined bold-faced letters. The mathematical definition of these peridynamic states is provided wherever they have been used. In this chapter, the explicit dependence on time, *t* is dropped to make the notation more concise.

2.2.1. State-Based Peridynamic Formulation of Single-phase Transport of Non-Newtonian and Compressible Fluid through Porous Media

The mass conservation equation for single-phase fluid flow in porous medium at position $\boldsymbol{x} \in \mathcal{B}$ and time *t*, using classical theory (Chen et al., 2006), is

$$\frac{\partial}{\partial t}(\rho[\boldsymbol{x}]\emptyset[\boldsymbol{x}]) = -\nabla\cdot(\rho[\boldsymbol{x}]\boldsymbol{u}[\boldsymbol{x}]) + R[\boldsymbol{x}], \qquad \boldsymbol{u}[\boldsymbol{x}] = -\frac{1}{\mu[\boldsymbol{x}]}\boldsymbol{K}[\boldsymbol{x}]\nabla\Phi[\boldsymbol{x}] \tag{2.1}$$

where ρ is the fluid density, $\emptyset$ is the medium porosity, $\boldsymbol{u}$ is the volumetric flux, $\boldsymbol{K}$ is the material permeability tensor, μ is the fluid viscosity, Φ is the flow potential and R is the mass generation per unit bulk volume per unit time. In peridynamics, a material is assumed to be composed of material points of known density, and every material point interacts with all the neighboring material points inside a non-local region around it. Each interaction pair of a material point with its neighboring material point is referred to as a “bond”.

In Katiyar et al. (2014), using variational arguments, a governing state-based peridynamic equation to simulate transport of single-phase flow of a liquid of small and constant compressibility through heterogeneous porous medium was developed. The resulting formulation is summarized in this sequel. With reference to the body $\mathcal{B}$ in Figure 1.6, the mass conservation equation for single-phase fluid flow in porous medium at position $\boldsymbol{x} \in \mathcal{B}$ and time *t*, using peridynamic theory, is

$$\frac{\partial}{\partial t}(\rho[\boldsymbol{x}]\emptyset[\boldsymbol{x}]) = \int_{\mathcal{H}_x} \left(\underline{Q}[\boldsymbol{x}]\langle\boldsymbol{\xi}\rangle - \underline{Q}[\boldsymbol{x}']\langle-\boldsymbol{\xi}\rangle\right) dV_{x'} + R[\boldsymbol{x}] \tag{2.2}$$

where $\mathcal{H}_x$ is the neighborhood of $\boldsymbol{x}$ referred as the “family of $\boldsymbol{x}$”, which is a ball of radius δ referred to as the “horizon”, $\underline{Q}$ is the peridynamic mass flow scalar state, $\boldsymbol{x}'$ is the position vector the neighboring points of $\boldsymbol{x}$ inside $\mathcal{H}_x$, $dV_{x'}$ is the differential volume of $\boldsymbol{x}'$, and $\underline{Q}[\boldsymbol{x}]\langle\boldsymbol{\xi}\rangle$ defined at position $\boldsymbol{x}$ operating on a “bond” $\boldsymbol{\xi} = \boldsymbol{x}' - \boldsymbol{x}$, maps the bond onto a net mass influx density in that bond. In the local limit, the integral on the right-hand side of equation (2.2) replaces the divergence of the volumetric flux term from the equivalent classical theory.

$$-\nabla.(\rho[\boldsymbol{x}]\boldsymbol{u}[\boldsymbol{x}]) = \lim_{\mathcal{H}_x \to 0} \int_{\mathcal{H}_x} \left(\underline{Q}[\boldsymbol{x}]\langle\boldsymbol{\xi}\rangle - \underline{Q}[\boldsymbol{x}']\langle-\boldsymbol{\xi}\rangle\right) dV_{x'} \tag{2.3}$$

For simplicity, an assumption is made that the governing peridynamic equation for porous flow remains the same for multiple fluid phases and the extension of the model to simulate non-Newtonian and compressible fluid is modeled through the constitutive response.

2.2.1.1. Constitutive model

We propose a modified constitutive model of the form (Katiyar et al., 2014; Seleson, 2010)

$$\underline{Q}[\boldsymbol{x}]\langle\boldsymbol{\xi}\rangle = \frac{\gamma}{2}\underline{\omega}\langle\boldsymbol{\xi}\rangle \frac{\boldsymbol{\xi}.\,\widehat{\mathbb{K}}[\boldsymbol{x}].\,\boldsymbol{\xi}}{\|\boldsymbol{\xi}\|^4}(\Phi[\boldsymbol{x}'] - \Phi[\boldsymbol{x}]), \tag{2.4}$$

where γ is a scaling factor dependent on dimension d of the domain and the horizon size δ, $\underline{\omega}\langle\boldsymbol{\xi}\rangle$ is the influence function that provides an additional mechanism to modulate the non-local interactions (Seleson and Parks, 2011) and $\widehat{\mathbb{K}}$ is a symmetric constitutive tensor defined such that it ensures the convergence of the non-local model to the corresponding local model in the limit of the horizon going to zero. To determine $\widehat{\mathbb{K}}[\boldsymbol{x}]$, a relationship between $\widehat{\mathbb{K}}$ and the material properties (medium permeability $\boldsymbol{K}[\boldsymbol{x}]$, fluid density $\rho[\boldsymbol{x}]$ and fluid viscosity $\mu[\boldsymbol{x}]$) is developed by imposing an equality between the non-local peridynamic model in the limit of horizon size $\delta \to 0$ and the corresponding well-established local model. Substituting equation (2.4) into the governing equation (2.2), we obtain

$$\frac{\partial}{\partial t}(\rho[\boldsymbol{x}]\emptyset[\boldsymbol{x}]) = \frac{\gamma}{2}\int_{\mathcal{H}_x}\underline{\omega}\langle\boldsymbol{\xi}\rangle \frac{\boldsymbol{\xi}.\left(\widehat{\mathbb{K}}[\boldsymbol{x}] + \widehat{\mathbb{K}}[\boldsymbol{x}']\right).\boldsymbol{\xi}}{\|\boldsymbol{\xi}\|^4}(\Phi[\boldsymbol{x}'] - \Phi[\boldsymbol{x}])dV_{x'} + R[\boldsymbol{x}]. \tag{2.5}$$

For the purpose of establishing a connection to the local model, we momentarily assume continuously differentiable fields in $\mathbb{K}$ and Φ such that the following Taylor's expansions are admitted

$$\widehat{\mathbb{K}}[\boldsymbol{x}'] = \widehat{\mathbb{K}}[\boldsymbol{x}] + \boldsymbol{\xi}\cdot\nabla\widehat{\mathbb{K}}[\boldsymbol{x}] + \mathcal{O}(\|\boldsymbol{\xi}\|^{\mathbf{2}}), \tag{2.6}$$

$$\Phi[x'] - \Phi[x] = (\boldsymbol{\xi}\cdot\nabla)\Phi[\boldsymbol{x}] + \frac{1}{2}(\boldsymbol{\xi}\cdot\nabla)(\boldsymbol{\xi}\cdot\nabla)\Phi[\boldsymbol{x}] + \mathcal{O}(\|\boldsymbol{\xi}\|^{\mathbf{3}}), \tag{2.7}$$

Giving

$$\widehat{\mathbb{K}}[\boldsymbol{x}] + \widehat{\mathbb{K}}[\boldsymbol{x}'] = 2\widehat{\mathbb{K}}[\boldsymbol{x}] + \boldsymbol{\xi}\cdot\nabla\widehat{\mathbb{K}}[\boldsymbol{x}] + \mathcal{O}(\|\boldsymbol{\xi}\|^{\mathbf{2}}). \tag{2.8}$$

Substituting equations (2.7) and (2.8) into equation (2.5), we obtain

$$\frac{\partial}{\partial t}(\rho[\boldsymbol{x}]\emptyset[\boldsymbol{x}]) = \gamma\int_{\mathcal{H}_x}\underline{\omega}\langle\boldsymbol{\xi}\rangle\frac{\boldsymbol{\xi}\cdot\left(\widehat{\mathbb{K}}[\boldsymbol{x}] + \frac{1}{2}\boldsymbol{\xi}\cdot\nabla\widehat{\mathbb{K}}[\boldsymbol{x}] + \mathcal{O}(\|\boldsymbol{\xi}\|^{\mathbf{2}})\right)\cdot\boldsymbol{\xi}}{\|\boldsymbol{\xi}\|^{4}}\times\Bigg((\boldsymbol{\xi}\cdot\nabla)\Phi[\boldsymbol{x}]$$
$$+\frac{1}{2}(\boldsymbol{\xi}\cdot\nabla)(\boldsymbol{\xi}\cdot\nabla)\Phi[\boldsymbol{x}] + \mathcal{O}(\|\boldsymbol{\xi}\|^{\mathbf{3}})\Bigg)dV_{x'} + R[\boldsymbol{x}].$$

Collecting terms

$$\frac{\partial}{\partial t}(\rho[\boldsymbol{x}]\emptyset[\boldsymbol{x}])$$
$$= \gamma\int_{\mathcal{H}_x}\left(\underline{\omega}\langle\boldsymbol{\xi}\rangle\frac{\xi_i\xi_m\widehat{\mathbb{K}}_{mn}[\boldsymbol{x}]\xi_n\xi_j\frac{\partial}{\partial x_i x_j}\Phi[\boldsymbol{x}] + \xi_i\xi_m\frac{\partial\widehat{\mathbb{K}}_{mn}[\boldsymbol{x}]}{\partial x_i}\xi_n\xi_j\frac{\partial}{\partial x_j}\Phi[\boldsymbol{x}]}{2\|\boldsymbol{\xi}\|^{4}}\right)dV_{x'}$$
$$+\mathcal{O}(\delta^2) + R[\boldsymbol{x}],$$

$$= \left[\gamma\int_{\mathcal{H}_x}\underline{\omega}\langle\boldsymbol{\xi}\rangle\frac{(\boldsymbol{\xi}\otimes\boldsymbol{\xi})\widehat{\mathbb{K}}[\boldsymbol{x}](\boldsymbol{\xi}\otimes\boldsymbol{\xi})}{2\|\boldsymbol{\xi}\|^{4}}dV_{x'}\right] : (\nabla\otimes\nabla)\Phi[\boldsymbol{x}]$$
$$+\nabla.\left[\int_{\mathcal{H}_x}\gamma\underline{\omega}\langle\boldsymbol{\xi}\rangle\frac{(\boldsymbol{\xi}\otimes\boldsymbol{\xi})\widehat{\mathbb{K}}[\boldsymbol{x}](\boldsymbol{\xi}\otimes\boldsymbol{\xi})}{2\|\boldsymbol{\xi}\|^{4}}dV_{x'}\right].\nabla\Phi[\boldsymbol{x}] + \mathcal{O}(\delta^2) + R[\boldsymbol{x}],$$

$$= \left(\frac{\rho[\boldsymbol{x}]}{\mu[\boldsymbol{x}]}\boldsymbol{K}[\boldsymbol{x}]\right) : (\nabla\otimes\nabla)\Phi[\boldsymbol{x}] + \nabla.\left(\frac{\rho[\boldsymbol{x}]}{\mu[\boldsymbol{x}]}\boldsymbol{K}[\boldsymbol{x}]\right).\nabla\Phi[\boldsymbol{x}] + \mathcal{O}(\delta^2) + R[\boldsymbol{x}],$$

$$= \nabla\cdot\left(\frac{\rho[\boldsymbol{x}]}{\mu[\boldsymbol{x}]}\boldsymbol{K}[\boldsymbol{x}]\nabla\Phi[\mathrm{x}]\right) + \mathcal{O}(\delta^2) + R[\boldsymbol{x}], \tag{2.9}$$

where,

$$\frac{\rho[\boldsymbol{x}]}{\mu[\boldsymbol{x}]}\boldsymbol{K}[\boldsymbol{x}] = \int_{\mathcal{H}_x} \gamma \underline{\omega}\langle\boldsymbol{\xi}\rangle \frac{(\boldsymbol{\xi}\otimes\boldsymbol{\xi})\widehat{\mathbb{K}}[\boldsymbol{x}](\boldsymbol{\xi}\otimes\boldsymbol{\xi})}{2\|\boldsymbol{\xi}\|^4}\, dV_{x'}. \tag{2.10}$$

Taking $\delta \to 0$, equation (2.1) is recovered from equation (2.9). By writing equation (2.10) in component form, a relationship between constitutive tensor $\widehat{\mathbb{K}}$ and material properties (medium permeability $\boldsymbol{K}[\boldsymbol{x}]$, fluid density $\rho[\boldsymbol{x}]$ and fluid viscosity $\mu[\boldsymbol{x}]$) is established with a judicious choice of scaling factor γ

$$\frac{\rho[\boldsymbol{x}]}{\mu[\boldsymbol{x}]}K_{ij}[\boldsymbol{x}] = \gamma\widehat{\mathbb{K}}_{nm}[\boldsymbol{x}] \int_{\mathcal{H}_x} \underline{\omega}\langle\boldsymbol{\xi}\rangle \frac{\xi_i\xi_n\xi_m\xi_j}{2\|\boldsymbol{\xi}\|^4}\, dV_{x'}. \tag{2.11}$$

Following Katiyar et al. (2014) and Seleson et al. (2013), it can be shown that the right hand side in equation (2.11) simplifies to

$$\begin{aligned}\frac{\rho[\boldsymbol{x}]}{\mu[\boldsymbol{x}]}K_{ij}[\boldsymbol{x}] &= \gamma\big(\widehat{\mathbb{K}}_{ij}[\boldsymbol{x}] + \widehat{\mathbb{K}}_{ji}[\boldsymbol{x}] + \widehat{\mathbb{K}}_{kk}[\boldsymbol{x}]\delta_{ij}\big)\mathrm{I}_\delta^d \text{ where } \mathrm{I}_\delta^d \\ &= \frac{1}{3}\int_{\mathcal{H}_x} \underline{\omega}\langle\boldsymbol{\xi}\rangle \frac{\boldsymbol{\xi}_1^4}{2\|\boldsymbol{\xi}\|^4}\, dV_{x'}.\end{aligned} \tag{2.12}$$

Choosing $\gamma = \frac{1}{2I_\delta^d}$, and using symmetry of $\widehat{\mathbb{K}}$, equation (2.11) becomes

$$\frac{\rho[\boldsymbol{x}]}{\mu[\boldsymbol{x}]}K_{ij}[\boldsymbol{x}] = \widehat{\mathbb{K}}_{ij}[\boldsymbol{x}] + \frac{1}{2}\widehat{\mathbb{K}}_{kk}[\boldsymbol{x}]\delta_{ij}. \tag{2.13}$$

Solving for $\widehat{\mathbb{K}}_{kk}$ for any dimension d,

$$\widehat{\mathbb{K}}_{kk}[\boldsymbol{x}] = \frac{2}{2+\mathrm{d}}K_{kk}[\boldsymbol{x}]\frac{\rho[\boldsymbol{x}]}{\mu[\boldsymbol{x}]}. \tag{2.14}$$

Substituting equation (2.14) into equation (2.13), we solve for $\widehat{\mathbb{K}}_{ij}$

$$\widehat{\mathbb{K}}_{ij}[\boldsymbol{x}] = \frac{\rho[\boldsymbol{x}]}{\mu[\boldsymbol{x}]}\left(K_{ij}[\boldsymbol{x}] - \frac{1}{2+d}K_{kk}[\boldsymbol{x}]\delta_{ij}\right). \tag{2.15}$$

Equation (2.15) relates the peridynamic constitutive tensor $\widehat{\mathbb{K}}$ with known material properties. In the next subsection, we derive the scaling factor based on the dimension of the problem and the choice of influence function.

2.2.1.2. Influence functions

(a) $\boldsymbol{\underline{\omega}\langle\xi\rangle = 1}$

This influence function gives the same weight to all the neighbors in the horizon. For 2-D ($d = 2$), the horizon is a circle of radius δ and using polar coordinates, $\xi_1 = r\cos(\theta)$ and $\xi_2 = r\sin(\theta)$. Then, the scaling factor in two dimensions with $\underline{\omega}\langle\boldsymbol{\xi}\rangle = 1$ is

$$\gamma = \frac{3}{2}\left[\int_0^{2\pi}\int_0^{\delta}\frac{{\xi_1}^4}{2r^4}rdrd\theta\right]^{-1} = \frac{8}{\pi\delta^2}. \tag{2.16}$$

For 3-D ($d = 3$), the horizon is a sphere of radius δ and using spherical coordinates, $\xi_1 = r\,sin(\varphi)\,cos(\theta)$, $\xi_2 = r\,sin(\varphi)\,sin(\theta)$ and $\xi_3 = r\,cos(\varphi)$. The scaling factor for three dimensions with $\underline{\omega}\langle\boldsymbol{\xi}\rangle = 1$ is

$$\gamma = \frac{3}{2}\left[\int_0^{2\pi}\int_0^{\pi}\int_0^{\delta}\frac{{\xi_1}^4}{2r^4}r^2\,sin(\varphi)\,drd\varphi d\theta\right]^{-1} = \frac{45}{4\pi\delta^3}. \tag{2.17}$$

(b) $\boldsymbol{\underline{\omega}\langle\xi\rangle = 1 - \frac{r}{\delta}}$

This influence function allows linearly varying contribution of the neighbors based on their proximity to the point of interest. Similar to equations (2.16) and (2.17), based on the dimension d, the following scaling factors are obtained for the constitutive model in equation (2.4)

$$\gamma = \begin{cases} \dfrac{3}{2}\left[\displaystyle\int_0^{2\pi}\int_0^{\delta}\left(1-\frac{\boldsymbol{r}}{\boldsymbol{\delta}}\right)\frac{{\xi_1}^4}{2r^4}\,r\,dr\,d\theta\right]^{-1} = \dfrac{24}{\pi\delta^2} \text{ for } d = 2 \text{ and} \\ \dfrac{3}{2}\left[\displaystyle\int_0^{2\pi}\int_0^{\pi}\int_0^{\delta}\left(1-\frac{\boldsymbol{r}}{\boldsymbol{\delta}}\right)\frac{{\xi_1}^4}{2r^4}\,r^2\sin\varphi\,dr\,d\varphi\,d\theta\right]^{-1} = \dfrac{45}{\pi\delta^3} \text{ for } d = 3. \end{cases} \tag{2.18}$$

Finally, for 2-D ($d = 2$), we substitute the scaling factor from equation (2.16) for $\underline{\omega}\langle\boldsymbol{\xi}\rangle = 1$ and the constitutive tensor from equation (2.15) into the original proposed constitutive model (2.4) to obtain

$$\underline{Q}[\boldsymbol{x}]\langle\boldsymbol{\xi}\rangle = \frac{\rho[\boldsymbol{x}]}{\mu[\boldsymbol{x}]}\frac{4}{\pi\delta^2}\frac{\boldsymbol{\xi}.\left(\boldsymbol{K}[\boldsymbol{x}]-\frac{1}{4}tr(\boldsymbol{K}[\boldsymbol{x}])\boldsymbol{I}\right).\boldsymbol{\xi}}{\|\boldsymbol{\xi}\|^4}(\Phi[\boldsymbol{x}']-\Phi[\boldsymbol{x}]), \tag{2.19}$$

$$-\underline{Q}[\boldsymbol{x}']\langle-\boldsymbol{\xi}\rangle = \frac{\rho[\boldsymbol{x}']}{\mu[\boldsymbol{x}']}\frac{4}{\pi\delta^2}\frac{\boldsymbol{\xi}.\left(\boldsymbol{K}[\boldsymbol{x}']-\frac{1}{4}tr(\boldsymbol{K}[\boldsymbol{x}'])\boldsymbol{I}\right).\boldsymbol{\xi}}{\|\boldsymbol{\xi}\|^4}(\Phi[\boldsymbol{x}']-\Phi[\boldsymbol{x}]), \tag{2.20}$$

$$\begin{aligned} &\frac{\partial}{\partial t}(\rho[\boldsymbol{x}]\emptyset[\boldsymbol{x}]) \\ &= \frac{4}{\pi\delta^2}\int_{\mathcal{H}_x}\frac{\boldsymbol{\xi}.\left(\frac{\rho[\boldsymbol{x}]}{\mu[\boldsymbol{x}]}\left(\boldsymbol{K}[\boldsymbol{x}]-\frac{1}{4}tr(\boldsymbol{K}[\boldsymbol{x}])\boldsymbol{I}\right)+\frac{\rho[\boldsymbol{x}']}{\mu[\boldsymbol{x}']}\left(\boldsymbol{K}[\boldsymbol{x}']-\frac{1}{4}tr(\boldsymbol{K}[\boldsymbol{x}'])\boldsymbol{I}\right)\right).\boldsymbol{\xi}}{\|\boldsymbol{\xi}\|^4}(\Phi[\boldsymbol{x}'] \\ &- \Phi[\boldsymbol{x}])dA_{\boldsymbol{x}'} + R[\boldsymbol{x}]. \end{aligned} \tag{2.21}$$

For constant influence function $\underline{\omega}\langle\boldsymbol{\xi}\rangle = 1$, equation (2.21) is the governing peridynamic equation of single fluid porous flow in an arbitrary heterogeneous two dimensional medium. Equation (2.21) is simplified for homogeneous and isotropic permeability, $\boldsymbol{K}[\boldsymbol{x}] = \boldsymbol{K}[\boldsymbol{x}'] = \kappa\boldsymbol{I}$ to obtain

$$\frac{\partial}{\partial t}(\rho[\boldsymbol{x}]\emptyset[\boldsymbol{x}]) = \frac{2}{\pi\delta^2}\int_{\mathcal{H}_x}\frac{\left(\frac{\rho[\boldsymbol{x}]}{\mu[\boldsymbol{x}]}+\frac{\rho[\boldsymbol{x}']}{\mu[\boldsymbol{x}']}\right)}{\|\boldsymbol{\xi}\|^2}(\Phi[\boldsymbol{x}']-\Phi[\boldsymbol{x}])dA_{\boldsymbol{x}'} + R[\boldsymbol{x}] \tag{2.22}$$

In the next subsection, we report the extension of the single-phase model to multicomponent-multiphase transport of fluid through porous media.

2.2.2. State-Based Peridynamic Formulation of Multicomponent-Multiphase Transport of Non-Newtonian and Compressible Fluid through Porous Media

Consider the permeable body $\mathcal{B}$ through which N_p phases consisting of N_c components flow. Neglecting diffusive mass transport, the mass conservation equation for a component α at any position $\boldsymbol{x} \in \mathcal{B}$ and time *t*, using the classical theory is

$$\frac{\partial}{\partial t}\left(\emptyset[\boldsymbol{x}]\sum_{\beta=1}^{N_p} S_\beta[\boldsymbol{x}]\rho_\beta[\boldsymbol{x}]w_{\alpha\beta}[\boldsymbol{x}]\right) = -\nabla.\left(\sum_{\beta=1}^{N_p}\rho_\beta[\boldsymbol{x}]\boldsymbol{u}_\beta[\boldsymbol{x}]w_{\alpha\beta}[\boldsymbol{x}]\right) + \sum_{\beta=1}^{N_p} w_{\alpha\beta}[\boldsymbol{x}]R_\beta[\boldsymbol{x}] \tag{2.23}$$

with constraints

$$\sum_{\beta=1}^{N_p} S_\beta[\boldsymbol{x}] = 1 \tag{2.24}$$

and

$$\sum_{\alpha=1}^{N_c} w_{\alpha\beta}[\boldsymbol{x}] = 1\,, \beta = 1,2, \dots \dots N_p \tag{2.25}$$

where S_β, ρ_β, and R_β are the saturation, density, and mass source of phase β respectively, $w_{\alpha\beta}$ is the mass fraction of component α in phase β, and $\boldsymbol{u}_\beta$ is the phase volumetric flux obtained by extending Darcy's law for the physical properties of respective phases;

$$\boldsymbol{u}_\beta[\boldsymbol{x}] = -\boldsymbol{K}[\boldsymbol{x}]\frac{k_{r_\beta}[\boldsymbol{x}]}{\mu_\beta[\boldsymbol{x}]}\nabla\Phi_\beta[\boldsymbol{x}]. \tag{2.26}$$

Here k_{r_β} is the relative permeability of phase β, accounting for the reduction in permeability due to presence of the other phases, μ_β is the viscosity of phase β and Φ_β is the flow potential in phase β.

Analogous to equation (2.3), we can represent the divergence of the mass flux of component α in equation (2.23) by

$$-\nabla.\left(\sum_{\beta=1}^{N_p}\rho_\beta[\boldsymbol{x}]\boldsymbol{u}_\beta[\boldsymbol{x}]w_{\alpha\beta}[\boldsymbol{x}]\right)=\lim_{\mathcal{H}_x\to 0}\int_{\mathcal{H}_x}\sum_{\beta=1}^{N_p}\left(\underline{Q}_{\alpha\beta}[\boldsymbol{x}]\langle\boldsymbol{\xi}\rangle-\underline{Q}_{\alpha\beta}[\boldsymbol{x}']\langle-\boldsymbol{\xi}\rangle\right)dV_{x'} \quad (2.27)$$

We propose the following constitutive model to relate the mass flow state $\overline{Q}_{\alpha\beta}[\boldsymbol{x}]\langle\boldsymbol{\xi}\rangle$ to the flow potential of phase β

$$\underline{Q}_{\alpha\beta}[\boldsymbol{x}]\langle\boldsymbol{\xi}\rangle=\underline{Q}_{\beta}[\boldsymbol{x}]\langle\boldsymbol{\xi}\rangle\, w_{\alpha\beta}[\boldsymbol{x}] \quad (2.28)$$

where

$$\underline{Q}_{\beta}[\boldsymbol{x}]\langle\boldsymbol{\xi}\rangle=\frac{\gamma}{2}\underline{\omega}\langle\boldsymbol{\xi}\rangle\left(\frac{\boldsymbol{\xi}.\widehat{\mathbb{K}}_\beta[\boldsymbol{x}].\boldsymbol{\xi}}{\|\boldsymbol{\xi}\|^4}\right)\left(\Phi_\beta[\boldsymbol{x}']-\Phi_\beta[\boldsymbol{x}]\right) \quad (2.29)$$

and the constitutive tensor $\widehat{\mathbb{K}}_\beta[\boldsymbol{x}]$ for respective phase is obtained in terms of material properties (medium permeability $\boldsymbol{K}[\boldsymbol{x}]$, relative phase permeability $k_{r_\beta}[\boldsymbol{x}]$, phase density $\rho_\beta[\boldsymbol{x}]$ and phase viscosity $\mu_\beta[\boldsymbol{x}]$), by imposing an equality between the non-local peridynamic model in the limit of horizon size $\delta\to 0$ and the corresponding local model

$$\widehat{\mathbb{K}}_{\beta_{\boldsymbol{ij}}}[\boldsymbol{x}]=\rho_\beta[\boldsymbol{x}]\left(\frac{k_{r_\beta}[\boldsymbol{x}]}{\mu_\beta[\boldsymbol{x}]}\right)\left(K_{ij}[\boldsymbol{x}]-\frac{1}{2+d}K_{kk}[\boldsymbol{x}]\delta_{ij}\right) \quad (2.30)$$

with constant scaling factor chosen the same as the single fluid formulation (Section 2.2.1). For example, in 2-dimensions and $\underline{\omega}\langle\boldsymbol{\xi}\rangle=1$, the above proposed constitutive model in equation (2.28) with appropriate scaling factor (equation (2.16)) becomes

$$\underline{Q}_{\alpha\beta}[\boldsymbol{x}]\langle\boldsymbol{\xi}\rangle=\frac{4}{\pi\delta^2}\rho_\beta[\boldsymbol{x}]\left(\frac{k_{r_\beta}[\boldsymbol{x}]}{\mu_\beta[\boldsymbol{x}]}\right)\frac{\boldsymbol{\xi}.\left(\boldsymbol{K}[\boldsymbol{x}]-\frac{1}{4}tr(\boldsymbol{K}[\boldsymbol{x}])\boldsymbol{I}\right).\boldsymbol{\xi}}{\|\boldsymbol{\xi}\|^4}(\Phi_\beta[\boldsymbol{x}']-\Phi_\beta[\boldsymbol{x}])w_{\alpha\beta}[\boldsymbol{x}] \quad (2.31)$$

With a known constitutive model, the governing peridynamic equation for multicomponent-multiphase flow can be obtained from equations (2.23) and (2.27).

For modeling multiphase fluid flow in reservoirs, generally three types of models are considered: compositional models, black-oil models, and immiscible two-phase models (Coats et al., 1998). In a compositional model, the composition of the hydrocarbon components and water can strongly vary with space and time in different phases (aqueous, oleic, and gaseous). To track the phase compositions accurately, conservation equations for each of the components and appropriate equations of state are required, thereby making compositional models numerically expensive. A less complex alternative is the black-oil model which is detailed in the following subsection.

2.2.2.1.Black-Oil Model

In a black-oil model, there are three phases namely, aqueous, oleic, and gaseous. A black-oil model is applicable when pressure is below the bubble point and mass can be transferred between the two hydrocarbon phases (Chen et al., 2006). It is assumed that no mass is transferred between the aqueous and the other two phases. Gas solubility in oleic phase is assumed to depend only on pressure. Thus, all the hydrocarbons are represented by two pseudo hydrocarbon components, namely oil and gas.

In the following discussion, the two subscripts in the variables refer to components and phases respectively, unless otherwise stated. In the first subscript, index 1, 2, and 3 correspond to water, oil, and, gas components, respectively. In the second subscript, index 1, 2, and 3 correspond to aqueous, oleic and gaseous phases respectively. It is assumed that water can occur only in the aqueous phase, whereas oil and gas components can occur in either of the two hydrocarbon phases. Thus, mass fractions translate as

$$\begin{aligned} &\text{Aqueous phase: } w_{11} = 1,\ w_{21} = 0,\ w_{31} = 0 \\ &\text{Oleic phase: } w_{12} = 0,\ w_{22} = w_{22},\ w_{32} = 1-w_{22} \\ &\text{Gaseous phase: } w_{13} = 0,\ w_{33} = w_{33},\ w_{23} = 1-w_{33} \end{aligned} \tag{2.32}$$

Neglecting capillary pressure (i.e., pressure difference between two immiscible phases due to surface and interfacial tension) between different phases, the LHS of equation (2.23) can be expanded as

$$\begin{aligned}\frac{\partial}{\partial t}&\left(\emptyset[\boldsymbol{x}]\sum_{\beta=1}^{N_p} S_\beta[\boldsymbol{x}]\rho_\beta[\boldsymbol{x}]w_{\alpha\beta}[\boldsymbol{x}]\right)\\ &=\left(\sum_{\beta=1}^{N_p} S_\beta[\boldsymbol{x}]\rho_\beta[\boldsymbol{x}]w_{\alpha\beta}[\boldsymbol{x}]\right)\emptyset[\boldsymbol{x}]c_r\frac{\partial p}{\partial t}\\ &+\emptyset[\boldsymbol{x}]\left[\sum_{\beta=1}^{N_p}\left(\rho_\beta[\boldsymbol{x}]w_{\alpha\beta}[\boldsymbol{x}]\frac{\partial S_\beta[\boldsymbol{x}]}{\partial t}+\rho_\beta[\boldsymbol{x}]S_\beta[\boldsymbol{x}]\frac{\partial w_{\alpha\beta}[\boldsymbol{x}]}{\partial t}\right.\right.\\ &\left.\left.+S_\beta[\boldsymbol{x}]w_{\alpha\beta}[\boldsymbol{x}]\rho_\beta c_\beta\frac{\partial p_\beta}{\partial t}\right)\right]\end{aligned}\tag{2.33}$$

where c_r and c_j are the rock and phase compressibility respectively and are functions of pressure:

$$c_r(p)=\frac{1}{\emptyset}\frac{d\emptyset}{dp}\tag{2.34}$$

and

$$c_\beta(p_\beta)=\frac{1}{\rho_\beta}\frac{d\rho_\beta}{dp_\beta}.\tag{2.35}$$

In equations (2.34) and (2.35), it is assumed that porosity is a function of pressure and phase densities are functions of phase pressures alone, which is generally applicable for reservoir engineering applications. For the black-oil model, equation (2.23) simplified with equations (2.27) and (2.33) can be solved with appropriate initial and boundary conditions and known material properties. The black-oil model can further be simplified to the immiscible two-phase flow model.

2.2.2.2. Immiscible Two-Phase flow

Immiscible two-phase flow is a special case of black-oil model, in which there is no gaseous phase and no mass transfer takes place between phases. It is applicable when pressure is above the bubble point so that all the gas remains dissolved in oleic phase. The aqueous phase consists of only water component. Using the index notation described in the previous subsection, the above assumption translates into following mass fractions

$$\begin{gathered}\text{Aqueous phase: } w_{11} = 1,\ w_{21} = 0,\ w_{31} = 0 \\ \text{Oleic phase: } w_{12} = 0,\ w_{22} = w_{22},\ w_{32} = 1\text{-}w_{22}\end{gathered} \tag{2.36}$$

(a) The Pressure Equation for Compressible Immiscible Two-Phase Flow

Adding the conservation equations of the gas and oil components gives one mass conservation equation for the oleic phase. From equations (2.23), (2.27), and (2.33), the conservation equation for each phase takes the following form:

$$\begin{aligned}\rho_\beta[\boldsymbol{x}]\left[\emptyset[\boldsymbol{x}]S_\beta[\boldsymbol{x}]\left(c_r\frac{\partial p}{\partial t}+c_\beta\frac{\partial p_\beta}{\partial t}\right)+\emptyset[\boldsymbol{x}]\frac{dS_\beta}{dt}\right] \\ =\int_{\mathcal{H}_x}\left(\underline{Q}_\beta[\boldsymbol{x}]\langle\boldsymbol{\xi}\rangle-\underline{Q}_\beta[\boldsymbol{x}']\langle-\boldsymbol{\xi}\rangle\right)dV_{x'}+R_\beta[\boldsymbol{x}], \beta=1,2.\end{aligned} \tag{2.37}$$

We divide equation (2.37) by $\rho_\beta[\boldsymbol{x}]$ and sum-up the resulting equation for both the phases to obtain

$$\begin{aligned}c_r\emptyset[\boldsymbol{x}]\frac{\partial p}{\partial t}+\emptyset[\boldsymbol{x}]\sum_{\beta=1}^{2}c_\beta S_\beta[\boldsymbol{x}]\frac{\partial p_\beta}{\partial t} \\ =\sum_{\beta=1}^{2}\frac{1}{\rho_\beta[\boldsymbol{x}]}\int_{\mathcal{H}_x}\left(\underline{Q}_\beta[\boldsymbol{x}]\langle\boldsymbol{\xi}\rangle-\underline{Q}_\beta[\boldsymbol{x}']\langle-\boldsymbol{\xi}\rangle\right)dV_{x'}+q_t[\boldsymbol{x}]\end{aligned} \tag{2.38}$$

where p is the total pressure, p_β is the phase pressure and $q_t[\boldsymbol{x}]=\left(\frac{R_1[\boldsymbol{x}]}{\rho_1[\boldsymbol{x}]}+\frac{R_2[\boldsymbol{x}]}{\rho_2[\boldsymbol{x}]}\right)$. Generally, total pressure is considered as the pressure in the aqueous phase and that the phase pressure in the oleic phase is obtained by accounting for capillary pressure.

Relationships such as Brooks-Corey curves (Brooks and Corey, 1964) are used to calculate capillary pressure in terms of the aqueous phase saturation.

$$\begin{gathered} p = p_1 \\ p_2 = p_1 + p_{c,21} \\ p_{c,21} = f(S_1) \end{gathered} \tag{2.39}$$

where $p_{c,21}$ refers to the capillary pressure between phases 1 and 2.

In the process of simplifying the integral term in RHS of equation (2.38), we introduce the phase mobility $\lambda_\beta = k_{r\beta}/\mu_\beta$. For tractability of the equations, we further choose to simplify the integral term for a two-dimensional problem with homogeneous and isotropic permeability and $\underline{\omega}\langle\boldsymbol{\xi}\rangle = 1$. The pressure and gravitational head scalar-states are defined respectively for each phase as:

$$\underline{P_\beta}[\boldsymbol{x}]\langle\boldsymbol{\xi}\rangle = p_\beta[\boldsymbol{x}'] - p_\beta[\boldsymbol{x}], \qquad \underline{H_\beta}[\boldsymbol{x}]\langle\boldsymbol{\xi}\rangle = g\big(\rho_\beta[\boldsymbol{x}']z[\boldsymbol{x}'] - \rho_\beta[\boldsymbol{x}]z[\boldsymbol{x}]\big) \tag{2.40}$$

where g is the acceleration due to gravity, and z is the height measured from a reference datum.

Thus, the equation (2.38) becomes

$$\begin{aligned} c_r \emptyset[\boldsymbol{x}] \frac{\partial p}{\partial t} + \emptyset[\boldsymbol{x}] \sum_{\beta=1}^{2} c_\beta S_\beta[\boldsymbol{x}] \frac{\partial p_\beta}{\partial t} & \\ = \frac{2\kappa}{\pi\delta^2} \Bigg[\int_{\mathcal{H}_x} \Bigg(\frac{\rho_\beta[\boldsymbol{x}']}{\rho_\beta[\boldsymbol{x}]} \lambda_\beta[\boldsymbol{x}'] & \\ + \lambda_\beta[\boldsymbol{x}] \Bigg) \frac{\big(\underline{P_\beta}[\boldsymbol{x}]\langle\boldsymbol{\xi}\rangle + \underline{H_\beta}[\boldsymbol{x}]\langle\boldsymbol{\xi}\rangle\big)}{\|\boldsymbol{\xi}\|^2} dA_{x'} \Bigg] + q_t[\boldsymbol{x}]. \end{aligned} \tag{2.41}$$

Equation (2.41) is the pressure equation for compressible two-phase immiscible flow.

(b) The Pressure Equation for Incompressible Immiscible Two-Phase Flow

Another simplifying assumption is to consider the rock and the two fluid phases incompressible, i.e. $c_r = c_1 = c_2 = 0$. The pressure equation (2.41) then reduces to

$$\frac{2\kappa}{\pi\delta^2}\left[\int_{\mathcal{H}_x} M_{\rho\lambda_\beta}[\boldsymbol{x},\boldsymbol{x}']\frac{\left(\underline{P_\beta}[\boldsymbol{x}]\langle\boldsymbol{\xi}\rangle+\underline{H_\beta}[\boldsymbol{x}]\langle\boldsymbol{\xi}\rangle\right)}{\|\boldsymbol{\xi}\|^2}\,dA_{x'}\right]+q_t[\boldsymbol{x}]=0 \tag{2.42}$$

where

$$M_{\rho\lambda_\beta}[\boldsymbol{x},\boldsymbol{x}']=\left(\frac{\rho_\beta[\boldsymbol{x}']}{\rho_\beta[\boldsymbol{x}]}\lambda_\beta[\boldsymbol{x}']+\lambda_\beta[\boldsymbol{x}]\right) \tag{2.43}$$

For better decoupling of the pressure equation from the saturation equation, we follow Chavent and Jaffre (1986) and Aarnes et al. (2007) and define a global pressure as $p^*=p_2-p_c$ that contains the saturation-dependent pressure terms p_c (capillary pressure) defined as

$$\begin{gathered}
p_c=\int_1^{S_1} f_1(\zeta)\frac{\partial p_{c_{21}}(\zeta)}{\partial\zeta}\,d\zeta,\, f_1=\frac{M_{\rho\lambda_1}}{\left[M_{\rho\lambda_1}+M_{\rho\lambda_2}\right]}\\
\Rightarrow p_c[\boldsymbol{x}']-p_c[\boldsymbol{x}]=f_1\left(P_{c_{21}}[\boldsymbol{x}']-P_{c_{21}}[\boldsymbol{x}]\right)\\
\Rightarrow \left(M_{\rho\lambda_1}+M_{\rho\lambda_2}\right)\underline{p_c}(S_1)[\boldsymbol{x}]\langle\boldsymbol{\xi}\rangle=M_{\rho\lambda_1}\underline{P_{c_{21}}}(S_1)[\boldsymbol{x}]\langle\boldsymbol{\xi}\rangle
\end{gathered} \tag{2.44}$$

where $\underline{P_c}[\boldsymbol{x}]\langle\boldsymbol{\xi}\rangle=p_c[\boldsymbol{x}']-p_c[\boldsymbol{x}],\underline{P_{c_{21}}}[\boldsymbol{x}]\langle\boldsymbol{\xi}\rangle=P_{c_{21}}[\boldsymbol{x}']-P_{c_{21}}[\boldsymbol{x}]$. Thus, the pressure equation (2.42) simplifies to

$$\begin{gathered}
\frac{4\kappa}{\pi\delta^2}\left[\int_{\mathcal{H}_x}\left(\left(M_{\rho\lambda_1}+M_{\rho\lambda_2}\right)\frac{\underline{P^*}[\boldsymbol{x}]\langle\boldsymbol{\xi}\rangle}{\|\boldsymbol{\xi}\|^2}+\frac{\left(M_{\rho\lambda_1}\underline{H_1}[\boldsymbol{x}]+M_{\rho\lambda_2}\underline{H_2}[\boldsymbol{x}]\right)\langle\boldsymbol{\xi}\rangle}{\|\boldsymbol{\xi}\|^2}\right)dA_{x'}\right]\\
+q_t[\boldsymbol{x}]=0
\end{gathered} \tag{2.45}$$

in only one pressure, p^* with $\underline{P^*}[\boldsymbol{x}]\langle\boldsymbol{\xi}\rangle=p^*[\boldsymbol{x}']-p^*[\boldsymbol{x}]$.

(c) The Saturation Equation for Incompressible Immiscible Two-Phase Flow

Along with phase pressures, the phase saturations also need to be determined. For the two–phase flow case, the unknown saturations are of aqueous (S_1) and oleic (S_2)

phases. However, the phase saturations are constrained by equation (2.24), so only one of the two phase-saturations needs to be determined and the common practice is to solve for S_1. From equation (2.37), the mass conservation equation for water component, with the incompressible rock and fluid assumption, is

$$\emptyset[\boldsymbol{x}]\frac{dS_1}{dt} = \frac{4\kappa}{\pi\delta^2}\int_{\mathcal{H}_x} M_{\rho\lambda_1}\frac{\left(\underline{P}^*[\boldsymbol{x}]\langle\boldsymbol{\xi}\rangle - \frac{M_{\rho\lambda_2}}{M_{\rho\lambda_1}}\underline{p_c}[\boldsymbol{x}]\langle\boldsymbol{\xi}\rangle\right) + \underline{H_1}[\boldsymbol{x}]\langle\boldsymbol{\xi}\rangle}{\|\boldsymbol{\xi}\|^2}\,dA_{x'} + R_1[\boldsymbol{x}] \qquad (2.46)$$

which serves as the saturation equation for incompressible immiscible two-phase flow. The pressure equation (2.45) is solved with the saturation dependent properties and the saturation equation is solved with the global pressure obtained from the pressure equation (2.45).

2.3. MODEL VERIFICATION

We verify the peridynamics multiphase flow model by solving the immiscible displacement of one fluid by another. One-dimensional flow is solved in a uniform horizontal reservoir with a fluid injection source at one end and a production sink at the other. For simplicity, it is assumed that the rate of fluid injection and the rate of fluid production at the respective ends are the same.

The model presented in this chapter can simulate complex fluids since it accounts for compressible and non-Newtonian behavior. In this section, two verification problems are considered – one in which Newtonian water displaces Newtonian oil and the other in which a non-Newtonian polymer solution displaces Newtonian oil. In the petroleum engineering community, these two displacement processes are known as ‘water flood’ and ‘polymer flood’ respectively. The fluids are assumed to be slightly compressible in both the problems.

2.3.1. Problem 1: Immiscible displacement of a Newtonian fluid (oil) by another Newtonian fluid (water) ─ Water flood

A schematic of this verification problem is shown in Figure 2.1. The model parameters are summarized in Table 2.1. A Brooks-Corey relationship (Brooks and Corey, 1964) is assumed for calculating relative permeability of the two phases:

$$k_{rw}(S_w) = k_{rw}^0 * (S_{wD})^{N_w} \tag{2.47}$$

$$k_{ro}(S_w) = k_{ro}^0 * (1 - S_{wD})^{N_o} \tag{2.48}$$

where S_w is water saturation, $k_{rw}{}^0$ and $k_{ro}{}^0$ are end-point relative permeabilities, and N_w and N_o are relative permeability exponents of aqueous and oleic phase respectively. S_{wD} is dimensionless water saturation and is defined as:

$$S_{wD} = \frac{S_w - S_{wr}}{1 - S_{or} - S_{wr}}. \tag{2.49}$$

where S_{wr} and S_{or} are residual saturations of water and oil respectively.

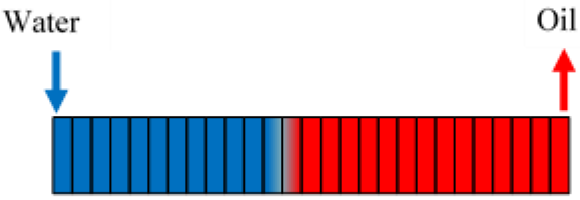

Figure 2.1. Schematic of water flood process. Cooler colors represent higher saturations of water, whereas warmer colors represent higher saturations of oil (scale in the width direction is highly exaggerated)

Table 2.1. Simulation parameters for the water flood problem

Length of domain, L_x (m)	200
Porosity, $\emptyset$	0.3
Permeability, κ (m^2)	1e-13
Initial pressure, P_{ini} (Pa)	20e6
Initial water saturation, $S_{w, ini}$	0.0
Residual saturations of both fluids, S_{wr} *and* S_{or}	0.0
End-point relative permeability for both fluids, k_{rw} *and* k_{ro}	1.0
Relative permeability exponents for both fluids, N_w *and* N_o	2
Density of both fluids, ρ_w *and* ρ_o (kg/m^3)	1
Viscosity of both fluids, μ_w *and* μ_o (Pa s)	0.001
Rate of injection and production, Q (kg/s)	4e-5

2.3.1.1. Numerical discretization

The computational domain is discretized into uniform grid cells of size $\Delta x = \Delta y = \Delta z = L_x/n_x$, where L_x is the length of the domain and n_x is the number of grid cells in x-direction. Since our objective is to simulate 1-D flow, there is just one cell in y- and z-directions. One computational node is assumed at the center of each grid cell and is assigned a volume equivalent to that of one cell, $(\Delta x)^3$.

2.3.1.2. Analytical local solution

The mobility ratio for an immiscible displacement process is defined as:

$$M = \frac{M_w}{M_o} = \frac{k_{rw}/\mu_w}{k_{ro}/\mu_o} \tag{2.50}$$

where M_w and M_o are the mobilities of aqueous and oleic phases respectively.

For *M ≤ 1*, a piston-like displacement occurs which is characterized by the formation of a shock-front. As in-situ fluid (oil in the current problem) is displaced, it moves from injector well towards the producer well. Before the shock-front reaches the producer well, only in-situ fluid is produced. When it has reached the producer well, the displacing fluid (water in the current problem) breaks through and both fluids are produced thereafter.

Neglecting gravity and capillary pressure between the aqueous and oleic phases, the analytical local solution can be obtained by using the fractional flow theory established by Buckley and Leverett (1941). For completeness, the steps for finding the analytical local solution have been summarized here.

- Fractional flow of water phase is given as:

$$f_w(S_w) = \frac{q_w}{q_w + q_o} = \frac{k_{rw}(S_w)/\mu_w}{k_{rw}(S_w)/\mu_w + k_{ro}(S_w)/\mu_o} \tag{2.51}$$

- The water saturation at the shock front (S_{wf}) is obtained by solving the following equation:

$$\left.\frac{\partial f_w}{\partial S_w}\right|_{S_{wf}} = \frac{f_{wf}}{S_{wf} - S_{w,ini}} \tag{2.52}$$

- The dimensionless position of the shock front from the injector (x_{Df}) at any dimensionless time (t_D) is determined as:

$$x_{Df} = \left.\frac{\partial f_w}{\partial S_w}\right|_{S_{wf}} * t_D. \tag{2.53}$$

  where x_D and t_D are defined as:

$$x_D = \frac{x}{L_x} \tag{2.54}$$

$$t_D = \frac{Q * t}{\rho * PV} \tag{2.55}$$

where Q is the injection rate (kg/s), ρ is density of injected fluid (kg/m^3), and PV is the pore volume injected (m^3) *(= Porosity * domain volume).*

- The reservoir behind the shock front is swept by water, thereby increasing water saturation in that region. For all water saturations greater than the shock front water saturation obtained in equation (2.52), $(\partial f_w / \partial S_w)|_{S_w}$ is calculated by differentiating equation (2.51).
- At a given t_D, the dimensionless position (x_D) of each water saturation greater than the shock front water saturation can be calculated as:

$$x_D = \left.\frac{\partial f_w}{\partial S_w}\right|_{S_w} * t_D \tag{2.56}$$

- The reservoir ahead of the shock front has not been swept by water yet. Thus, in the region ahead of the shock-front:

$$S_w = S_{w,ini} \tag{2.57}$$

2.3.1.3. Peridynamic solution

Figure 2.2 shows the analytical local and peridynamic solutions to the classical Buckley Leverett problem for *M=1*. Dimensionless water saturation is plotted against dimensionless distance from the injector well at dimensionless time = 0.2.

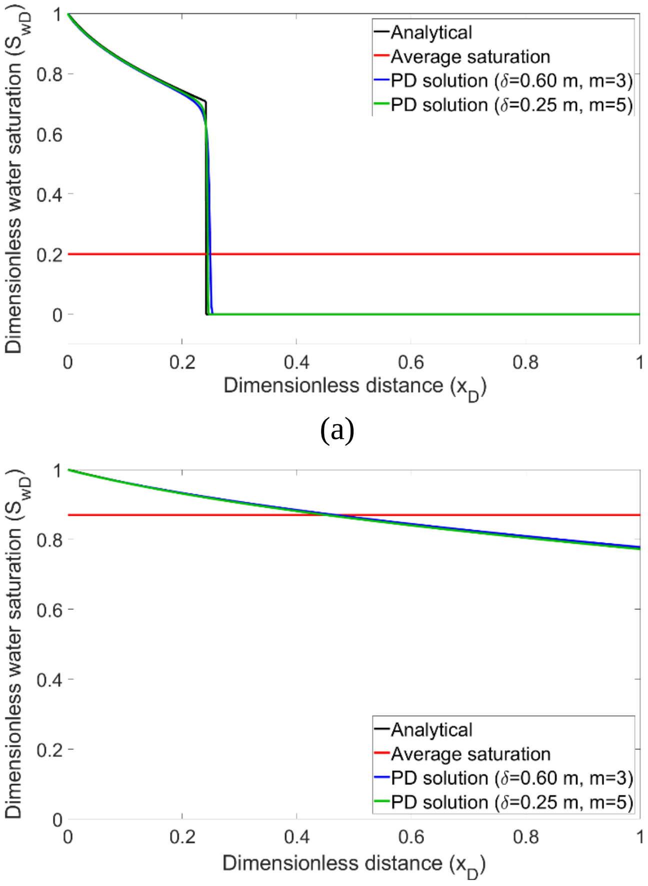

(a)

(b)

Figure 2.2. Analytical local and peridynamic (PD) saturation profiles for water flood problem. (a): before breakthrough (at $t_D = 0.2$). (b): after breakthrough (at $t_D = 1.2$). *m* is the number of non-local neighbors for each cell (described in more detail in Section 2.3.1.4)

The sharp discontinuity in analytical local solution is the shock-front described in Section 2.3.1.2. Except for the smearing of the shock-front in Figure 2.2a, the peridynamic solution matches water saturation from the analytical local solution very well, both behind and ahead of the shock-front, and both before and after the breakthrough. It should be noted that the smearing of the shock-front is a characteristic of the non-local contributions to diffusion terms in equations (2.1) and (2.23). These non-local contributions become smaller as the horizon size is shrunk (Bobaru and Ha, 2011). Using the curves shown in these figures, a convergence study for the waterflood problem is discussed in the next subsection.

2.3.1.4. Convergence study

Peridynamics is a non-local formulation and accounts for interactions from all its neighboring nodes within a characteristic length scale, called horizon *(δ)*. If a 1-D domain is discretized into uniform cell size of length Δx, the number of non-local neighbors to each cell is m $(=\delta/\Delta x)$ in each direction.

The non-local peridynamic solution converges to the local solution in the limit of δ going to zero and m being infinitely large simultaneously. Such a convergence study is referred to as δ-m convergence study (Bobaru et al, 2009). Please note that this study is different from the m-convergence study taken up in Katiyar et al. (2014). The objective in that work was to find an optimum choice for both δ and m by varying m for different values of δ. The objective here is to show that the local solution can be recovered from non-local solution in the limiting case.

Four cases were considered with successively smaller δ and larger m. The values for these parameters are given in Table 2.2.

Table 2.2. Horizon size (δ) and number of non-local neighbors (m) for convergence study

Case	**Horizon size *(δ)***	**Number of non-local neighbors *(m)***
1	0.80 m	2
2	0.60 m	3
3	0.40 m	4
4	0.25 m	5

Figure 2.3 demonstrates the convergence of non-local solution towards the local solution by plotting relative differences for the four cases. With reference to Figure 2.2, relative difference is defined as:

$$\text{Relative difference} = \frac{\sum_x \left| S_{w,analytical} - S_{w,numerical} \right|}{A_{analytical}} * 100 \qquad (2.58)$$

where $A_{analytical}$ is the area under the analytical local curves in Figure 2.2.

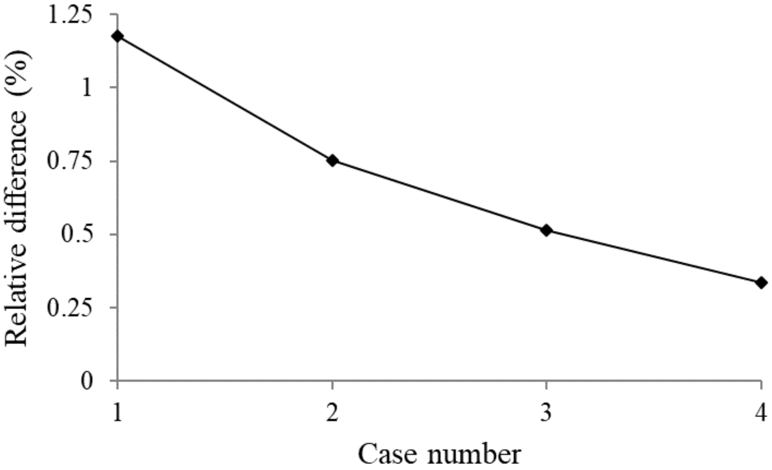

Figure 2.3. Relative difference in water saturation profile as horizon size *(δ)* decreases and number of non-local neighbors *(m)* increases simultaneously as shown in Table 2.2.

A higher number of non-local neighbors requires higher computational resources owing to denser coefficient matrices. Thus, unless otherwise stated, we use *m=3* in the subsequent simulations to get a reasonably accurate non-local solution, while retaining a low computational cost. The choice of this value of *m* comes from our experience gained so far with peridynamic simulations.

2.3.2. Problem 2: Immiscible displacement of a Newtonian fluid (oil) by a non-Newtonian fluid (polymer) – Polymer flood

In this verification problem, Newtonian oil is displaced by a shear-thinning polymer solution and a schematic is shown in Figure 2.4. Polymer solution is injected at different rates to study the effect of injection rate on oil recovery. Except for the viscosity of the displacing fluid and the injection and production rates, the rest of the parameters remain the same as in verification problem 1 and are summarized in Table 2.3. Power law relationship is assumed between polymer viscosity and shear rate:

$$\mu_p = H * (\dot{\gamma})^{n-1} \tag{2.59}$$

where μ_p is the polymer viscosity, $\dot{\gamma}$ is the shear rate, H is the intrinsic viscosity, and n is the power law exponent.

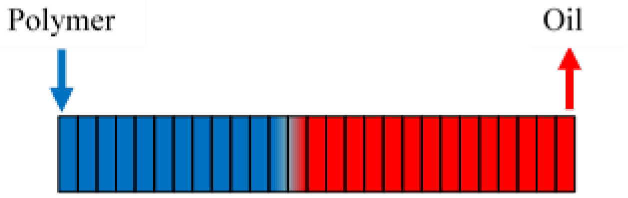

Figure 2.4. Schematic of polymer flood process. Cooler colors represent higher saturations of polymer, whereas warmer colors represent higher saturations of oil (scale in vertical direction is highly exaggerated)

Table 2.3. Simulation parameters for the polymer flood problem

Length of domain, L_x (m)	200
Porosity, $\emptyset$	0.3
Permeability, κ (m^2)	1e-13
Initial pressure, P_{ini} (Pa)	20e6
Initial polymer saturation, $S_{w, ini}$	0.0
Residual saturations of both fluids, S_{wr} *and* S_{or}	0.0
End-point relative permeability for both fluids, k_{rw} *and* k_{ro}	1.0
Relative permeability exponents for both fluids, N_w *and* N_o	2
Density of both fluids, ρ_w *and* ρ_o (kg/m^3)	1
Viscosity of oil, μ_o (Pa s)	1e-3
Intrinsic viscosity of polymer, H (Pa s)	1e-3
Power law exponent, n	0.5
Rate of injection and production, Q (kg/s)	4e-5 in fast injection rate 4e-6 in slow injection rate

2.3.2.1. Analytical local solution

Following the incompressibility assumption, total flow of both the fluids at any cross-section should remain constant with time and should be equal to the injection rate:

$$u(t) = u_{injection} = u_{oil} + u_{polymer} \tag{2.60}$$

Using Darcy's law, flow rates of oil and polymer solution can be written as:

$$u_{oil} = -\kappa \frac{k_{r,oil}}{\mu_{oil}} \frac{\partial P}{\partial x} \tag{2.61}$$

$$u_{polymer} = -\kappa \frac{k_{r,polymer}}{\mu_{polymer}} \frac{\partial P}{\partial x} \tag{2.62}$$

We used the relationship for equivalent non-Newtonian viscosity derived by Wu et al. (1991). Combining the above three equations with the constitutive relations (2.47), (2.48), and (2.59), they plotted the pressure gradients as a function of non-Newtonian fluid saturation (polymer saturation) for different injection rates.

Figure 2.5 demonstrates that at faster injection rates of the polymer, the pressure gradients are higher for any given polymer saturation. This leads to higher shear rates, which in turn result in lower viscosity of the shear thinning polymer. From Buckley-Leverett analysis, it is known that lower viscosity of the displacing fluid leads to reduced sweep efficiency and hence less oil recovery. This idea is used to verify the peridynamic solution for immiscible displacement by a non-Newtonian fluid.

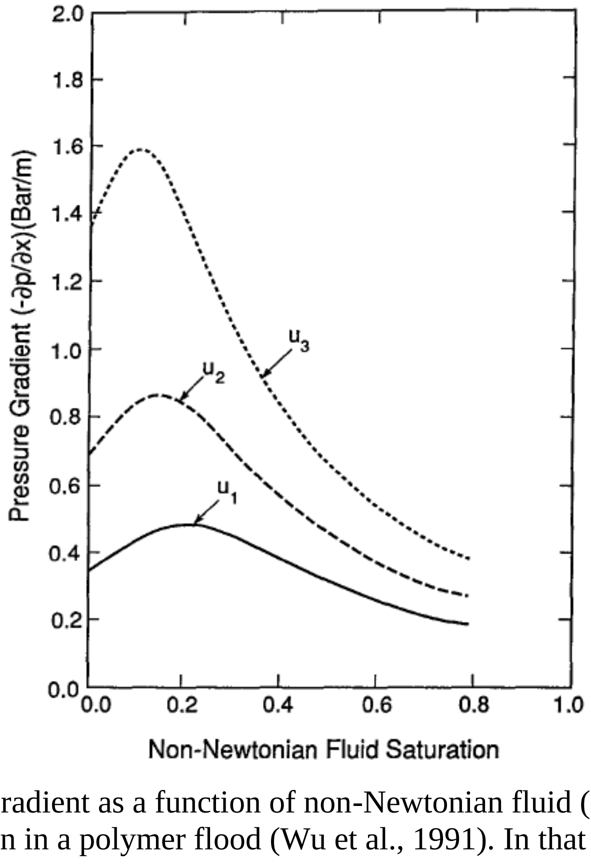

Figure 2.5. Pressure gradient as a function of non-Newtonian fluid (polymer solution) saturation in a polymer flood (Wu et al., 1991). In that study, it is assumed that $u_3 > u_2 > u_1$.

2.3.2.2. Peridynamic solution

Figure 2.6 shows the saturation profiles for two different injection rates before the displacing polymer solution breaks through at the producer well. Again, except for the smearing of the shock-front, the peridynamics solution captures the polymer saturation very well both behind and ahead of the shock-front.

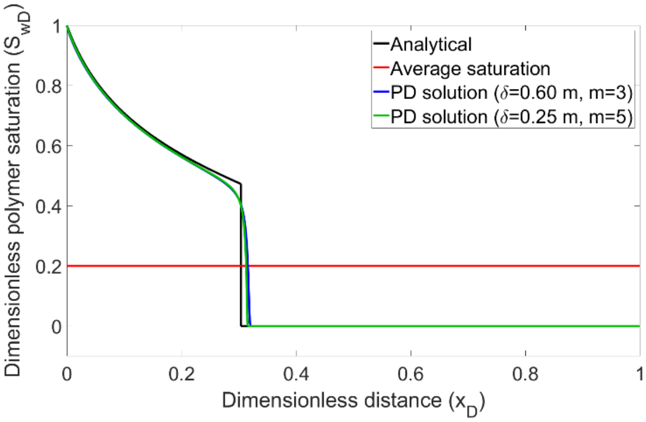

(a)

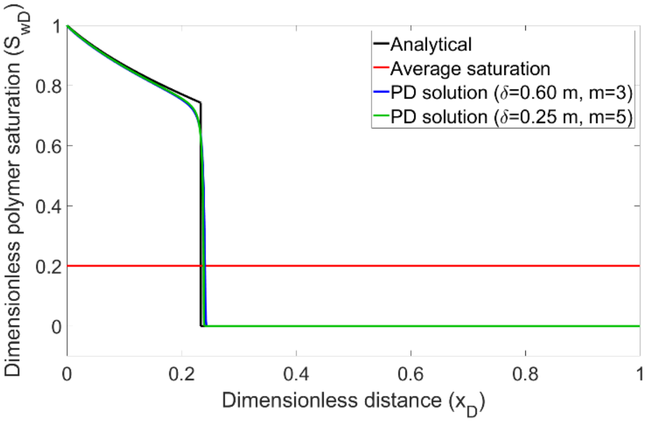

(b)

Figure 2.6. Analytical local and peridynamic (PD) saturation profiles before breakthrough (at t_D = 0.2) for polymer flood problem. (a) at fast injection rate (4e-5 kg/s), (b) at slow injection rate (4e-6 kg/s)

Figure 2.7 shows the saturation profiles for the same injection rates after the polymer solution breaks through the producer well.

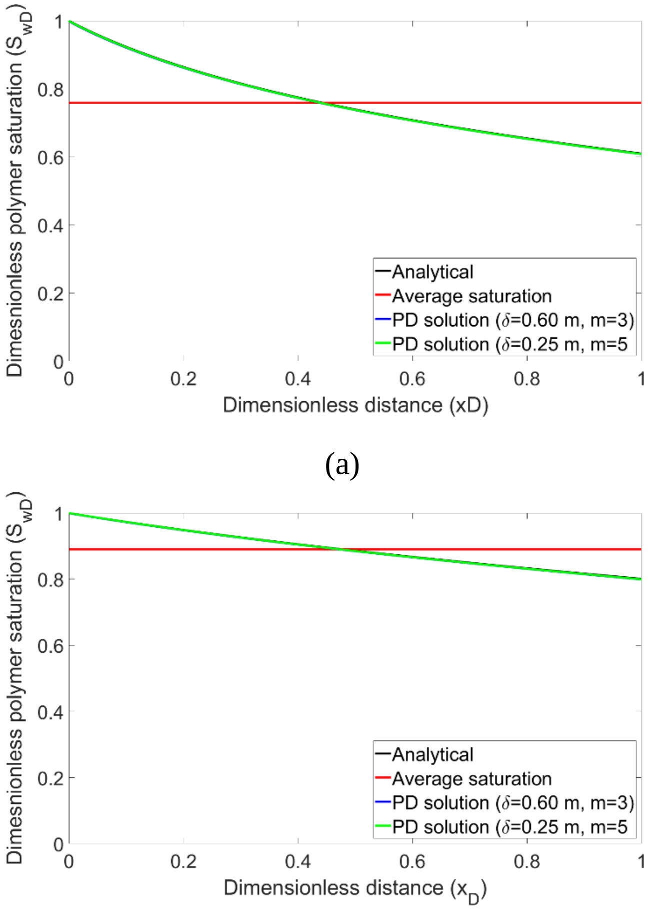

(a)

(b)

Figure 2.7. Analytical local and peridynamic (PD) saturation profiles after breakthrough (at t_D = 0.2) for polymer flood problem. (a) at fast injection rate (4e-5 kg/s), (b) at slow injection rate (4e-6 kg/s)

Figure 2.8 shows the recovery plots for the corresponding injection rates. There is an excellent match with the analytical local solution in these plots. At slower injection rate, the peridynamic simulations predict a higher oil recovery which is consistent with the findings of Wu et al. (1991).

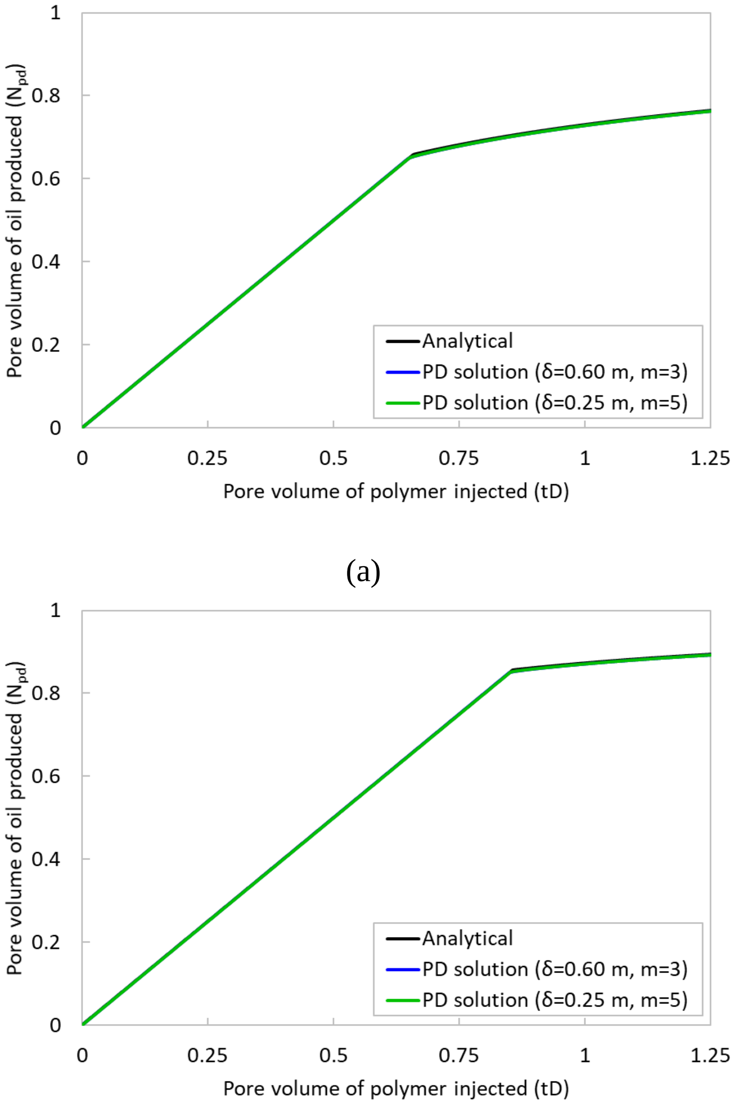

(a)

(b)

Figure 2.8. Analytical local and peridynamic (PD) recovery plots for polymer flood problem. (a) at fast injection rate (4e-5 kg/s), (b) at slow injection rate (4e-6 kg/s)

2.3.2.3. Convergence study

Following the same procedure as outlined in Section 2.3.1.4, Figure 2.9 has been obtained to show the convergence of non-local solution towards the analytical local solution. The differences in this case are larger compared to those in the waterflood problem (Figure 2.3) because the shock-front is smeared out further. However, they are still within the acceptable range of errors for engineering applications and more accurate results can be obtained at the expense of higher computational resources.

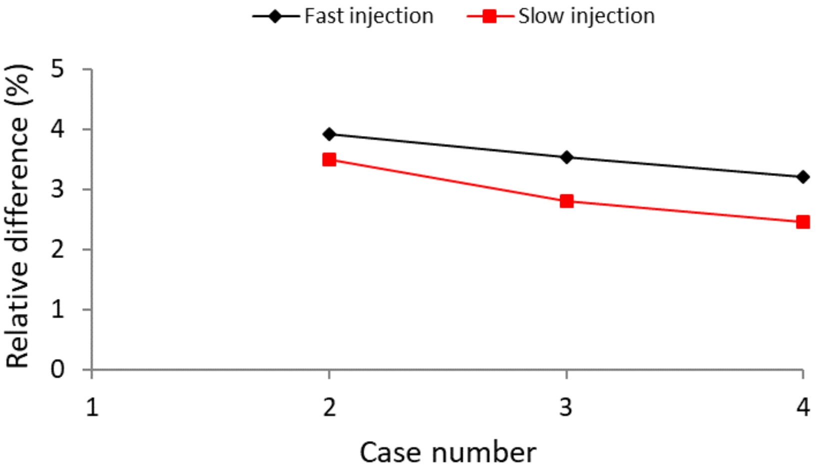

Figure 2.9. Relative difference in polymer saturation profile as horizon size *(δ)* decreases and number of non-local neighbors *(m)* increases simultaneously as shown in Table 2.2.

Figure 2.10 shows the relative differences in oil recovery at t_D = 0.2 PV. It should be noted that although the shock-fronts in the saturation profiles are smeared out further, the relative differences in oil recovery are negligible. This signifies that the mass conservation is honored in these simulations.

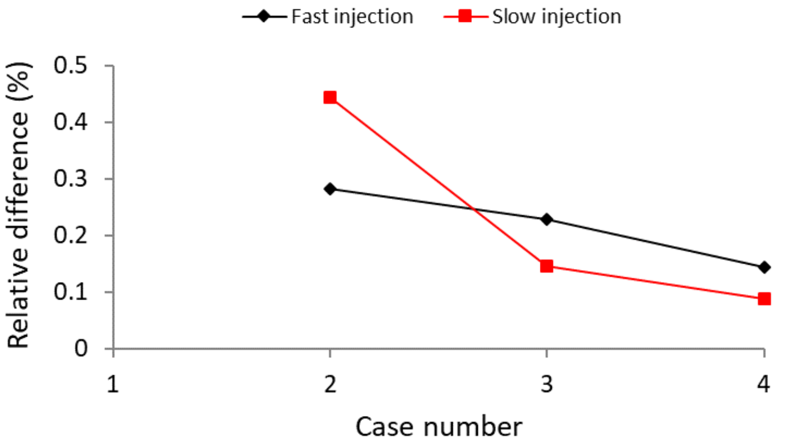

Figure 2.10. Relative difference in oil recovery as horizon size *(δ)* decreases and number of non-local neighbors *(m)* increases simultaneously as shown in Table 2.2.

2.4. CONCLUSIONS

In Katiyar et al. (2014), a state-based peridynamic formulation for single phase convective transport of a fluid with small, constant compressibility and Newtonian flow characteristics was presented. In this chapter, we have generalized the model to multi-phase, multi-component fluids showing varying compressibility and non-Newtonian behavior. These non-local fluid flow models have been derived for applications to our peridynamics-based hydraulic fracturing simulator (Ouchi, 2016), which are presented in Chapter 3 of this dissertation. Thus, we have chosen to simplify the derived equations for different kinds of multiphase models used in petroleum engineering. A compositional model is not presented because of its associated computational costs. Less expensive models such as black-oil and immiscible two-phase flow models are presented in detail.

We have demonstrated application of the multiphase model by solving 1-D linear, immiscible displacement of oil by water (water flood) and by a shear-thinning polymer (polymer flood). Saturation profiles show a characteristic shock front in such problems, which is smeared out in our peridynamic solutions due to it being a non-local formulation.

A δ-*m* convergence study is performed to recover the analytical local solution from the numerical non-local solution by shrinking the horizon size *(δ)* and increasing the number of non-local neighbors *(m)* simultaneously. Thus, saturation profiles retrieve the shock front for the two problems. Moreover, convergence of oil recovery plots to the analytical local solution verifies overall mass conservation in the proposed non-local model. In the polymer flood problem, our simulations also capture the observation that oil recovery decreases at higher injection rates of a shear-thinning polymer.

We validated our peridynamics model in higher dimensions with laboratory-scale hydraulic fracturing experiments involving multiple phases. This work is discussed in Chapter 3.

CHAPTER 3: DEVELOPMENT OF AN IMMISCIBLE TWO-PHASE PERIDYNAMICS-BASED HYDRAULIC FRACTURING MODEL*

3.1. INTRODUCTION

In this chapter, we develop an immiscible, two-phase hydraulic fracturing model by generalizing the single-phase hydraulic fracturing model developed by Ouchi et al. (2015). The immiscible two-phase fluid flow model presented in Chapter 2 is used for this purpose. Although we derived the more computationally expensive compositional, and black-oil fluid flow formulations, an immiscible two-phase hydraulic fracturing model is developed for computational tractability. However, either or both phases can be non-Newtonian or compressible. Hydrocarbon reservoirs typically have in-situ fluids in three different phases – namely, aqueous, oleic, and gaseous. If the subsurface pressure is above the bubble point, the gaseous phase remains soluble in the oleic phase, such that there is only one hydrocarbon phase in addition to the aqueous phase. In such cases, an immiscible two-phase model is used to simulate the flow of reservoir fluids.

In the following section, the modifications to the single-phase peridynamics-based hydraulic fracturing model reviewed in Chapter 1 are presented. New governing equations for the transport of pore fluids are developed and the corresponding constitutive relations are modified. In the subsequent section, we validate our immiscible two-phase hydraulic fracturing model against our laboratory experiments conducted on specimens with different initial saturations of the pore fluids. Since analytical solutions are not available for the verification of the multiphase hydraulic fracturing models, these experiments present a unique opportunity to validate our model.

---

*Agrawal, S; Ouchi, H; AlTammar, M; and Sharma, M.M. 2018. “Mechanistic Explanation of the Impact of Pore Pressure on Hydraulic Fracture Propagation.” in 52nd U.S. Rock Mechanics/Geomechanics Symposium. Agrawal extended the fracturing simulator developed by Ouchi and conducted and documented the research. AlTammar provided the experimental expertise and Sharma supervised on the paper.

3.2. MATHEMATICAL MODEL

The modifications to the existing hydraulic fracturing model presented in this section assumes that the pore space is occupied by two immiscible phases (Figure 3.1). Although aqueous and oleic terminology is used for the phases, they can represent any general compressible, non-Newtonian fluids, such as glycerine and air in Section 3.3. In the single-phase hydraulic fracturing simulator, each element could potentially have five primary unknowns corresponding to x-, y-, and z- displacements, matrix pore pressure P, and fracturing fluid pressure P_f (Ouchi 2016). The displacements, matrix pore pressure, and fracturing fluid pressure are contributed by the rock momentum balance, pore fluid mass balance, and fracturing fluid mass balance equations, respectively. In the immiscible two-phase simulator, each element has an additional unknown corresponding to the water saturation S_w, which is solved for using another pore fluid mass balance equation for the second phase. As explained in the development of the original fracturing model, the fracturing fluid pressure P_f is solved for only in the elements that have a fracture space. Thus, as a hydraulic fracture propagates, the number of primary unknowns adaptively increases from five to six.

Next, we present the additional governing equations and constitutive relations implemented in our hydraulic fracturing model, which are solved in combination with those reviewed in Chapter 1.

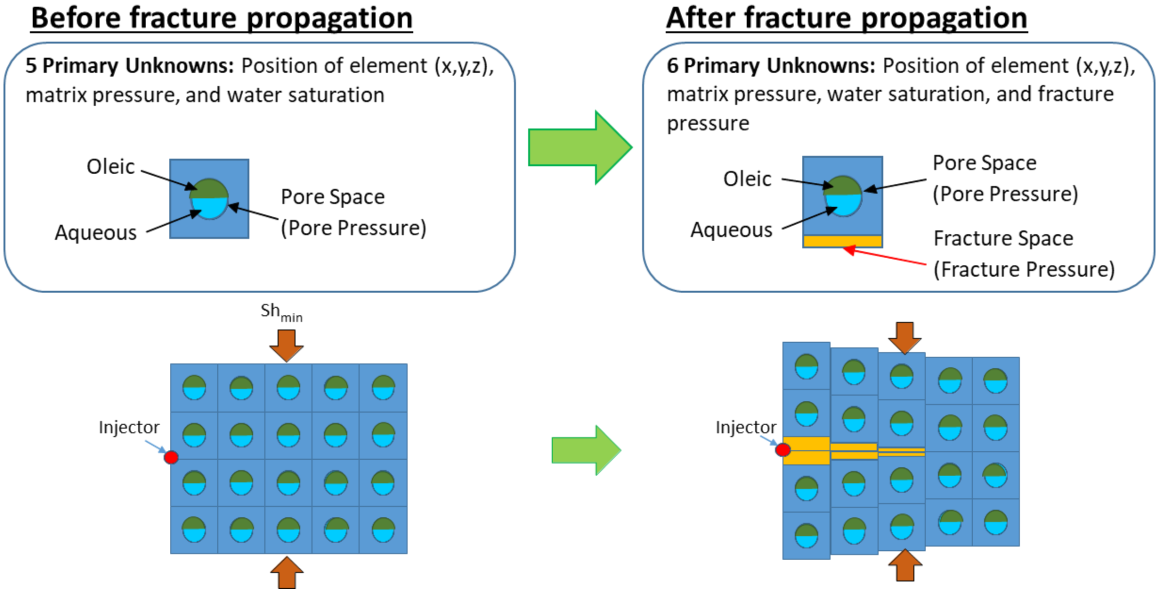

Figure 3.1. Immiscible two-phase hydraulic fracturing simulator (adapted from Ouchi, 2016)

3.2.1. Momentum conservation for the rock and the damage model

The formulation for rock deformation and the damage model are unaffected by whether the pore fluids comprise a single phase or multiple phases. Thus, the corresponding equations are the same as those in Sections 1.6.1 and 1.6.2.

3.2.2. Mass conservation for the pore fluid

The mass balance equations for the aqueous and oleic phases in the pore space are solved along with the relative permeability equations (2.47), (2.48), and (2.49) and the constraint equation (2.24) forcing a unit sum of the two saturations. Although our generalized fluid flow formulation in Chapter 2 accounted for the capillary pressure between different phases, we choose to neglect the same in the development of our two-phase hydraulic fracturing simulator.

3.2.2.1. Aqueous phase

The accumulation term in the mass balance equation of the aqueous phase accounts for its saturation. The leak-off term is multiplied by a binary factor depending on whether the fracturing fluid is an aqueous phase or an oleic phase.

$$\frac{\partial}{\partial t}(\rho_w[\boldsymbol{x}]S_w[\boldsymbol{x}]\phi[\boldsymbol{x}]) = \int_{\mathcal{H}_x} (\underline{Q_w}[\boldsymbol{x}]\langle\boldsymbol{\xi}\rangle - \underline{Q_w}[\boldsymbol{x}']\langle-\boldsymbol{\xi}\rangle)\, dV_{x'} + R_w[\boldsymbol{x}] + \chi I_w[\boldsymbol{x}] \qquad (3.1)$$

where the various quantities are as described in Section 1.5.2 and the subscript w refers to the aqueous phase. χ is a binary factor, which is 1 if an aqueous based fluid is used for fracturing and 0 otherwise.

Compared to the constitutive relation for the single-phase mass flow scalar state in equation (1.13), those for the two-phase flow in equations (3.2) and (3.5) are multiplied by the respective relative permeabilities to account for the reduction in permeability due to the presence of the other phase.

$$\underline{Q_w}[\boldsymbol{x}]\langle\boldsymbol{\xi}\rangle = \frac{\gamma k_{rw}}{2\mu_w}\underline{\omega}\langle\boldsymbol{\xi}\rangle\rho_w \frac{\boldsymbol{\xi}\mathbb{K}[\boldsymbol{x},\boldsymbol{x}']\boldsymbol{\xi}}{||\boldsymbol{\xi}||^4}(\Phi[\boldsymbol{x}'] - \Phi[\boldsymbol{x}]) \qquad (3.2)$$

The leak-off terms in equations (3.3) and (3.6) are also scaled by the phase relative permeability.

$$I_w[\boldsymbol{x}] = -\frac{\rho_w[\boldsymbol{x}]k_{leak}A}{V\mu_w}\frac{dP}{dl} = \frac{\rho_w[\boldsymbol{x}]k_{rw}k_{leak}\Delta A_p[\boldsymbol{x}](\Phi_f[\boldsymbol{x}] - \Phi[\boldsymbol{x}])}{\Delta V[\boldsymbol{x}]\mu_w(l_p/2)} \qquad (3.3)$$

3.2.2.2. Oleic phase

The formulation for the oleic phase in the pore space is similar to that for the aqueous phase.

$$\frac{\partial}{\partial t}(\rho_o[\boldsymbol{x}]S_o[\boldsymbol{x}]\phi[\boldsymbol{x}]) = \int_{\mathcal{H}_x} (\underline{Q_o}[\boldsymbol{x}]\langle\boldsymbol{\xi}\rangle - \underline{Q_o}[\boldsymbol{x}']\langle-\boldsymbol{\xi}\rangle)\, dV_{x'} + R_o[\boldsymbol{x}] + (1-\chi)I_o[\boldsymbol{x}] \qquad (3.4)$$

$$\underline{Q_o}[\boldsymbol{x}]\langle\boldsymbol{\xi}\rangle = \frac{\gamma k_{ro}}{2\mu_o}\underline{\omega}\langle\boldsymbol{\xi}\rangle\rho_o \frac{\boldsymbol{\xi}\mathbb{K}[\boldsymbol{x},\boldsymbol{x}']\boldsymbol{\xi}}{||\boldsymbol{\xi}||^4}(\Phi[\boldsymbol{x}'] - \Phi[\boldsymbol{x}]) \tag{3.5}$$

$$I_o[\boldsymbol{x}] = -\frac{\rho_o[\boldsymbol{x}]k_{leak}A}{V\mu_o}\frac{dP}{dl} = \frac{\rho_o[\boldsymbol{x}]k_{ro}k_{leak}\Delta A_p[\boldsymbol{x}](\Phi_f[\boldsymbol{x}] - \Phi[\boldsymbol{x}])}{\Delta V[\boldsymbol{x}]\mu_o(l_p/2)} \tag{3.6}$$

3.2.3. Mass conservation for the fracturing fluid

We assume the fracturing fluid to be comprised of a single-phase. However, to simulate fracturing with non-aqueous fluids, we incorporate a binary switch χ to select the phase of the fracturing fluid.

$$I[\boldsymbol{x}] = \chi I_w[\boldsymbol{x}] + (1-\chi)I_o[\boldsymbol{x}] \tag{3.7}$$

The rest of the treatment for modeling fluid flow in a fracture remains the same as described in Section 1.6.4.

3.3. EXPERIMENTAL VALIDATION

Production of fluids from a reservoir reduces the pore pressure and creates pressure gradients in the rock. This modifies the stress state from its initial in-situ condition (Warpinski and Branagan, 1989; Wright et al., 1994). Numerous field studies have reported this phenomenon in the literature (Siebrits et al., 2000; Weng and Siebrits, 2007; Roussel and Sharma, 2012). In addition, laboratory experiments are often performed to understand the underlying mechanisms (Bruno and Nakagawa, 1991; Liu et al., 2008). Further insights into refracturing process are obtained by mathematical modeling and numerical simulations (Berchenko and Detournay, 1997; Wang et al., 2013; Agrawal and Sharma 2018).

Bruno and Nakagawa (1991) conducted fracturing experiments in the presence of a non-uniform pore pressure field and isotropic stresses. They observed that both mechanical and hydraulic fractures are attracted to the high pore pressure region. Their observations were justified by Berchenko and Detournay (1997) based on a deviation of the maximum stress trajectory towards the injector well. Recently, fracture propagation in the presence of different configurations of injection sources has been studied experimentally by AlTammar et al. (2018). It should be noted that all these laboratory experiments were conducted at low confining stresses. Under these conditions the tensile strength of the rock controls fracture propagation (not the total stress). In the field, where confining stresses are high (much higher than the tensile strength of the rock) fracture opening is dominated by the total stress (not the tensile strength of the rock). In such cases a reduction in pore pressure causes a reduction in the total stress, resulting in the fractures being attracted to regions of low pore pressure.

In this section, we validate our immiscible two-phase hydraulic fracturing simulator by comparing the simulation results with experiments and explain them using an effective stress law. We also investigate the effect of pore pressure, fluid injection scheme, saturation conditions, and applied stress on fracture growth in a low far-field stress environment.

3.3.1. Simulation setup

The experiments simulated in this work were performed on both dry and saturated synthetic specimens using glycerin as the fracturing fluid (AlTammar et al., 2018). Samples are modeled with air as the initial saturating fluid. Corey-type relative permeability curves are assumed with glycerin as the wetting phase and air as the non-wetting phase (Figure 3.2). These curves are chosen because they are typical of a water-wet rock with two immiscible fluids. A far-field stress was applied to the left and right boundaries, whereas the top and bottom boundaries were at constant atmospheric stress (Figure 3.3). Thus, the maximum stress acts along the *x*-axis (horizontal) and the minimum stress acts along the *y*-axis (vertical) in all the simulations. The main experimental and simulation parameters are summarized in Table 3.1.

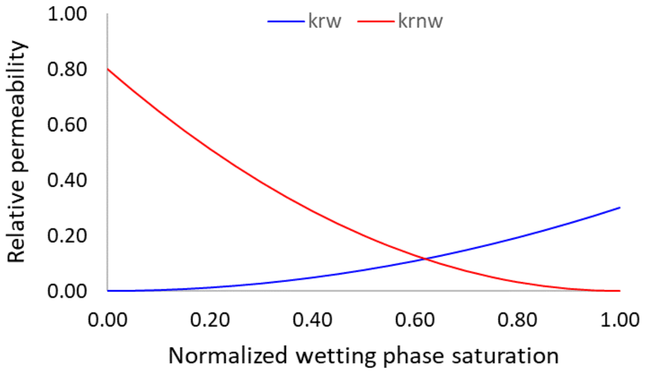

Figure 3.2. Relative permeability curves for the two phases. Glycerin is the wetting phase and air is the non-wetting phase.

Table 3.1. Experimental and simulation parameters

Specimen length in each direction, L (m)	0.15
Horizontal stress, S_H (MPa)	Variable
Vertical stress, S_V (MPa)	0.10
Young's modulus, E (GPa)	1.14
Poisson ratio, v	0.25
Tensile strength, T (MPa)	0.25
Fracture toughness, K_{IC} (MPa m$^{0.5}$)	0.17
Porosity, ϕ (%)	54
Permeability, k (mD)	74
Biot constant, α	0.9
Initial pore pressure, P_0 (MPa)	0.10
Glycerin density, ρ_{gly} (kg/m^3)	1260
Glycerin viscosity, μ_{gly} (cP)	942
Air density, ρ_{air} (kg/m^3)	1.225
Air viscosity, μ_{air} (cP)	1.85e-2
Air compressibility, c_{air}	Ideal air
Number of elements	150 x 150

3.3.2. Effect of injection scheme

In the experiments conducted by AlTammar et al. (2018), three wells were cast while preparing the samples. These wells are modeled as injection source terms. A notch for initiating fracture growth coincides with each of the wells (Figure 3.3). Damage in peridynamics, as shown in the figure, represents material damage, and a value exceeding certain critical limit (usually 0.25) corresponds to a fracture. A horizontal stress of 0.55 MPa is applied in the simulations in Sections 3.3.2 and 3.3.3. The only important difference between these simulations and the experiments is that constant rate injection wells are used here, in contrast to pressure-controlled injection wells in the experiments.

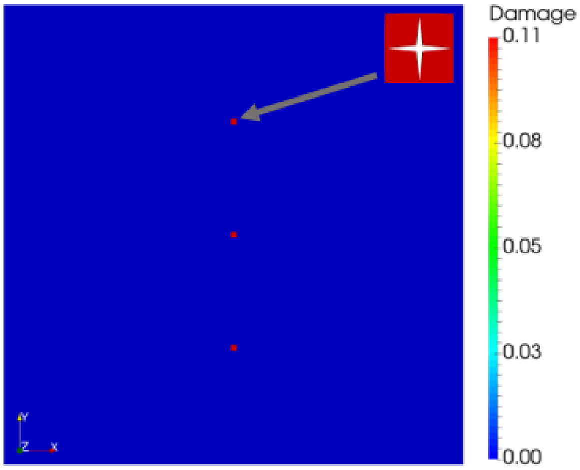

Figure 3.3. Simulation domain used in Sections 3.3.2 and 3.3.3. Red damage zones show the location of the wells. Each well has two starter notches along the principal directions.

3.3.2.1. *Dry rock, injection only in the center well*

A base case with injection only (5e-5 kg/m/s) in the center well of a dry sample is considered. Since permeability is relatively high, it takes about a minute for the pressure to build up for crack growth (Figure 3.4). As expected, the fracture propagates horizontally in the direction of maximum stress (Figure 3.5).

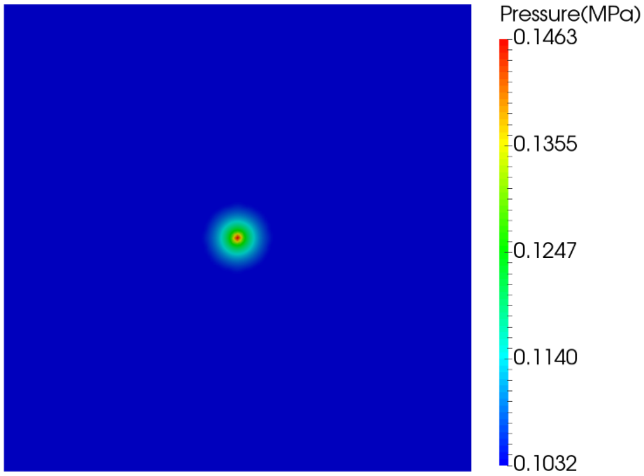

Figure 3.4. Pressure profile just before a crack begins to grow (Case 3.3.2.1)

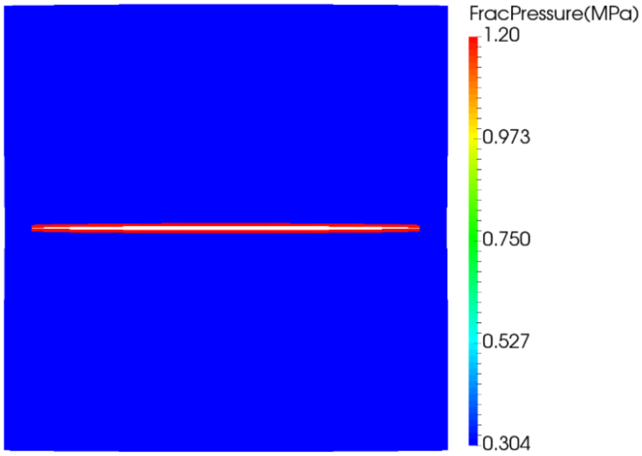

Figure 3.5. Growth direction and fracture pressure (Case 3.3.2.1)

3.3.2.2. Dry rock, injection in all three wells

To investigate the effect of the injection scheme, a simulation was run with fluid being injected at the same rate as in Case 3.3.2.1 in each of the 3 wells. Pressures are higher because of greater cumulative fluid injection (Figure 3.6). Interestingly, crack growth is now reversed to the vertical direction in this case as shown in Figure 3.7. Before the 3 fractures coalesce with each other, some tortuosity is evident because of the stress shadow of one fracture on another (Fisher et al., 2004). This result is consistent with that reported by AlTammar et al. (2018) and is reproduced in Figure 3.8 for comparison.

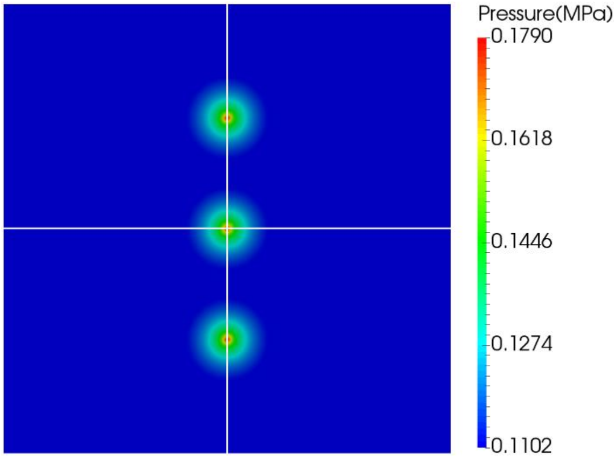

Figure 3.6. Higher pressures before fracture propagation (Case 3.3.2.2). Two centerlines in white are used for analyzing stresses.

The reversal in fracture growth direction can be explained based on an effective stress law for tensile failure. Considering tensile stress to be negative, a material will fail in tension at a location where the effective stress is smaller than the tensile strength (Hubbert and Willis, 1957).

$$\sigma_{effective} < T \tag{3.8}$$

$$\sigma_{effective} = S_{total} - \alpha P \delta_{ij} \tag{3.9}$$

where T is tensile strength of the material (a negative number in the convention followed here), P is pore pressure, and δ_{ij} is Kronecker delta function.

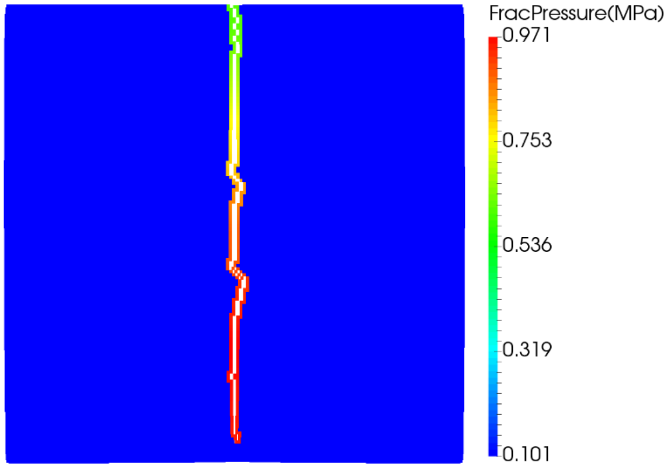

Figure 3.7. Reversed growth direction and lower fracture pressure (Case 3.3.2.2)

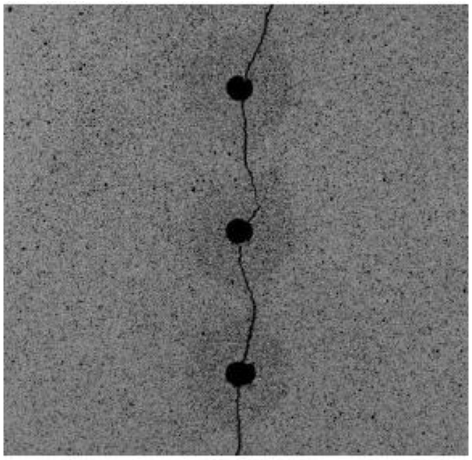

Figure 3.8. Experimental result by AlTammar et al. (2018)

Figure 3.9 illustrates the difference of effective stresses and the tensile strength along the 2 centerlines of the sample. These lines are highlighted in white in Figure 3.6. Each centerline intersects with a starter notch as shown in Figure 3.3. Effective stress is more tensile at the tip of vertical notch as compared to the horizontal one, thereby resulting in crack growth along the vertical centerline. Another important observation is that the injection pressure (292.9 psi) is significantly lower than the base case (507.5 psi) (Figure 3.10). Owing to a more tensile effective stress, it is easier to propagate the fracture, which manifests in a lower injection pressure. The corresponding injection pressures in the experiment were 278 psi for injection in all the three wells and 393 psi for injection in the center well only. The differences in the experimental and simulation results are because of pressure-controlled wells in the experiments and rate-controlled wells in the simulations. While using the experimental pressure-ramping scheme in the simulations, we observed that the fluid continued to leak-off into the high permeability specimen and breakdown was not achieved.

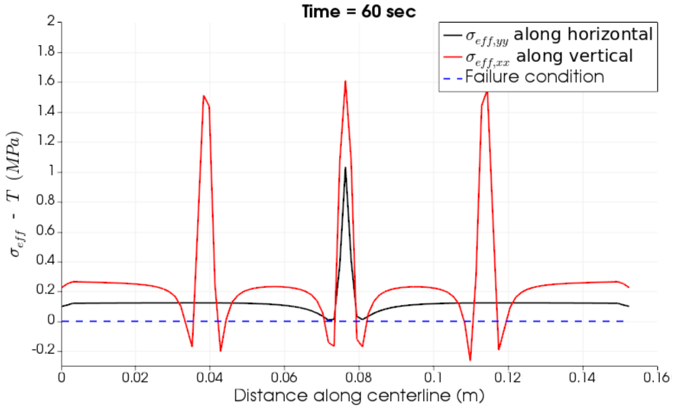

Figure 3.9. Comparison of effective stresses along horizontal and vertical centerlines (Case 3.3.2.2)

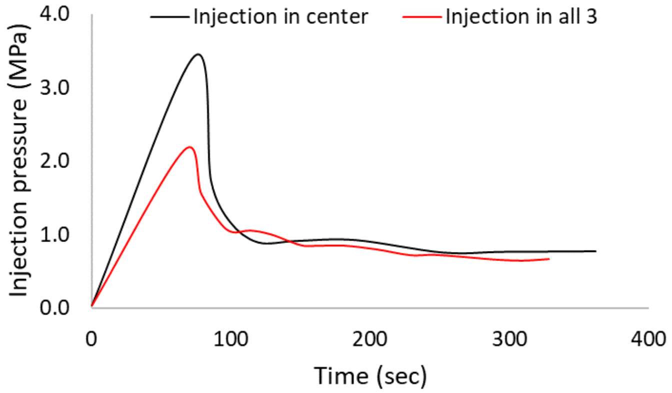

Figure 3.10. Effect of injection scheme on injection pressure (simulation results).

3.3.3. Effect of fluid saturation

3.3.3.1. Saturated rock, injection in all three wells

In this section, the 3-well configuration is utilized again. Fluid is injected in each of the wells at a low rate of 5e-7 kg/m/s for 12 hours, resulting in almost complete saturation with glycerin. Pressure and saturation profiles at the end of this time are shown in Figure 3.11. Because of fluid injection for longer time, pressures are higher as compared to those in Case 3.3.2.2.

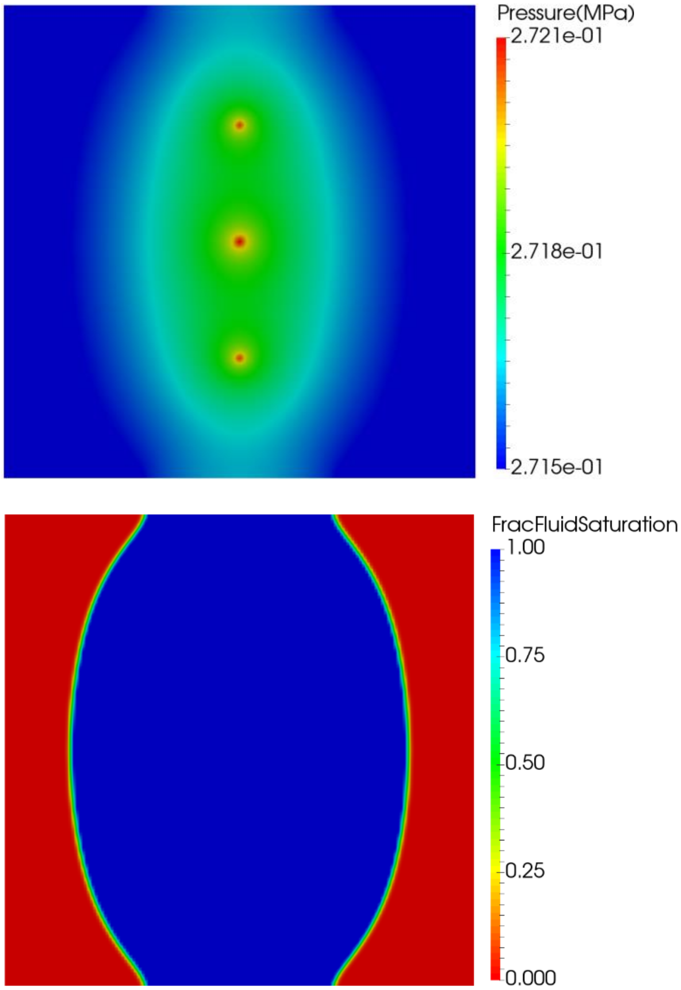

Figure 3.11. Pressure and saturation profiles (top and bottom pictures respectively) after 12 hours (Case 3.3.3.1)

After saturating the sample, the injection rate is increased to 5e-5 kg/m/s in all the wells. The fracture propagates vertically in this case too (Figure 3.12). The fracture pressure is comparatively lower than for a similar simulation in a dry sample. Effective stresses, shown in Figure 3.13, reveal that those along the vertical centerline are lower. Thus, this result is also justified based on an effective stress law.

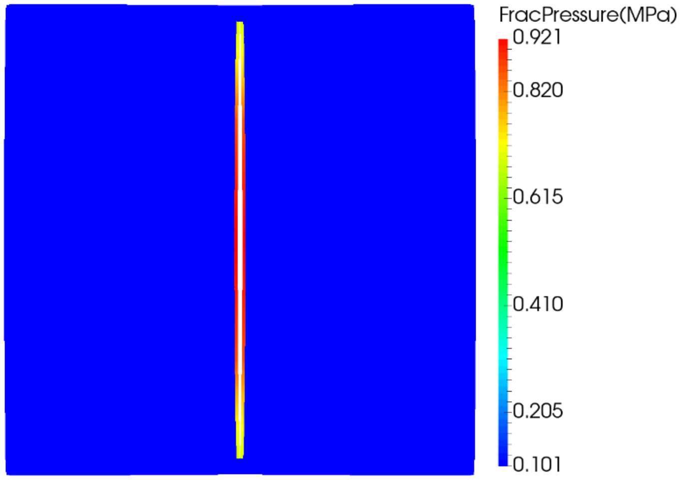

Figure 3.12. Reversed growth direction and further lower fracture pressure (Case 3.3.3.1)

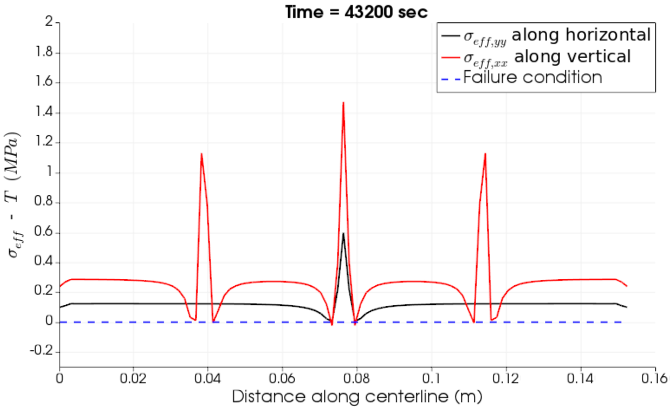

Figure 3.13. Comparison of effective stresses along horizontal and vertical centerlines (Case 3.3.3.1)

3.3.4. Effect of Applied Stress

The effect of applied stress on fracture propagation in the presence of a non-uniform pore pressure field is demonstrated in this subsection. A 5-well pattern, similar to that used by AlTammar et al. (2018), is modeled (Figure 3.14). For brevity, only 2 of the experiments with partially saturated specimens are presented. A horizontal stress of 0.45 MPa and 0.55 MPa respectively were applied in the 2 cases. Both were performed in 3 steps. In the first step, they injected fluid in all the wells to saturate the sample. In the second, fluid was selectively injected in the top-right well to create a non-uniform pore pressure field. Eventually, the center well was hydraulically fractured. These steps, which will be referred to as the saturation period, pressurization period, and fracturing period respectively, are summarized in Table 3.2. They remain the same in the 2 cases.

Table 3.2. Injection steps for simulations in Section 3.3.4

Injection steps	**Well**	**Time (s)**	**Rate (kg/m/s)**
Saturation	All	1200	5e-7
Pressurization	Top right	90	1e-5
Fracturing	Center	0.05	5e-5

3.3.4.1. 5-wells, lower stress contrast

In the first case, a horizontal stress of 0.45 MPa is applied. Figure 3.14 shows pressure and saturation profiles at the end of the saturation period, along with the direction of maximum stress. Since the wells are located symmetrically and injection rates are equal, the maximum stress is not re-oriented from its initial horizontal direction.

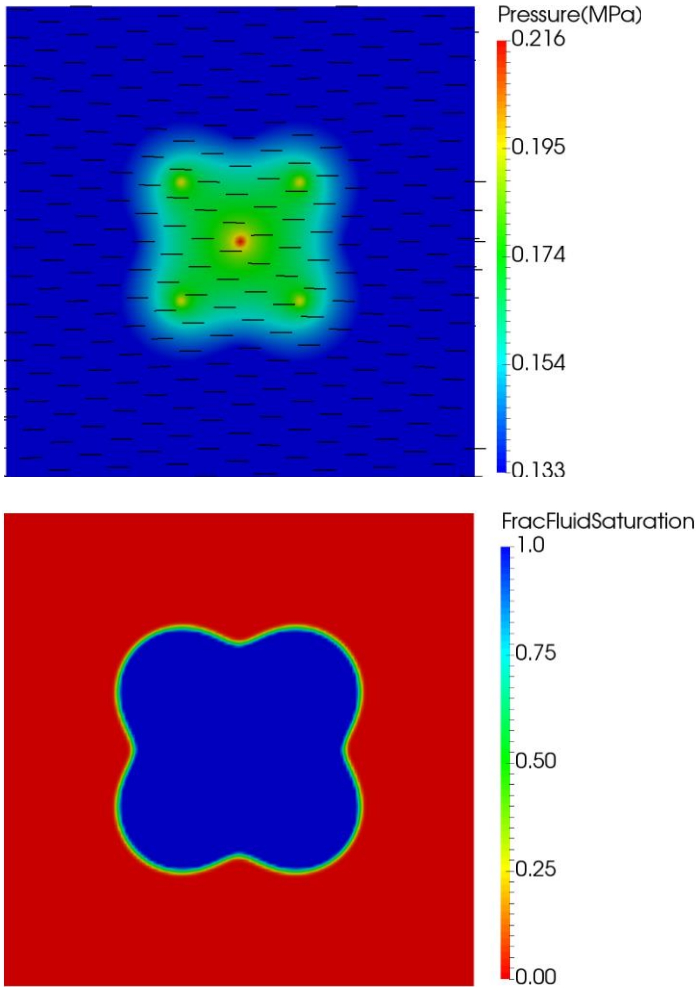

Figure 3.14. Pressure and saturation profiles (top and bottom pictures respectively) after saturation period. Black lines in the top picture represent maximum stress direction (Case 3.3.4.1)

Figure 3.15 shows pressure and saturation profiles at the end of the pressurization period. Maximum stress is re-oriented towards the pressurized top-right well, which is in agreement with analytical solutions in the literature (Detournay & Cheng, 1993; Coussy, 2004).

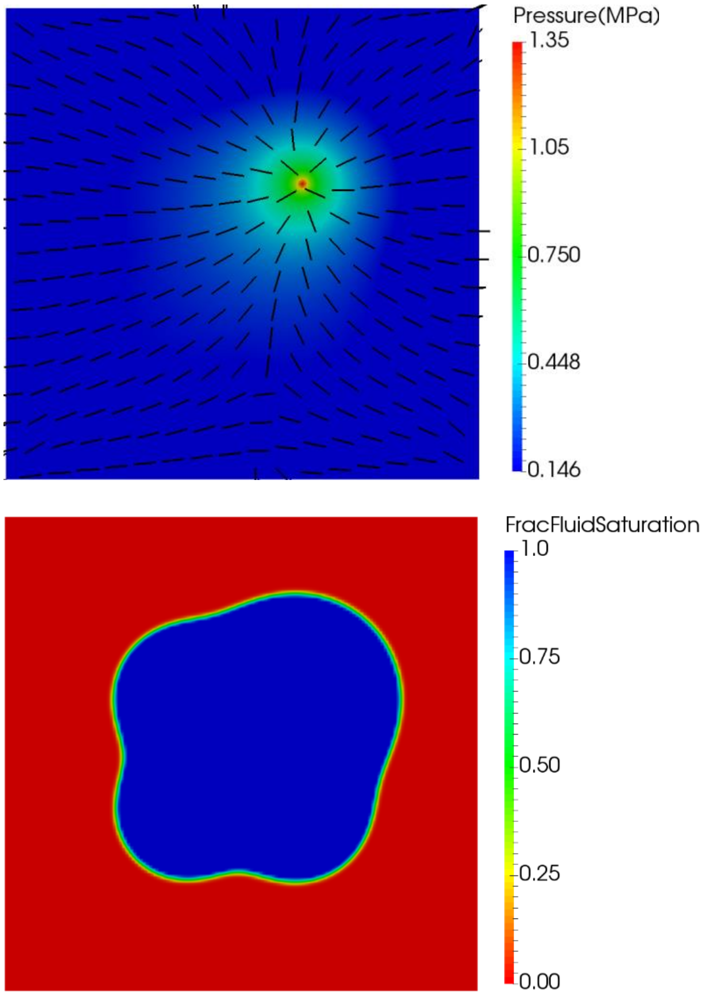

Figure 3.15. Pressure and saturation profiles (top and bottom pictures respectively) after pressurization period (Case 3.3.4.1)

In the presence of such a non-uniform pore pressure field, the fracture is attracted towards the injector well or high-pressure region as shown in Figure 3.16. This result is consistent with the one reported by AlTammar et al. (2018) and Bruno and Nakagawa (1991). It can also be explained by the effective stress law. Equation (3.9) implies that effective stress is more tensile near the high pore pressure region, thereby attracting the fracture towards itself.

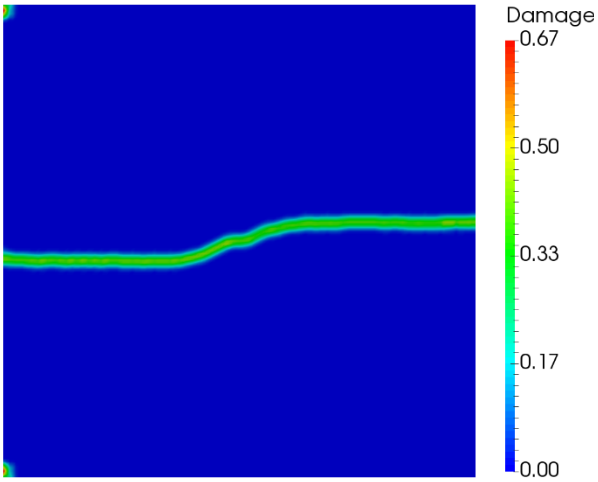

Figure 3.16. Fracture propagation in lower stress contrast (Case 3.3.4.1)

3.3.4.2. 5-wells, higher stress contrast

In the second case, the horizontal stress is increased to 0.55 MPa. Pressure and saturation profiles at the end of the saturation period are almost identical to the previous case. However, at the end of the pressurization period, maximum stress is not re-oriented as much towards the pressurized well as in the previous case (Figure 3.17). This is because the re-orientation effect has been suppressed by the higher far-field stress in this case.

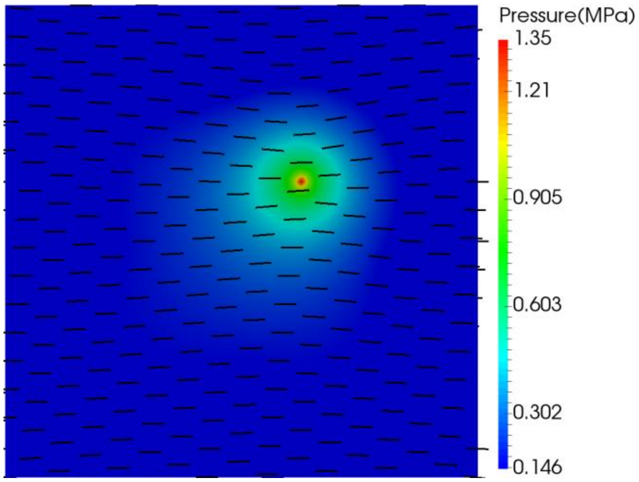

Figure 3.17. Pressure profile (top and bottom pictures respectively) after pressurization period (Case 3.3.4.2)

Since stress re-orientation is less pronounced, the fracture is not attracted towards the high-pressure region as strongly as in the previous case with lower far-field stress (Figure 3.18). In this case the effect of the increase in total stress in the high pore pressure region is more pronounced and the tensile strength is less relevant.

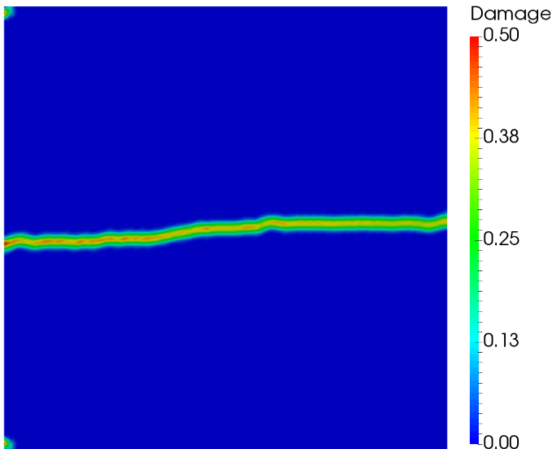

Figure 3.18. Fracture propagation in lower stress contrast (Case 3.3.4.2)

3.4. CONCLUSIONS

In this chapter, an immiscible two-phase hydraulic fracturing simulator based on the non-local theory of peridynamics has been developed and validated against laboratory experiments. The effect of induced changes in pore pressure (using multiple injection sources) on fracture growth has been investigated in detail.

The following are the key conclusions:

- Fractures initiating from multiple injection points can grow towards each other by opening against the maximum stress.
- Saturating a specimen with fluid prior to fracturing can significantly lower the breakdown pressure.

- In low stress environments in the laboratory, fractures are always attracted towards the high pore pressure region. The strength of this attraction depends on both the magnitude of the pore pressure and the pressure gradients.

It should be pointed out that for a tensile fracture to propagate, two conditions must be met. First, the rock must fail under tension, which is governed by the effective stress becoming smaller than the tensile strength of the rock (considering compression to be positive). Second, the fracture pressure must exceed the minimum total stress outside the fracture for it to attain a finite width.

In the laboratory-scale experiments modeled in this chapter, the tensile strength of the rock is much greater than the confining stresses and tensile failure governs the propagation of a hydraulic fracture. According to the Terzaghi principle, an increase in pore pressure results in a decrease in the effective stress. Thus, at low confining stresses in the laboratory, tensile failure is more conducive around high pore pressure regions with lower effective stress and this results in a hydraulic fracture being attracted towards high pore pressure regions.

Under field conditions, the confining stresses are much greater than the tensile strength of the rock and finite fracture width condition governs the propagation of a hydraulic fracture. A decrease in pore pressure results in a decrease in the total stress. Thus, at high confining stresses in the field, attaining a finite fracture width is more conducive around low pore pressure regions with lower total stress. This results in a fracture originating from a new (child) well to be attracted towards the depleted regions of an old (parent) well and is demonstrated in the next chapter.

CHAPTER 4: APPLICATION OF THE IMMISCIBLE TWO-PHASE PERIDYNAMICS-BASED HYDRAULIC FRACTURING MODEL*

4.1. INTRODUCTION

Hydrocarbons are economically produced from unconventional reservoirs by hydraulically fracturing wells. However, production from these fractures declines rapidly due to the ultra-low matrix permeability of shale reservoirs. It is common to drill and fracture new child (or infill) wells in the regions left undrained by the parent well fractures. These child well fractures see the modified stress state due to production from the parent well, rather than the in-situ stress state.

The influence of non-uniform pore pressure fields on fracture propagation has been investigated both experimentally and numerically (Bruno & Nakagawa 1991, Berchenko & Detournay 1997, Agrawal et al. 2018). Changes in magnitude and orientation of stresses around producing fractures have gained interest due to the popularity of infill well drilling (Singh et al. 2008, Roussel et al. 2013, Manchanda et al. 2018). In addition to the depleted pressure field, these stress changes play a crucial role in determining the geometry of the child well fractures (Gupta et al. 2012, Rezaei et al. 2017, Safari et al. 2017, Ajisafe et al. 2017). When the horizontal stress anisotropy is low, Gupta et al. (2012) revealed that stress reversal may occur close to the infill well leading to the formation of longitudinal fractures. Rezaei et al. (2017) argued that asymmetric fracture propagation towards depleted regions leads to fracture interference and ineffective reservoir stimulation. Such interference has been shown to be manifested in the form of pressure hits and microseismic data (Yadav and Motealleh 2017, Kumar et al. 2018, Courtier et al. 2016).

---

*Agrawal, S; and Sharma, M.M. 2018. “Impact of Pore Pressure Depletion on Stress Reorientation and Its Implications on the Growth of Child Well Fractures.” in SPE/AAPG/SEG Unconventional Resources Technology Conference. Agrawal conducted and documented the research, with technical discussions and supervision from Sharma.

In this research, a poroelastic hydraulic fracturing simulator based on the non-local theory of peridynamics has been utilized. Stress changes around multiple producing fractures is presented first. This is followed by a sensitivity analysis on Biot's constant, pressure drawdown and reservoir fluid type. Subsequently, a fracture from the child well is propagated and its trajectory is analyzed based on the current stress state in the depleted reservoir.

4.2. MODEL DESCRIPTION

We recently added the functionality of reservoir simulation to our peridynamics-based hydraulic fracturing model. Details regarding mathematical formulation, solution scheme, and model validation have been reported by Katiyar et al. (2019). Some of the capabilities of the model include:

1) Fully coupled and poroelastic
2) Any scale of heterogeneity can be modeled
3) No explicit criterion required for fracture initiation
4) Black-oil with relative permeability effects

4.3. STRESSES AROUND A SINGLE FRACTURE

Before getting into the discussion of stress reorientation around fractures of a parent well, it is useful to look at total normal stresses around a propagating and a producing fracture. When a fracture propagates, the rock at the fracture tips is under relative tension to create new fracture volume, and that around the fracture faces is under relative compression since it is pushed away due to opening of the fracture (Figure 4.1a). In contrast, the opposite happens when reservoir fluids are produced from a fracture. The rock at the fracture tip is under relative compression and that around the fracture faces is under relative tension (Figure 4.1b).

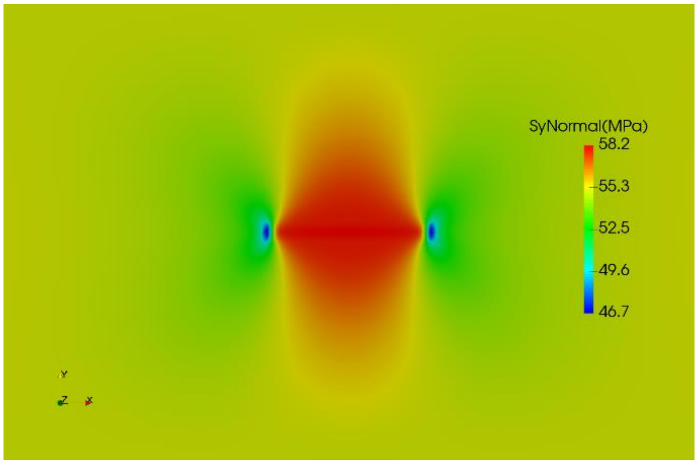

(a)

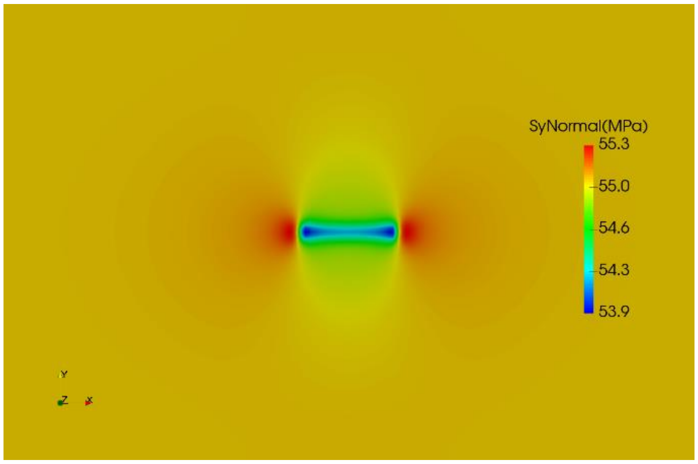

(b)

Figure 4.1. Total normal stresses around a single fracture. (a) propagating fracture, (b) producing fracture

4.4. MODEL SETUP

A schematic of the model setup used in this research has been illustrated in Figure 4.2. A 2-D domain with plane strain assumption is considered such that fracture height growth is not modeled in this work. A traction-free boundary condition is applied on the boundaries of the domain. Laterals of two parent wells with two fractures each and a child well with a perforation in its middle are displayed. The white dashed line BB’ shows a potential path of the fracture initiating from the child well perforation. The parent well fractures are simulated as high permeability grid blocks. The reservoir is assumed to be saturated with in-situ hydrocarbon fluid.

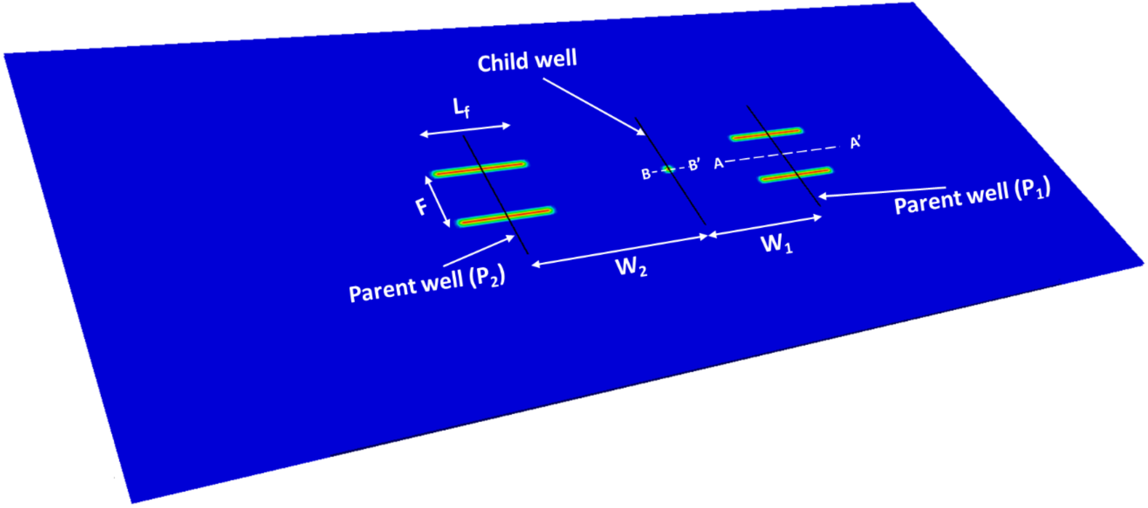

Figure 4.2. Model setup for investigating parent-child well interaction. W_1 and W_2 are well spacing, F is fracture spacing, and L_f is length of each fracture of the two parent wells (P_1 and P_2).

4.5. STRESSES AROUND MULTIPLE PRODUCING FRACTURES

The typical well geometry shown above is used to demonstrate the impact of stress reorientation around multiple producing fractures. The Biot's constant, pressure drawdown, and reservoir fluid type is varied to show the impact of these important parameters. The results of this analysis are used in Section 4.6 to make recommendations and conclusions for methods to avoid frac hits from a child well.

4.5.1. Base case

Important model parameters for the base case have been summarized in Table 4.1. Pressure depletion from the two fractures of the right parent well (P_1) and resulting stress reorientation are shown in Figure 4.3a. It is evident that the stresses reorient much farther away from the fracture as compared to the pore pressure. In shales, pore pressure depletion may be felt only a few feet or tens of feet from the fracture (because of the ultra-low permeability), however, the changes in stresses can extent several tens or hundreds of feet. It is also important to note that both the magnitude and the orientation of the stresses is altered as a result of fluid production. This is because stresses are affected not only by pressure, but also by pressure gradients.

In Figure 4.4, changes in total normal stress due to production are analyzed along probe line AA’. These stress changes are a cumulative effect of pressure depletion and the accompanying mechanical deformation of the rock. There is a tensile region between the producing fractures and a compressive region just ahead of the fracture tips. It can be noted that the magnitude of compression is significantly smaller than that of tension, resulting in a tensile cliff being generated close to the fracture tips. Thus, a fracture propagating from the child well along BB’ may be attracted towards this tensile region, as demonstrated in Section 4.6.

Table 4.1. Parameters for the Base Case in metric units

Fracture length (L_f) : Well spacing (W)	0.50
Fracture spacing (F) : Well spacing (W)	0.33
Shmax, S_{xx} (Mpa)	57.5
Shmin, S_{yy} (Mpa)	55.0
Pore pressure (Mpa)	48.0
Bottomhole pressure (Mpa)	25.0
Production time (days)	150
Young’s modulus (GPa)	10.0
Permeability (m^2)	300e-19
Oil viscosity (mPa.s)	0.25
Fracturing fluid viscosity (mPa.s)	1.00
Poisson ratio (ν)	0.25
Biot constant (α)	0.7

4.5.2. Effect of poroelasticity

Poroelasticity is turned off in this case by setting Biot constant = 0. As illustrated in Figure 4.3b, the pressure depletion around the fractures remains similar to that in the Base Case. However, as the effects of poroelasticity are ignored, stress reorientation is not observed, thereby highlighting the importance of considering poroelasticity in unconventional rocks. It should be noted that since the parent well fractures are modeled as high permeability grids in this chapter, stress changes due to fracture closure during production are not captured.

Similar negligence of changes in the stress is observed in the stress profile along AA' (Figure 4.5). The total normal stress between the fractures remains the same as in the initial condition.

4.5.3. Effect of higher pressure drawdown

For studying the sensitivity on drawdown, the bottomhole pressure at the parent well (P_1) is reduced from 25 MPa to 20 MPa. This results in higher pressure gradients around the fractures and thus, more pronounced stress reorientation (Figure 4.3c). The distance of pressure diffusion and stress reorientation away from the fractures remains the same suggesting that it depends only on the diffusivity of the fluid.

4.5.4. Effect of saturating fluid

In this case, the reservoir is assumed to be saturated with natural gas of ideal gas compressibility and 0.025 cP viscosity. For the same pressure drawdown over the same period of time, pressure diffuses to smaller distances due to the high compressibility of the gas. Consequently, stress reorientation remains more localized than in the Base Case (Figure 4.3d).

As shown in Figure 4.5, the tensile cliff generated is shallower in the presence of gas as a saturating fluid.

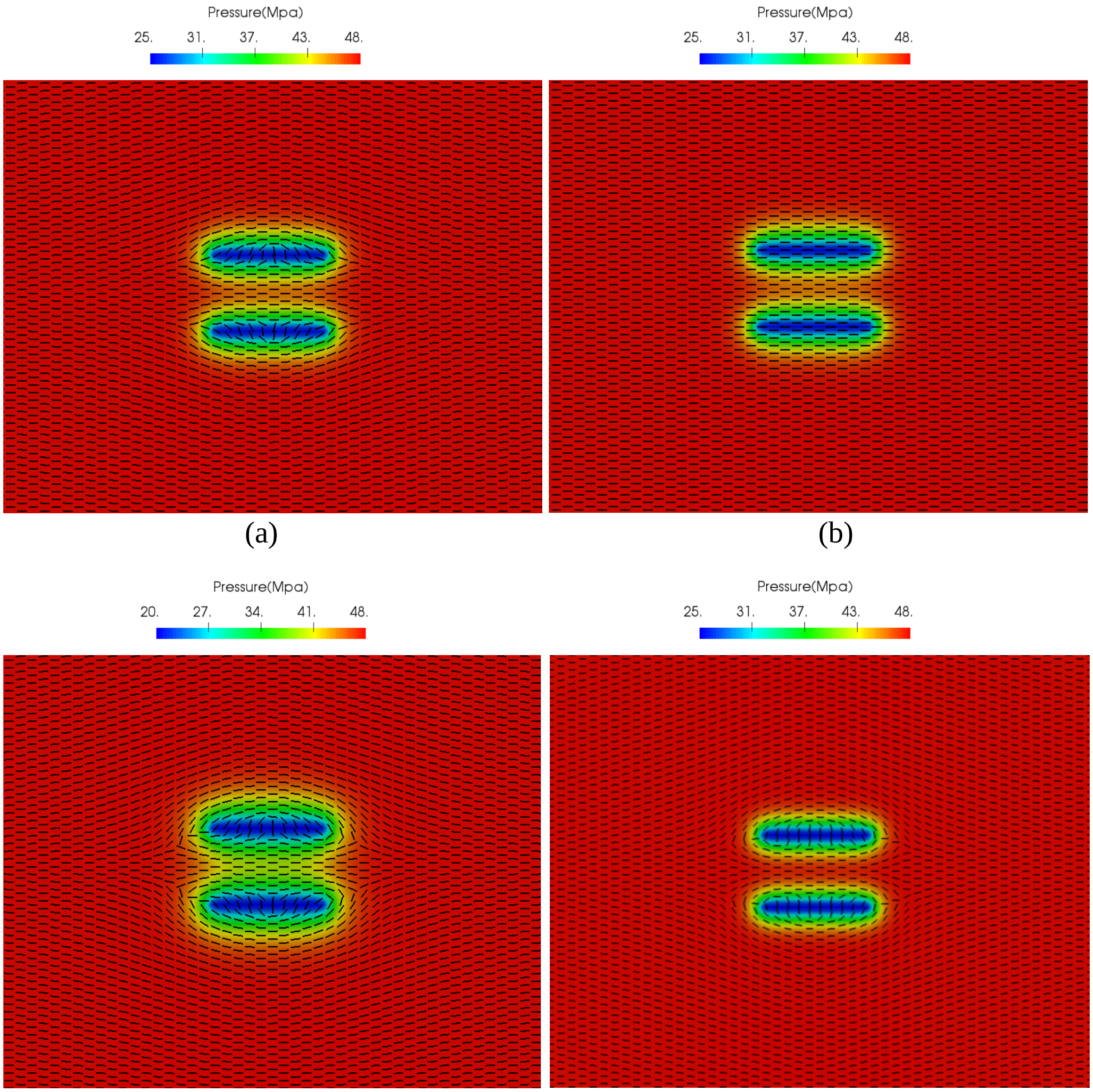

(a) (b)

(c) (d)

Figure 4.3. Pressure profiles for the four cases in Section 4.5. Black lines correspond to the direction of maximum principal stress in each image. (a) Base case, (b) No poroelasticity, (c) Higher pressure drawdown, (d) Gas reservoir

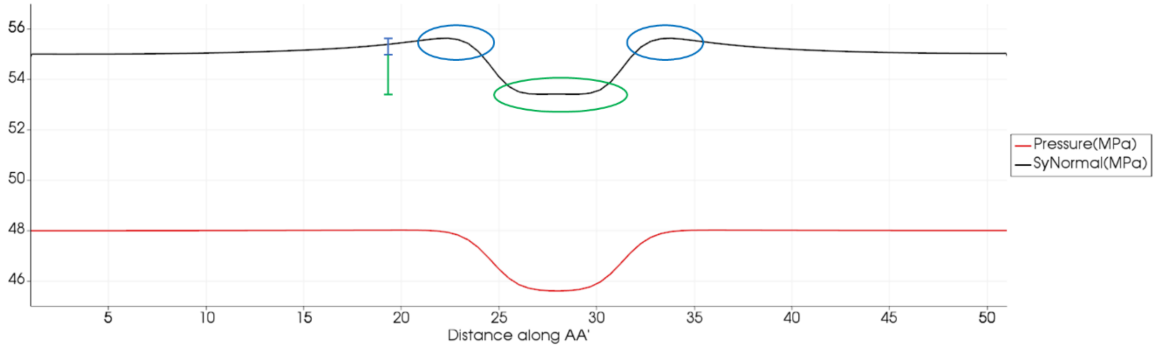

Figure 4.4. Pressure and total normal stress plots along line AA’ shown in Figure 4.2. The green circle represents the tension created between the producing fractures and the blue circles represent the small compressive regions.

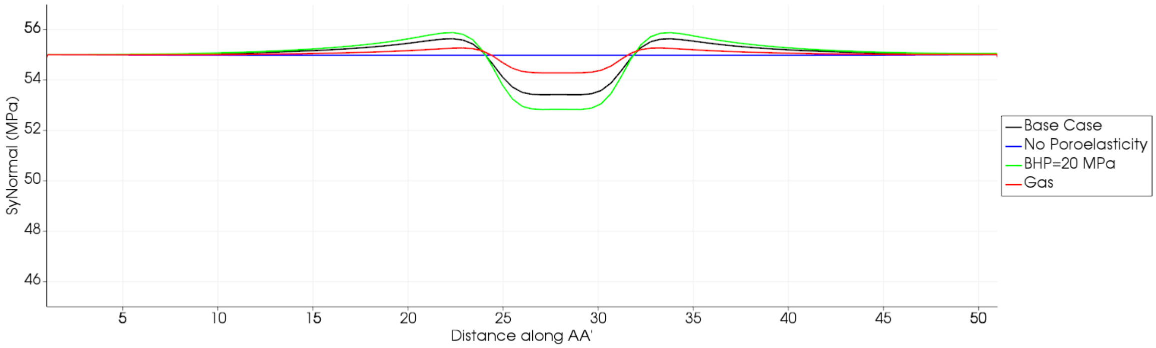

Figure 4.5. Comparison of total normal stresses in the four cases in Section 4.5.

4.6. FRACTURE PROPAGATION FROM CHILD WELL

4.6.1. Only P_1 is depleted

In the model setup introduced in Figure 4.2, stress reorientation because of depletion from parent well (P_1) was demonstrated (in Section 4.5). The parent wells are shut-in and a fracture is propagated from the child well for this Base Case as illustrated in Figure 4.6. Since the permeability of the medium is very small and the time scale of fracturing is much smaller than that of reservoir depletion, the pressure profile remains unchanged during child well fracture propagation. The fracture grows symmetrically till it sees the tensile region between the two fractures of well P_1. Once it experiences this lower stress region, the right wing of the fracture grows preferentially towards the parent well due to the lower total normal stress. This is consistent with the literature, which shows that there is asymmetric fracture growth towards the depleted area.

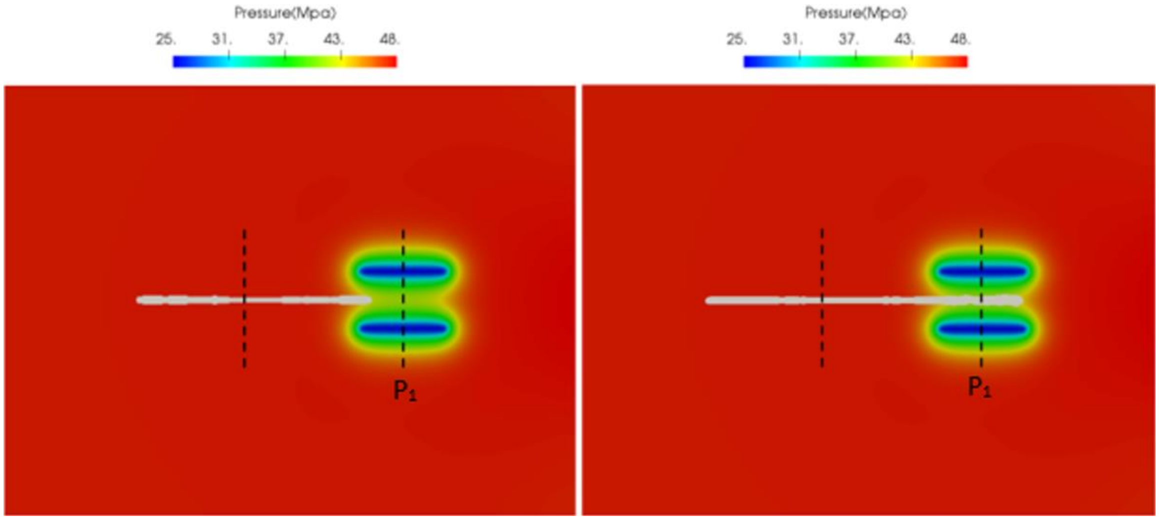

(a) (b)

Figure 4.6. Geometry of the child well fracture. (a) Symmetric growth till it sees the depleted region, (b) Asymmetric growth afterwards.

4.6.2. Both P_1 and P_2 depleted equally, child well not centered

In ideal field operations, child well lateral may be centrally landed between the parent wells (W_1=W_2 in Figure 4.2). However, practical operations often necessitate an asymmetric positioning of the child well. This may be due to operational reasons or to avoid reservoir heterogeneities, such as faults. This situation is modeled here by setting the well spacing W_1 as 75% to be well spacing W_2.

After producing from both the parent wells at a bottomhole pressure of 25 MPa, a fracture is propagated from the child well. The resulting fracture trajectory is shown in white in Figure 4.7. Due to the proximity of the child well to the parent well on the right (P_1), the right wing of the child well fracture sees the tensile region first. Consequently, the right wing takes off, while the left wing stops propagating. Due to this asymmetric growth, almost 16% of the undepleted region between the two parent wells remains unstimulated.

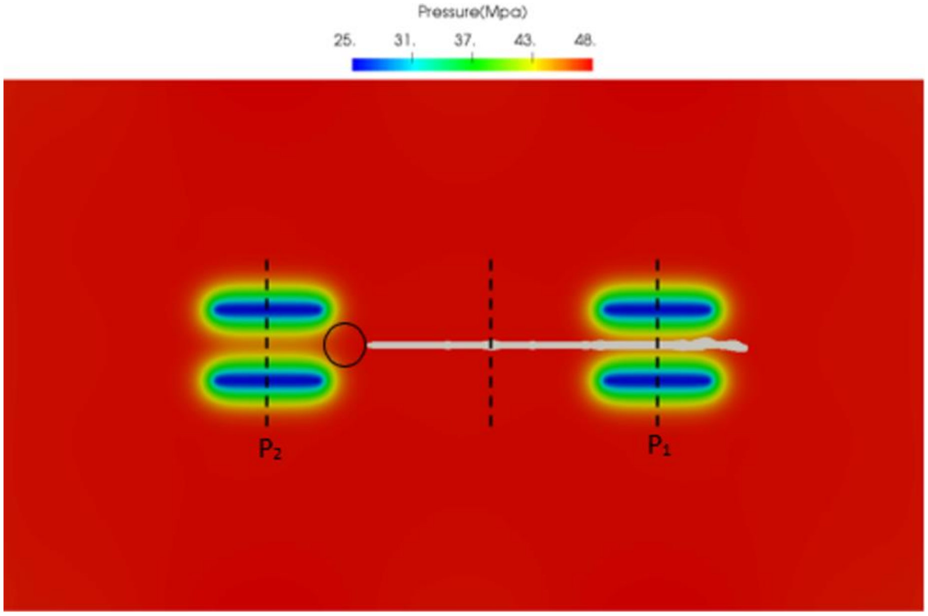

Figure 4.7. Geometry of the child well fracture for Case 4.6.2. Black circle indicates part of the reservoir left unstimulated.

4.6.3. P_1 depleted faster than P_2, child well not centered

To study the effect of the extent of depletion, the parent well to the right of the child well (P_1) is depleted at a lower bottomhole pressure of 20 MPa. As expected, the child well fracture is attracted more strongly towards well P_1 (Figure 4.8) as compared to the previous case. This is because of the more tensile region formed between the fractures of well P_1, which has been depleted at a higher drawdown (Figure 4.5). Thus, asymmetry in the geometry of the child well fracture is further accentuated, thereby resulting in a 22% unstimulated area near well P_2.

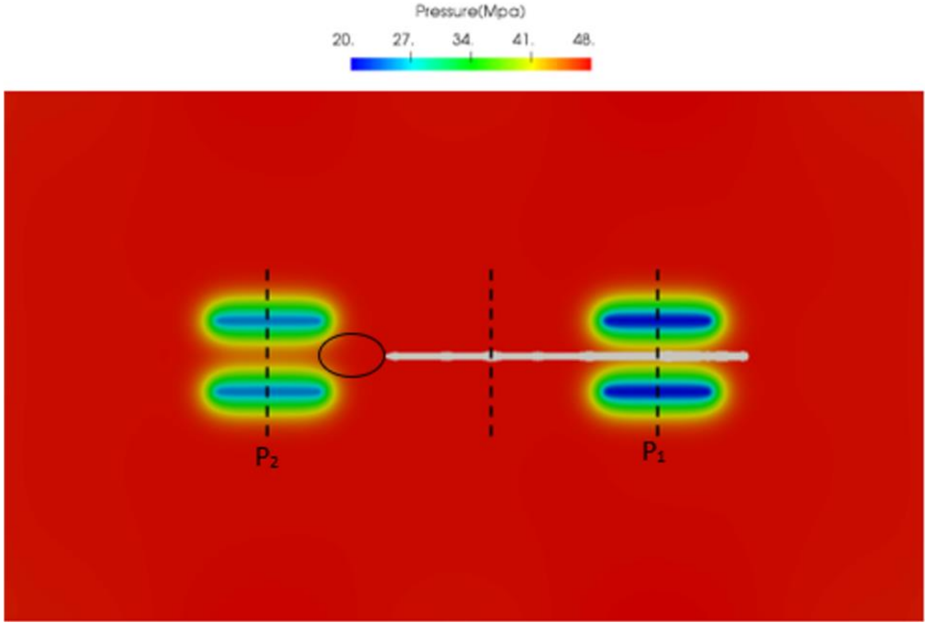

Figure 4.8. Geometry of the child well fracture for Case 4.6.3. A longer black circle indicates that a bigger part of the reservoir is left unstimulated.

4.6.4. Both P_1 and P_2 produce gas, child well not centered

The impact of depletion for a gas reservoir (compared to an oil reservoir) is studied in this case. The reservoir is depleted equally from the two parent wells in this case. The depleted pressure distribution and corresponding fracture trajectory are displayed in Figure 4.9. This figure clearly shows that fracture from the child well is not attracted as strongly towards the depleted region of well P_1. The decreased strength of this attraction can also be explained by the less tensile region formed in a gas reservoir as illustrated in Figure 4.5. In this case, 12% of the undepleted region is left unstimulated. It is clear that gas reservoirs are less susceptible to depletion and stress changes than oil reservoirs (for the same drawdown) due to their much smaller compressibility which causes the stress changes to be more localized near the parent well fractures.

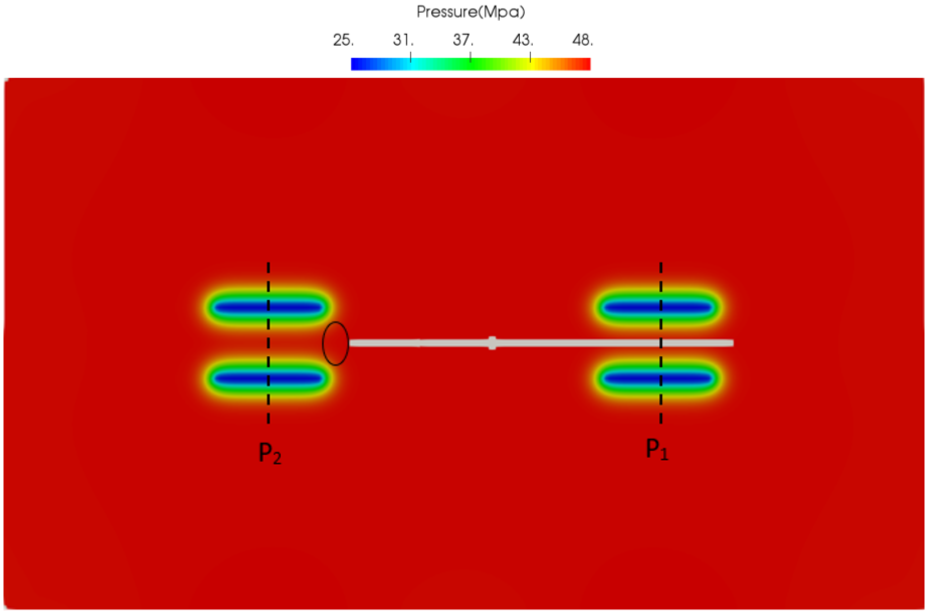

Figure 4.9. Geometry of the child well fracture for Case 4.6.4.

It must be noted that these parent-child well simulations have been performed with a 2-D plane strain model, which assumes that the fracture height is much greater than the fracture length. Though we have scaled down the injection rates to account for the differences between the fracture height in our simulations and that in the field, there would be differences in the geometry of the child well fracture. In a 2-D plane strain model, a longer fracture is more likely to propagate. In the field where a fracture has a finite height, its further growth scales with its height. Thus, our observation of the right wing continuing to grow after coming out of the low tensile stress region between the depleted fractures of well P_1 might be a result of the 2-D plane strain assumption. This should be investigated further with 3-D simulations and the exercise is not taken up in this dissertation.

4.7. MITIGATION BY RE-PRESSURIZATION

In the previous section, preferential fracture growth from a child well towards the depleted regions of parent wells was presented. This preferential propagation led to a part of the reservoir being unstimulated. In this section, re-pressurization of parent well fractures is explored as a potential solution for mitigating asymmetric fracture growth from the child well. The costs and economics of injecting large volumes of fluid into parent wells are not addressed in this paper and must be considered before such a strategy is applied in the field.

The depleted reservoir of Section 4.6.3 is re-pressurized at a bottomhole pressure of 51 MPa for 10 days. The resulting pressure profile and stress reorientation are shown in Figure 4.10. In the short injection time simulated in this case, pressure diffuses to a small distance within the depleted region. However, except for the near-tip regions, the stresses orient back close to their original in-situ state. Figure 4.11 shows that between the parent well fractures along line AA’, the pressure increases by 2 MPa, whereas the total normal stress increases by nearly 3 MPa. This compressive region formed due to re-pressurization may act as a barrier for fracture growth between the parent well fractures. The pros and cons of re-pressurization using different injection fluids and different injection schemes need to be considered so that and this process can be optimized.

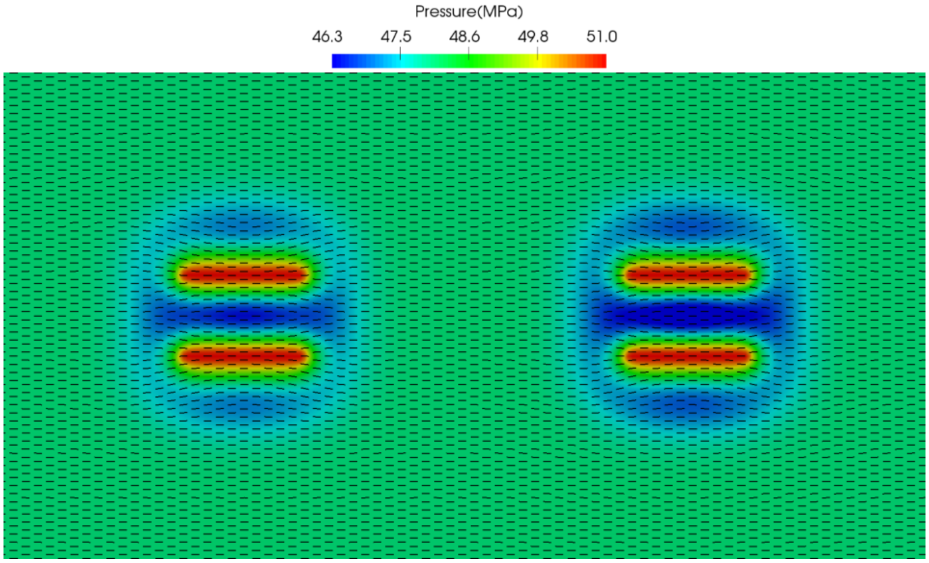

Figure 4.10. Pressure profile and stress reorientation after re-pressurizing the parent well fractures.

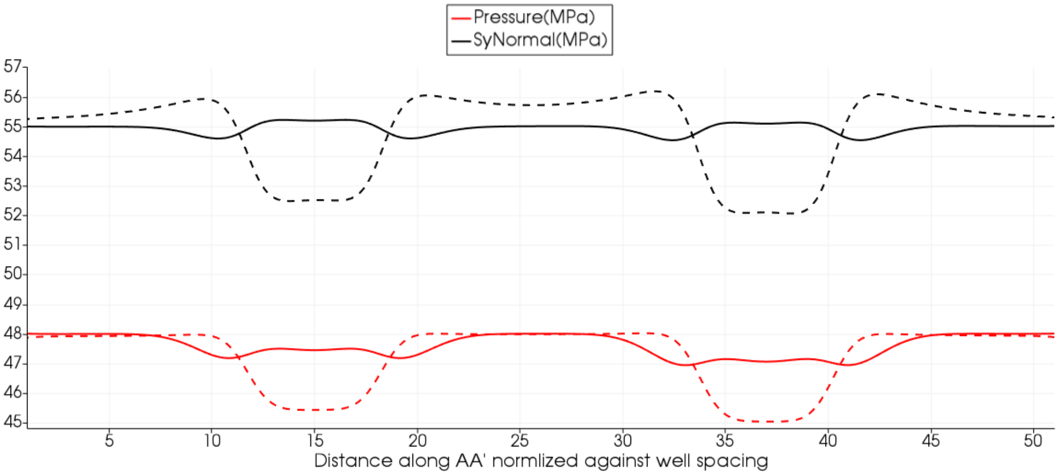

Figure 4.11. Comparison of pressure and total normal stress before and after re-pressurization. Broken and solid lines represent respectively the values before and after re-pressurization.

After re-pressurizing the two parent wells, a fracture is propagated from the child well. The fracture grows almost symmetrically till the right wing experiences compression between the re-pressurized P_1 fractures and stops (Figure 4.12a). Thereafter, the left wing propagates and covers the entire undepleted region (Figure 4.12b). Both the wings eventually stop growing in length due to the compressive stress barrier on each side. Thus, re-pressurization of parent well fractures leads to a more effective child well stimulation and reduces the chances of frac hits in the parent well.

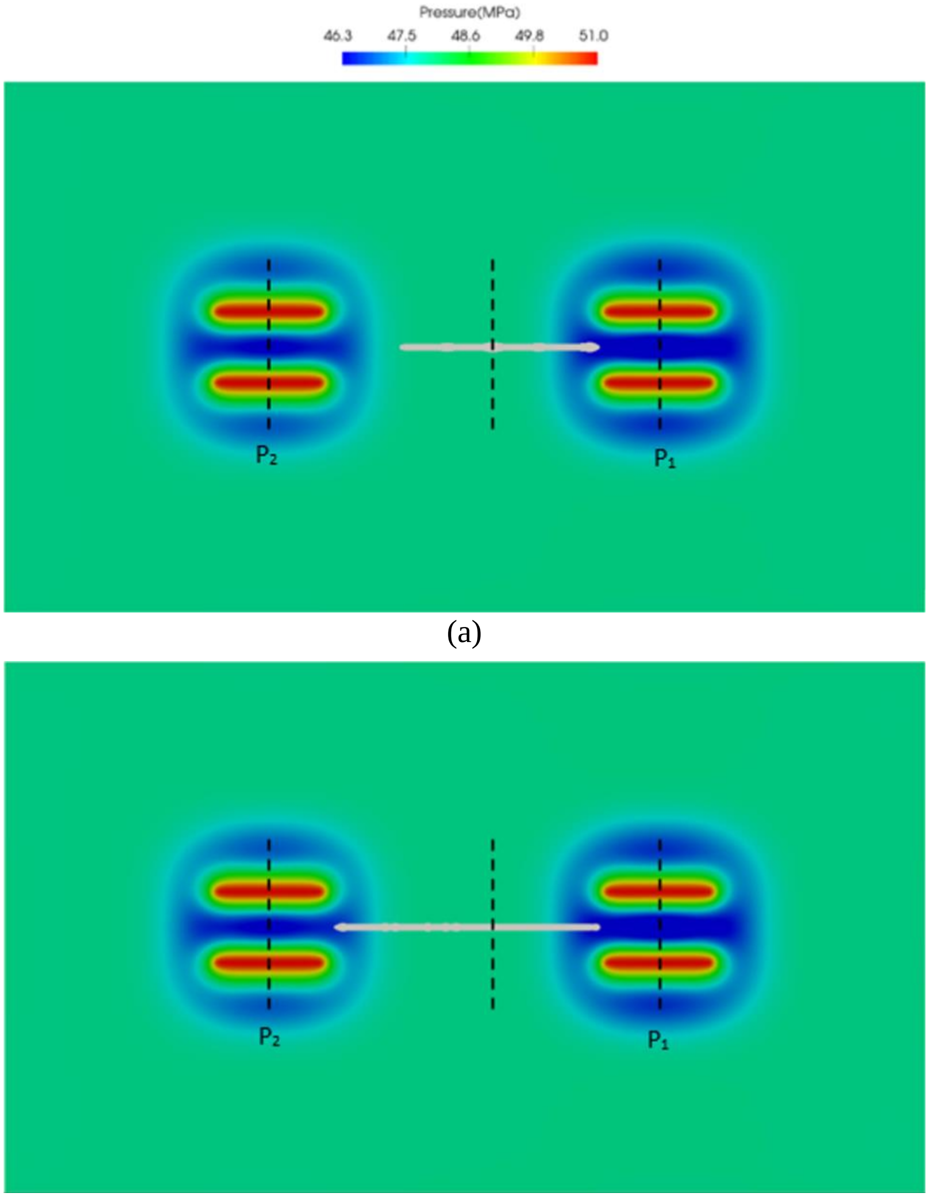

(a)

(b)

Figure 4.12. Geometry of the child well fracture for Case 4.7. (a) Right wing stops growing on seeing the compressive region between the re-pressurized parent well fractures. (b) Left wing grows further to cover the entire region left undepleted by the parent well fractures.

4.8. CONCLUSIONS

Pressure depletion and stress reorientation around multiple fractures of a parent well have been investigated using a poroelastic peridynamics-based fracturing simulator. Subsequently, fracture growth from a child well in this non-uniform pressure field is simulated. The following key conclusions can be drawn from this research:

(a) Hydrocarbon production from parent well fractures leads to the formation of a region of lower compressive stress between them. This effect is less pronounced in gas reservoirs and increases as the pressure drawdown and the volume of fluids produced is increased.

(b) The spatial extent of the region of altered stress is much larger than the region in which the pore pressure is reduced.

(c) Significant stress reorientation occurs as well. This is primarily controlled by the pore pressure gradients in the reservoir.

(d) The lower compressive stress region formed between the parent well fractures attracts the child well fractures. This attraction directly correlates with the magnitude of the stress reduction.

(e) Preferential fracture growth towards depleted regions results in under-stimulation of the undepleted parts of the reservoir.

(f) Re-pressurizing the parent well fractures reorients the stresses back, close to the in-situ stress state. This reduces the attraction of the child well fracture towards the depleted regions, thus leading to a better stimulation of the reservoir.

CHAPTER 5: EFFECT OF SHEAR SLIPPAGE ON THE INTERACTION OF HYDRAULIC FRACTURES WITH NATURAL FRACTURES

5.1. INTRODUCTION

In unconventional formations, hydraulic fracturing operations often lead to the formation of complex fracture networks (Gale et al, 2007). This fracture complexity is evident in mineback experiments and core samples retrieved from the fractured wells (Warpinski & Teufel, 1987; Gale et al, 2018). Various fracture diagnostic methods such as microseismic mapping, tracer flowback data, and pressure interference analysis also suggest the formation of complex fracture networks in naturally fractured formations (Fisher et al, 2004; Aimene & Ouenes, 2015; Damani et al, 2012; Kumar et al, 2018; Seth et al, 2018; Seth et al, 2019). The primary mechanism for the formation of complex fracture networks has been identified as the interaction of hydraulic fractures (HFs) with natural fractures (NFs) (Gale et al, 2007). Thus, modeling these networks requires careful investigation of the interaction behavior.

When a HF interacts with a NF, it can exhibit different types of propagation such as crossing, kinking (or jogging), arresting (or terminating), dilating, and branching depending on in-situ stress ratio, angle of approach, and NF characteristics (Figure 5.1). To model these different behaviors, Renshaw & Pollard (1995) derived an analytical crossing criterion for the orthogonal intersection of HF with NF and showed that the stress ratio and coefficient of friction of the NF affect the crossing and turning behavior of the HF. Gu & Weng (2010) extended this criterion to non-orthogonal intersection of HF and NF. Wu & Olson (2014) included both mode I and mode II stress intensities in the criteria

---

*Agrawal, S; Shrivastava, K; and Sharma, M.M. 2018. "Effect of Shear Slippage on the Interaction of Hydraulic Fractures with Natural Fractures." In SPE Hydraulic Fracturing Technology Conference and Exhibition. Agrawal conducted and documented the research. Shrivastava pointed Agrawal to the experiments. Sharma advised and supervised on the paper.

and further extended them. Besides these analytical models, several numerical studies have addressed different aspects of HF-NF interaction. Chuprakov et al (2011) examined the effect of net pressure on the elastic interaction of a HF with a NF. Dahi Taleghani & Olson (2013) researched the interaction of HFs with cemented NFs.

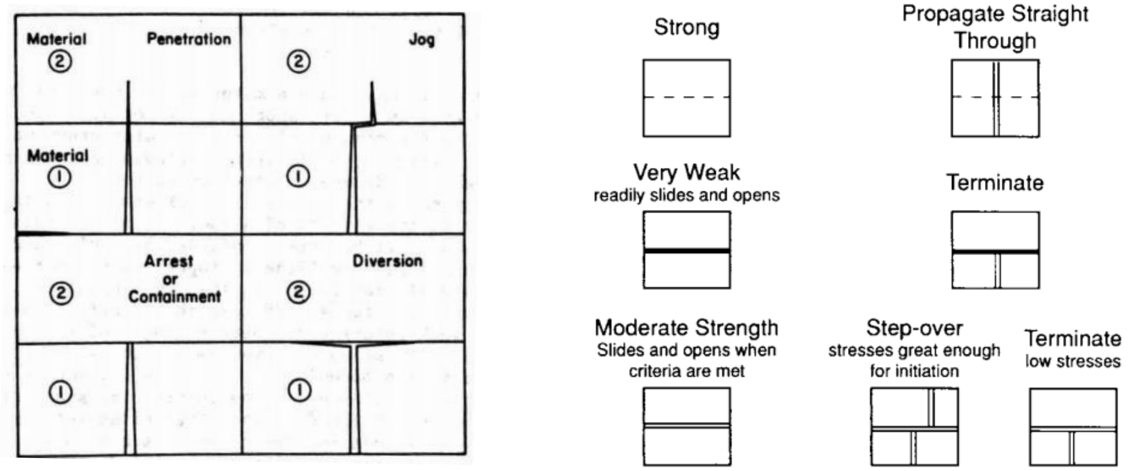

(a) (b)

Figure 5.1. HF-NF interaction behaviors reported previously. (a) Thiercelin et al (1987), (b) Cooke & Underwood (2001)

In addition to numerical modeling, laboratory experiments often provide a useful means for calibrating and validating the hydraulic fracturing models (Gu et al, 2012; Aimene et al, 2018). Zhou et al (2008) showed that besides the stress ratio and angle of approach, shear strength of the NF also affects HF propagation. AlTammar et al (2019) demonstrated the effect of contrast in mechanical properties on HF initiation and propagation. Bahorich et al (2012) revealed that the HF-NF interaction in 3-D can be substantially different than in 2-D.

Wang (2017) has reported an increase in approach angle of a HF prior to the intersection with a NF. Our research in the current chapter is motivated by this experimental observation in high permeability specimens. We model and explain these experiments using our poroelastic peridynamics-based hydraulic fracturing simulator. We also investigate the sensitivity of the increase in HF approach angle on matrix permeability. Subsequently, the simulator is validated against the analytical fracture crossing criteria by neglecting the effects of remote shear failure of the NF prior to being intersected by the HF and those of poroelasticity. Modifications to these criteria are presented while accounting for the aforementioned effects.

5.2. SIMULATION METHOD AND MODEL SETUP

In our peridynamics-based hydraulic fracturing model, a natural fracture can be assigned a weaker tensile strength compared to the intact rock by using a multiplier, α_{NF} (Ouchi et al., 2015b). A natural fracture is treated as a frictional surface and its shear failure is modeled using the Mohr-Coulomb failure criterion. Using a compression positive sign convention, the natural fracture undergoes shear failure when the following stress conditions are met.

$$|\tau_\beta| \geq S_{NF} + \mu_{NF}\sigma_{n\beta} \tag{5.1}$$

Once the shear failure criterion is satisfied, the natural fracture slips and the friction between its surfaces changes from static to dynamic. This is accounted for by multiplying the tangential component of the force acting on the NF by a factor, β_{NF} (Figure 5.2).

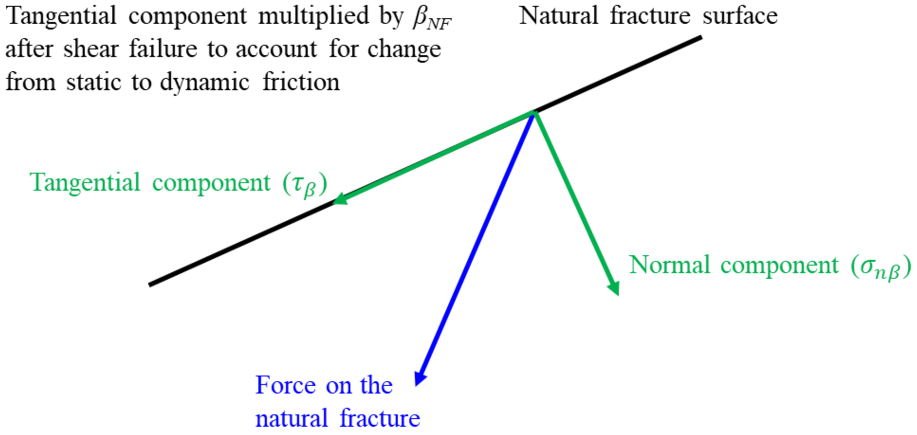

Figure 5.2. Modification of tangential force on natural fracture upon shear failure (Adapted from Ouchi et al., 2015b)

A schematic of the 2-D plane strain model used is shown in Figure 5.3. A natural fracture is considered at different angles (β) ranging from 30^o-90^o with increments of 15^o. A hydraulic fracture is propagated by injecting fluid into the well. The stresses on the natural fracture as the hydraulic fracture approaches it are analyzed to predict the shear failure of the natural fracture. For this purpose, a dimensionless fracture half-length (x_D) is defined such that

$$x_D = x/L \tag{5.2}$$

where x and L are the respective half-lengths of the hydraulic fracture before and at the time of intersection with the natural fracture.

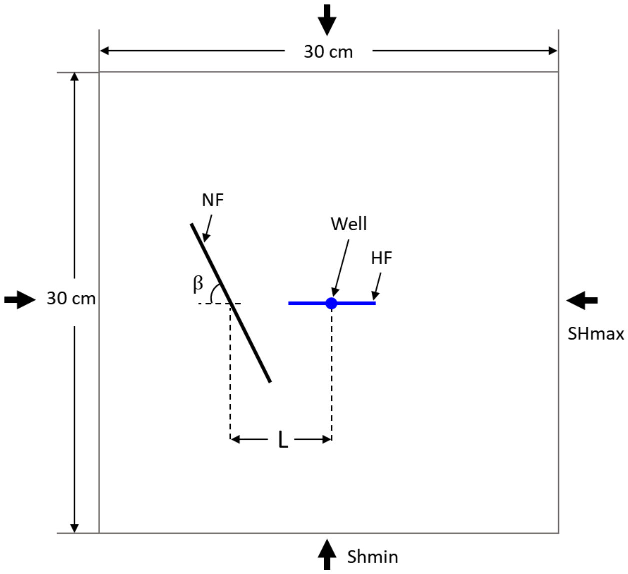

Figure 5.3. Schematic of simulation domain

5.3. INCREASE IN APPROACH ANGLE DUE TO REMOTE SHEAR FAILURE IN HIGH PERMEABILITY ROCKS

Recently, Wang (2017) conducted semi-circular bending tests in hydrostone-plaster specimens to study the interaction between a natural fracture and an induced fracture. They reported an increase in approach angle of the induced fracture before it intersected with the natural fracture (Figure 5.4). They captured the same observation in their finite element simulations as well. In this section, we tested our simulator with these experiments to find out the reason for this increase in approach angle. The model parameters, which are the same as in the experiments, have been summarized in Table 5.1. There are a few key differences between the experiments and the simulations:

- The natural fracture is treated as a frictional interface in our simulations, while it was molded as a plaster inclusion in a hydrostone sample in the experiments.
- The fracture in the simulations is induced hydraulically, whereas that in the experiments was induced mechanically.
- The simulations utilize a rectangular domain, whereas the experiments utilized a semi-cylindrical domain, which may lead to a difference in the boundary conditions.

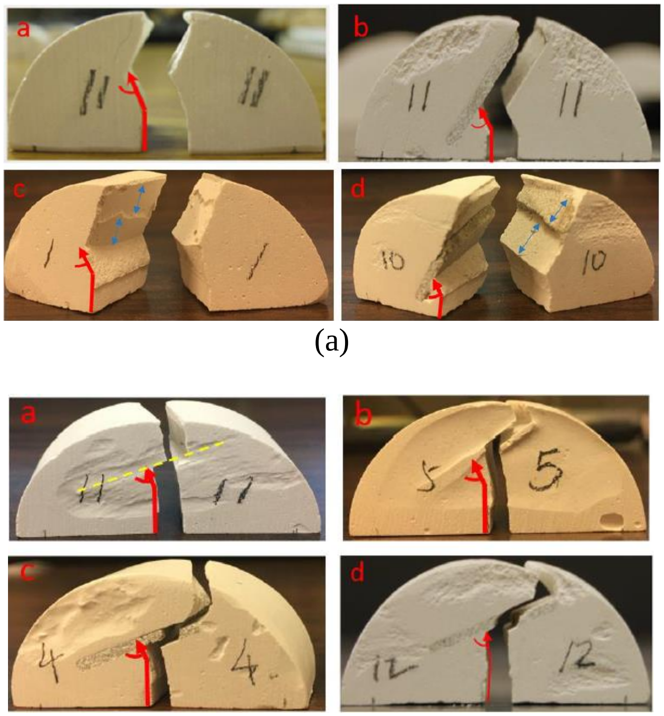

(a)

(b)

Figure 5.4. Rock samples showing modification in approach angles for different initial orientation of the natural fracture with respect to the induced fracture (Wang 2017). (a) β=30°, and (b) β=60°

Table 5.1. Model parameters for high permeability cases (Wang 2017, except *)

Bulk modulus, E (GPa)	6.18
Poission ratio, v	0.32
Permeability, k (mD)	10
Porosity, φ (%)	28
Tensile strength, T_0 (MPa)	4.82
Fracture toughness, K_{IC} (MPa m$^{0.5}$)	0.42
*Cohesion of natural fracture, S_{NF} (MPa)	0
*Friction coefficient, μ_{NF}	0.6
*Tensile strength multiplier, α_{NF}	0.5
*Friction multiplier, β_{NF}	0.5
Initial pressure, P_0 (MPa)	0.1
Minimum principal stress, S_{hmin} (MPa)	0.1
Stress ratio	1
*Injected fluid viscosity, μ (cP)	1

5.3.1. 30^o interaction

For a 30^o angle of interaction, Figure 5.5 shows the trajectory of the hydraulic fracture at its different half lengths obtained from peridynamics simulations. The natural fracture starts to fail in shear even before being intersected by the hydraulic fracture. The remote shear failure is exaggerated by the significant poroelastic effects due to the high permeability of the medium. Once the natural fracture fails in shear, the friction between its surfaces changes from static to dynamic, leading to a decrease in the tangential component of the force acting on the natural fracture. Consequently, the direction of the maximum stress around the natural fracture is reoriented as demonstrated in Figure 5.6. Since the hydraulic fracture experiences the reoriented stresses, it bends towards the natural fracture before intersection. It should be noted that the modified angle of intersection is approximately 80^o, which is in good agreement with the experimental range of 70^o-80^o

reported by Wang (2017). Figure 5.7 shows a plot of the Mohr-Coulomb criterion evaluated on the natural fracture surface as the hydraulic fracture propagates. The natural fracture fails in shear when this criterion falls below the red line, which first happens when the hydraulic fracture has propagated about two-thirds of its half-length at intersection, i.e., at $x_D = 0.67$.

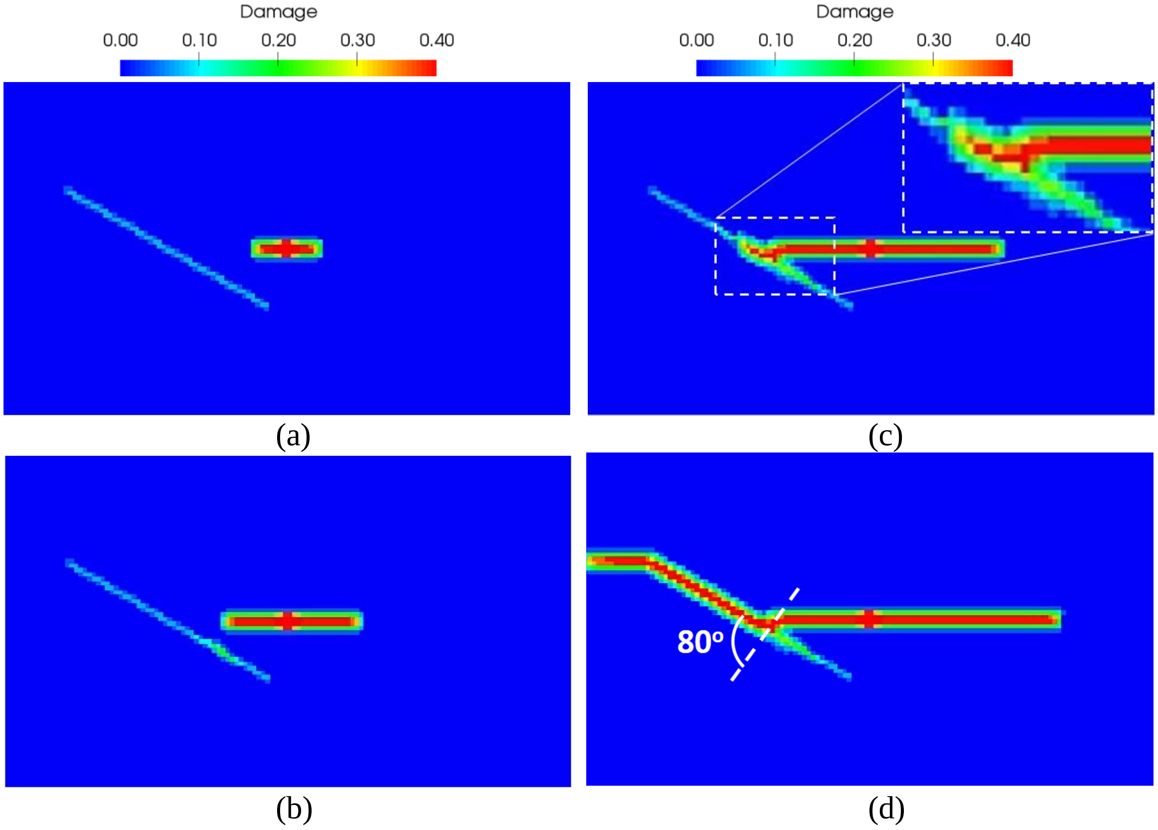

(a) (c)

(b) (d)

Figure 5.5. Trajectory of the HF at different half lengths for 30° angle of interaction in a high permeability rock. (a) $x_D = 0.33$, (b) $x_D = 0.67$, (c) $x_D = 1.0$ (magnified view of fracture bending in the inset), and (d) Final trajectory

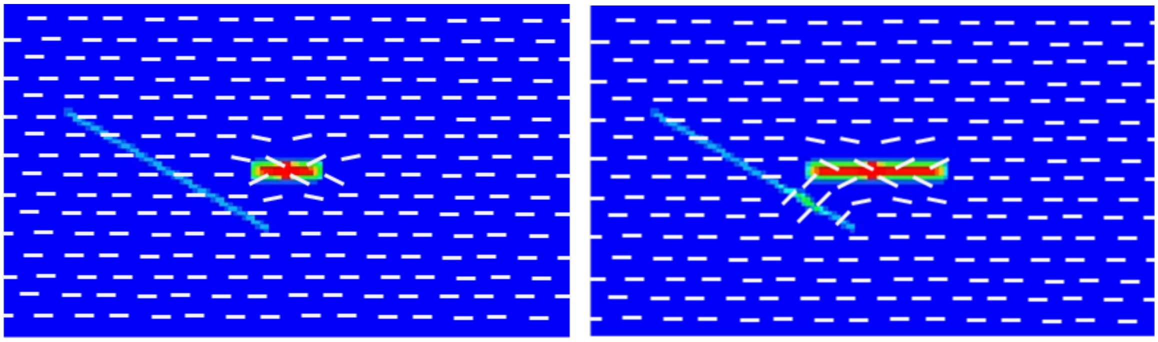

(a) (b)

Figure 5.6. Stress reorientation due to the shear failure of the natural fracture. (a) $x_D = 0.33$, (b) $x_D = 0.67$

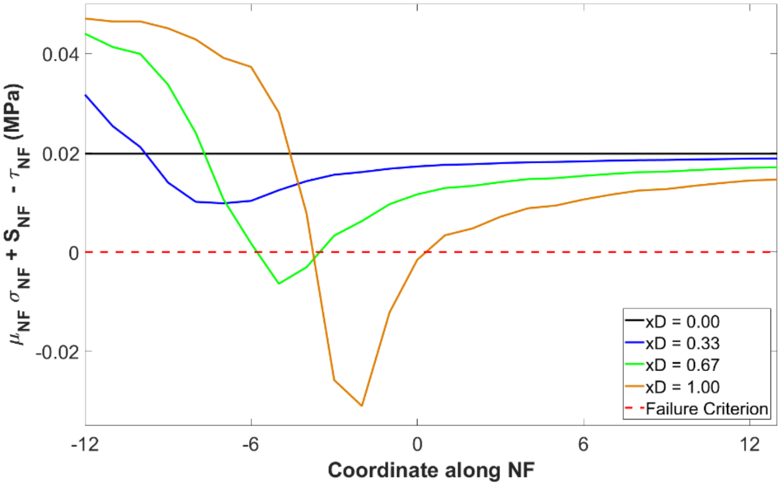

Figure 5.7. Mohr Colulomb criterion evaluated on the natural fracture at different half lengths of the hydraulic fracture. Negative and positive coordinates along the natural fracture correspond its lower and upper halves respectively.

5.3.2. 60° interaction

Next, the results for a 60° fracture interaction are presented. It is evident that the natural fracture fails in shear much before being intersected by the hydraulic fracture (Figure 5.8). Similar to the 30° interaction case, the stress relaxation caused by this remote shear failure invites the hydraulic fracture to bend towards the natural fracture (Figure 5.9). The modified approach angle is computed as 85°, which is close to the 73° approach angle observed in the experiments.

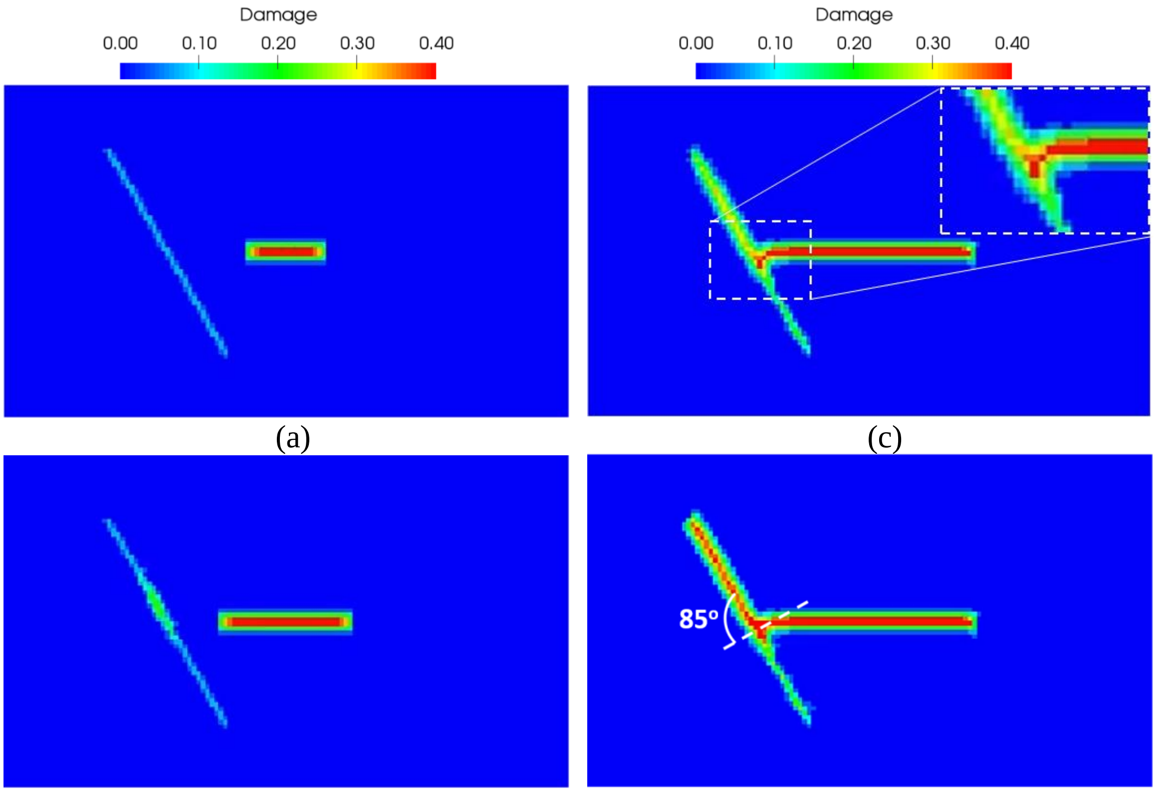

(a)

(c)

(b)

(d)

Figure 5.8. Trajectory of the HF at different half lengths for 60° angle of interaction in a high permeability rock. (a) $x_D = 0.33$, (b) $x_D = 0.67$, (c) $x_D = 1.0$ (magnified view of fracture bending in the inset), and (d) Final trajectory

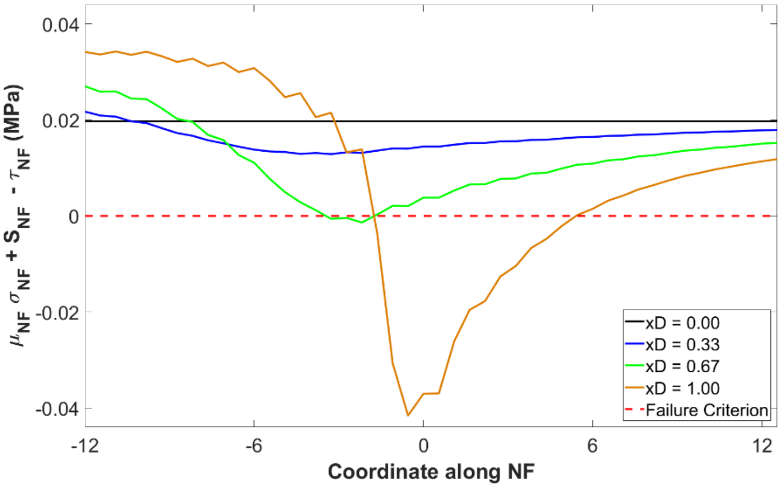

Figure 5.9. Mohr Colulomb criterion evaluated on the natural fracture at different half lengths of the hydraulic fracture. Negative and positive coordinates along the natural fracture correspond its lower and upper halves respectively.

5.4. INCREASE IN APPROACH ANGLE DUE TO REMOTE SHEAR FAILURE IN LOW PERMEABILITY ROCKS

In the previous section, the bending of hydraulic fracture towards the natural fracture was illustrated in high permeability specimens. In this section, hydraulic fracture-natural fracture interaction is considered in low permeability rocks with matrix permeabilities of the order of 100 nD. The mechanical properties and stress conditions used are also representative of low permeability rocks such as shales (Table 5.2). The results with and without considering remote shear failure of the natural fracture are presented.

Table 5.2. Model parameters for low permeability cases

Bulk modulus, E (GPa)	8.0
Poission ratio, v	0.25
Permeability, k (nD)	100
Porosity, φ (%)	5
Tensile strength, T_0 (MPa)	0
Fracture toughness, K_{IC} (MPa $m^{0.5}$)	1
Cohesion of natural fracture, S_{NF} (MPa)	0
Friction coefficient, μ_{NF}	Variable
Tensile strength multiplier, α_{NF}	0.5
Friction multiplier, β_{NF}	0.5
Initial pressure, P_0 (MPa)	25
Minimum principal stress, S_{hmin} (MPa)	40
Stress ratio	Variable
Injected fluid viscosity, μ (cP)	1

5.4.1. 30° interaction

In Figure 5.10, panels (a), (b) and (c) show the hydraulic fracture trajectory for a 30° interaction if remote shear failure is modeled in our simulator, while panels (d), (e) and (f) show the same if it is not modeled. It can be noted that intersection angle is significantly modified to 50° if remote shear failure is accounted for. The corresponding stress profiles are plotted in panels (a) and (b) respectively of Figure 5.11. The shear failure criterion is first satisfied on the natural fracture when the hydraulic fracture has propagated 90% of its half-length at intersection. If this is considered in our fracturing simulator, there is a stress relaxation around the natural fracture, which increases the approach angle of the hydraulic fracture. However, if it is ignored, the stress relaxation is under-predicted, leading to a very small change in approach angle.

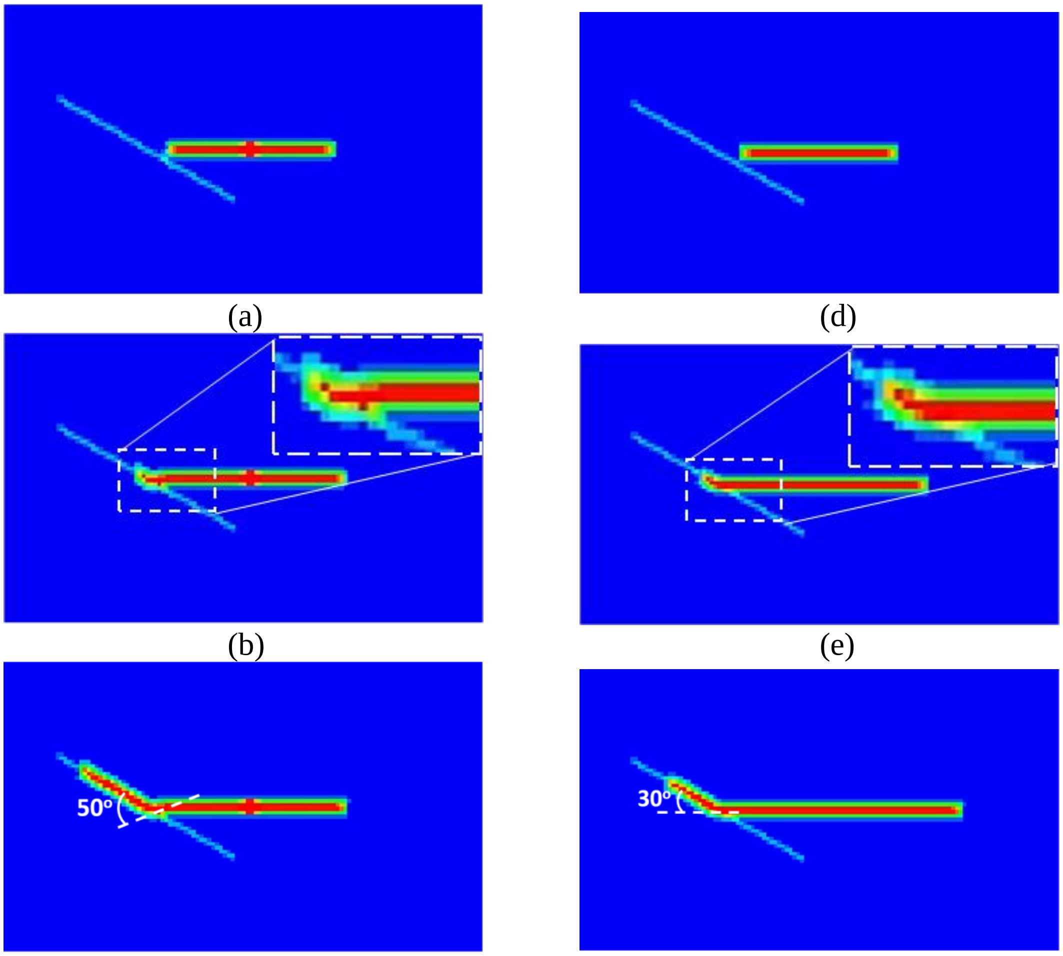

(a) (d)

(b) (e)

(c) (f)

Figure 5.10. Trajectory of the HF at different half lengths for 30° angle of interaction in a low permeability rock. (a) $x_D = 0.90$, (b) $x_D = 1.0$, and (c) Final trajectory when remote shear failure is accounted. (d) $x_D = 0.90$, (e) $x_D = 1.0$, and (f) Final trajectory when remote shear failure is not accounted.

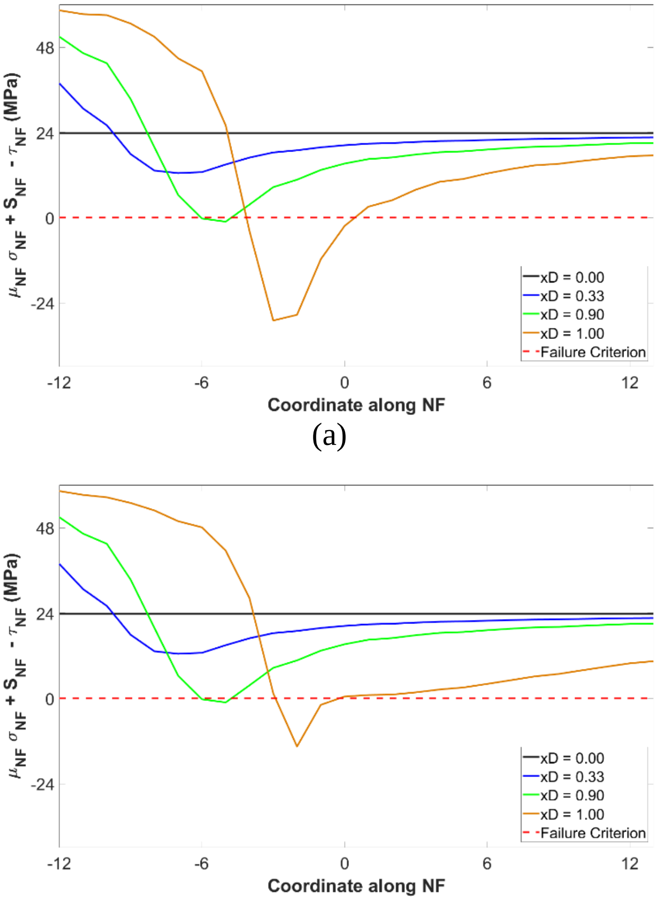

(a)

(b)

Figure 5.11. Mohr Colulomb criterion evaluated on the natural fracture at different half lengths of the hydraulic fracture. (a) when remote shear failure is accounted, (b) when remote shear failure is not accounted

On comparing Figure 5.7 and Figure 5.11, it can be concluded that remote shear failure of a natural fracture in a higher matrix permeability rock causes higher stress relaxation relative to the initial stresses and thus more prominent modification in approach angle of the hydraulic fracture.

5.4.2. 60° interaction

The results for hydraulic fracture-natural fracture interaction at 60° are presented next. Similar to the interaction at 30°, Figure 5.12 and Figure 5.13 show the hydraulic fracture trajectory and the stress profiles respectively. Considering the remote shear failure of the natural fracture prior to intersection increases the approach angle from 60° to 75° due to stress relaxation.

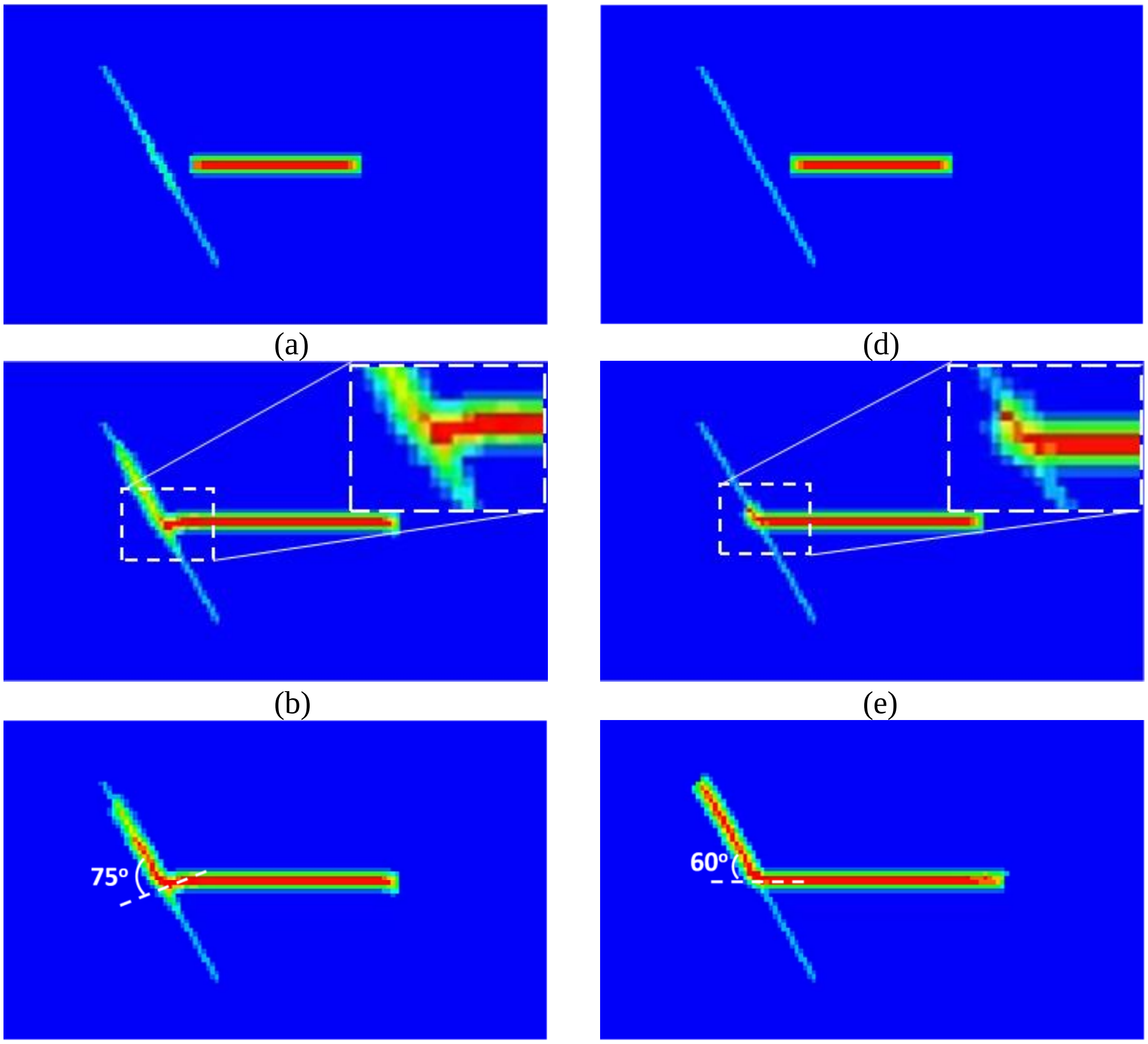

(a) (d)

(b) (e)

(c) (f)

Figure 5.12. Trajectory of the HF at different half lengths for 60° angle of interaction in a low permeability rock. (a) $x_D = 0.80$, (b) $x_D = 1.0$, and (c) Final trajectory when remote shear failure is accounted. (d) $x_D = 0.80$, (e) $x_D = 1.0$, and (f) Final trajectory when remote shear failure is not accounted.

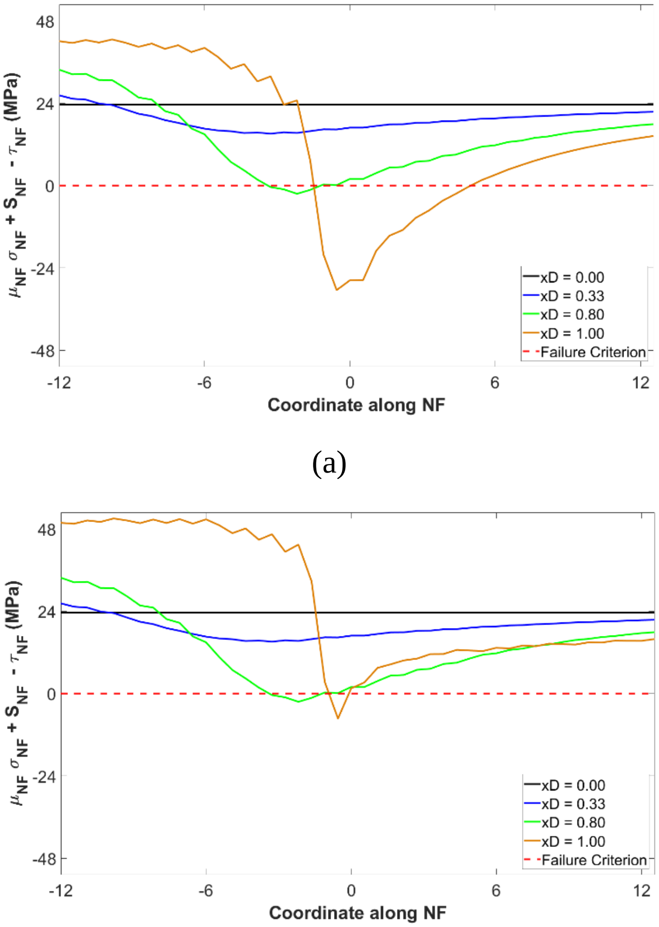

(a)

(b)

Figure 5.13. Mohr Colulomb criterion evaluated on the natural fracture at different half lengths of the hydraulic fracture. (a) when remote shear failure is accounted, (b) when remote shear failure is not accounted.

5.5. VALIDATION OF HF-NF INTERACTION AGAINST ANALYTICAL CROSSING CRITERIA

The crossing criteria that were developed in the past were based on Linear Elastic Fracture Mechanics (LEFM). As shown in Figure 5.14, they essentially solved for the stresses at the tip of the hydraulic fracture that would prevent the natural fracture from slipping (Gu & Weng, 2010). Thus, these criteria neglected the possibility of remote shear failure of the natural fracture due to poroelastic effects prior to its intersection with the hydraulic fracture.

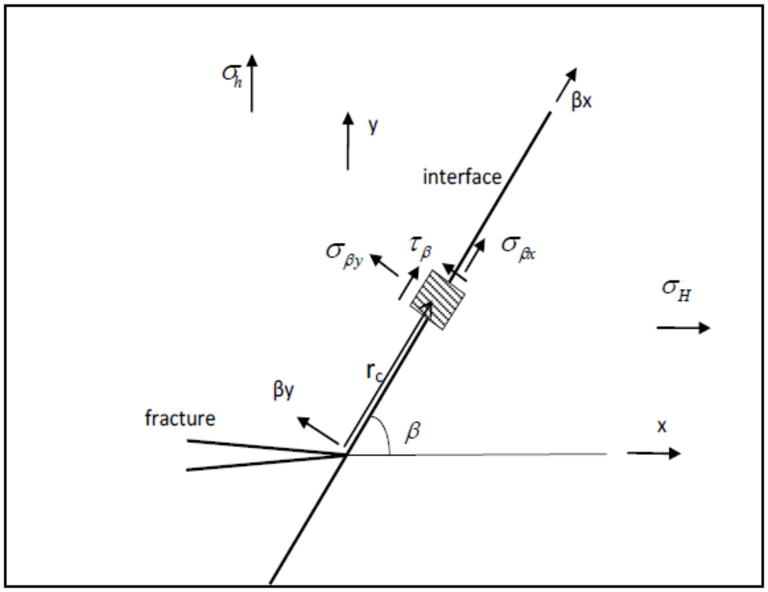

Figure 5.14. Shear failure evaluated at intersection (Gu & Weng, 2010).

The LEFM-based crossing criteria derived by Gu & Weng (2010) have been reproduced in Figure 5.15. The region to the right of each curve represents the crossing of the hydraulic fracture when it intersects with the natural fracture. In general, these criteria suggest that as the friction coefficient of a natural fracture increases, the tendency of a hydraulic fracture to cross the natural fracture increases. In addition, for a given friction coefficient and angles of interaction smaller than 60^o, the crossing tendency decreases with increasing stress ratio. However, for a given friction coefficient and angles of interaction larger than 60^o, the crossing tendency increases with an increase in stress ratio. These contrasting results can be explained based on two competing factors – an increase in stress ratio causes the natural fracture to easily fail in shear, but causes the hydraulic fracture to spend more energy to propagate in a direction other than that of the maximum stress. From these results, it can be concluded that the first factor dominates when angles of interaction are smaller than 60° and the second one dominates when angles of interaction are larger than 60°.

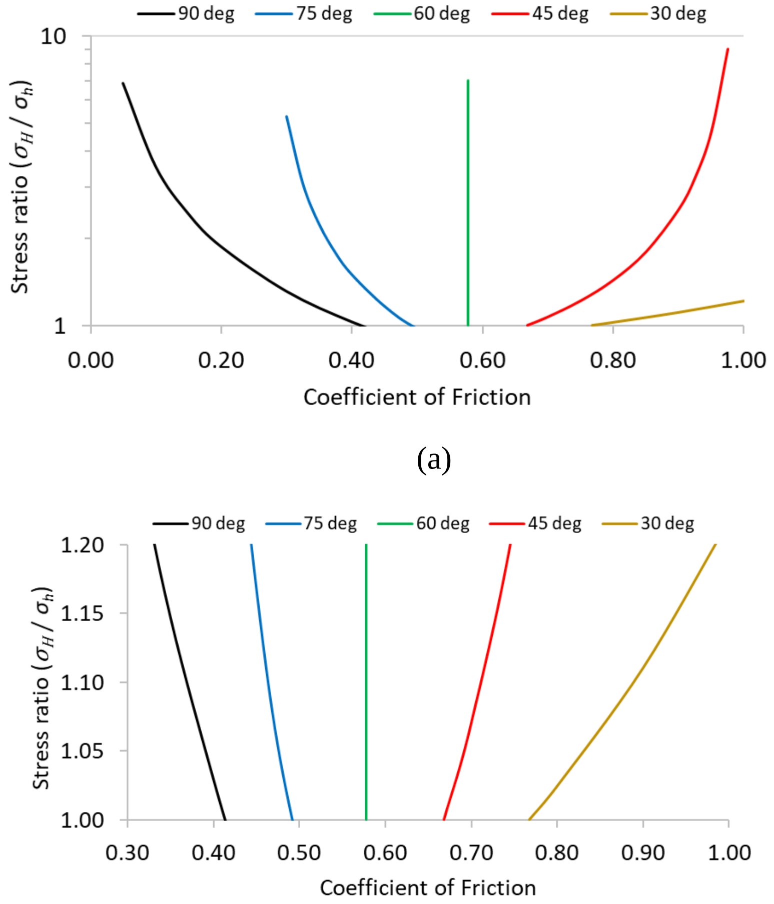

(a)

(b)

Figure 5.15. LEFM-based crossing criteria (adapted from Gu & Weng, 2010).

(a) For stress ratios larger than 1. (b) For stress ratios commonly found in the subsurface

We demonstrate that the peridynamics-based hydraulic fracturing simulator successfully reproduces the LEFM crossing criteria when we neglect remote shear failure of the natural fracture prior to its intersection with the hydraulic fracture in our simulator. For each angle of interaction, simulation cases were run close to the corresponding analytical crossing criteria and the results were plotted (Figure 5.16). The results are in agreement with the existing criteria, except for slight overprediction in turning for low angles of interaction (Figure 5.16b) and slight overprediction in crossing for high angles of interaction (Figure 5.16d).

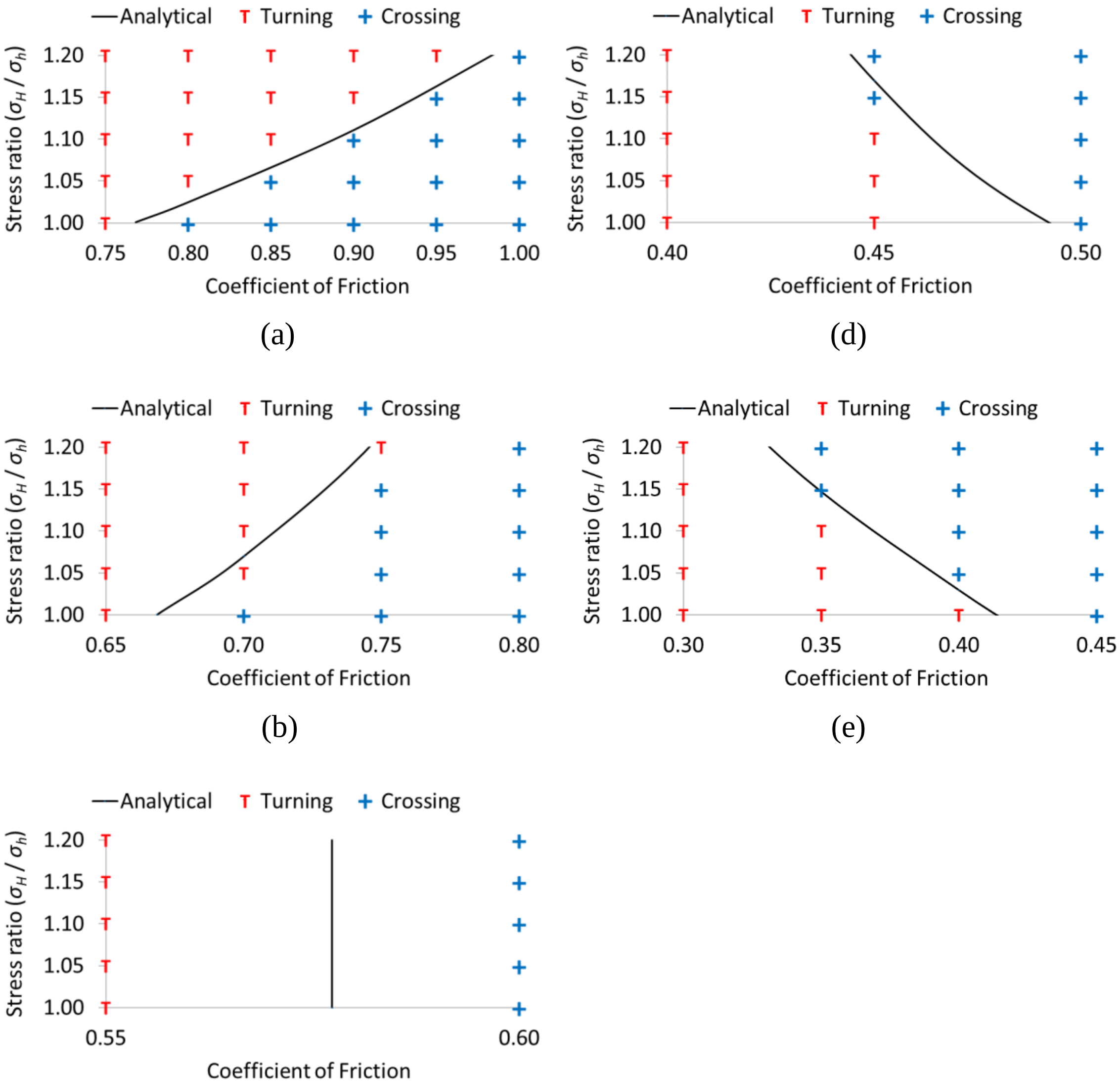

(a) (d)

(b) (e)

(c)

Figure 5.16. Validation of the analytical crossing criteria for different angles of interaction using the peridynamics simulator. (a) $\beta = 30^o$, (b) $\beta = 45^o$, (c) $\beta = 60^o$, (d) $\beta = 75^o$, (e) $\beta = 90^o$

5.6. DEVELOPMENT OF POROELASTIC CROSSING CRITERIA

In the previous sections, we showed that a natural fracture may remotely fail in shear prior to being intersected by a hydraulic fracture and that the analytical crossing criteria did not account for this phenomenon. Moreover, it was also recognized that the fracture interaction behavior can vary significantly between high and low permeability rocks. In this section, we reconsider the past criteria for hydraulic fracture-natural fracture interaction while accounting for remote shear failure of the natural fracture induced by poroelasticity for two widely different rock permeabilities. These permeabilities are representative of synthetic rock specimens used in the experiments (10 mD) and low permeability rocks such as shales (100 nD). The predicted interaction behaviors are used to develop numerical poroelastic crossing criteria. It is worth mentioning here that unlike the other fracturing simulators, the peridynamics model does not require a crossing criterion as an input, rather it can predict the interaction behavior based on local stresses.

The friction coefficient of natural fractures is not an easily measurable quantity. However, a range of 0.1-0.9 has been suggested by several researchers (Jaeger & Cook, 1976; Renshaw & Pollard, 1995; Gu et al., 2012). In the following analysis, weak natural fractures with friction coefficient smaller than 0.4 are not considered since a hydraulic fracture will always turn along them, irrespective of the stress ratio or the angle of approach (Figure 5.15b).

The fracture jogging or stepping-over behavior, shown in Figure 5.1, is observed in some of the simulations for a high angle of approach (>60^o), a high stress ratio (close to 1.1) and a moderate friction coefficient (0.6-0.7). However, since this kind of interaction ultimately results in fracture crossing, it is classified as crossing hereafter.

5.6.1. High permeability rocks

Figure 5.17 summarizes the results of fracture interaction for a range of friction coefficients in high permeability rocks. The blue circle in each panel represents regions where the analytical criteria would have predicted fracture crossing, whereas the peridynamics model predicts fracture turning. Remote shear failure of the natural fracture relaxes the stresses around it to a great extent due to prominent poroelastic effects. Thus, as compared to the analytical crossing criteria, much more fracture turning is observed in high permeability cases. The differences occur for all the stress ratios considered in this study, ranging between 1.0 and 1.2.

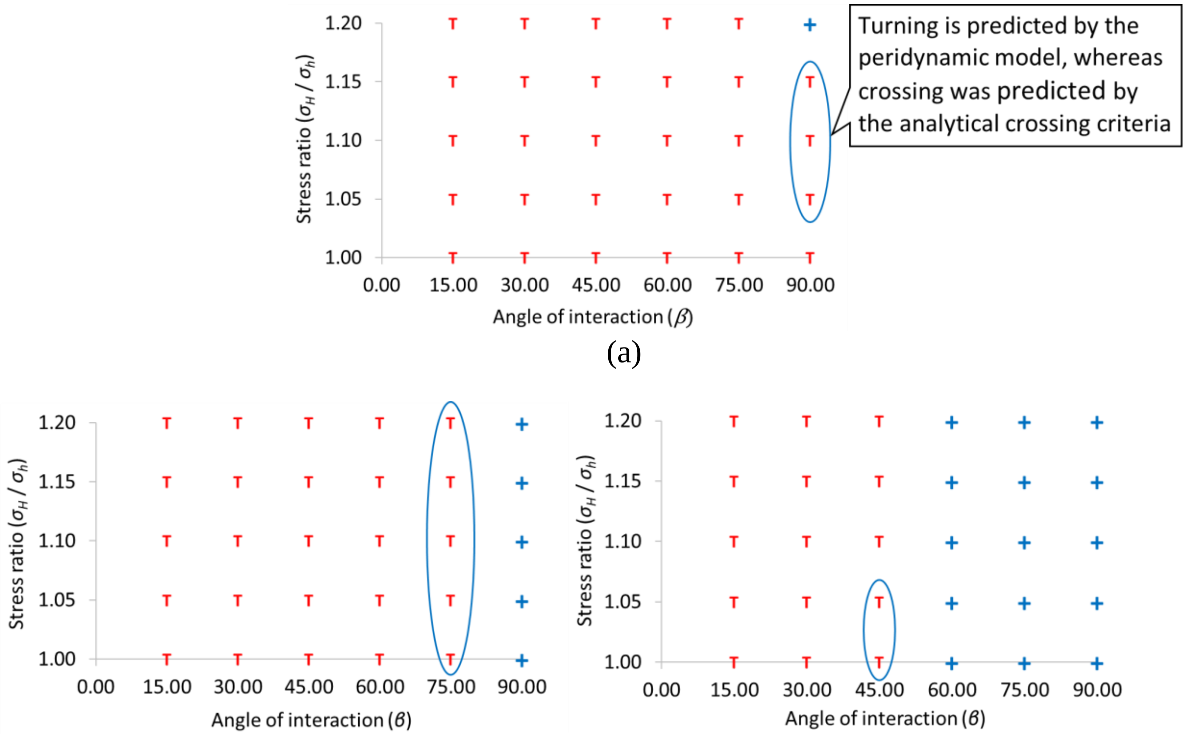

Turning is predicted by the peridynamic model, whereas crossing was predicted by the analytical crossing criteria

(a)

(b)

(d)

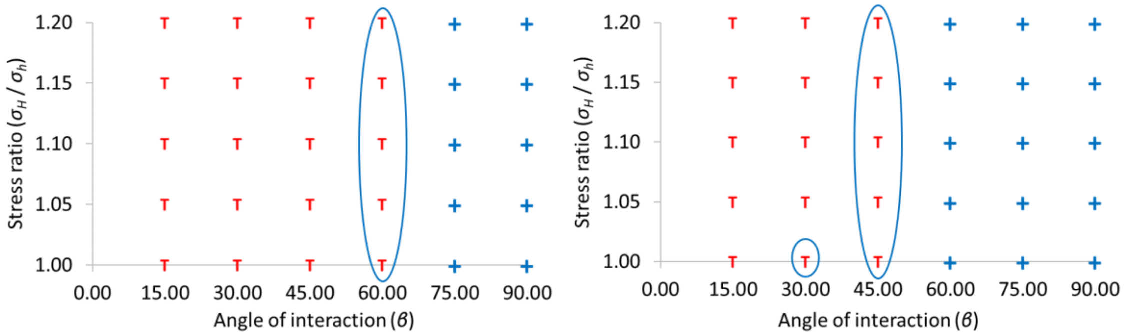

(c) (e)

Figure 5.17. Crossing (blue +) and turning (red T) behavior for common friction coefficients of NF in high permeability rocks. (a) $\mu_{NF} = 0.4$, (b) $\mu_{NF} = 0.5$, (c) $\mu_{NF} = 0.6$, (d) $\mu_{NF} = 0.7$, (e) $\mu_{NF} = 0.8$

We fine-tuned the prediction of fracture interaction behavior in our model. For each angle of interaction, several simulation cases were run by varying the stress ratio and friction coefficient of the natural fracture to identify the switch from fracture turning to fracture crossing. The results of this exercise are shown in Figure 5.18. Quadratic functions of the following form were regressed on the results to obtain the poroelastic crossing criteria.

$$Stress\ ratio\ (\sigma_H/\sigma_h) = a * \mu_{NF}^2 + b * \mu_{NF} + c \tag{5.3}$$

The poroelastic criteria for different angles of interaction are mentioned at the top of the respective panels (and recapitulated in Table 5.3). For comparison, the analytical crossing criteria corresponding to each angle of interaction are plotted. It is noticed that the previous criteria remarkably underpredicted fracture turning for low angles of approach or low stress ratios. The discrepancy becomes smaller for higher angles of approach and higher stress ratios.

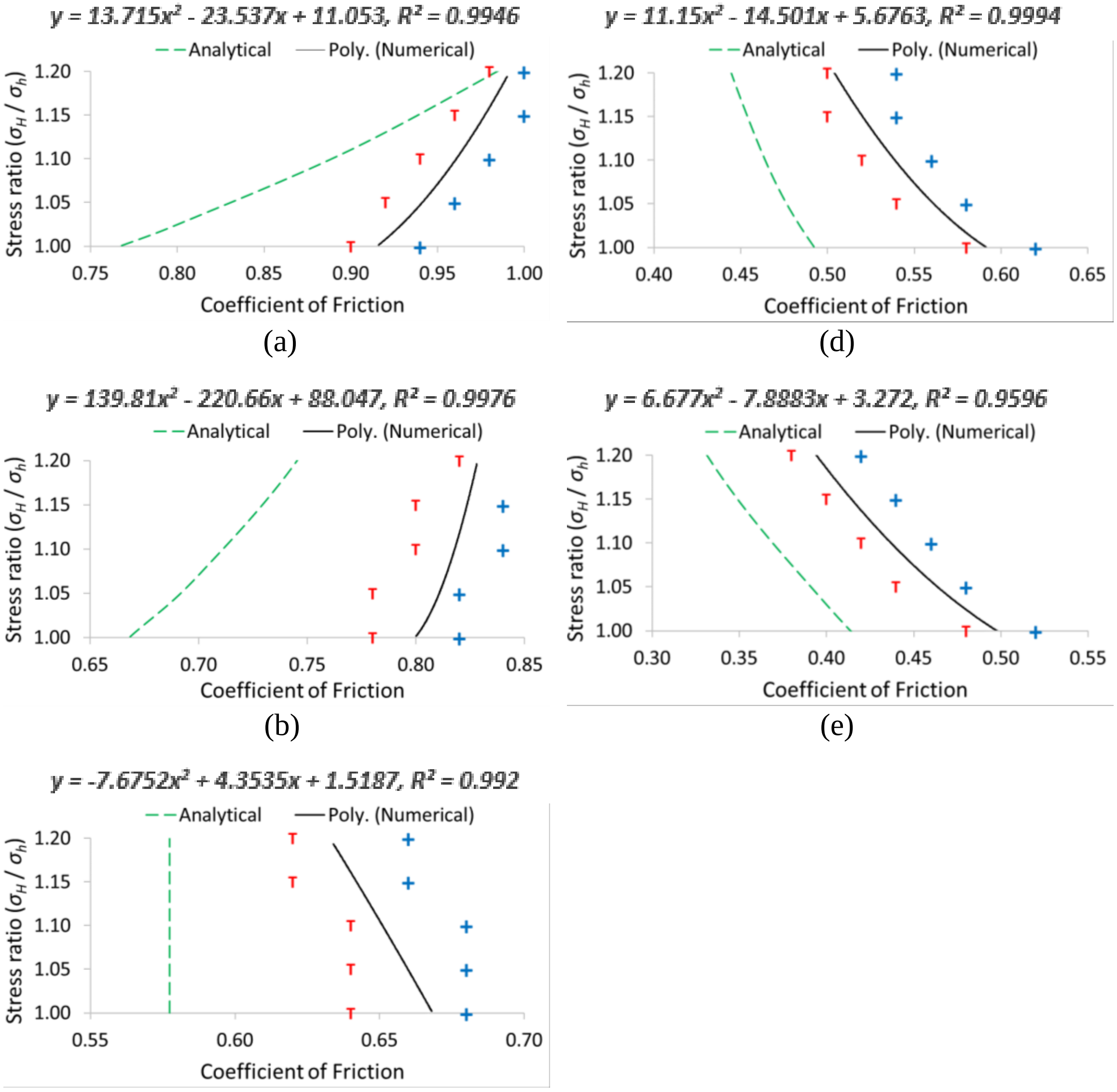

(a) (d)

(b) (e)

(c)

Figure 5.18. Proposed poroelastic crossing criteria for different angles of interaction in high permeability rocks. (a) $\beta = 30^o$, (b) $\beta = 45^o$, (c) $\beta = 60^o$, (d) $\beta = 75^o$, (e) $\beta = 90^o$

5.6.2. Low permeability rocks

Figure 5.19 demonstrates the fracture interaction behavior in low permeability rocks. Compared to the predictions by the analytical model, the differences occur for stress ratios between 1.0 and 1.1, which are important for the shale formations with in-situ stresses in this range. Due to smaller poroelastic stress relaxation in low permeability rocks, the corresponding propagation behavior do not change as much as for the high permeability rocks.

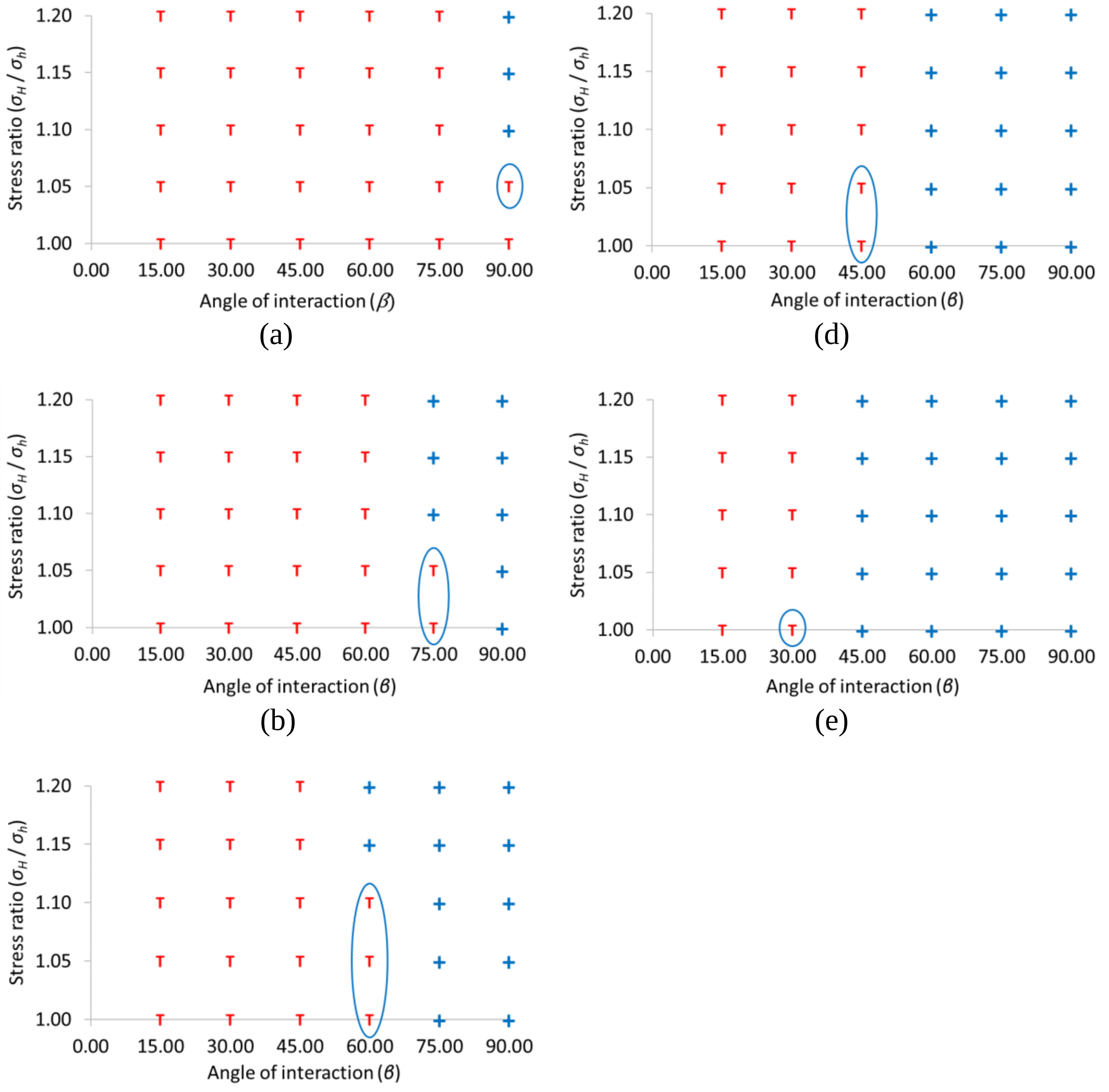

(a) (d) (b) (e) (c)

Figure 5.19. Crossing (blue +) and turning (red T) behavior for common friction coefficients of NF in low permeability rocks. (a) $\mu_{NF} = 0.4$, (b) $\mu_{NF} = 0.5$, (c) $\mu_{NF} = 0.6$, (d) $\mu_{NF} = 0.7$, (e) $\mu_{NF} = 0.8$

Using the same approach as described in the previous subsection, poroelastic crossing criteria are developed for fracture interaction in low permeability rocks. Figure 5.20 shows that significantly more fracture turning should be expected in such rocks as compared to that predicted by the analytical crossing criteria.

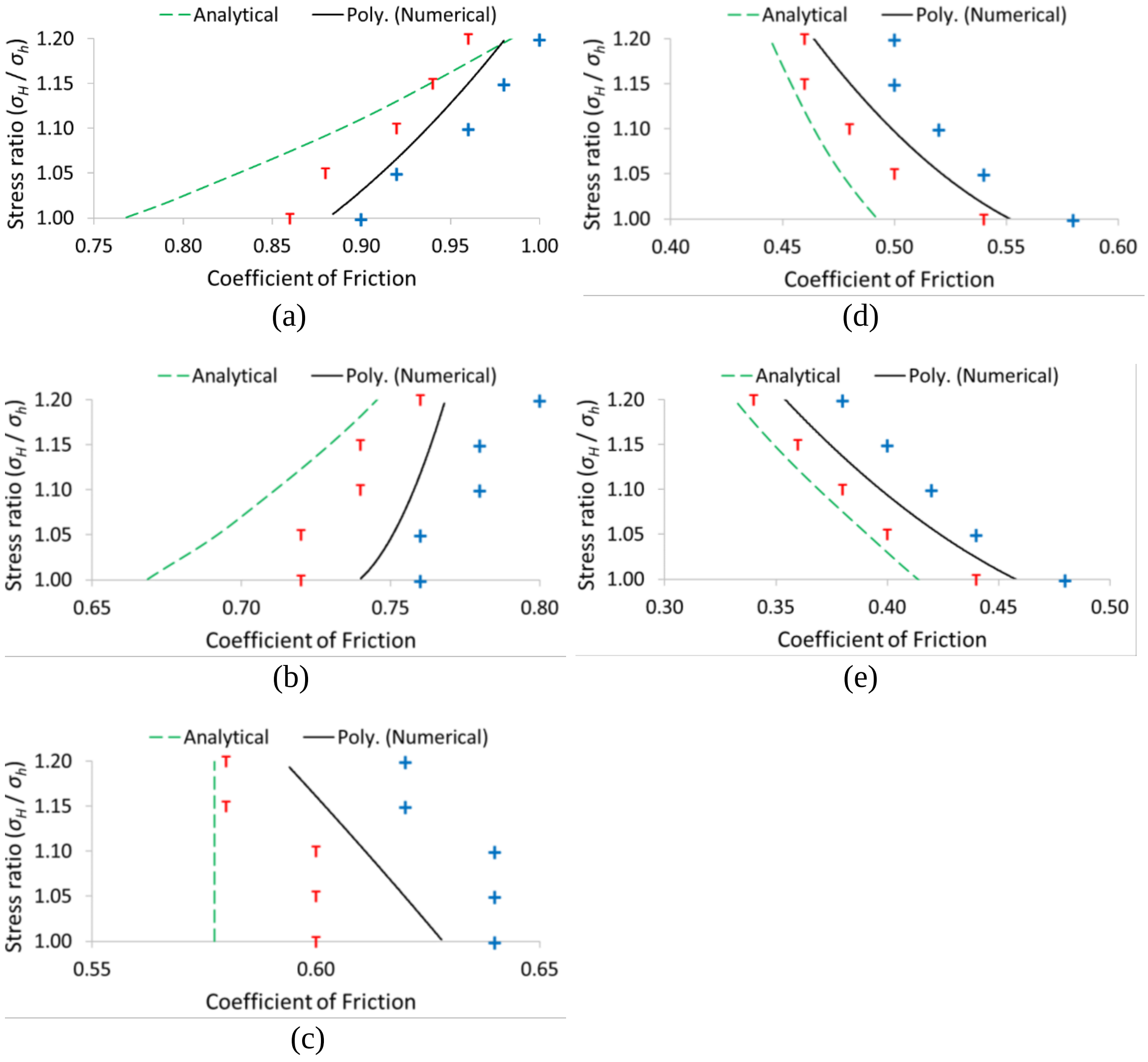

(a)

(d)

(b)

(e)

(c)

Figure 5.20. Proposed poroelastic crossing criteria for different angles of interaction in low permeability rocks. (a) $\beta = 30^o$, (b) $\beta = 45^o$, (c) $\beta = 60^o$, (d) $\beta = 75^o$, (e) $\beta = 90^o$

The poroelastic crossing criteria developed in this section can be used by discrete fracture models simulating the growth of complex fracture networks. The proposed criteria can be used as continuous quadratic functions for known angles of interaction (Table 5.3). Moreover, they can be used as discrete if-then-else scenarios for known friction coefficients of the natural fractures (Figure 5.17 and Figure 5.19). Generally, the more the hydraulic fractures turn into the existing natural fractures, the more complex is the resulting fracture network (Weng et al, 2011; Suarez-Rivera et al. 2013). The higher tendency of fracture turning predicted by the proposed crossing criteria suggests that the resulting fracture network should be more complex than those formed by using LEFM-based analytical crossing criteria.

Table 5.3. Coefficients for poroelastic crossing criteria derived for different angles of interaction in high and low perm rocks

Angle of interaction (β)	**High permeability rocks (10 mD)**			**Low permeability rocks (100 nD)**		
	a	**b**	**c**	**a**	**b**	**c**
30º	13.715	- 23.537	11.053	4.8623	- 7.0451	3.4325
45º	139.81	- 220.66	88.047	139.81	- 203.88	75.311
60º	-7.6752	4.3535	1.5187	-7.6752	3.7395	1.6806
75º	11.15	- 14.501	5.6763	11.15	- 13.609	5.1141
90º	6.677	- 7.8883	3.272	6.677	- 7.3542	2.9672

5.7. CONCLUSIONS

Using our peridynamics-based poroelastic fracturing simulator, it was recognized that shear failure of a natural fracture should be evaluated throughout the hydraulic fracture-natural fracture interaction, not just at the time of intersection. Some of the key conclusions from this research are summarized below:

(a) Remote shear failure of a natural fracture prior to being intersected by a hydraulic fracture relaxes the stresses around the natural fracture. This stress relaxation causes the hydraulic fracture to bend towards the natural fracture before intersection as has been observed in the experiments.

(b) The bending of the hydraulic fracture depends on the stress relaxation relative to the initial stresses caused by the failure of the natural fracture. Though these effects are significant even in low permeability rocks (100 nD), they are more pronounced in high permeability rocks (10 mD).

(c) When the effects of poroelasticity and remote shear failure of the natural fracture are ignored, the LEFM-based analytical crossing criteria are verified. However, when these effects are accounted, the fracture interaction behavior is substantially different.

(d) For low matrix permeabilities, the poroelastic criteria predict more fracture turning at stress ratios commonly occurring in shale formations (1.0-1.1). For high matrix permeabilities, these criteria predict more fracture turning even at moderate stress ratios (1.0-1.2).

(e) New crossing criteria are presented that consider the effects of poroelasticity and remote shear failure of the natural fracture These poroelastic crossing criteria are developed for widely different matrix permeabilities and can serve as direct inputs to discrete fracture models simulating the growth of complex fracture networks.

CHAPTER 6: COUPLING OF PERIDYNAMICS-BASED POROELASTIC MODEL WITH FINITE VOLUME METHOD

6.1. INTRODUCTION

Poroelastic fluid flow in geological processes, such as that in heterogeneous or fractured subsurface reservoirs is a multiscale problem. While the flow at larger length scales may be sufficiently described by classical models including FEM or FVM, the "scale-dependent dispersion" at smaller length scales are better captured by non-local models such as Peridynamics (Katiyar et al., 2014). Unlike the classical models, it does not require the continuity of field variables. However, since it accounts for non-local interactions, it requires significantly more computational resources than the classical models.

To simulate various interesting multiscale physics within reasonable computational times, different schemes for coupling of Peridynamics with classical models have been developed. Macek and Silling (2007) coupled PD and FEM meshes by using embedded nodes and elements. Kilic and Madenci (2010) introduced an overlap region at the interface of PD and FV domains, in which both the equations were solved. In Agwai et al. (2009) and Oterkus (2010), global modeling was performed with FEM, whereas sub-modeling to predict material failure was performed with PD. In Lubineau et al. (2012), the coupling was performed using morphing functions, which were based on energy equivalence. These functions affected the constitutive parameters only, thereby allowing the model to behave as purely non-local, purely local, or a hybrid. Liu and Hong (2012) coupled the FEM and PD domains with interface elements and devised two different coupling schemes. Seleson et al. (2013) derived a consistent force-based blended model using non-local weights comprised of integrals of the blending functions.

While the above researchers have illustrated the validity of their methodologies, they make some approximation regarding the interface region or its mathematical treatment. Addressing these shortcomings, Galvanetto et al. (2016) proposed a PD-FEM coupling scheme for static equilibrium problems. They later extended this scheme for brittle fracture analysis (Shojaei et al., 2016). In this chapter, the formulation development for multiscale poroelastic problems is inspired by their work.

6.2. COUPLING FOR POROUS FLUID FLOW

The coupling scheme is demonstrated by considering steady state Darcy fluid flow in a 1-D, horizontal, homogeneous, isotropic reservoir (Figure 6.1). The reservoir is discretized uniformly into volumetric cells. The green and red color cells are solved using FVM and PD respectively. Each cell has one computational node represented by a black circle. Flow equations for both the discretizations are presented in the subsequent paragraphs.

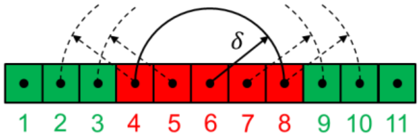

Figure 6.1. PD-FVM coupling scheme for 1-D flow in a horizontal reservoir. PD and FV cells are shown in red and green colors respectively.

In classical theory, a computational node interacts with the adjacent nodes only. The governing equation for steady state Darcy flow in Finite Volume (FV) cells of the described reservoir is given by classical theory:

$$-\nabla.(\rho_w \boldsymbol{u}) + R = 0 \tag{6.1}$$

where ρ_w is fluid density, $\boldsymbol{u}$ is the volumetric flow rate, R is the mass generation rate, and $\nabla.$ is the divergence operator.

$$\boldsymbol{u} = -\frac{1}{\mu_w}\boldsymbol{K}A\nabla P \tag{6.2}$$

where μ_w is fluid viscosity, $\boldsymbol{K}$ is permeability tensor of the porous medium, A is the cross-sectional area for flow, and P is fluid pressure. For a homogeneous, isotropic reservoir, $\boldsymbol{K} = k\boldsymbol{I}$.

For the 1-D flow problem discretized using FVM, the cell transmissibility matrix for a fluid of constant density, T_{FVM} is computed as:

$$T_{FVM} = f \begin{bmatrix} 1 & -1 \\ -1 & 1 \end{bmatrix} \tag{6.3}$$

such that

$$f = \frac{kA}{\mu_w l} \tag{6.4}$$

where l is the cell spacing.

In PD theory, a node at position $\boldsymbol{x} \in \mathcal{B}$ interacts with all the other nodes at position $\boldsymbol{x}'$ within a length scale called a horizon, $\mathcal{H}_x$ (Figure 1.6). The horizon is a circle/sphere of radius δ depending on the dimensionality of the problem and in Figure 6.1, $\delta = 2l$. The governing equation for steady state Darcy flow in a PD cell at position $\boldsymbol{x} \in \boldsymbol{B}$ is obtained by setting the accumulation term as zero in equation (1.12):

$$\int_{\mathcal{H}_x} (\underline{Q}[\boldsymbol{x}]\langle\xi\rangle - \underline{Q}[\boldsymbol{x}']\langle-\xi\rangle)\, dV_{x'} + R[\boldsymbol{x}] = 0 \tag{6.5}$$

where the various terms are as defined in Chapter 1.

Similar to the stiffness matrix in Galvanetto et al. (2016), the cell transmissibility matrix, T_{PD} for 1-D flow between PD nodes i and j is defined as:

$$T_{PD} = p \begin{bmatrix} 1 & -1 \\ -1 & 1 \end{bmatrix} \tag{6.6}$$

such that

$$p = \frac{\gamma k}{\mu_w l_{ij,mult} l} V_{ij,mult} V_j V_i \tag{6.7}$$

where γ is the scaling factor derived for different dimensionalities of the problem in Section 2.2.1.2. V_i and V_j are the volumes associated with PD nodes i and j respectively, $V_{ij,mult}$ is the fraction of volume of node j that is within the horizon of node i, and $l_{ij,mult}$ times l is the distance between these nodes. In Figure 6.1, considering the interaction of node 6 with node 5, node 5 is completely inside the horizon of node 6. Thus, $l_{ij,mult} = 1$ and $V_{ij,mult} = 1$ should be used in equation (6.7). However, considering the interaction of node 6 with node 4, only half of node 4 is inside the horizon of node 6. Thus, $l_{ij,mult} = 2$ and $V_{ij,mult} = 0.5$ should be used in equation (6.7).

The global transmissibility matrix is assembled by adding together the cell transmissibility matrices in equations (6.3) and (6.6). Equation (6.8) shows the global matrix for the problem under consideration with FV and PD equations in green and red colors respectively. The equations for the cells close to the PD-FVM interface are developed by treating the neighbors to be of the same type as the owner (Galvanetto et al., 2016). For example, in Figure 6.1, while computing the flow in/out of cell 3, cell 4 is treated as a FV cell. However, while computing the flow in/out of cell 4, cells 2 and 3 are treated as PD cells.

$$\begin{bmatrix} f & -f & & & & & & & & & \\ -f & 2f & -f & & & & & & & & \\ & -f & 2f & -f & & & & & & & \\ & -0.25p & -p & 2.5p & -p & -0.25p & & & & & \\ & & -0.25p & -p & 2.5p & -p & -0.25p & & & & \\ & & & -0.25p & -p & 2.5p & -p & -0.25p & & & \\ & & & & -0.25p & -p & 2.5p & -p & -0.25p & & \\ & & & & & -0.25p & -p & 2.5p & -p & -0.25p & \\ & & & & & & & -f & 2f & -f & \\ & & & & & & & & -f & 2f & -f \\ & & & & & & & & & -f & f \end{bmatrix} \begin{bmatrix} P_1 \\ P_2 \\ P_3 \\ P_4 \\ P_5 \\ P_6 \\ P_7 \\ P_8 \\ P_9 \\ P_{10} \\ P_{11} \end{bmatrix} = \begin{bmatrix} b_1 \\ b_2 \\ b_3 \\ b_4 \\ b_5 \\ b_6 \\ b_7 \\ b_8 \\ b_9 \\ b_{10} \\ b_{11} \end{bmatrix} \qquad (6.8)$$

6.2.1. Length and volume multipliers for PD nodes in 2-D problems

Figure 6.2 shows a PD node at the origin interacting with the neighboring nodes within its horizon for a 2-D problem. Some of these nodes are completely within the horizon (the ones in white color), whereas the others are partially within the horizon (the ones in grey color). The cells in black color do not interact with the PD node at the origin since they are outside its horizon. Thus, $V_{ij,mult}$ for the partial nodes requires the computation of area under the curve using integration. For example, $V_{ij,mult}$ for the node outlined in broken blue can be computed as:

$$V_{ij,mult} = \frac{\left|\int_{-1}^{-3}\int_{-5}^{-\sqrt{36-y^2}} dxdy\right|}{2*2} = 0.3117 \tag{6.9}$$

$l_{ij,mult}$ can be calculated using trigonometric rules.

Table 6.1 and Table 6.2 show the multipliers for all the neighboring nodes. The multipliers for other horizon sizes or for problems in 1-D or 3-D can be obtained similarly.

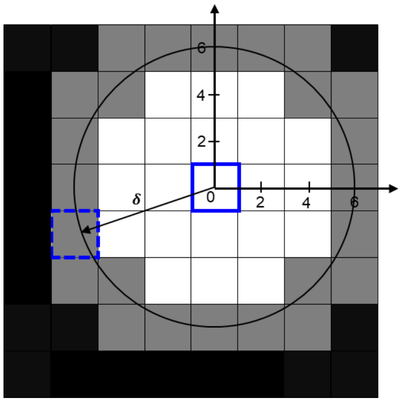

Figure 6.2. A PD node at the origin (in solid blue) interacting with the neighboring nodes within its horizon, which is 3 times the cell spacing (l) here. Only the cell associated with each node is shown for clarity.

Table 6.1. $l_{ij,mult}$, for horizon size 3 times the cell spacing for a 2-D problem.

		3.6056	3.1623	3	3.1623	3.6056	
	3.6056	2.8284	2.2361	2	2.2361	2.8284	3.6056
	3.1623	2.2361	1.4142	1	1.4142	2.2361	3.1623
	3	2	1	Node i	1	2	3
	3.1623	2.2361	1.4142	1	1.4142	2.2361	3.1623
	3.6056	2.8284	2.2361	2	2.2361	2.8284	3.6056
		3.6056	3.1623	3	3.1623	3.6056	

Table 6.2. $V_{ij,mult}$, for horizon size 3 times the cell spacing for a 2-D problem.

		0.0079	0.3117	0.4861	0.3117	0.0079	
	0.0079	0.7012	1	1	1	0.7012	0.0079
	0.3117	1	1	1	1	1	0.3117
	0.4861	1	1	Node i	1	1	0.4861
	0.3117	1	1	1	1	1	0.3117
	0.0079	0.7012	1	1	1	0.7012	0.0079
		0.0079	0.3117	0.4861	0.3117	0.0079	

6.2.2. Different approaches for assembly of coupled PD-FVM global transmissibility matrix

For a given domain with the same reservoir and fluid properties (Figure 6.3), the cell transmissibility entries for a FV cell remain the same irrespective of the dimensionality of the problem (equation (6.4)). However, those for a PD cell are different due to dependence of the micro-permeability function, and the length and volume multipliers on dimensionality (equation (6.7)). The global transmissibility matrix is obtained by adding together the cell transmissibility matrices and by treating the PD-FVM interface cells in a similar manner as described earlier. FVM equations in the resulting global matrix form a penta-diagonal bandwidth; however, PD equations form a non-sparse structure due to the non-local interactions (Figure 6.4a). Such a method of matrix assembly follows the connectivity of the cells and is referred to as *cell major* in this study.

In addition to the difference in the sparsity pattern, the magnitudes of PD and FV entries are also different due to the presence of different length scale terms in equations (6.4) and (6.7). Thus, another matrix assembly method is to shift all the PD equations at the end, while honoring the cell connectivity (Figure 6.4b). Such a method follows the type of equation and is referred to as *equation major* in this study. Although this method compromises the banded FV matrix structure and requires some additional bookkeeping, it improves the condition number of the matrix and thus the computational performance as shown in Subsection 6.3.2 later.

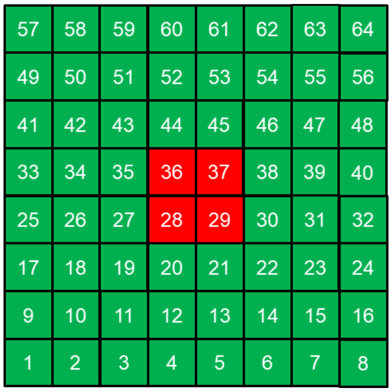

57	58	59	60	61	62	63	64
49	50	51	52	53	54	55	56
41	42	43	44	45	46	47	48
33	34	35	36	37	38	39	40
25	26	27	28	29	30	31	32
17	18	19	20	21	22	23	24
9	10	11	12	13	14	15	16
1	2	3	4	5	6	7	8

Figure 6.3. 2-D domain showing PD and FV cells in red and green colors respectively.

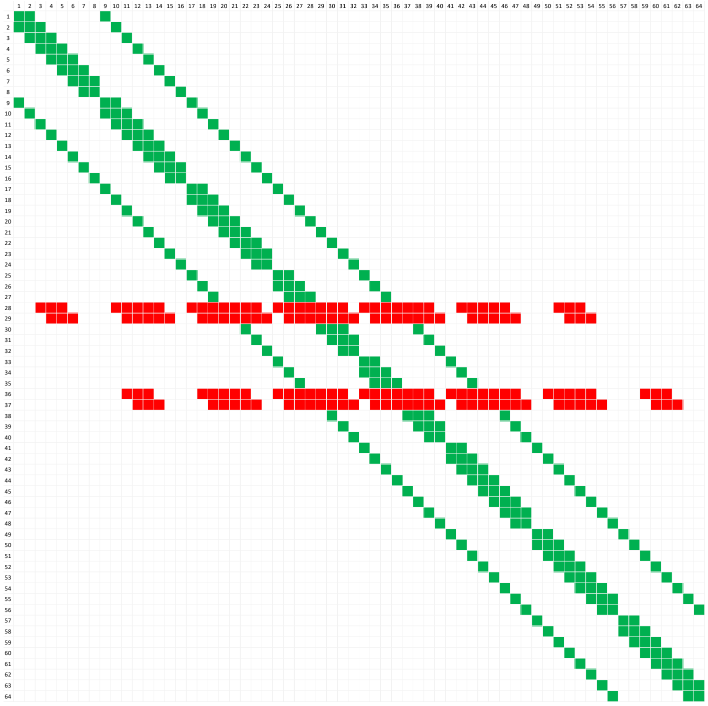

(a)

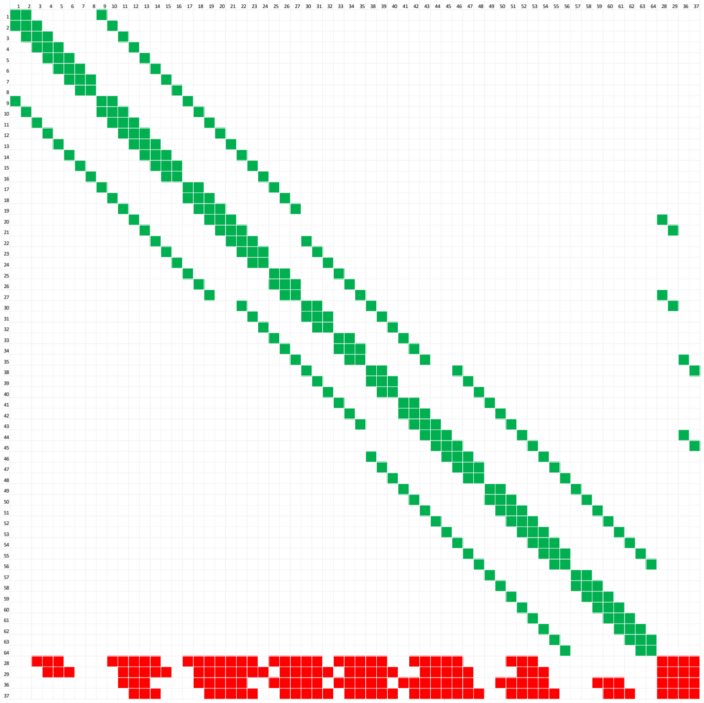

(b)

Figure 6.4. Matrix structure for the 2-D global transmissibility matrix. Green boxes correspond to non-zero FVM entries and red boxes to non-zero PD entries. (a) Cell major, (b) Equation major

6.2.3. Numerical example: Five spot pattern problem

The five-spot pattern problem described in Katiyar et al. (2014) is solved using the coupled PD-FVM formulation. In this problem, four injector wells (positive point source) are located at the corners of a square-shaped 2-D homogeneous reservoir and a producer well (negative point source) lies in the center (Figure 6.5). No flow boundary conditions are assumed on all the boundaries. Each quarter of the pattern is a repeatable unit and only one quarter is considered to save computational resources. The simulation parameters are summarized in Table 6.3.

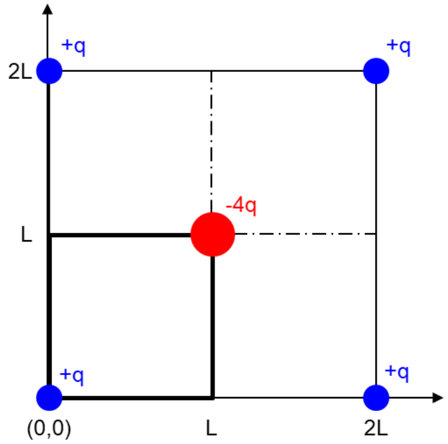

Figure 6.5. Schematic diagram for the five-spot pattern problem. The quarter square in the bottom-left is the smallest repeatable unit that is considered for computations.

Table 6.3. Simulation parameters for the five-spot problem.

Permeability, k (m^2)	1e-13
Viscosity, μ_f (Pa s)	1e-3
Rate for each well, $\dot{q}$ (m^3/m/s)	1e-3
Length of computational domain, L (m)	50
Cell spacing, l (m)	Variable
Horizon length, δ (m)	$3l$

The analytical solution to this problem is given as (Ansari and Johns, 2006):

$$\bar{P}(\bar{x},\bar{y}) = \sum_{i=1}^{N} \bar{P}_i(\bar{x},\bar{y}) = -\sum_{i=1}^{N} \ln[(\bar{x}-\bar{x}_i)^2 + (\bar{y}-\bar{y}_i)^2] \qquad (6.10)$$

where $(\bar{x},\ \bar{y})$ are the dimensionless coordinates. $\bar{P}_i$ is the dimensionless pressure drop caused by a well i located at $(\bar{x}_i, \bar{y}_i)$ such that

$$\bar{x} = x/L, \qquad \bar{y} = y/L, \qquad \bar{P}_i = \frac{P_{ini}-P}{\mu_f \dot{q}_i/4\pi k} \qquad (6.11)$$

The computational domain is shown in Figure 6.6. Again, the green and red cells are discretized and solved using FVM and PD formulations respectively. Radial pressure diffusion around the injector and producer wells is captured by the pressure contours in Figure 6.7a. The red box shows the location of the PD cells. No spurious behavior is observed at the PD-FVM interface. The same observation has been reported while solving the static solid mechanics problems using the coupled PD-FEM model (Galvanetto et al., 2016). Figure 6.7b shows a comparison of the numerical results with the analytical solution (equation (6.10)). There is very good agreement between the two and no spurious behavior is observed at the PD-FVM interface.

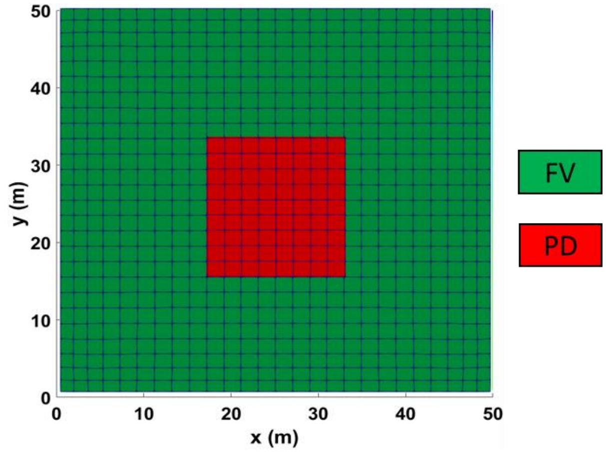

Figure 6.6. Discretized computational domain comprising the quarter square highlighted in Figure 6.5.

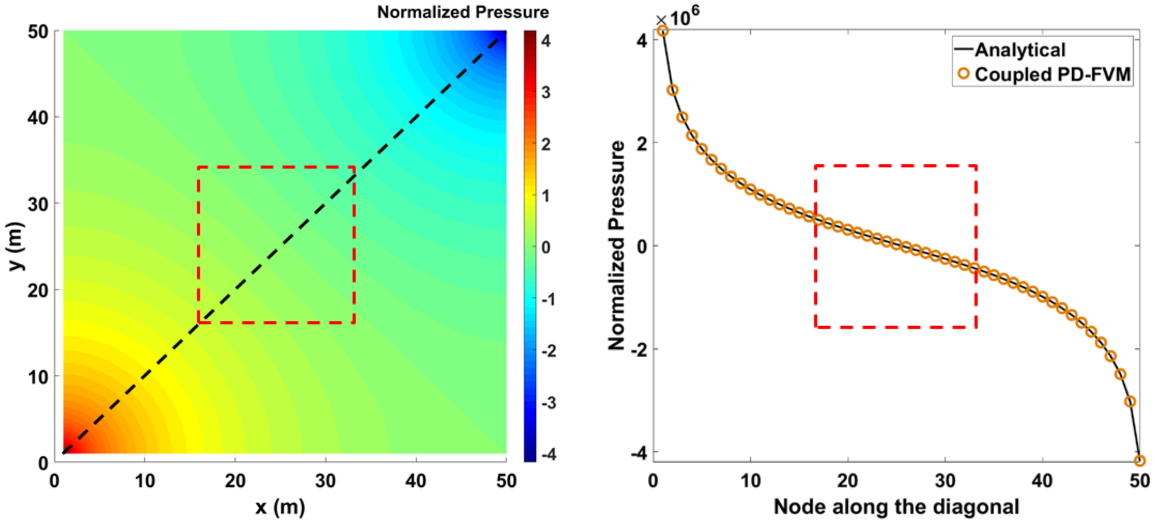

(a) (b)

Figure 6.7. (a) Pressure contours, (b) Dimensionless pressure along the diagonal line shown in (a).

6.2.4. Comparison of computational performance between pure PD and coupled PD-FVM models

Figure 6.8a shows the improvement in computational performance when using the coupled PD-FVM model as opposed to the pure PD model for solving the five-spot pattern problem. The improvement is represented by the ratio of time taken by the two models (equation (6.12)), including the time spent in global matrix assembly and solution.

$$\text{Computational time relative to pure PD} = \frac{\text{Time for coupled PD-FVM model}}{\text{Time for pure PD model}} \qquad (6.12)$$

The performance comparison is presented for a different number of total nodes and for different percentages of PD nodes in the computational domain (Figure 6.6). Moreover, one level of cell coarsening in the FV region is also used to demonstrate the potential for further improvement in performance (Figure 6.8b). It should be noted that within the horizon of PD cells in the coarsened model, FV cells have the same discretization as the PD cells ($\delta = 3l$, where l is the spacing between PD cells). This is to ensure consistent discretization in the horizon of PD cells close to the PD-FVM interface. The coarsened model has fewer total cells than the other corresponding models in Figure 6.8a.

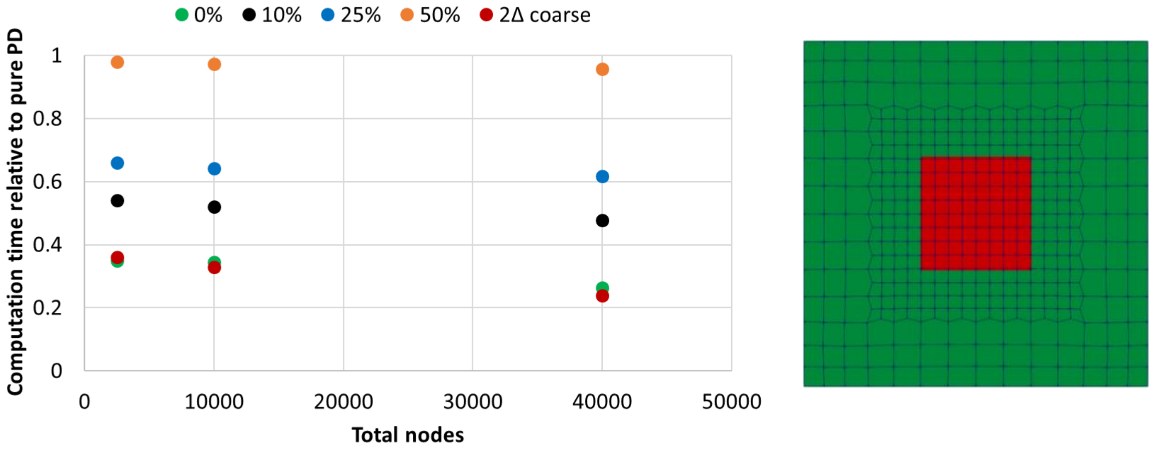

(a) (b)

Figure 6.8. (a) Relative computational performance for different percentage of PD nodes in the domain, (b) The coarsened model domain (2Δ coarse) in (a)

For 50% PD nodes, the performance is slightly better than the pure PD model. However, for a given number of total nodes, it improves substantially with a decrease in the percentage of PD nodes. The coupled formulation outperforms the pure FVM formulation for higher number of cells in the coarsened model. These observations are in agreement with those reported by York (2018).

6.3. COUPLING FOR POROELASTIC PROBLEMS

Geomechanics problems such as flow in subsurface aquifers or in hydrocarbon reservoirs typically involve the solution of poroelastic equations, which comprise coupled rock momentum and fluid mass balance laws (Coussy, 2004). Thus, the coupled PD-FVM porous flow formulation presented in Section 6.2 is extended to include the rock momentum equation. For this purpose, the hydraulic fracturing simulators developed by Zheng et al. (2019) using FVM and by Ouchi et al. (2015) using PD are combined. Only the geomechanics functionality of these simulators is used in this study. The application of this method to hydraulic fracturing (using the coupled PD-FVM model) will be demonstrated in Chapter 7. For more details of these models, the respective references mentioned above should be consulted. However, for completeness the main equations for both the models are summarized below.

The rock momentum balance and fluid mass balance equations in FVM for a control volume Ω, with reference to Figure 6.9 are given as (Zheng et al., 2019):

$$\oint_{\Gamma} [(K_b + 4G/3)\boldsymbol{n}.\boldsymbol{\nabla u_n} + (K_b - 2G/3)\boldsymbol{n}tr.(\boldsymbol{\nabla_t u_t}) + G\boldsymbol{n}.\boldsymbol{\nabla u_t} + G\nabla_t \boldsymbol{u_n} + \boldsymbol{\sigma_0} + \alpha P\boldsymbol{I}]\, d\Gamma = 0 \tag{6.13}$$

$$\int_{\Omega} \frac{1}{M}\frac{dp}{dt} d\Omega = \int_{\Omega} \nabla.\left(\frac{k}{\mu_f}\nabla P\right) d\Omega - \int_{\Omega} \alpha \frac{\partial}{\partial t}(\boldsymbol{\nabla}.\mathbf{u}) d\Omega \tag{6.14}$$

where $\boldsymbol{n}$ is face normal vector, Γ is face area, $\boldsymbol{u_n}$ and $\boldsymbol{u_t}$ are normal and tangential components of displacement respectively, K_b is bulk modulus of the rock, G is shear modulus of the rock, $\boldsymbol{\sigma_0}$ is in-situ stress, α is Biot coefficient, and M is Biot modulus.

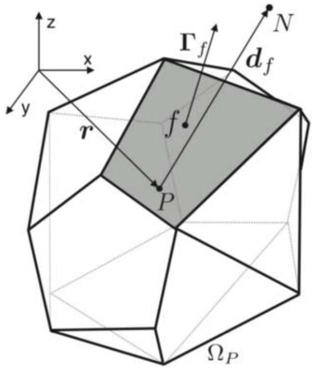

Figure 6.9. Polyhedral control volume (Cardiff et al., 2016)

The governing equations for the rock momentum balance and the fluid mass balance reviewed in Section 1.5 are used in this section.

Zheng et al. (2019) implemented a block-coupled scheme to solve non-linear multi-physics problems. Their FV formulation has been adapted to develop the coupled PD-FVM model by incorporating the PD equations and the mutual interaction terms with the FV equations. In most of the problems that we intend to solve with the new model, including those considered in this study, the PD cells would be surrounded by the FV cells. Thus, using a typical mesh generation package, the cells would be indexed in such a way that while assembling the global matrix, there would be a choice of interspersing the PD equations in between the FV equations (Figure 6.4a) or appending all the PD equations at the end (Figure 6.4b).

The coupled PD-FVM poroelastic equations are non-linear due to the non-linearity in PD governing equations (1.5) and (1.12). The Newton-Raphson method, which has been demonstrated to work well with non-linear systems, is used to solve the coupled set of equations. The Newton-Raphson method requires construction of a Jacobian matrix, the individual terms of which are computed by taking partial derivatives of the equations with respect to the primary unknowns. For brevity, only the equation major form of the Jacobian matrix is shown in Figure 6.10. The cell major form can be constructed by following the cell connectivity map. The off-diagonal derivative terms highlighted in brown in the figure constitute the mutual interaction between the PD and FV cells.

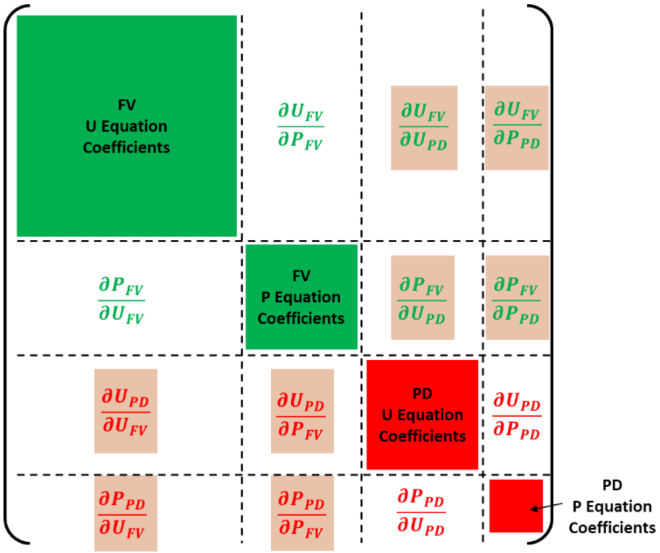

Figure 6.10. Equation major form of the Jacobian matrix for poroelastic problems.

6.3.1. Numerical example: 1-D Biot consolidation problem

The classical 1-D Biot consolidation problem is solved to verify the coupled PD-FVM poroelastic formulation. In this problem, a poroelastic medium extends from $z = 0$ to $z = h$ and rests on its bottom surface (Figure 6.11). The initial conditions are no flow on all the boundaries and no lateral deformation on the x and y boundaries. Moreover, the medium is initially at a uniform pore pressure of P_0 and a normal traction T_z is applied at the top boundary. This results in the deformation of the poroelastic layer and increases the pore pressure to P_{ref} due to the Skepmton effect. At time $t = 0$, the top boundary is exposed to atmospheric pressure P_b. As a result, pore fluid drains out until the pore pressure equilibrates to atmospheric pressure and the top boundary continues to deform downward. The change in pore pressure $P(z, t)$ and deformation $w(z, t)$ can be obtained by analytical expressions (Jaeger and Cook, 2007).

$$\bar{P}(\bar{z}, \bar{t}) = 1 - \sum_{n=0}^{\infty} (-1)^n \left[erfc\left(\frac{2n + \bar{z}}{\sqrt{8\bar{t}}}\right) + erfc\left(\frac{2(n+1) - \bar{z}}{\sqrt{8\bar{t}}}\right) \right] \tag{6.15}$$

$$\overline{w}(\bar{z},\bar{t}) = \frac{1}{K_b + 4G/3}\left[T_z(1-\bar{z}) + \alpha P_{ref}\sum_{n=1,3,..}^{\infty}\frac{8}{n^2\pi^2}\cos\left(\frac{n\pi\bar{z}}{2}\right)\exp\left(-\frac{n^2\pi^2\bar{t}}{2}\right)\right] \tag{6.16}$$

where the dimensionless quantities are defined as:

$$\bar{z} = z/h, \qquad \bar{t} = t/t_{eq}, \qquad \bar{P} = (P_{ref} - P)/(P_{ref} - P_b) \tag{6.17}$$

where equilibration time t_{eq}, and increased pore pressure P_{ref} are given as:

$$t_{eq} = 2\mu_f S h^2/k, \qquad P_{ref} = \alpha M T_z/(K_b + 4G/3 + \alpha^2 M) \tag{6.18}$$

where storage coefficient S is given as:

$$S = \left[c_f - \frac{1}{K_m}\right]\phi + \left[1 - \frac{2(1-2\upsilon)}{3(1-\upsilon)}\alpha\right]\frac{\alpha}{K_b} \tag{6.19}$$

where c_f is fluid compressibility, K_m is bulk modulus of the rock matrix/grains, υ is drained Poisson ratio. The values of these parameters are summarized in Table 6.4.

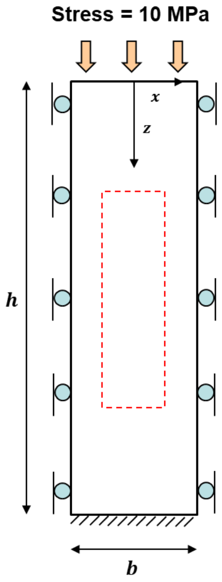

Figure 6.11. Schematic diagram for the 1-D Biot consolidation problem. The cells within the red box are PD cells.

Table 6.4. Simulation parameters for the 1-D Biot consolidation problem.

Porosity, ϕ	0.2
Permeability, k (m^2)	6e-15
Viscosity, μ_f (Pa s)	1e-3
Fluid compressibility, c_f (1/Pa)	5e-10
Bulk modulus of rock, K_b (Pa)	20e9
Bulk modulus of rock matrix/grains, K_m (Pa)	400e9
Shear modulus of rock, G (Pa)	12e9
Applied normal traction, T_z (Pa)	10e6
Initial pressure, P_0 (Pa)	0.1e6
Boundary pressure, P_b (Pa)	0.1e6
Domain length, h (m)	162
Domain breadth, b (m)	108
Cell spacing, l (m)	1
Horizon length, δ (m)	3

Figure 6.11 shows a schematic of the computational domain discretized uniformly into volumetric cells. The cells within the red box are solved using a PD formulation, whereas the remaining cells are solved using a FV formulation. The box covers 50% of the dimensions in each direction and is located symmetrically.

Dimensionless pressures and displacements are obtained as a function of dimensionless depth and time from the coupled PD-FVM simulator. The numerical results are compared against the corresponding analytical solutions in equations (6.15) and (6.16). The data points corresponding to the PD equations are highlighted in the red box (Figure 6.12). The numerical results are in good agreement with the analytical solutions for all dimensionless depths and times, including those at the interface of PD and FVM regions. This confirms that the coupled PD-FVM poroelastic formulation does not exhibit any spurious behavior at the interface of the two regions.

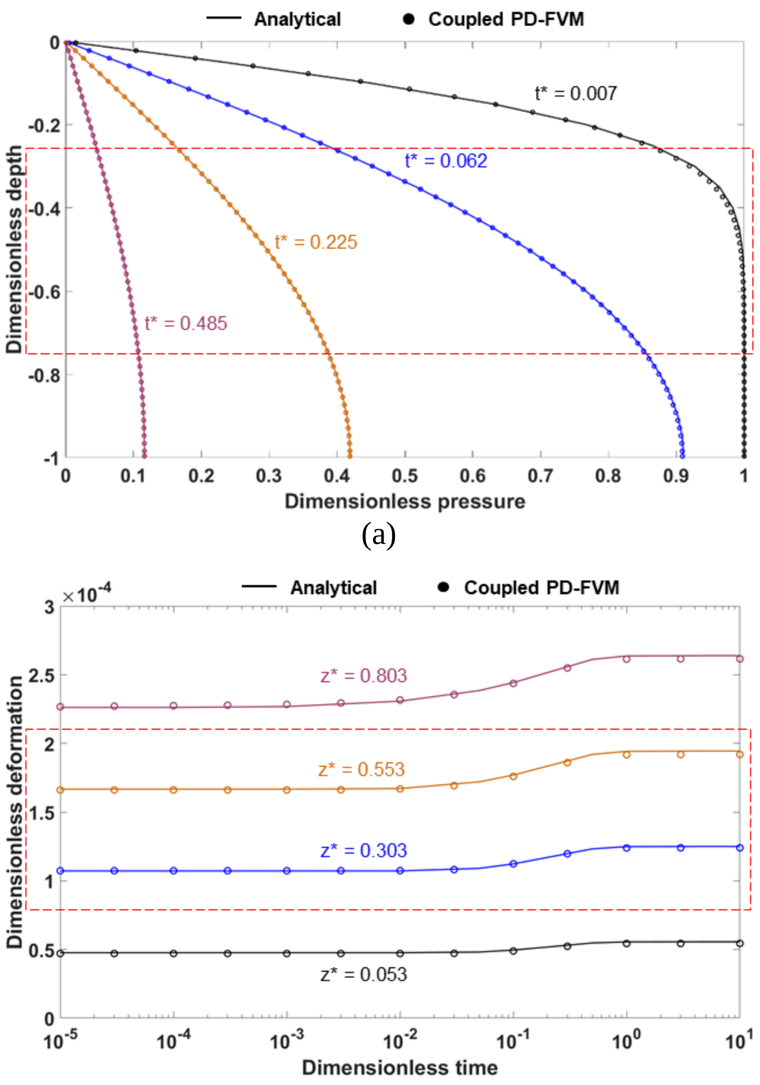

(a)

(b)

Figure 6.12. Coupled PD-FVM numerical results compared against the analytical solutions. (a) Dimensionless pressure, (b) Dimensionless deformation. Red boxes show the data for PD cells.

6.3.2. Comparison of matrix assembly approaches

The computational performance of the two matrix assembly approaches proposed in Subsection 6.2.2 are compared. The Biot consolidation problem is solved using both of them. Figure 6.13a shows the ratio of condition number of the Jacobian matrix obtained from the equation major approach to that obtained from the cell major approach against the total number of nodes. It is evident that by appending the PD equations at the end, the Jacobian matrix is conditioned better for all the discretizations. This is because of differences in the sparsity patterns and differences in the magnitudes of PD and FV partial derivative terms. Figure 6.13b shows the effect of the assembly approaches on the convergence of displacement and pressure equations. Both the equations converge in almost half the number of iterations while using the equation major approach. Tolerance of 1e-3 and 1e-4 were used for the relative residuals of the displacement and pressure equations respectively.

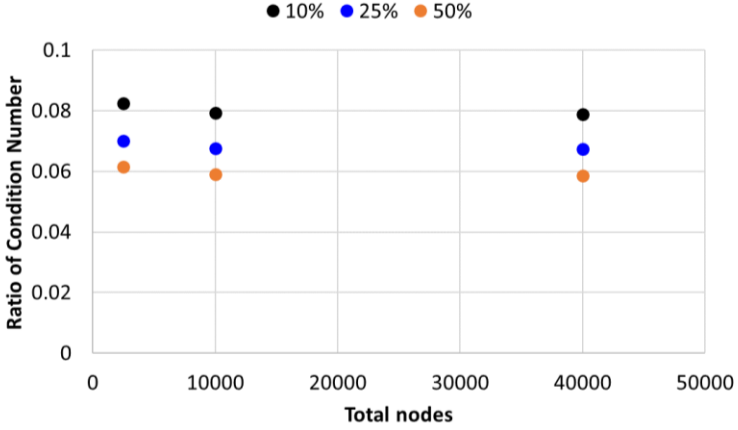

(a)

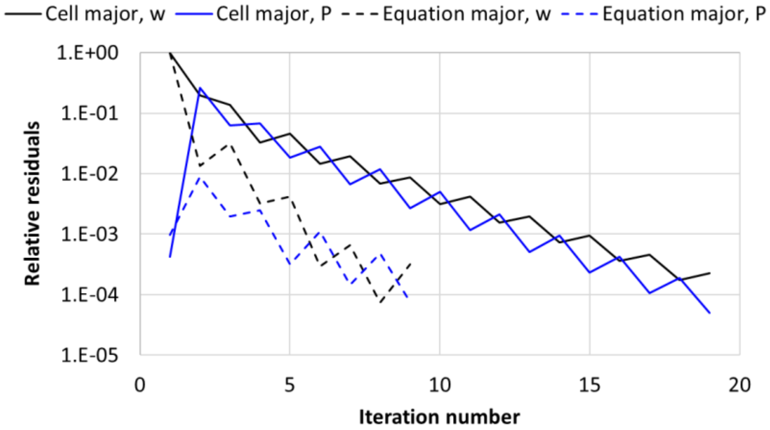

(b)

Figure 6.13. (a) Ratio of condition numbers of Jacobian matrix from equation major approach to that from cell major approach, (b) Convergence of displacement and pressure equations using the two approaches.

6.4. CONCLUSIONS

Based on the Peridynamic and Finite Element coupling scheme proposed by Galvanetto et al. (2016), we have presented a coupled Peridynamic and Finite Volume poroelastic model for multiscale problems in porous media. We have developed the formulation for porous fluid flow using a fluid mass balance, and have extended it for poroelastic problems to include a rock momentum balance. By solving the classical verification problems, significant improvements in computational performance of the coupled model over the pure peridynamic model are illustrated. No spurious behavior is observed near the PD-FVM interface region. Moreover, due to differences in the sparsity patterns and the magnitudes of PD and FVM transmissibility/Jacobian terms, it is shown that appending the PD equations after all the FV equations in the global matrix has additional computational benefits.

The application of the coupled model in simulating the growth of hydraulic fractures in heterogeneous subsurface reservoirs is demonstrated in Chapter 7.

CHAPTER 7: FRACTURING SIMULATIONS USING THE COUPLED PERIDYNAMIC-FINITE VOLUME MODEL

7.1. INTRODUCTION

A Peridynamics-based hydraulic fracturing simulator has been shown to capture various interesting phenomena, such as stress shadow effect and complicated interactions with different scales of reservoir heterogeneities (Ouchi, 2016). However, to accurately capture the displacement and pressure fields, the simulator requires several orders of magnitude finer discretization as compared to classical methods such as FEM or FVM. Moreover, the discretization should be uniform unless some special PD formulation is adapted. These requirements combined with the dense matrices resulting from the non-local PD interactions lead to longer computational times. Thus, simulating field-scale problems with a pure PD model is prohibitively time consuming.

In this chapter, the coupled PD-FVM poroelastic model derived in Chapter 6 is extended for hydraulic fracturing applications. The hydraulic fracturing feature of the simulators developed by Zheng et al. (2019) using FVM and by Ouchi et al. (2015) using PD are utilized. In the coupled model, a hydraulic fracture can be propagated using PD or FVM by incorporating an injection source of the fracturing fluid in the respective computational domain. For both the options, the model is verified against analytical solutions and laboratory experiments in the subsequent sections. A performance improvement of the coupled model compared to the pure PD model is also presented. In the final section, an application of the coupled model to estimate the Stimulated Reservoir Volume (SRV) around a hydraulic fracture is demonstrated.

7.2. FRACTURE PROPAGATION USING PD IN THE COUPLED PD-FVM MODEL

In this section, the coupled PD-FVM model is applied to hydraulic fracture propagation and the improvement in performance compared to the pure PD model is illustrated. A computational domain is divided into two parts, one of which is discretized and solved using PD and the other with FVM. All the potential fractures are restricted within the PD subdomain and their growth is modeled with the PD formulation. The next two subsections implement different methods of solving the coupled domain with increasing levels of computational efficiency, as introduced by York (2018). The simulation parameters for these cases are summarized in Table 7.1.

7.2.1. Static Peridynamic Region Method

The first method assumes a static PD region encompassing all the fractures. Figure 7.1a shows a domain with one fracture, in which the cells inside the red box are discretized and solved with PD and the rest with FV. In other words, the red box serves as a PD-FVM interface. Fine discretization is used in the PD region to ensure the accuracy of the non-local formulation. The same fine discretization is maintained immediately outside of the PD region (between the red and the green boxes) so that the PD cells at the interface have a complete set of non-local neighbors within their horizons (δ=3 in these cases). Outside of the green box, the FV cells are progressively coarsened for improving the computational efficiency. In the problems presented in this section, 3 levels of mesh coarsening are used. More levels could be used as needed in bigger domains. Initially, only a starter notch or a well perforation comprise the damaged cells. Minimum and maximum stresses are applied in the vertical and horizontal directions respectively. When fluid is injected into the well, a horizontal fracture propagates as governed by the applied stresses (Figure 7.1b).

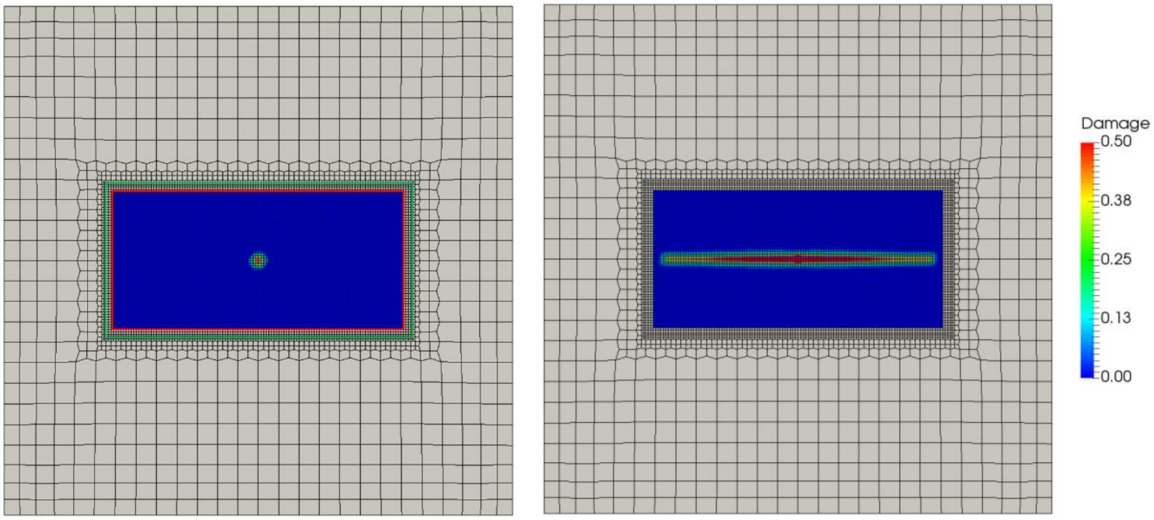

(a) (b)

Figure 7.1. Static PD region coupling. The cells within the red box are PD cells and the rest are FV cells. (a) Before fracture propagation, (b) After fracture propagation

7.2.2. Dynamic Peridynamic Region Method

The next method allows for the PD region (denoted by the solid red box in Figure 7.2a) to grow with the fracture inside a designated refined discretization (denoted by the broken red box). Since these refined cells may potentially be converted to PD cells, the initialization of the non-local parameters are performed at the start of the simulation. This is in contrast to the dynamic initialization performed by York (2018), each time the fracture propagates. The initial PD region comprises the damaged cells and their non-local neighbors. As the hydraulic fracture grows, the non-local neighbors of the newly damaged PD cells are dynamically converted from FV to PD cells. To accomplish this conversion, we compute PD Jacobian entries for these cells instead of the corresponding FV Jacobian entries. The hydraulic fracture resulting from the dynamic PD region method is shown in Figure 7.2b. Compared to the static PD region method in the last subsection, this method has an additional computational advantage of solving for the more expensive PD formulation only around the damaged cells.

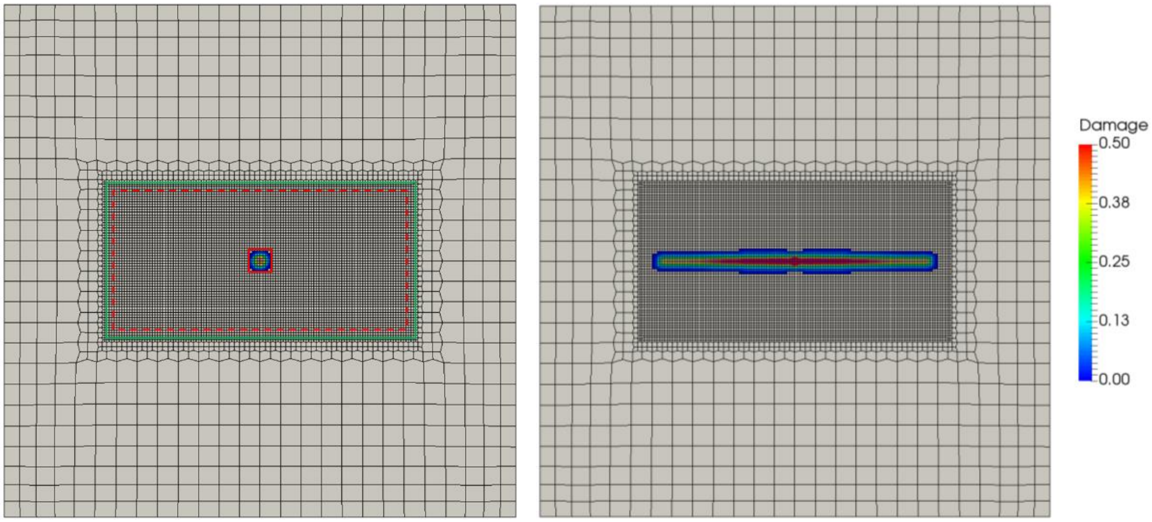

(a) (b)

Figure 7.2. Dynamic PD region coupling. The cells within the solid red box are PD cells and the rest are FV cells. (a) Before fracture propagation, (b) After fracture propagation

7.2.3. KGD verification

To verify the PD-FVM coupling schemes described in the previous two subsections, we consider the propagation of a KGD fracture in a homogeneous isotropic medium under the plane strain assumption. The fracturing fluid is assumed to be Newtonian, and slightly compressible and the flow is considered to be laminar. Moreover, fluid leak-off from the fracture is neglected. The analytical solutions for fluid injection pressure P_{inj}, fracture half-length l_f, and maximum fracture width w_{max} are given by the following expressions.

$$P_{inj} = S_{h,min} + 1.09\left(E'^2\mu_f\right)^{1/3} t^{-1/3} \tag{7.1}$$

$$l_f = 0.539\left(\frac{E' q^3}{\mu_f}\right)^{1/6} t^{2/3} \tag{7.2}$$

$$w_{max} = 2.36\left(\frac{q^3\mu_f}{E'}\right)^{1/6} t^{1/3} \tag{7.3}$$

where $S_{h,min}$ is the minimum horizontal stress, μ_f is the fracturing fluid viscosity, q is the fracturing fluid volumetric injection rate, t is time, and E' is given as:

$$E' = \frac{E}{1 - \upsilon^2} \tag{7.4}$$

where E is the Young's modulus and υ is the Poisson ratio of the medium.

The model setup shown in Figure 7.2 is used to simulate the growth of the KGD fracture. The simulation parameters are the same as those used by Ouchi (2016) and are summarized in Table 7.1.

Table 7.1. Simulation parameters for KGD verification (same as Ouchi, 2016)

Boundary stress in *x*-direction, S_{xx} (MPa)	12.0
Boundary stress in *y*-direction, S_{yy} (MPa)	8.0
Initial pore pressure, P_0 (MPa)	3.2
Bulk modulus, K (GPa)	60.0
Shear modulus, G (GPa)	24.0
Permeability, k (nD)	10.0
Fracturing fluid mass injection rate, Q (kg/m/s)	0.025
Fracturing fluid density, ρ (kg/m^3)	1000
Fracturing fluid viscosity, μ_f (Pa s)	0.001
Domain length in *x*-direction, L_x (m)	40.0
Domain length in *y*-direction, L_y (m)	32.0
Cell spacing in PD region, Δx (m)	0.2
Horizon length, δ (m)	0.6

The numerical results from our dynamic PD region method closely match the analytical solution, except for the over-prediction in fracture width which is consistent with that reported by Ouchi (2016) using a pure PD-based model.

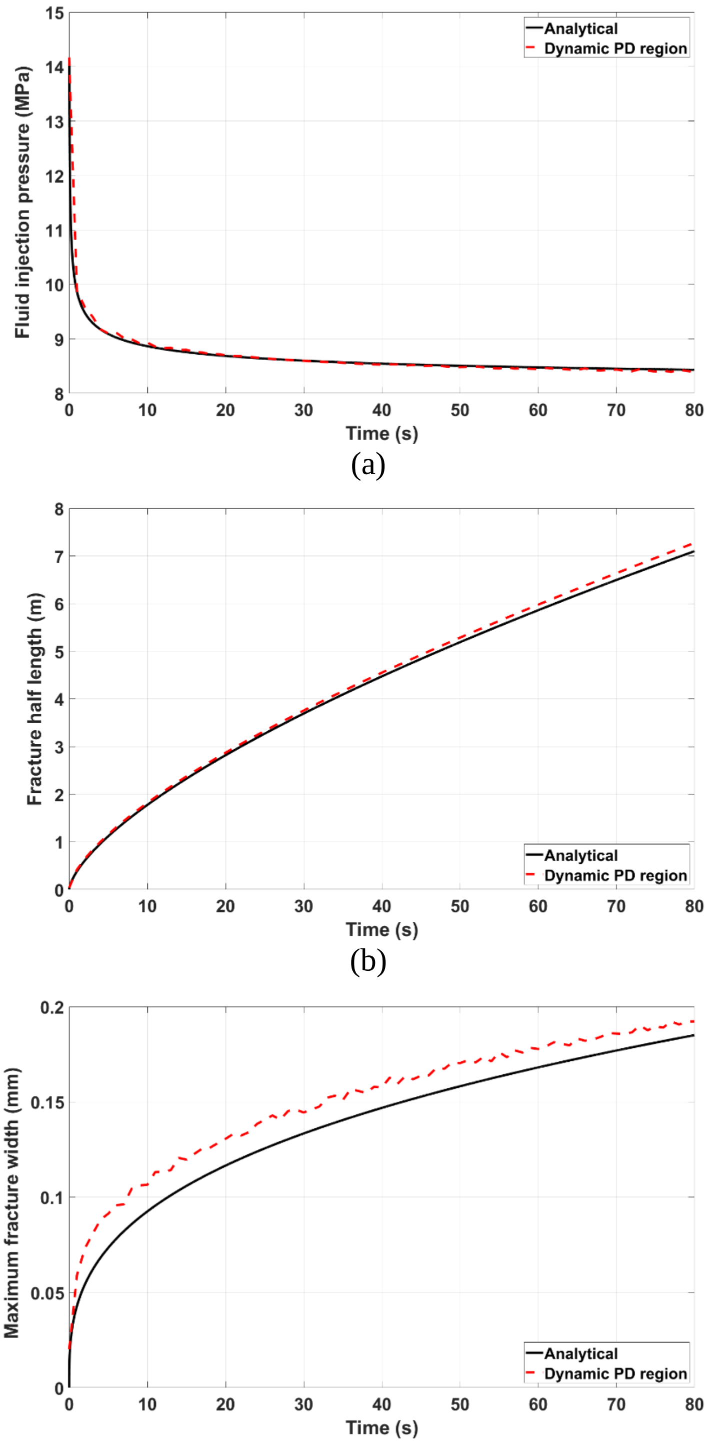

(a)

(b)

(c)

Figure 7.3. Verification of the dynamic PD region method against the analytical KGD solution. (a) Fluid injection pressure, (b) Fracture half length, (c) Maximum fracture width.

7.2.4. Comparison of computational performance against pure PD model

In this subsection, we present the computational benefits of the coupled PD-FVM model over the pure PD model. Since the pure PD model requires a uniform fine discretization throughout, the domain in Figure 7.1 is uniformly discretized with the finest cell size as shown in Figure 7.4. The following ratios are defined based on three different metrics to compare the performance improvements.

$$\text{Metric Ratio} = \frac{\text{Metric for the pure PD model}}{\text{Metric for the coupled PD} - \text{FVM model}} \tag{7.5}$$

where the metric in equation (7.5) can be degrees of freedom (DOF), number of PD cells, or the computational time.

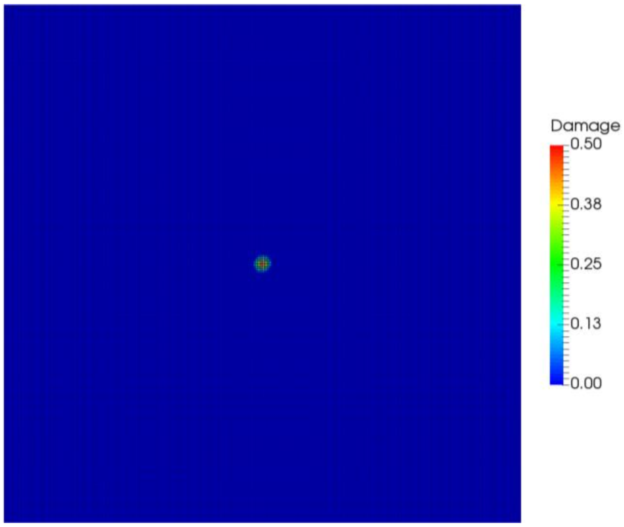

Figure 7.4. Uniform refined discretization considered for pure PD simulations.

We first demonstrate the computational complexity of the pure PD model by simulating the propagation of a single fracture with varying levels of mesh refinement. In each run, the number of cells in both the length and the breadth directions are increased by 40%, thereby doubling the total degrees of freedom. The computational times are plotted in Figure 7.5. The model exhibits a complex computational behavior because of different types of operations involved, including computation of cell matrices, their assembly into a global matrix, and solving the problem using a linear solver.

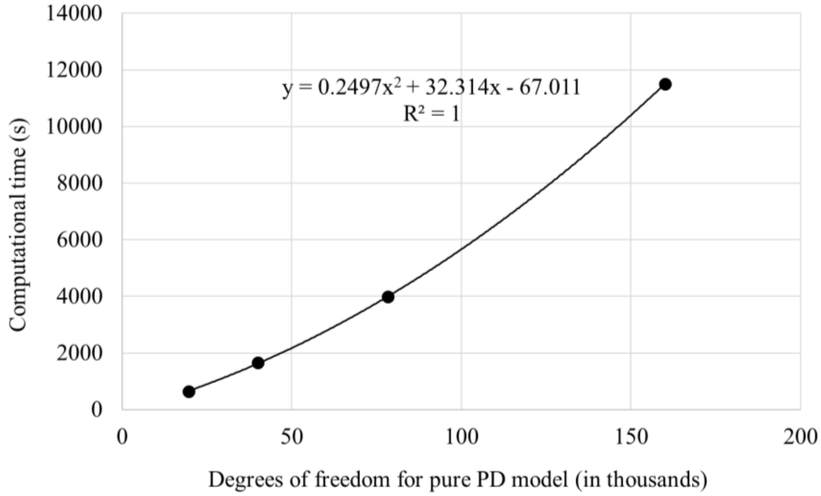

Figure 7.5. Computational complexity of the pure PD model for a single fracture propagation.

To demonstrate the performance improvement, increasing levels of consistent refinement in both the PD and FV subdomains are considered. In other words, if the discretization in the PD subdomain is halved, the corresponding discretization in the FV subdomain is also halved. The lengths of the PD and FV subdomains are maintained constant in all the cases. The first 20 time-steps of fracture propagation are simulated with both the coupled PD-FVM methods.

Figure 7.6a shows the performance comparison of the static PD region method relative to the pure PD model. Cell coarsening in the FV region reduces the DOF in the coupled model as compared to that in the pure PD model. This reduction in DOF results in about an order of magnitude speed-up for the discretizations typically considered in the pure PD-based fracturing simulations in the previous chapters.

Figure 7.6b shows the performance comparison of the dynamic PD region method relative to the pure PD model. In this method, the refined cells outside the horizon of the damaged cells are solved using the less expensive FVM. This leads to a significantly smaller number of PD cells in the dynamic region method as compared to that in the static region method. It should be noted that the PD cells ratio shown in Figure 7.6b is for the last time-step in these simulations. This reduction in the PD cells ratio results in a further 2 times speed-up over the static region method and about a 20 times speed-up over the pure PD model.

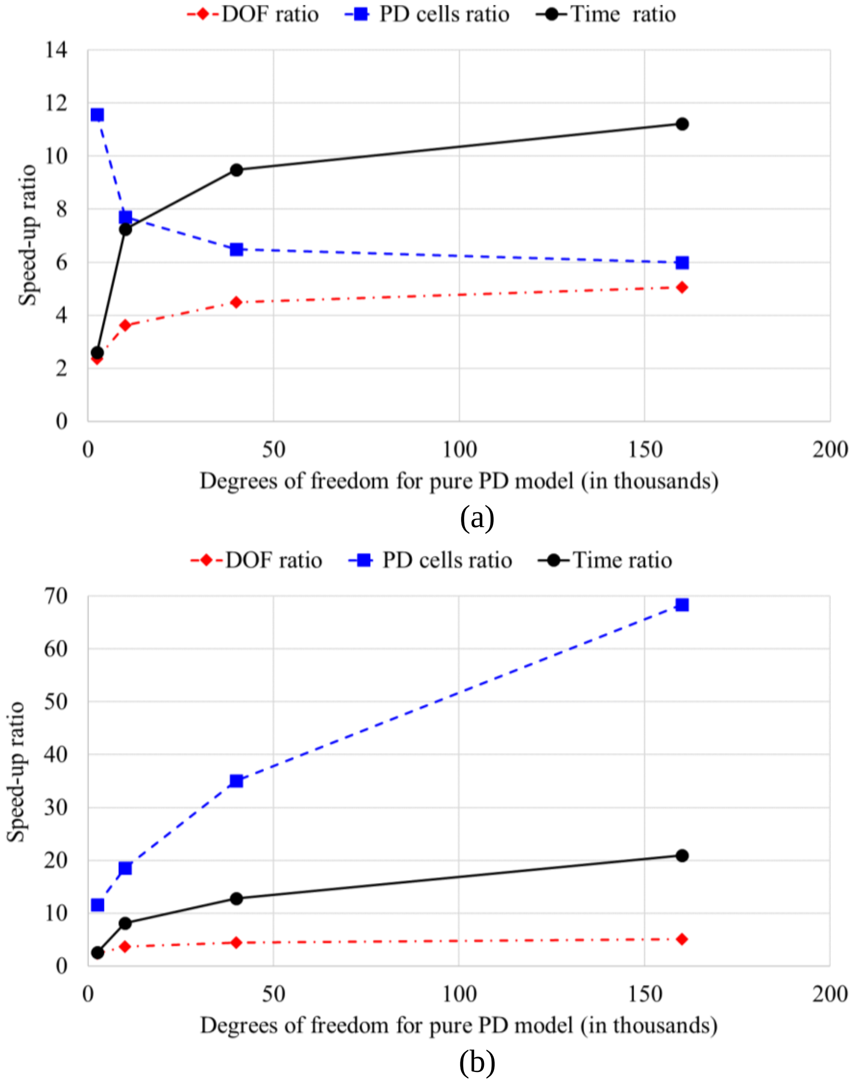

Figure 7.6. Comparison of computational performance of the coupled models relative to the pure PD model. (a) Static PD method, (b) Dynamic PD method

Further improvements in computational performance can be achieved by implementing adaptive mesh refinement/coarsening in the FV region of the dynamic PD region method (York, 2018).

7.2.5. Application to HF-NF interaction

Next, we apply our coupled PD-FVM schemes to validate with experiments on the interaction of a hydraulic fracture (HF) with a natural fracture (NF) (Zhou et al., 2008). The HF-NF interaction was investigated for different angles of approach of the HF and for different applied stresses (Figure 7.7). For low approach angles and low stress contrasts, the HF dilated the NF. For high approach angles and high stress contrasts, the HF crossed the NF. For intermediate values of these parameters, the HF was arrested by the NF.

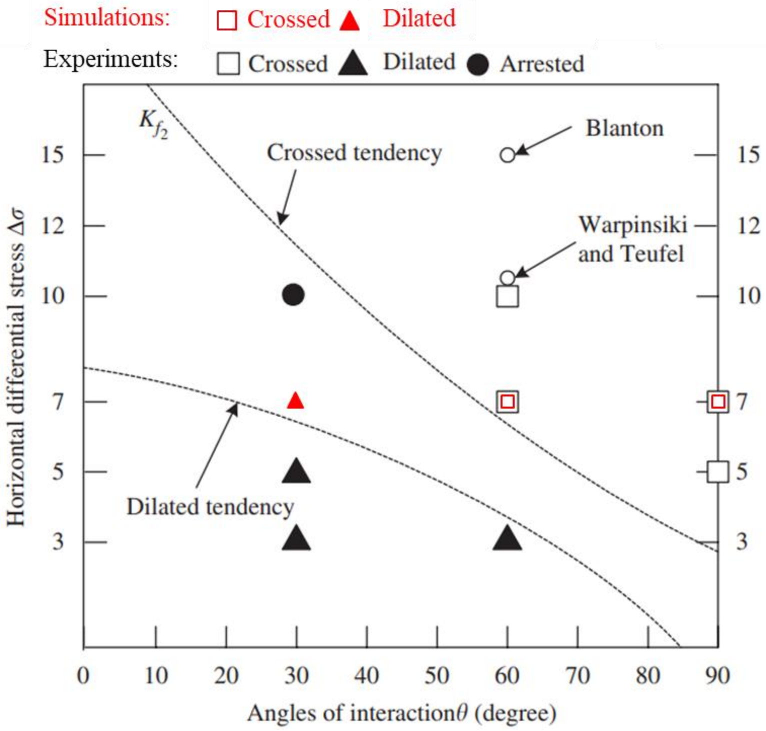

Figure 7.7. Comparison of the coupled PD-FVM model against HF-NF interaction experiments

The cases highlighted in red markers in Figure 7.7 are simulated with both the coupled PD-FVM schemes. The model setup described in detail by Ouchi (2016) has been adopted. The simulation parameters are restated in Table 7.2. The discretization used in the coupled PD-FVM simulations ensures that both the HF and the NF are meshed with fine cells, suitable for the PD formulation. FV cells with gradual coarsening are used away from these fractures.

Table 7.2. Simulation parameters for experimental validation of HF-NF interaction (same as Ouchi, 2016)

Boundary stress in x-direction, S_{xx} (MPa)	10.0
Boundary stress in y-direction, S_{yy} (MPa)	3.0
Bulk modulus, K (GPa)	5.18
Poisson ratio, v (GPa)	0.23
Porosity, φ	0.0185
Permeability, k (nD)	0.1
Cohesion of the NF, S_{NF} (MPa)	3.2
Friction coefficient of the NF, μ_{NF} (MPa)	0.89
Tensile strength multiplier	0.5
NF length (m)	0.08
Distance of NF from the well (m)	0.08
Fracturing fluid injection rate, q (m^3/s)	2.1e-8
Fracturing fluid viscosity, μ_f (Pa s)	0.135
Domain length in x-direction, L_x (m)	0.30
Domain length in y-direction, L_y (m)	0.30
Cell spacing in PD region, Δx (m)	0.0015
Horizon length, δ (m)	0.0045

The first simulation is for the case of a HF approaching a NF at 90^{o} at an applied stress contrast of 7 MPa. The resulting fracture trajectory is shown in Figure 7.8. Consistent with the experimental observation, the HF crosses the NF. Both the static and dynamic PD region methods predict similar trajectories and there seems to be no difference between the two.

In the next examples, the approach angle between the HF and the NF is changed to 60° and 30° (Figure 7.9 and Figure 7.10). For 60° interaction, the HF still crosses the NF; however, for 30° interaction, the HF turns along the NF. These results are also consistent with the experimental findings. Moreover, since no difference in the fracture trajectories is noted for the static and dynamic PD region methods, it can be concluded that neither of them induce a spurious computational behavior in the model.

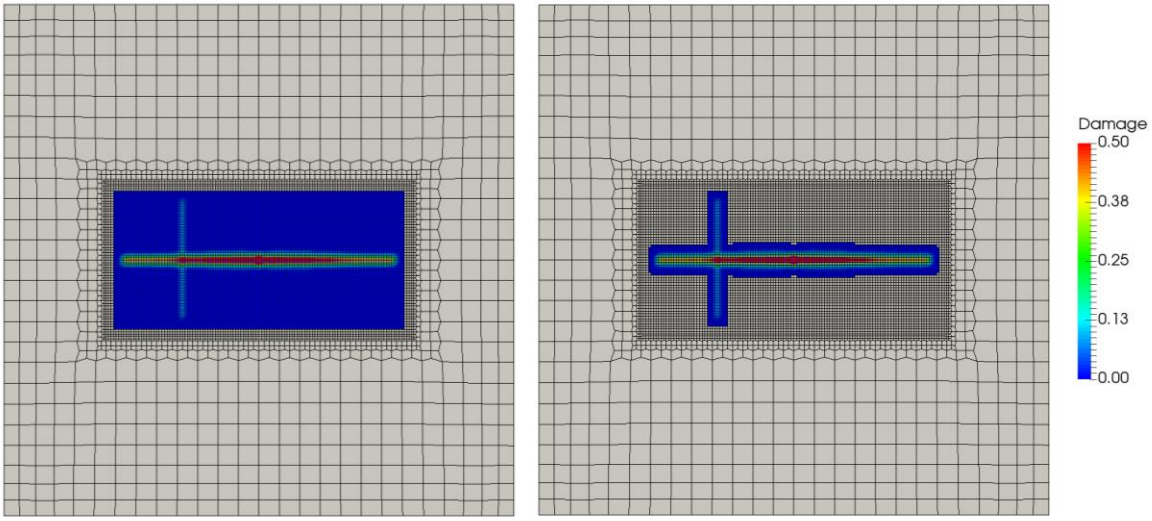

(a) (b)

Figure 7.8. 90° interaction at 7 MPa stress contrast. (a) Static PD, (b) Dynamic PD

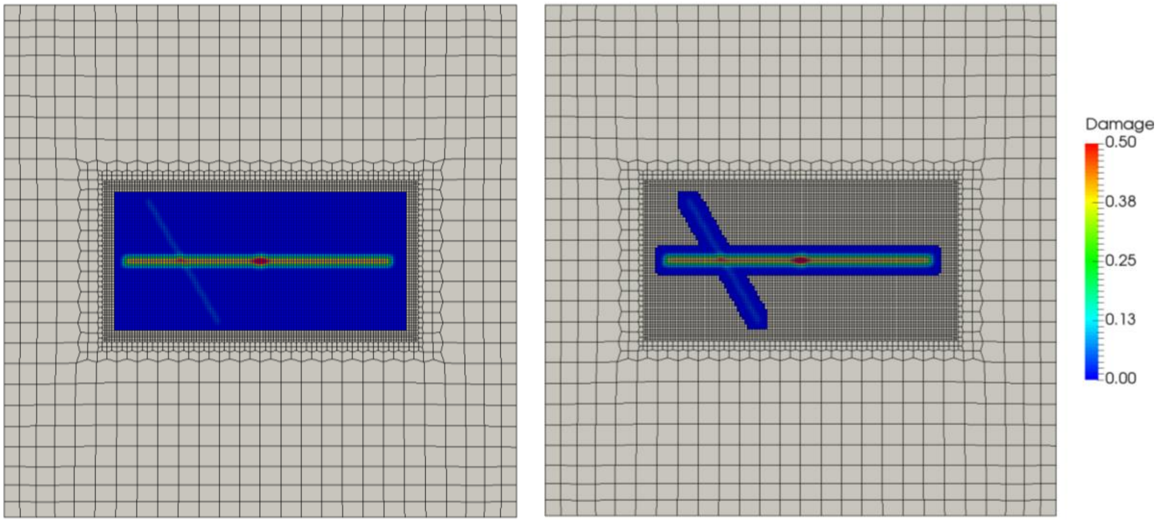

(a) (b)

Figure 7.9. 60^{o} interaction at 7 MPa stress contrast. (a) Static PD, (b) Dynamic PD

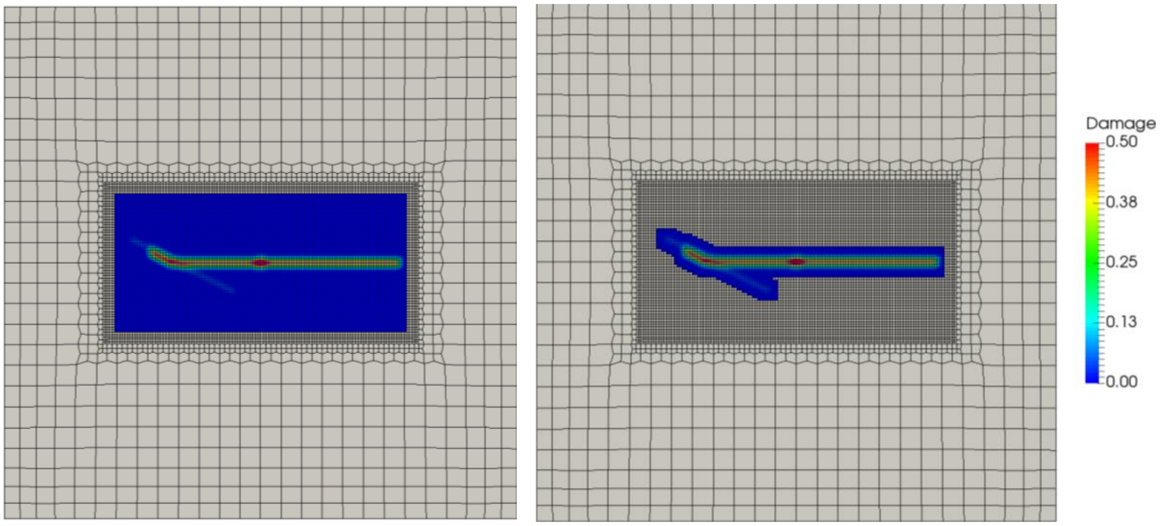

(a) (b)

Figure 7.10. 30^{o} interaction at 7 MPa stress contrast. (a) Static PD, (b) Dynamic PD

7.3. Fracture Propagation using FVM in the Coupled PD-FVM Model

In this section, within the framework of our coupled PD-FVM model, we propagate a hydraulic fracture using the FV formulation and monitor the resulting remote material damage using the PD formulation. The propagating hydraulic fracture causes poroelastic stress changes around it, which may lead to shear failure of the surrounding natural fractures or that of the weak mineral interfaces. In the case of unconventional reservoirs, these shear failure cracks may undergo sufficient permeability enhancement to allow for the flow of reservoir fluids in an otherwise virtually impermeable rock matrix. This region of enhanced permeability around the main hydraulic fracture is referred to as the Stimulated Reservoir Volume (SRV) (Mayerhofer et al., 2010).

In the following, we validate our approach of modeling the remote shear failure of weak mineral interfaces against a recent experiment conducted by Ratzlaff et al. (2019). Subsequently, we demonstrate the application of our model to estimate the extent of the SRV in unconventional reservoirs.

7.3.1. Experimental Validation

Ratzlaff et al. (2019) conducted fracturing experiments in a Tennessee sandstone sample to investigate the SRV induced around the primary hydraulic fracture. They fractured a 6” long by 4” diameter core under triaxial stress conditions by injecting a low viscosity epoxy. With the aid of a Scanning Electron Microscope (SEM) and an advanced software for SEM image analysis, multiple thin sections were analyzed for fracture density, distribution, orientation, symmetry, length, width, and stimulated reservoir area (SRA).

We simulate the experiment by considering a 2-D plane strain computational domain representing a horizontal cross-section of the experimental core as shown in Figure 7.11a. The domain is discretized with varying levels of refinement to capture the details at different length scales. The cells in the red box are solved with PD and the rest are solved with FVM. The green box contains a well that is located centrally and injects fluid to propagate a hydraulic fracture. The PD cells consist of mineral heterogeneity consistent with the mineral composition of the Tennessee sandstone used in the experiment (Figure

7.11b). The adhesion between the minerals in a rock can be weak as defined by the surface energy (Miller, 2010). We model this weak adhesion by reducing the critical energy density of the PD bonds crossing the mineral interfaces to 50% of their original values (Ouchi et al., 2017). The simulation parameters and mechanical properties of the minerals are summarized in Table 7.3 and Table 7.4 respectively.

Using the described computational domain, we demonstrate the capability of our coupled PD-FVM model in predicting remote material damage due to poroelastic stress changes caused by a propagating hydraulic fracture. Subsequently, using variations of the domain, we develop and validate a workflow for determining the SRV extent around the primary fracture against the experimental results.

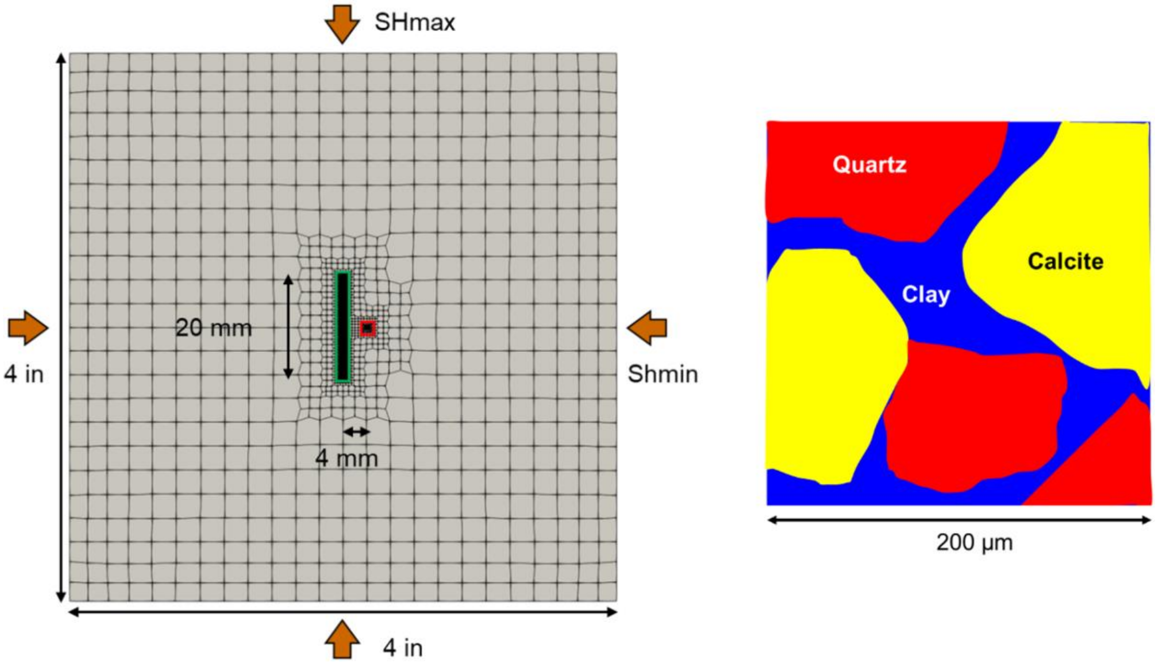

(a) (b)

Figure 7.11. Computational domain for SRV experimental validation. (a) Discretization, (b) Mineral heterogeneity in the PD subdomain

Table 7.3. Simulation parameters for SRV experimental validation (Ratzlaff et al., 2019; *Warpinski et al., 1982)

Boundary stress in *x*-direction, S_{hmin} (MPa)	3.45
Boundary stress in *y*-direction, S_{Hmax} (MPa)	13.79
Initial pore pressure, P_0 (MPa)	0.1
Bulk modulus, K (GPa)	59
Poisson ratio, ν (GPa)	0.25
Porosity, φ	0.1
*Permeability, k (μD)	10
Fracturing fluid injection rate, q (m^3/s)	2.1e-8
Fracturing fluid viscosity, μ_f (Pa s)	0.062
Domain length in *x*-direction, L_x (m)	0.1016
Domain length in *y*-direction, L_y (m)	0.1016
Cell spacing in PD region, Δx (m)	4e-6
Horizon length, δ (m)	12e-6

Table 7.4. Mechanical properties of the minerals (Atkinson & Meredith, 1987; Mavko et al., 2009)

Mineral	**Young's modulus (GPa)**	**Shear modulus (GPa)**	**Fracture toughness (MPa $m^{0.5}$)**
Quartz	95.6	44.3	2.40
Calcite	83.8	32.0	0.19
Clay	10.0	4.0	0.50

7.3.1.1. Base case: Single PD region

In the base case, the domain shown in Figure 7.11 with a single PD region is simulated. When fluid is injected into the well, the pressure builds up, however a significant amount of the fluid leaks-off into the sandstone. After 27 seconds of injection, the breakdown pressure is reached, and a fracture starts propagating. 2 seconds later, the fracture length is 10 mm and the maximum width is 33 μm (Figure 7.12a). At this instant, the first material damage appears on the weak clay-calcite interface (Figure 7.12b). 3 seconds further into the injection, the fracture attains its final length of 20 mm and a maximum width of 52 μm (Figure 7.13a). Material damage in the PD region shows that most of the clay-calcite interfaces are damaged at the end of injection (Figure 7.13b).

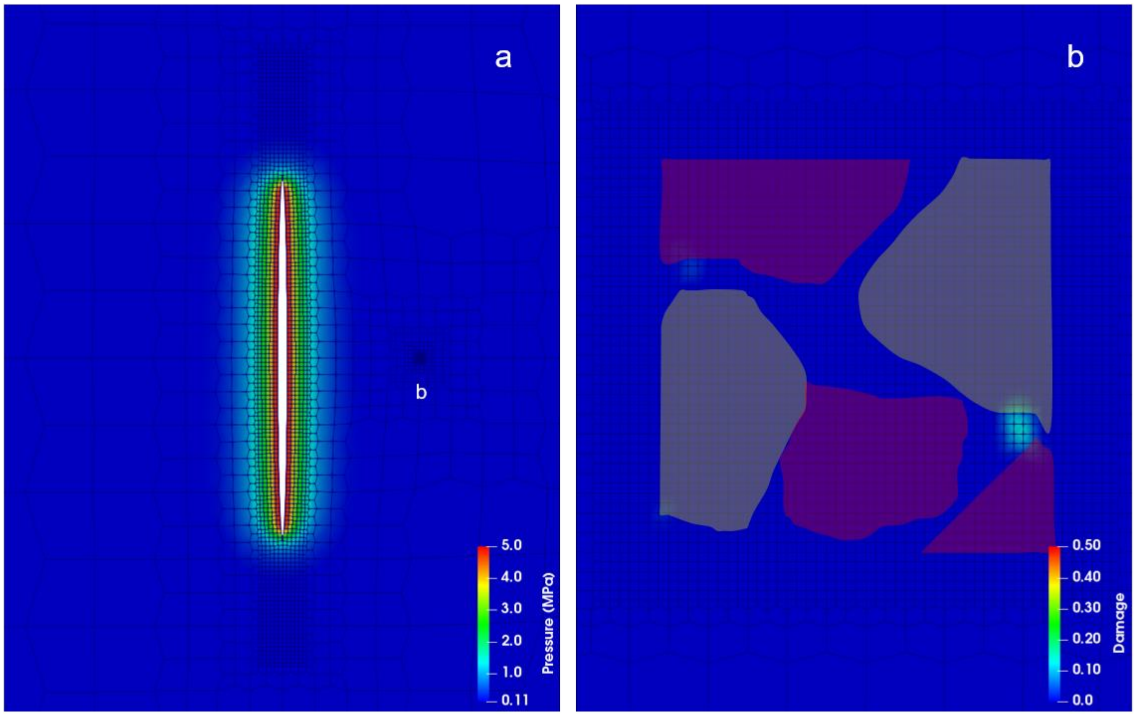

Figure 7.12. Base case, time = 29 sec. (a) Fracture geometry and PD region, (b) Damage map in the PD region.

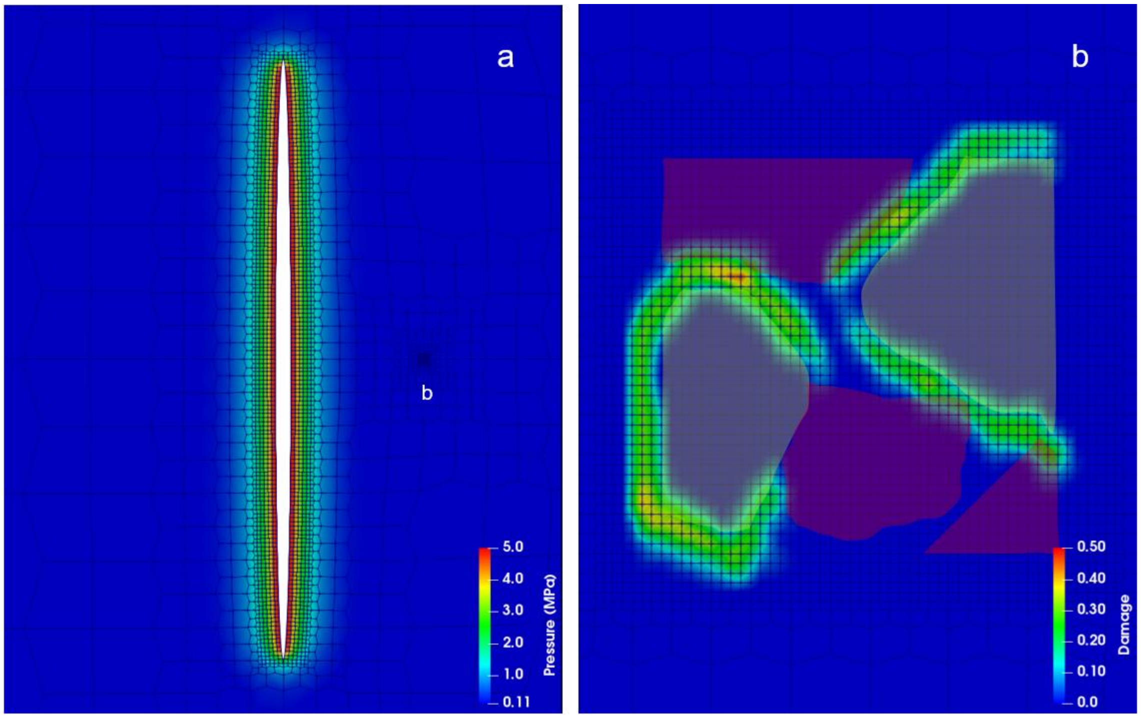

Figure 7.13. Base case, time = 32 sec. (a) Fracture geometry and PD region, (b) Damage map in the PD region.

7.3.1.2. Multiple PD regions away from the fracture face

The domain in the base case is modified to include two PD regions, 2mm and 4mm away from the primary fracture, each comprising the same mineral heterogeneity as in the base case. The final fracture geometry remains unchanged from the base case, implying that the remote material damage does not affect the fracture propagation (Figure 7.14a). This is partly because we are not modeling the flow of the fracturing fluid from the primary tensile fracture (which is modeled with FVM) into the shear failure damage zones (which are modeled with PD). The final damage maps in the two PD regions are shown in Figure 7.14b-c. The 2mm distant region, b, undergoes significantly more damage than the 4mm distant region in the base case since it experiences higher stress changes due to its proximity to the propagating fracture. The damage in region b causes sufficient stress relaxation around it such that region c does not undergo any damage in this case.

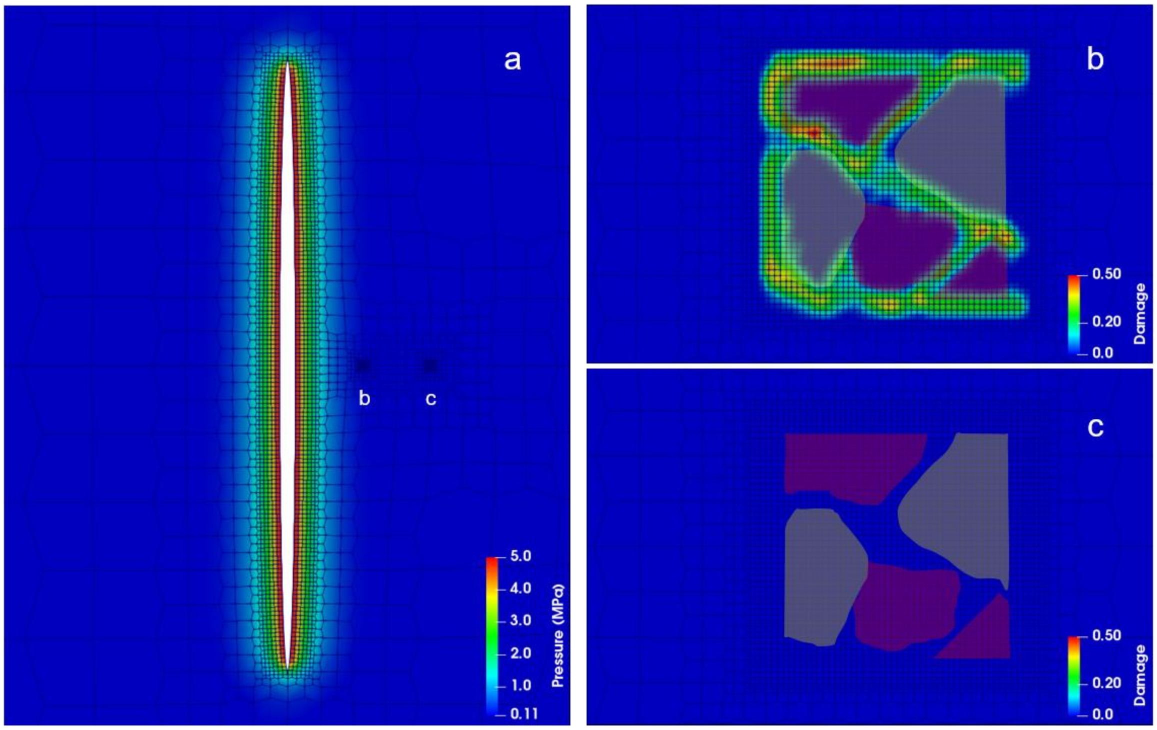

Figure 7.14. Multiple PD regions away from the fracture face, time = 32 sec. (a) Fracture geometry and PD regions, (b)-(c) Damage map in the PD regions.

7.3.1.3. Multiple PD regions along the fracture face

Next, another PD region, c, with mineral heterogeneity is added along the fracture face 2mm away from the PD region, b, in the base case. Figure 7.15 shows the fracture geometry and material damage in the two PD regions after 29.5 seconds of injection. The symmetrically located PD region, b, endures damage first and relaxes the stresses around it. However, in this case, the asymmetrically located PD region, c, experiences stress changes directly due to the propagating fracture. Thus, eventually region c also endures similar damage as region b (Figure 7.16).

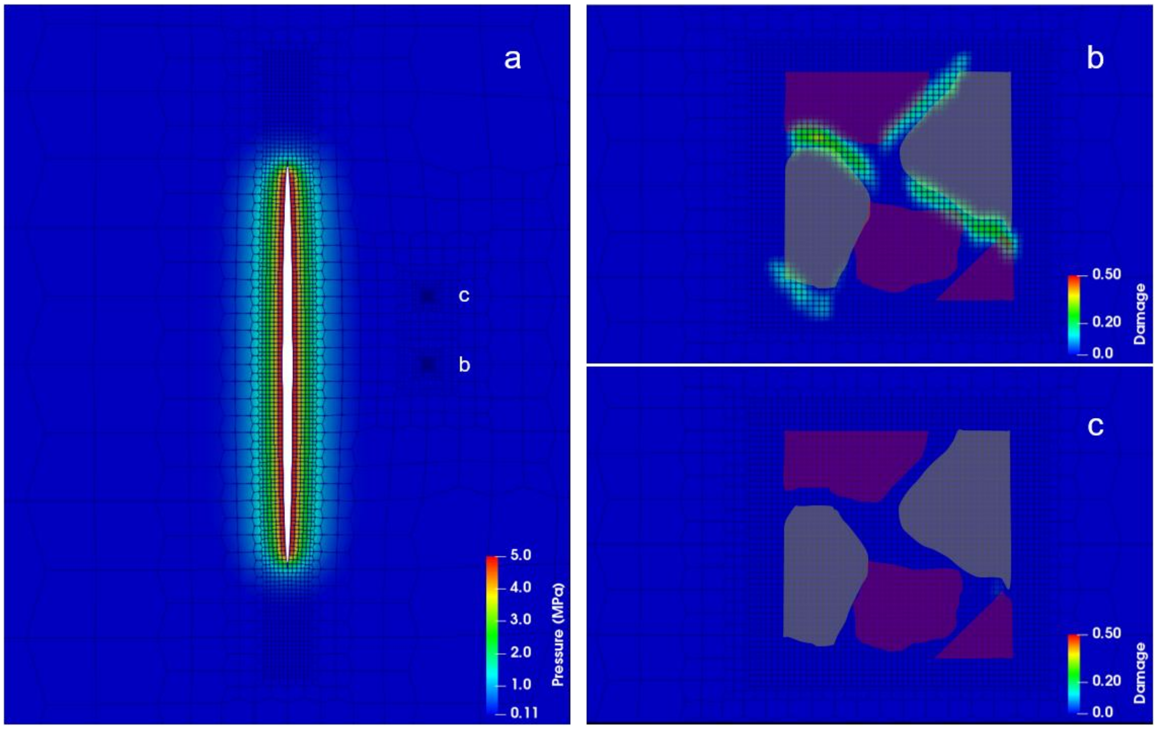

Figure 7.15. Multiple PD regions along the fracture face, time = 29.5 sec. (a) Fracture geometry and PD regions, (b)-(c) Damage map in the PD regions.

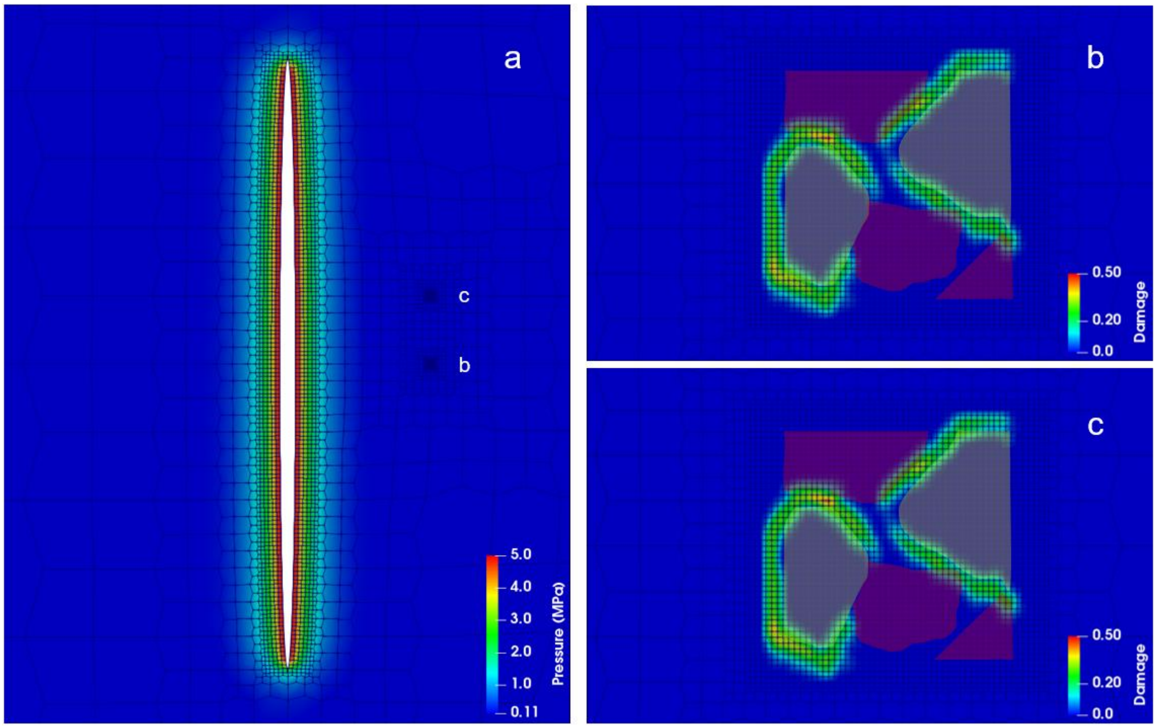

Figure 7.16. Multiple PD regions along the fracture face, time = 32 sec. (a) Fracture geometry and PD regions, (b)-(c) Damage map in the PD regions.

7.3.1.4. Estimating SRV extent using multiple PD regions away from the fracture face

Rocks are heterogeneous at all length scales. To accurately capture the material damage and the resulting stress relaxation due to a propagating fracture, multiple heterogeneous PD regions should be included around the fracture. The distance to which the material damage extends can be used as an estimate of the extent of the SRV. However, owing to the fine discretization within the PD regions, it is computationally expensive to use too many of these for this estimation. Thus, analyzing the damage maps in Cases 7.3.1.1 and 7.3.1.2, we learn that multiple PD regions should be used in the direction perpendicular to the fracture face. This is to ensure that we do not neglect or miscalculate the stress relaxation caused by the PD regions closer to the fracture on those farther away. Moreover, analyzing the damage maps in Cases 7.3.1.1 and 7.3.1.3, it is learnt that the PD regions along the fracture face experience stress changes directly due to the propagating fracture. Thus, it is concluded that different PD regions located equidistantly along the fracture face will endure similar damage profiles.

Four PD regions, at a distance of 1mm from each other comprising the same mineral heterogeneity, are considered for the SRV estimation. Figure 7.17a shows that the final fracture geometry is identical to those in the previous three cases. The maximum fracture width is 52 μm, which is in the range of experimental width of 40-70 μm observed by Ratzlaff et al. (2019). In Figure 7.17b, the damage maps follow the same trend (as in case 7.3.1.2) of progressively lesser damage farther away from the fracture. This is again because the farther PD regions feel the relaxed stresses due to damage in the closer regions, rather than the direct stress changes due to the primary fracture.

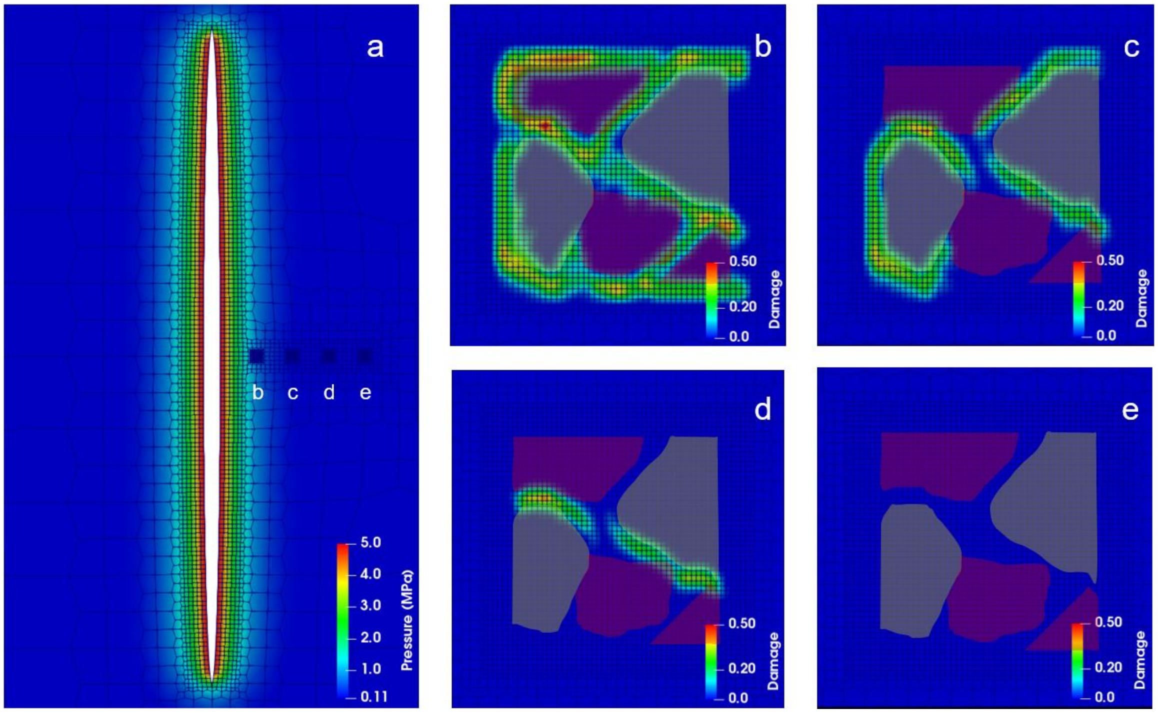

Figure 7.17. Estimation of SRV extent with multiple PD regions away from the fracture face. (a) Fracture geometry and PD regions, (b)-(e) Damage map in the PD regions.

In equation (7.6), we define the average damage in a PD region. Figure 7.18 shows a plot of average damage in the four PD regions against their distances from the fracture face. Since region d (3mm away) undergoes damage and region e (4mm away) does not, the SRV extent is estimated as 3.5mm. Although an overestimate compared to the experimental range of 2.1-2.4 mm, our SRV extent is useful for engineering applications.

$$\text{Average damage in a PD region}=\frac{\sum_{\text{all cells in the PD region}} \text{Damage in a cell}}{\text{Number of cells in the PD region}} \qquad (7.6)$$

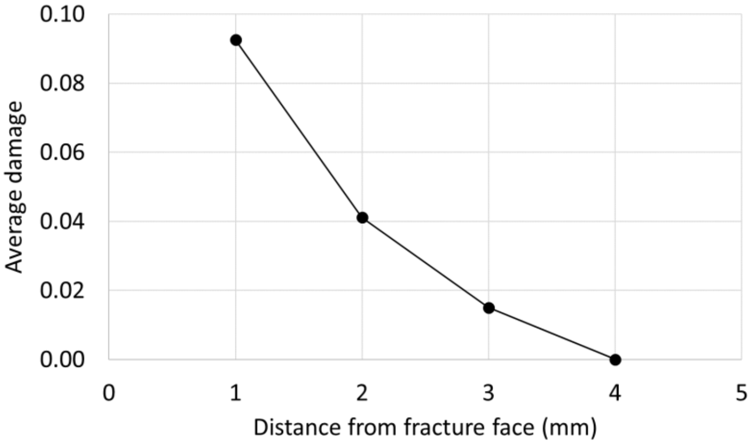

Figure 7.18. Average damage vs distance from the fracture face for the PD regions in Figure 7.17.

7.3.2. Estimating SRV extent in the field

We apply the above procedure to estimate the extent of SRV in unconventional reservoirs. This important parameter is typically obtained by analyzing the flow-back or early production data (Clarkson & Williams-Kovacs, 2013; Alkouh et al., 2014). The SRV is believed to be comprised of the shear failure micro-cracks formed during the stimulation, which get connected to the primary fracture and contribute to the flow of reservoir fluids. Thus, our workflow serves an independent tool for estimating the SRV extent and comparing it to that obtained from the flowback calculations.

7.3.2.1. Base case

A field-scale computational domain is discretized and solved using the coupled PD-FVM model (Figure 7.19). Except for the pore-scale heterogeneous regions like those in the previous cases which are solved with the PD method, all the cells are solved with the FVM. Multiple PD regions at intervals of 5ft are considered and material damage inside each is monitored. The mineral composition from the previous cases is used since it is representative of an unconventional formation, which is also mostly comprised of sedimentary rock. The other simulation parameters including the initial and boundary conditions, rock properties, and treatment design, typical of a fracturing job, are summarized in Table 7.5.

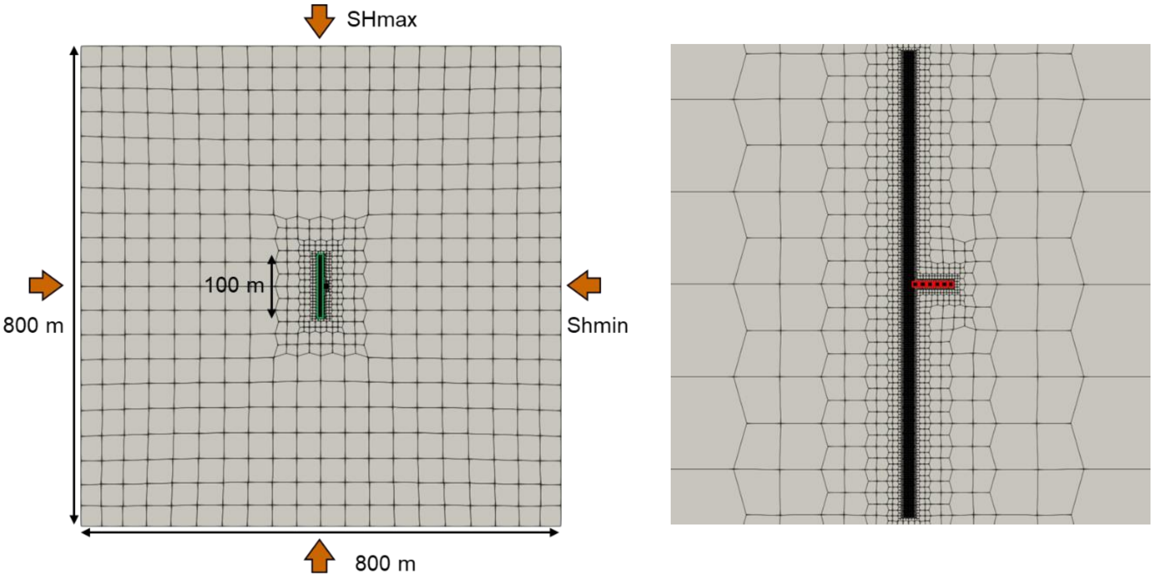

(a) (b)

Figure 7.19. Computational domain for SRV estimation in unconventional reservoirs. (a) Discretization, (b) Mineral heterogeneity in the PD subdomain

Table 7.5. Simulation parameters for the base case of SRV estimation in unconventional reservoirs

Boundary stress in x-direction, S_{hmin} (MPa)	48.0
Boundary stress in y-direction, S_{Hmax} (MPa)	52.0
Initial pore pressure, P_0 (MPa)	40.0
Bulk modulus, K (GPa)	15
Poisson ratio, v (GPa)	0.25
Porosity, φ	0.01
Permeability, k (nD)	500
Fracturing fluid injection rate, q (m^3/s)	0.0027
Fracturing fluid viscosity, μ_f (Pa s)	0.001
Treatment time (s)	60
Domain length in x-direction, L_x (m)	800
Domain length in y-direction, L_y (m)	800
Cell spacing in PD region, Δx (m)	4e-6
Horizon length, δ (m)	12e-6
Distance between the PD regions (m)	1.52

Figure 7.20 shows the fracture geometry and the resulting damage in the PD regions at the end of the treatment. The fracture length is 68.0m and the maximum width is 2.8mm. The PD regions endure gradually smaller damage with increasing distance from the fracture face. Figure 7.21 shows average damage in the PD regions plotted against their distances from the primary fracture. Region e and f (20ft and 25ft away) are the last damaged region and the first undamaged region respectively. Thus, the SRV extent is estimated to be 22.5ft in the base case.

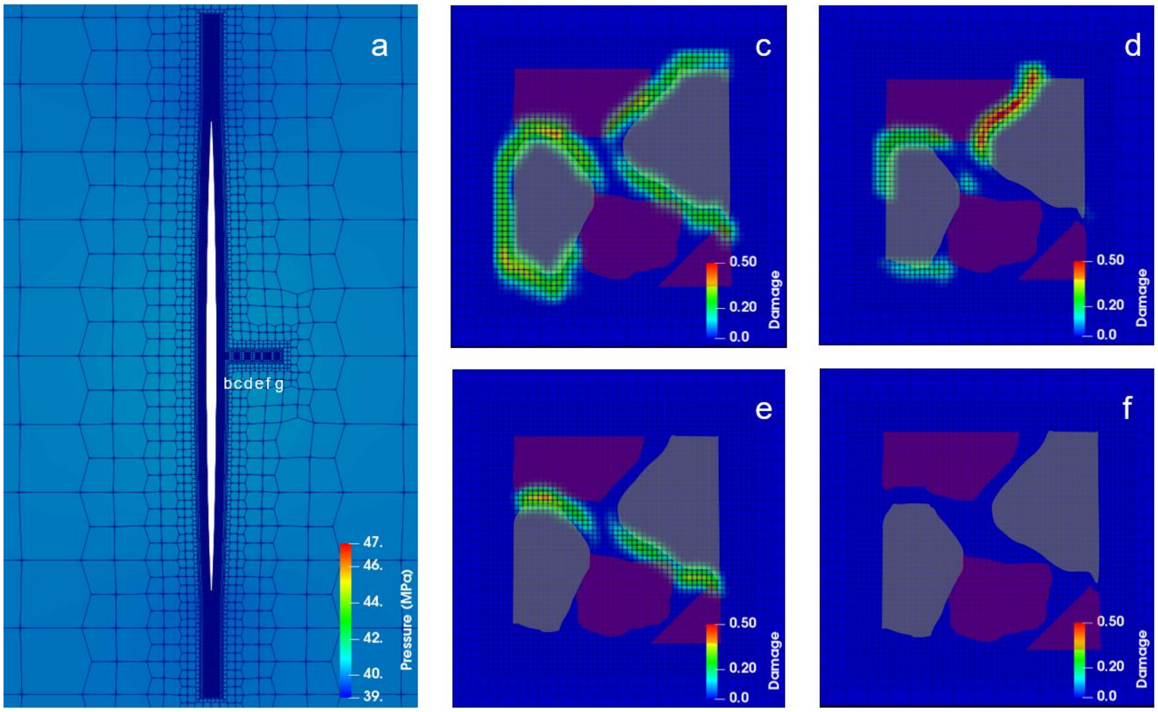

Figure 7.20. Base case. (a) Fracture geometry and PD regions, (c)-(f) Damage map in the PD regions.

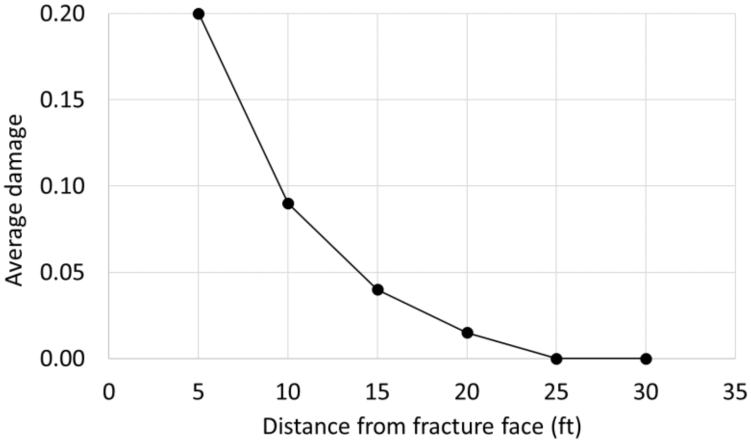

Figure 7.21. Average damage vs distance from the fracture face for the PD regions in the base case.

7.3.2.2. Sensitivity to Bulk modulus

Next, we investigate the sensitivity of the SRV extent to the bulk modulus of the formation. The bulk modulus is halved from 15 GPa in the base case to 7.5 GPa in this one.

Figure 7.22 shows that the resulting fracture is shorter and wider compared to the base case, following the analytical KGD solution (equations (7.2) and (7.3)). At the end of the treatment, the fracture length is 64.1m and the maximum width is 3.0mm. Referring to Figure 7.23, region f (25ft away) is the farthest one to endure damage at the grain boundaries, leading to an SRV estimate of 27.5ft when the bulk modulus of the formation is halved to 7.5 GPa.

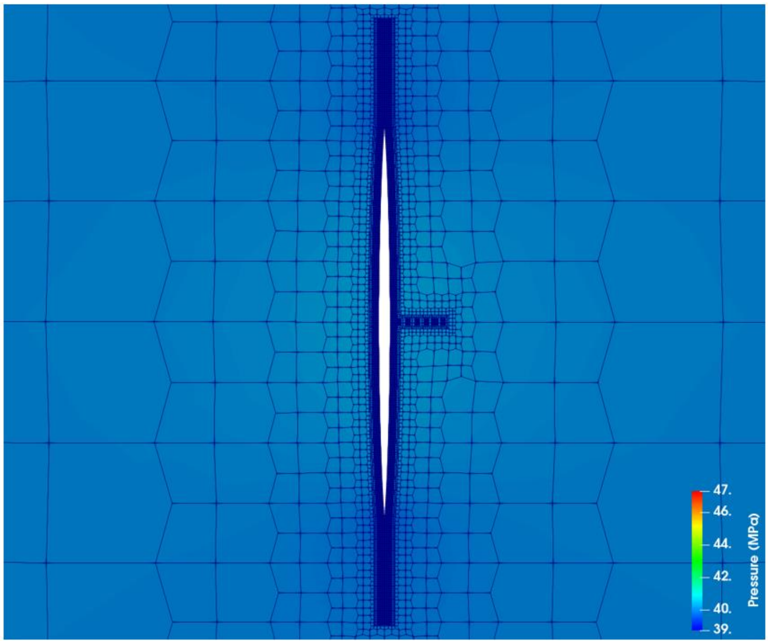

Figure 7.22. Fracture geometry when the formation bulk modulus is halved.

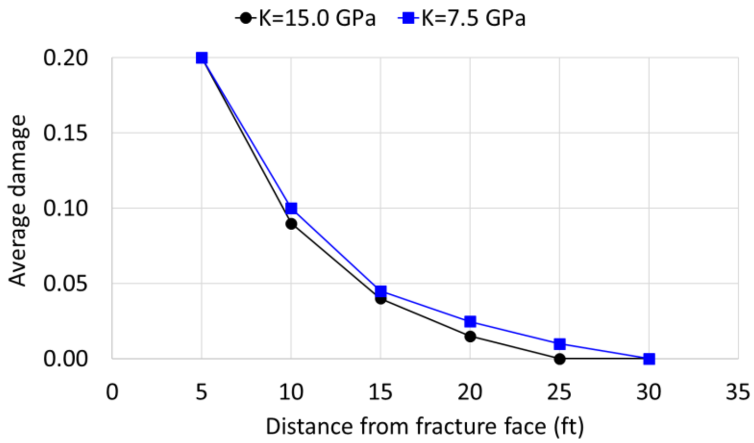

Figure 7.23. Average damage vs distance from the fracture face for the PD regions when the formation bulk modulus is halved. The base case results are plotted in black circles for comparison.

7.3.2.3. Sensitivity to injection rate

In this case, the injection rate is doubled from 1 bbl/min to 2 bbl/min. Consistent with the KGD solution, Figure 7.24 shows a longer and wider fracture than the base case, with the final fracture length and maximum width being 98.2m and 3.8mm respectively. Due to a longer and wider fracture, the stress changes travel deeper into the reservoir. Thus, region g (30ft away) also endures some non-zero damage (Figure 7.25), resulting in an SRV estimate of about 30ft.

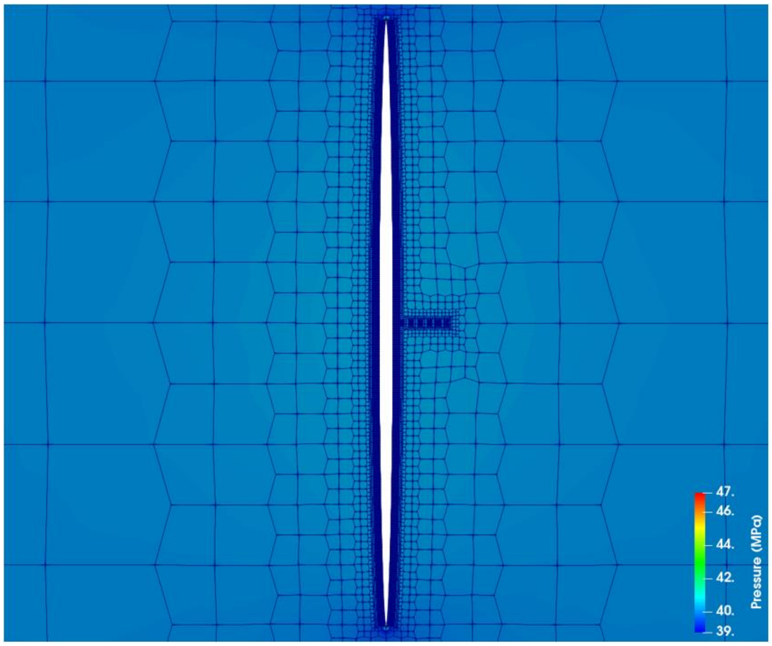

Figure 7.24. Fracture geometry when the injection rate is doubled.

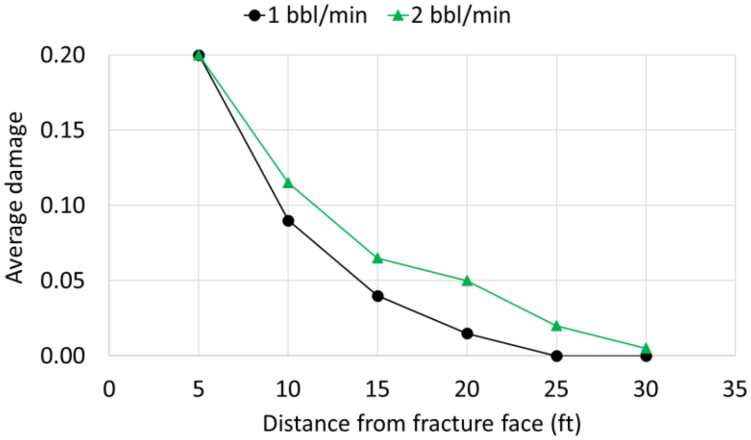

Figure 7.25. Average damage vs distance from the fracture face for the PD regions when the injection rate is doubled. The base case results are plotted in black circles for comparison.

7.3.2.4. Sensitivity to reservoir fluid type

The reservoir fluid is changed to a gas with 0.03 cP viscosity and ideal gas compressibility. A comparison between Figure 7.20 and Figure 7.26 shows that the fracture geometries are identical, irrespective of the reservoir fluid type. However, due to the much higher compressibility of gas than oil, changes in pore pressure and poroelastic stresses due to the propagating fracture are confined closer to it. Consequently, damage in the PD regions is more localized, leading to a smaller SRV of about 15ft (Figure 7.27).

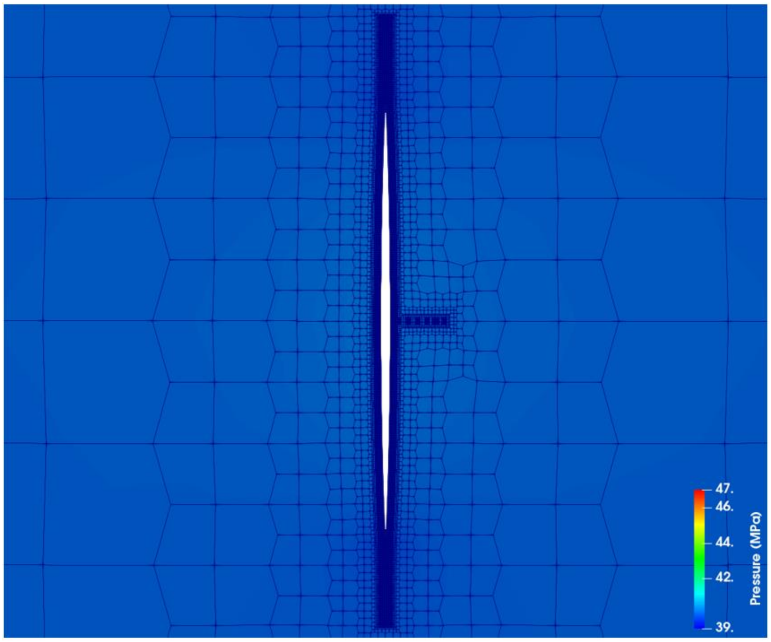

Figure 7.26. Fracture geometry in a gas reservoir.

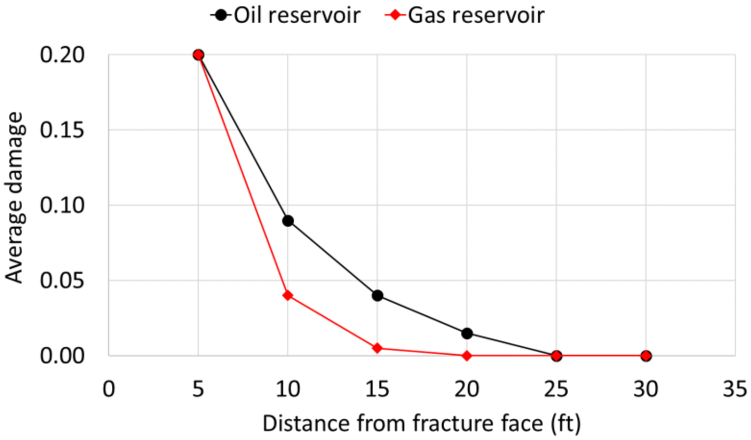

Figure 7.27. Average damage vs distance from the fracture face for the PD regions in a gas reservoir. The base case results are plotted in black circles for comparison.

Figure 7.28 shows a plot of process zone width against fault length, originally compiled by Zang & Stephansson (2010), for different geologic-scale and laboratory-scale faults detailed in the literature. As pointed out by Ratzlaff et al. (2019), these data were reported for faults in different stress regimes, which are not the same as the hydraulic fractures. However, for potential upscaling applications, we plot the estimates of SRV obtained from our coupled PD-FVM model for the various laboratory-scale and field-scale cases considered in this subsection. Our estimates lie close to the upper bound of the original regression line. It is clear from our data that the SRV around hydraulic fractures depends on several factors such as elastic properties of the rock, injection schedule, and reservoir fluid type. The first two parameters alter the SRV extent by directly affecting the fracture length, whereas the reservoir fluid type does it by affecting the poroelastic stresses around the primary fracture in a different manner.

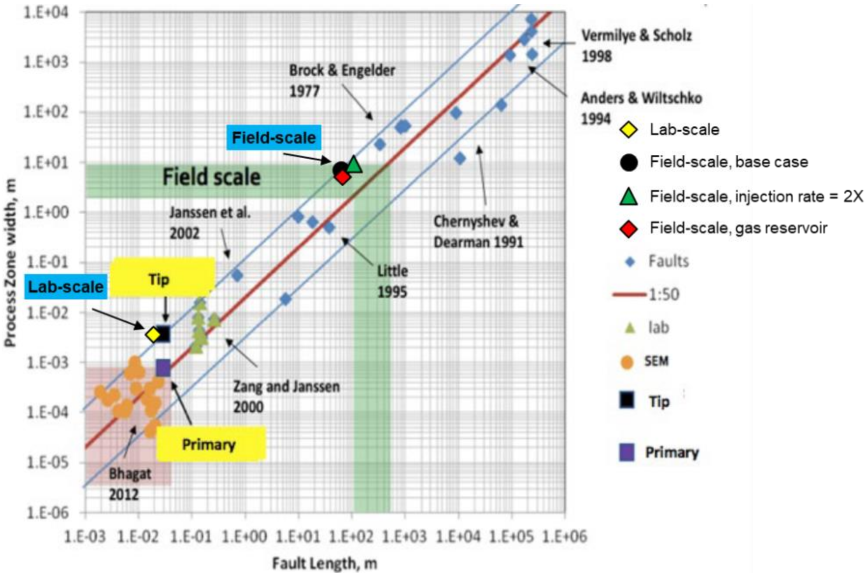

Figure 7.28. Upscaling plot with the SRV estimates from the coupled PD-FVM model (in blue highlight) and from the experiment (in yellow highlight) (Ratzlaff et al., 2019)

7.4. CONCLUSIONS

In this chapter, we extended the coupled poroelastic PD-FVM model developed in Chapter 6 for simulating hydraulic fracturing problems. A computational domain is divided into different subdomains that are solved with either PD or FVM formulations. The computationally expensive PD method is restricted to as few cells as possible. A well for injecting fracturing fluid can be assigned to either of the subdomains and fracture propagation can be simulated by the corresponding formulation.

Using our coupled model, we simulated a single KGD fracture in the PD subdomain. Two coupling methods, namely static PD region method and dynamic PD region method are presented. In the static method, a fixed number of cells are solved with PD, whereas in the dynamic method, the number of PD cells adaptively changes with the propagating hydraulic fracture. Compared to the pure PD method, an order of magnitude improvement in computational performance is achieved with the static method. An additional two-fold improvement is obtained with the dynamic method. Furthermore, these two methods are applied to simulate the interaction of a hydraulic fracture with a natural fracture. The interaction behaviors reported by Ouchi (2016) with a pure PD model are consistently reproduced with both the methods.

Subsequently, the growth of a planar fracture in the FV subdomain is simulated and the stress changes around it are monitored. Using PD subdomains with pore-scale heterogeneity, we demonstrate the capability of our coupled model to capture the material damage in the PD regions due to stress changes caused by the propagating fracture. Multiple PD regions are used to reasonably account for stress relaxation in the regions farther from the fracture due to material damage in the ones closer to the fracture. This approach is then extended to estimate the extent of the Stimulated Reservoir Volume (SRV). The estimation approach is validated against recent laboratory experiments in

Tennessee sandstone and a good agreement is obtained. Then, we estimated the SRV extent in an unconventional oil and gas formation, with representative reservoir properties and treatment schedules. A sensitivity study with a few key parameters is performed. SRV extent is shown to increase with lower elastic modulus of the rock and with higher injection rates. In a gas reservoir, due to high fluid compressibility, the stress changes are more localized near the fracture. Thus, the SRV extent is considerably smaller than in an oil reservoir with everything else remaining the same.

We have shown that our coupled PD-FVM model has significant computational benefits compared to a pure PD model, and that it can be a useful tool for developing better insights for new applications such as estimation of the SRV extent around a propagating hydraulic fracture.

The workflow developed for estimating the SRV extent in this chapter is based on the analysis of remote material damage caused by the poroelastic stress changes due to a propagating hydraulic fracture. Although the trends in our 2-D analyses were not affected by the mineralogy in the PD regions, the damage profile maybe different in 3-D due to the packing of the mineral grains (for example, some mineral grains that are disconnected in 2-D might be connected in 3-D). Moreover, difference in damage profiles may also arise from the difference in stress profiles. As discussed in Section 4.6.4, the stress profile generated by a plane-strain fracture maybe different than that generated by a 3-D fracture. Thus, there is a motivation to conduct the material damage simulations in 3-D to compare with the results presented in this chapter.

CHAPTER 8: CONCLUSIONS AND FUTURE WORK

8.1. SUMMARY AND CONCLUSIONS

The main objectives of this research were to extend the capabilities of our existing peridynamics-based hydraulic fracturing model developed by Ouchi (2016) to multi-phase flow and improve its computational performance by coupling it with the less expensive Finite Volume Method (FVM).

We developed a peridynamics (PD) multiphase, multicomponent flow model for non-Newtonian, compressible fluids by generalizing our previous single-phase flow model for Newtonian, slightly compressible fluids. We use this general flow model with a fracture propagation model to simulate fracture propagation in depleted reservoirs. We investigated the interaction of a hydraulic fracture with a natural fracture and developed numerical crossing criteria accounting for remote shear failure and poroelasticity. Finally, we developed a coupled PD-FVM fracturing simulator by combining our PD model with the FVM. We show good agreement of model results against laboratory experiments and demonstrated significant improvements in computational performance compared to the pure PD model. Finally, we presented a novel application of the coupled simulator for estimating the extent of the Stimulated Reservoir Volume (SRV) around a primary hydraulic fracture.

The following are the conclusions from each of the chapters.

8.1.1. General Peridynamics Flow Model

a) The state-based peridynamic formulation for single phase transport of Newtonian, slightly, compressible fluids is extended to multiphase, multicomponent transport of non-Newtonian, compressible fluids.

b) Due to the computational costs associated with a compositional model, only results from the less expensive models such as black-oil and immiscible two-phase flow models are presented.

c) Applications of the multiphase model for solving 1-D linear, immiscible displacement of oil by water (water flood) and by a shear-thinning polymer (polymer flood) are demonstrated.

d) A δ-m convergence study is performed to recover the analytical local solution from the numerical non-local solution by shrinking the horizon size (δ) and increasing the number of non-local neighbors (m) simultaneously.

e) Convergence of oil recovery plots to the analytical local solution verifies overall mass conservation in the proposed non-local model.

8.1.2. Immiscible Two-Phase Peridynamics Hydraulic Fracturing Model

a) An immiscible two-phase peridynamics-based hydraulic fracturing simulator is presented by combining the generalized flow model developed in Chapter 2 with our existing single-phase fracturing simulator.

b) The simulation results are compared with laboratory experiments performed under low confining stresses. The effect of induced changes in pore pressure (using multiple injection sources) on fracture growth is investigated in detail.

c) Fractures initiating from multiple injection points can grow towards each other by opening against the maximum stress.

d) Saturating a specimen with fluid prior to fracturing can significantly lower the breakdown pressure.

e) In low stress environments in the laboratory, fractures are always attracted towards the high pore pressure region. The strength of this attraction depends on both the magnitude of the pore pressure and the pressure gradients.

f) All these results are in agreement with the effective stress law.

8.1.3. Applications of the Immiscible Two-Phase Peridynamics Hydraulic Fracturing Model

a) Under high confining stresses found in the field, pressure depletion and stress reorientation around multiple fractures of a parent well are investigated. Fracture growth from a child well in this non-uniform pressure field is simulated.

b) Hydrocarbon production from parent well fractures leads to the formation of a region of lower compressive stress between them. This effect is less pronounced in gas reservoirs (due to the high compressibility of the gas) and increases as the pressure drawdown and the volume of fluids produced is increased.

c) The spatial extent of the region of altered stress is much larger than the region in which the pore pressure is reduced.

d) The lower compressive stress region formed between the parent well fractures attracts the child well fractures. This attraction directly correlates with the magnitude of the stress reduction.

e) Preferential fracture growth towards depleted regions results in under-stimulation of the undepleted parts of the reservoir.

f) Re-pressurizing the parent well fractures reorients the stresses back, close to the in-situ stress state. This reduces the attraction of the child well fracture towards the depleted regions, thus leading to better stimulation of the reservoir.

8.1.4. Interaction between a Hydraulic Fracture and a Natural Fracture

a) A propagating hydraulic fracture causes poroelastic stress changes, which may lead to remote shear failure of a natural fracture.

b) The shear failure relaxes the stress on the natural fracture, inviting the hydraulic fracture to bend towards it before intersection as observed in recent laboratory experiments.

c) The bending of the hydraulic fracture depends on the stress relaxation relative to the initial stresses caused by the failure of the natural fracture. Though these effects are significant even in low permeability rocks (100 nD), they are more pronounced in high permeability rocks (10 mD).

d) When the effects of poroelasticity and remote shear failure of the natural fracture are ignored, the LEFM-based analytical crossing criteria are recovered. However, when these effects are accounted, the fracture interaction behavior is substantially different.

e) For low matrix permeabilities, the poroelastic criteria predict more fracture turning at stress ratios commonly occurring in shale formations (1.0-1.1). For high matrix permeabilities, these criteria predict more fracture turning even at moderate stress ratios (1.0-1.2).

f) Poroelastic crossing criteria are developed for widely different matrix permeabilities and can serve as direct inputs to discrete fracture models simulating the growth of complex fracture networks.

8.1.5. Coupling of Peridynamics Poroelastic Model with Finite Volume Method

a) Based on the Peridynamic and Finite Element coupling scheme proposed by Galvanetto et al. (2016), we have presented a coupled Peridynamic (PD) and Finite Volume (FVM) poroelastic model for multiscale problems in porous media.

b) We have developed the formulation for porous fluid flow using a fluid mass balance, and have extended it for poroelastic problems to include a rock momentum balance.

c) Significant improvements in computational performance of the coupled model over the pure peridynamic model are illustrated for several model problems.

d) No spurious behavior is observed near the PD-FVM interface region.

e) Moreover, due to differences in the sparsity patterns and the magnitudes of PD and FVM transmissibility/Jacobian terms, it is shown that appending the PD equations after all the FV equations in the global matrix has additional computational benefits.

8.1.6. Fracturing Applications of the Coupled Peridynamic–Finite Volume Model

a) The coupled poroelastic PD-FVM model developed in Chapter 6 is extended for simulating hydraulic fracturing problems.

b) A computational domain is divided into different subdomains that are solved with either PD or FVM formulations. The computationally expensive PD method is restricted to as few cells as possible.

c) A well for injecting fracturing fluid can be assigned to either of the subdomains and fracture propagation can be simulated by the corresponding formulation.

d) Using our coupled model, we simulated a single KGD fracture in the PD subdomain. Two coupling methods, namely static PD region method and dynamic PD region method are presented.

e) In the static method, a fixed number of cells are solved with PD, whereas in the dynamic method, the number of PD cells adaptively changes with the propagating hydraulic fracture.

f) Compared to the pure PD method, an order of magnitude improvement in computational performance is achieved with the static method. An additional two-fold improvement is obtained with the dynamic method.

g) Both the methods consistently reproduce the interaction of a hydraulic fracture with a natural fracture as reported by Ouchi (2016).

h) The growth of a planar fracture in the FV subdomain is simulated and the stress changes around it are monitored.

i) Using PD subdomains with pore-scale heterogeneity, we demonstrate the capability of our coupled model to capture the material damage in the PD regions due to stress changes caused by the propagating fracture.

j) Multiple PD regions are used to reasonably account for stress relaxation in the regions farther from the fracture due to material damage in the ones closer to the fracture. This approach is then extended to estimate the extent of the Stimulated Reservoir Volume (SRV).

k) The SRV estimation approach is validated against recent laboratory experiments in Tennessee sandstone and a good agreement is obtained.

l) We estimated the SRV extent in an unconventional oil and gas formation, with representative reservoir properties and treatment schedules.

m) SRV extent is shown to increase with lower elastic modulus of the rock and with higher injection rates.

n) In a gas reservoir, due to high fluid compressibility, the stress changes are more localized near the fracture. Thus, the SRV extent is considerably smaller than in an oil reservoir with everything else remaining the same.

8.2. FUTURE WORK

The avenues for improvement of the current hydraulic fracturing model are summarized below.

a) The computational performance of the coupled Peridynamics (PD)–Finite Volume (FVM) fracturing simulator can be improved further by introducing adaptive mesh refinement in the dynamic PD region method (York, 2018).

b) Moreover, computational performance of the coupled model can be improved by orders of magnitude by using the modern HPC techniques. Both the PD-based and FV-based fracturing simulators can run on multiple processors using the domain decomposition method. However, efficient ways of load balancing the coupled PD-FVM simulator should be developed.

c) The SRV permeability can be estimated using the coupled model by introducing a method to model the fracturing fluid leak-off from the FV subdomain to the PD subdomain.

d) A local flow model for proppant transport can be implemented in the PD code. An additional scalar transport equation for the proppant transport would be solved inside the fracture. Two-way coupling between the fracturing fluid equation and the proppant transport equation would be implemented.

e) By simulating fracture growth in 3-D using the coupled model, proppant transport in complex non-planar geometries can be investigated.

References

Aarnes, Jørg E., Tore Gimse, and Knut-Andreas Lie. 2007. "An Introduction to the Numerics of Flow in Porous Media Using Matlab." In *Geometric Modelling, Numerical Simulation, and Optimization: Applied Mathematics at SINTEF*, Springer Berlin Heidelberg, 265–306.

Abé, H, T Mura, and L M Keer. 1976. "Growth Rate of a Penny-Shaped Crack in Hydraulic Fracturing of Rocks." *Journal of Geophysical Research (1896-1977)* 81(29): 5335–40. https://doi.org/10.1029/JB081i029p05335.

Adachi, J, E Siebrits, A Peirce, and J Desroches. 2007. "Computer Simulation of Hydraulic Fractures." *International Journal of Rock Mechanics and Mining Sciences* 44(5): 739–57. http://www.sciencedirect.com/science/article/pii/S1365160906001870.

Agrawal, Shivam, Hisanao Ouchi, Murtadha J. AlTammar, and Mukul M. Sharma. 2018. "Mechanistic Explanation of the Impact of Pore Pressure on Hydraulic Fracture Propagation." In *52nd US Rock Mechanics / Geomechanics Symposium*,.

Agrawal, Shivam, and Mukul M. Sharma. 2018. "Impact of Pore Pressure Depletion on Stress Reorientation and Its Implications on the Growth of Child Well Fractures." In *6th Unconventional Resources Technology Conference*,.

Agwai, A, I Guven, and E Madenci. 2009. "Damage Prediction for Electronic Package Drop Test Using Finite Element Method and Peridynamic Theory." In *2009 59th Electronic Components and Technology Conference*, , 565–69.

Aimene, Yamina E., and Ahmed Ouenes. 2015. "Geomechanical Modeling of Hydraulic Fractures Interacting with Natural Fractures — Validation with Microseismic and Tracer Data from the Marcellus and Eagle Ford." *Interpretation* 3(3): SU71-SU88. http://library.seg.org/doi/10.1190/INT-2014-0274.1.

Aimene, Yamina, Chad Hammerquist, John A Nairn, and Ahmed Ouenes. 2018. "3D Anisotropic Damage Mechanics for Modeling Interaction Between Hydraulic and Natural Fracture Planes in a Layered Rock - Application to Eagle Ford and Wolfcamp." *SPE/AAPG/SEG Unconventional Resources Technology Conference*.

Ajisafe, Foluke O., Efe Ejofodomi, and Matteo Marongiu Porcu. 2017. "Understanding Impact of Well Spacing and Interference on Production Performance in Unconventional Reservoirs, Permian Basin." *Proceedings of the 5th Unconventional Resources Technology Conference*. http://archives.datapages.com/data/doi/10.15530/urtec-2017-2690466.

Alkouh, Ahmad, Steven McKetta, and Robert A. Wattenbarger. 2014. "Estimation of Effective-Fracture Volume Using Water-Flowback and Production Data for Shale-Gas Wells." *Journal of Canadian Petroleum Technology* 53(5): 290–303.

AlTammar, M.J., M.M. Sharma, and R. Manchanda. 2018. "The Effect of Pore Pressure on Hydraulic Fracture Growth: An Experimental Study." *in preparation*.

AlTammar, Murtadha J, Shivam Agrawal, and Mukul M Sharma. 2019. "Effect of Geological Layer Properties on Hydraulic Fracture Initiation and Propagation: An Experimental Study." *SPE Journal* (Accepted): SPE-184871-PA.

Ansari, R. Z., and R. T. Johns. 2006. "Steady-State Coning Solutions with Multiple Wells and Reservoir Boundaries." *Proceedings - SPE Symposium on Improved Oil Recovery* 2: 866–75.

Atkinson, Barry Kean, and Philip George Meredith. 1987. "11 - EXPERIMENTAL FRACTURE MECHANICS DATA FOR ROCKS AND MINERALS." In ed. BARRY KEAN B T - Fracture Mechanics of Rock ATKINSON. London: Academic Press, 477–525. http://www.sciencedirect.com/science/article/pii/B9780120662661500168.

Bahorich, Ben, Jon Edward Olson, and Jon Holder. 2012. "Examining the Effect of Cemented Natural Fractures on Hydraulic Fracture Propagation in Hydrostone Block Experiments." *SPE Annual Technical Conference and Exhibition*. http://www.onepetro.org/doi/10.2118/160197-MS.

Barree, R D. 1983. "A Practical Numerical Simulator for Three-Dimensional Fracture Propagation in Heterogeneous Media." *SPE Reservoir Simulation Symposium*: 12.

Berchenko, I, and E Detournay. 1997. "Deviation of Hydraulic Fractures through Poroelastic Stress Changes Induced by Fluid Injection and Pumping." *International Journal of Rock Mechanics and Mining Sciences* 34(6): 1009–19. http://www.sciencedirect.com/science/article/pii/S136516099780010X.

Bobaru, Florin et al. 2009. "Convergence , Adaptive Refinement , and Scaling in 1D Peridynamics." *International Journal for Numerical Methods in Engineering* (August 2008): 852–77.

Bobaru, Florin, and Monchai Duangpanya. 2010. "The Peridynamic Formulation for Transient Heat Conduction." *International Journal of Heat and Mass Transfer* 53(19–20): 4047–59. http://dx.doi.org/10.1016/j.ijheatmasstransfer.2010.05.024.

Bobaru, Florin, and Youn Doh Ha. 2011. "Adaptive Refinement and Multiscale Modeling in 2D Peridynamics." *International Journal for Multiscale Computational Engineering* 9(6): 635–60.

Brooks, R H, and a T Corey. 1964. "Hydraulic Properties of Porous Media." *Hydrology Papers, Colorado State University. Fort Collins CO* 3(3): 27 pgs.

Bruno, M.S., and F.M. Nakagawa. 1991. "Pore Pressure Influence on Tensile Fracture Propagation in Sedimentary Rock." *International Journal of Rock Mechanics and Mining Sciences & Geomechanics Abstracts* 28(4): 261–73. http://linkinghub.elsevier.com/retrieve/pii/014890629190593B.

Buckley, S E, and M C Leverett. 1942. "Mechanism of Fluid Displacement in Sands." *Transactions of the AIME* 146: 107–16.

Cardiff, P., Tuković, H. Jasak, and A. Ivanković. 2016. "A Block-Coupled Finite Volume Methodology for Linear Elasticity and Unstructured Meshes." *Computers and Structures* 175: 100–122.

Chavent, G., and J. Jaffre. 1986. *Mathematical Models and Finite Elements for Reservoir Simulation*. Elsevier.

Chen, Zhangxin, Guanren Huan, and Yuanle Ma. 2006. *Computational Methods for Multiphase Flows in Porous Media*. Society for Industrial and Applied Mathematics.

Chuprakov, Dmitry A, Anna V Akulich, Eduard Siebrits, and Marc Thiercelin. 2011. "Hydraulic-Fracture Propagation in a Naturally Fractured Reservoir." *SPE*

Production & Operations 26(1): 88–97.

Clarkson, C. R., and J. D. Williams-Kovacs. 2013. “Modeling Two-Phase Flowback of Multifractured Horizontal Wells Completed in Shale.” *SPE Journal* 18(4): 795–812.

Cleary, M P, Michael Kavvadas, and K Y Lam. 1983. “Development of a Fully Three-Dimensional Simulator for Analysis and Design of Hydraulic Fracturing.” *SPE/DOE Low Permeability Gas Reservoirs Symposium*: 12. https://doi.org/10.2118/11631-MS.

Clifton, Rodney J, and Ahmed S Abou-Sayed. 1981. “A Variational Approach To The Prediction Of The Three-Dimensional Geometry Of Hydraulic Fractures.” *SPE/DOE Low Permeability Gas Reservoirs Symposium*: 9.

Coats, K H, L K Thomas, and R G Pierson. 1998. “Compositional and Black Oil Reservoir Simulation.” *SPE Reservoir Evaluation & Engineering* 1(04): 372–79.

Cooke, Michele L., and Chad A. Underwood. 2001. “Fracture Termination and Step-over at Bedding Interfaces Due to Frictional Slip and Interface Opening.” *Journal of Structural Geology* 23(2–3): 223–38.

Cortis, Andrea, and Brian Berkowitz. 2004. “Anomalous Transport in ‘Classical’ Soil and Sand Columns.” *Soil Science Society of America Journal* 68(5): 1539.

Courtier, James et al. 2016. “Legacy Well Protection Refrac Mitigates Offset Well Completion Communications in Joint Industry Project.” *SPE Liquids-Rich Basins Conference - North America*. http://www.onepetro.org/doi/10.2118/181767-MS.

Coussy, O. 2004. John Wiley & Sons *Poromechanics*. http://onlinelibrary.wiley.com/doi/10.1002/cbdv.200490137/abstract.

Dahi-Taleghani, Arash, and Jon E Olson. 2011. “Numerical Modeling of Multistranded-Hydraulic-Fracture Propagation: Accounting for the Interaction Between Induced and Natural Fractures.” *SPE Journal* 16(03): 575–81. https://doi.org/10.2118/124884-PA.

Dahi Taleghani, Arash, and Jon E. Olson. 2013. “How Natural Fractures Could Affect Hydraulic-Fracture Geometry.” *SPE Journal* 19(01): 161–71. http://www.onepetro.org/doi/10.2118/167608-PA.

Damani, Akash, Abhishek Sharma, Carl H. Sondergeld, and Chandra Shekhar Rai. 2012. “Mapping of Hydraulic Fractures under Triaxial Stress Conditions in Laboratory Experiments Using Acoustic Emissions.” *SPE Annual Technical Conference and Exhibition*: 1–12. http://www.onepetro.org/doi/10.2118/159604-MS.

Detournay, E., and Alexander H.D. Cheng. 1993. “Fundamentals of Poroelasticity.” *Analysis and Design Methods* II: 113–71.

Fisher, M.K. et al. 2004. “Optimizing Horizontal Completion Techniques in the Barnett Shale Using Microseismic Fracture Mapping.” *SPE Annual Technical Conference and Exhibition*.

Foster, J. T., S. A. Silling, and W. Chen. 2011. “An Energy Based Failure Criterion for Use with Peridynamic States.” *International Journal for Multiscale Computational Engineering* 9(6): 675–87.

Foster, J T, S A Silling, and W W Chen. 2010. “Viscoplasticity Using Peridynamics.” *International Journal for Numerical Methods in Engineering* 81(10): 1242–58.

https://doi.org/10.1002/nme.2725.

Fung, R L, S Vilayakumar, and Donald E Cormack. 1987. “Calculation of Vertical Fracture Containment in Layered Formations.” *SPE Formation Evaluation* 2(04): 518–22. https://doi.org/10.2118/14707-PA.

Gale, Julia F. W., Sara J. Elliott, and Stephen E. Laubach. 2018. “Hydraulic Fractures in Core From Stimulated Reservoirs: Core Fracture Description of HFTS Slant Core, Midland Basin, West Texas.” *Proceedings of the 6th Unconventional Resources Technology Conference* (1993). http://archives.datapages.com/data/doi/10.15530/urtec-2018-2902624.

Gale, Julia F.W., Robert M. Reed, and Jon Holder. 2007. “Natural Fractures in the Barnett Shale and Their Importance for Hydraulic Fracture Treatments.” *AAPG Bulletin* 91(4): 603–22.

Galvanetto, Ugo, Teo Mudric, Arman Shojaei, and Mirco Zaccariotto. 2016. “An Effective Way to Couple FEM Meshes and Peridynamics Grids for the Solution of Static Equilibrium Problems.” *Mechanics Research Communications* 76: 41–47. http://dx.doi.org/10.1016/j.mechrescom.2016.06.006.

Ganti, Vamsi et al. 2010. “Normal and Anomalous Diffusion of Gravel Tracer Particles in Rivers.” *Journal of Geophysical Research* 115: 1–12.

Geertsma, J, and F De Klerk. 1969. “A Rapid Method of Predicting Width and Extent of Hydraulically Induced Fractures.” *Journal of Petroleum Technology* 21(12): 1571–81. https://doi.org/10.2118/2458-PA.

Gu, H., and X. Weng. 2010. “Criterion for Fractures Crossing Frictional Interfaces at Non-Orthogonal Angles.” *44th US Rock Mechanics Symposium and 5th U.S.-Canada Rock Mechanics Symposium, 27-30 June, Salt Lake City*: 1–6.

Gu, Hongren et al. 2012. “Hydraulic Fracture Crossing Natural Fracture at Nonorthogonal Angles: A Criterion and Its Validation.” *SPE Production & Operations* 27(01): 20–26. http://www.onepetro.org/doi/10.2118/139984-PA.

Gupta, J.K. et al. 2012. “Integrated Methodology for Optimizing Development of Unconventional Gas Resources.” *SPE Hydraulic Fracturing Technology Conference*.

Ha, Youn Doh, and Florin Bobaru. 2010. “Studies of Dynamic Crack Propagation and Crack Branching with Peridynamics.” *International Journal of Fracture* 162(1–2): 229–44.

Haddad, Mahdi, and Kamy Sepehrnoori. 2016. “XFEM-Based CZM for the Simulation of 3D Multiple-Cluster Hydraulic Fracturing in Quasi-Brittle Shale Formations.” *Rock Mechanics and Rock Engineering* 49(12): 4731–48. https://doi.org/10.1007/s00603-016-1057-2.

Hubbert, Mk, and Dg Willis. 1957. “Mechanics of Hydraulic Fracturing.” *Journal for Petroleum Technology* 9(6): 153–66. http://archives.datapages.com/data/specpubs/methodo2/data/a075/a075/0001/0200/0239.htm.

Jaeger, J.C., and N.G.W. Cook. 1976. *Fundamentals of Rock Mechanics*. New York: Wiley.

Katiyar, Amit et al. 2019. "A General Peridynamics Model for Multiphase Transport of Non-Newtonian Compressible Fluids in Porous Media." *under review*.

Katiyar, Amit, John T. Foster, Hisanao Ouchi, and Mukul M. Sharma. 2014. "A Peridynamic Formulation of Pressure Driven Convective Fluid Transport in Porous Media." *Journal of Computational Physics* 261: 209–29. http://dx.doi.org/10.1016/j.jcp.2013.12.039.

Khristianovic, S A, and Y P Zheltov. 1955. "3. Formation of Vertical Fractures by Means of Highly Viscous Liquid." *4th World Petroleum Congress*: 8. https://doi.org/.

Kilic, Bahattin, and Erdogan Madenci. 2010. "Coupling of Peridynamic Theory and the Finite Element Method." *Journal of Mechanics of Materials and Structures* 5(5): 707–33.

Koch, D.L.; Brady, J.F. 1988. "Anomalous Diffusion in Heterogeneous Porous Media." *Physics of Fluids* 31(5): 965.

Kumar, Ashish et al. 2018. "Well Interference Diagnosis through Integrated Analysis of Tracer and Pressure Interference Tests." *Proceedings of the 6th Unconventional Resources Technology Conference*. http://archives.datapages.com/data/doi/10.15530/urtec-2018-2901827.

Liu, He et al. 2008. "Evaluation of Refracture Reorientation in Both Laboratory and Field Scales." *SPE International Symposium and Exhibition on Formation Damage Control*. http://www.onepetro.org/doi/10.2118/112445-MS.

Liu, Wenyang, and Jung Wuk Hong. 2012. "A Coupling Approach of Discretized Peridynamics with Finite Element Method." *Computer Methods in Applied Mechanics and Engineering* 245–246: 163–75. http://dx.doi.org/10.1016/j.cma.2012.07.006.

Lubineau, Gilles et al. 2012. "A Morphing Strategy to Couple Non-Local to Local Continuum Mechanics." *Journal of the Mechanics and Physics of Solids* 60(6): 1088–1102. http://dx.doi.org/10.1016/j.jmps.2012.02.009.

Macek, Richard W., and Stewart A. Silling. 2007. "Peridynamics via Finite Element Analysis." *Finite Elements in Analysis and Design* 43(15): 1169–78.

Manchanda, Ripudaman. 2015. "A General Poro-Elastic Model for Pad-Scale Fracturing of Horizontal Wells."

Manchanda, Ripudaman, Prateek Bhardwaj, Jongsoo Hwang, and Mukul M. Sharma. 2018. "Parent-Child Fracture Interference: Explanation and Mitigation of Child Well Underperformance." *SPE Hydraulic Fracturing Technology Conference and Exhibition*. http://www.onepetro.org/doi/10.2118/189849-MS.

Matthew Miller, Clint. 2010. "Adhesion and the Surface Energy Components of Natural." Texas A&M University. http://oaktrust.library.tamu.edu/bitstream/handle/1969.1/ETD-TAMU-2010-08-8237/MILLER-THESIS.pdf?sequence=3. 04/16/2018.

Mavko, Gary, Tapan Mukerji, and Jack Dvorkin. 2009. *The Rock Physics Handbook: Tools for Seismic Analysis of Porous Media*. 2nd ed. Cambridge: Cambridge University Press. https://www.cambridge.org/core/books/rock-physics-handbook/A53F53ADFDD5D72EF01A9E4C6E9454A7.

Mayerhofer, M. J. et al. 2010. “What Is Stimulated Reservoir Volume?” *SPE Production and Operations* 25(1): 89–98.

McClure, Mark William. 2012. “Modeling and Characterization of Hydraulic Stimulation and Induced Seismicity in Geothermal and Shale Gas Reservoirs.” *Sgp-Tr-199* (December): 1–369.

Meyer, B R. 1989. “Three-Dimensional Hydraulic Fracturing Simulation on Personal Computers: Theory and Comparison Studies.” *SPE Eastern Regional Meeting*: 18. https://doi.org/10.2118/SPE-19329-MS.

Mikelić, Andro., Mary F Wheeler, and Thomas. Wick. 2015. “A Phase-Field Method for Propagating Fluid-Filled Fractures Coupled to a Surrounding Porous Medium.” *Multiscale Modeling & Simulation* 13(1): 367–98. https://doi.org/10.1137/140967118.

Morita, Nobuo, Donald L Whitfill, and Harry A Wahl. 1988. “Stress-Intensity Factor and Fracture Cross-Sectional Shape Predictions From a Three-Dimensional Model for Hydraulically Induced Fractures.” *Journal of Petroleum Technology* 40(10): 1329–42.

Nordgren, R P. 1972. “Propagation of a Vertical Hydraulic Fracture.” *Society of Petroleum Engineers Journal* 12(04): 306–14. https://doi.org/10.2118/3009-PA.

Olson, J. E. 2008. “Multi-Fracture Propagation Modeling: Applications to Hydraulic Fracturing in Shales and Tight Gas Sands.” *42nd U.S. Rock Mechanics - 2nd U.S.-Canada Rock Mechanics Symposium*.

Olson, Jon E. 2004. “Predicting Fracture Swarms -- the Influence of Subcritical Crack Growth and the Crack-Tip Process Zone on Joint Spacing in Rock.” *Geological Society, London, Special Publications* 231(1): 73–88.

Oterkus, Erkan. 2010. “Peridynamic Theory for Modeling Three-Dimensional Damage Growth in Metallic and Composite Structures.” The University of Arizona. http://www.agu.org/pubs/crossref/2008/2007GC001699.shtml.

Ouchi, Hisanao, Amit Katiyar, Jason York, et al. 2015. “A Fully Coupled Porous Flow and Geomechanics Model for Fluid Driven Cracks: A Peridynamics Approach.” *Computational Mechanics* 55(3): 561–76.

Ouchi, Hisanao. 2016. “Development of a Peridynamics-Based Hydraulic Fracturing Model for Fracture Growth in Heterogeneous Reservoirs.” The University of Texas at Austin. http://pge.utexas.edu/images/pdfs/theses16/ouchi.pdf.

Ouchi, Hisanao, Shivam Agrawal, John T. Foster, and Mukul M. Sharma. 2017. “Effect of Small Scale Heterogeneity on the Growth of Hydraulic Fractures.” *SPE Hydraulic Fracturing Technology Conference and Exhibition*. http://www.onepetro.org/doi/10.2118/184873-MS.

Ouchi, Hisanao, Amit Katiyar, John T Foster, and Mukul M Sharma. 2015. “A Peridynamics Model for the Propagation of Hydraulic Fractures in Naturally Fractured Reservoirs Peridynamics Based Hydraulic Fracturing Model.” (August).

Perkins, T K, and L R Kern. 1961. “Widths of Hydraulic Fractures.” *Journal of Petroleum Technology* 13(09): 937–49. https://doi.org/10.2118/89-PA.

Perrin, Jack, and Emily Geary. 2019. “EIA Adds New Play Production Data to Shale Gas and Tight Oil Reports.” *EIA*. https://www.eia.gov/todayinenergy/detail.php?id=38372.

Ratzlaff, C W et al. 2019. “SEM Investigation of the Fracture Network (Stimulated Reservoir Volume) Induced by Hydraulic Fracturing in Tennessee Sandstone.” *53rd U.S. Rock Mechanics/Geomechanics Symposium*: 13. https://doi.org/.

Renshaw, C. E., and D. D. Pollard. 1995. “An Experimentally Verified Criterion for Propagation across Unbounded Frictional Interfaces in Brittle, Linear Elastic Materials.” *International Journal of Rock Mechanics and Mining Sciences and* 32(3): 237–49.

Rezaei, Ali et al. 2017. “The Role of Pore Pressure Depletion in Propagation of New Hydraulic Fractures during Refaracturing of Horizontal Wells.” *SPE Annual Technical Conference and Exhibition*.

Roussel, N.P., H.A. Florez, and A.A. Rodriguez. 2013. “Hydraulic Fracture Propagation from Infill Horizontal Wells.” *Proceedings - SPE Annual Technical Conference and Exhibition* 7(October).

Roussel, Nicolas P, and Mukul M Sharma. 2012. “Role of Stress Reorientation in the Success of Refracture Treatments in Tight Gas Sands.” *SPE Production & Operations* 27(4): 346–55. http://www.onepetro.org/mslib/app/Preview.do?paperNumber=SPE-134491-PA&societyCode=SPE.

Safari, Reza et al. 2017. “Infill-Well Fracturing Optimization in Tightly Spaced Horizontal Wells.” *SPE Journal* 22(02): 582–95. http://www.onepetro.org/doi/10.2118/178513-PA.

Seleson, Pablo, Samir Beneddine, and Serge Prudhomme. 2013. “A Force-Based Coupling Scheme for Peridynamics and Classical Elasticity.” *Computational Materials Science* 66: 34–49. http://dx.doi.org/10.1016/j.commatsci.2012.05.016.

Seleson, Pablo D. 2010. “Peridynamic Multiscale Models for the Mechanics of Materials: Constitutive Relations, Upscaling from Atomistic Systems, and Interface Problems.” Florida State University.

Seleson, Pablo, Max Gunzburger, and Michael L. Parks. 2013. “Interface Problems in Nonlocal Diffusion and Sharp Transitions between Local and Nonlocal Domains.” *Computer Methods in Applied Mechanics and Engineering* 266: 185–204. http://dx.doi.org/10.1016/j.cma.2013.05.018.

Seleson, Pablo, and Michael Parks. 2011. “On the Role of the Influence Function in the Peridynamic Theory.” *International Journal for Multiscale Computational Engineering* 9(6): 689–706.

Sesetty, V, and A Ghassemi. 2012. “Simulation of Hydraulic Fractures And Their Interactions With Natural Fractures.” *46th U.S. Rock Mechanics/Geomechanics Symposium*: 9. https://doi.org/.

Seth, Puneet et al. 2019. “Poroelastic Pressure Transient Analysis: A New Method for Interpretation of Pressure Communication between Wells during Hydraulic Fracturing.” In *SPE Hydraulic Fracturing Technology Conference and Exhibition*,.

Seth, Puneet, Ripudaman Manchanda, Ashish Kumar, and Mukul M Sharma. 2018.

“Estimating Hydraulic Fracture Geometry by Analyzing the Pressure Interference Between Fractured Horizontal Wells.” In *SPE Annual Technical Conference and Exhibition,*.

Settari, Antonin, and Michael P Cleary. 1984. “Three-Dimensional Simulation of Hydraulic Fracturing.” *Journal of Petroleum Technology* 36(07): 1177–90. https://doi.org/10.2118/10504-PA.

Shimizu, Hiroyuki, Sumihiko Murata, and Tsuyoshi Ishida. 2011. “The Distinct Element Analysis for Hydraulic Fracturing in Hard Rock Considering Fluid Viscosity and Particle Size Distribution.” *International Journal of Rock Mechanics and Mining Sciences* 48(5): 712–27. http://dx.doi.org/10.1016/j.ijrmms.2011.04.013.

Shojaei, A., T. Mudric, M. Zaccariotto, and U. Galvanetto. 2016. “A Coupled Meshless Finite Point/Peridynamic Method for 2D Dynamic Fracture Analysis.” *International Journal of Mechanical Sciences* 119(July): 419–31. http://dx.doi.org/10.1016/j.ijmecsci.2016.11.003.

Siebrits, E et al. 2000. “Refracture Reorientation Enhances Gas Production in Barnett Shale Tight Gas Wells.” *SPE Annual Technical Conference and Exhibition*: 1–7. http://www.onepetro.org/doi/10.2118/63030-MS.

Silling, S. A. et al. 2007. 88 Journal of Elasticity *Peridynamic States and Constitutive Modeling*.

Silling, S. A., and E. Askari. 2005. “A Meshfree Method Based on the Peridynamic Model of Solid Mechanics.” *Computers and Structures* 83(17–18): 1526–35.

Silling, Stewart Andrew. 2000. “Reformulation of Elasticity Theory for Discontinuities and Long-Range Forces.” *Journal of the Mechanics and Physics of Solids* 48(1): 175–209.

Simonson, E R, A S Abou-Sayed, and R J Clifton. 1978. “Containment of Massive Hydraulic Fractures.” *Society of Petroleum Engineers Journal* 18(01): 27–32.

Singh, V.V, N.P Roussel, and M.M Sharma. 2008. “Stress Reorientation Around Horizontal Wells.” *SPE Annual Technical Conference and Exhibition* (September): 21–24. http://scholar.google.com/scholar?hl=en&btnG=Search&q=intitle:Stress+Reorientation+Around+Horizontal+Wells#0.

Suarez-Rivera, Roberto et al. 2013. “Understanding the Effect of Rock Fabric on Fracture Complexity for Improving Completion Design and Well Performance.” *International Petroleum Technology Conference*. http://www.onepetro.org/doi/10.2523/17018-MS.

Thallak, Sitharam, Leo Rothenburg, and Maurice Dusseault. 1991. “Simulation of Multiple Hydraulic Fractures In a Discrete Element System.” *The 32nd U.S. Symposium on Rock Mechanics (USRMS)*: 12. https://doi.org/.

Thiercelin, M., J.C. Roegiers, T.J. Boone, and A.R. Ingraffea. 1987. “An Investigation of the Material Parameters That Govern the Behavior of Fracturesvapproaching Rock Interfaces.” *6th ISRM Congress*: 263–69. http://www.onepetro.org/mslib/servlet/onepetropreview?id=ISRM-6CONGRESS-1987-049.

Wang, S. Y. et al. 2013. “Numerical Modeling of Pore Pressure Influence on Fracture Evolution in Brittle Heterogeneous Rocks.” *Rock Mechanics and Rock Engineering* 46(5): 1165–82.

Wang, Weiwei. 2017. “The Effect of Cemented Natural Fractures on Hydraulic Fracture Propagation.” The University of Texas at Austin.

Warpinski, N.R., and L.W. Teufel. 1987. “Influence of Geologic Discontinuities on Hydraulic Fracture Propagation (Includes Associated Papers 17011 and 17074).” *Journal of Petroleum Technology* 39(02): 209–20. http://www.onepetro.org/doi/10.2118/13224-PA.

Warpinski, N R, Z Moschovidis, C Parker, and I. S. Abou-Sayed. 1993. Perspective *Hydraulic Fracture Model Comparison Study: Complete Results*.

Warpinski, Norman R., James A. Clark, Richard A. Schmidt, and Clarence W. Huddle. 1982. “Laboratory Investigation on the Effect of In-Situ Stresses on Hydraulic Fracture Containment.” *Society of Petroleum Engineers journal* 22(3): 333–40.

Warpinski, Norman R, and Paul T Branagan. 1989. “Altered-Stress Fracturing.” *Journal of Petroleum Technology, SPE-17533-PA* 41(09): 990–97.

Weng, X et al. 2011. “Modeling of Hydraulic Fracture Network Propagation in a Naturally Fractured Formation.” *Simulation* i(November): 368–80.

Weng, Xiaowei et al. 2011. “Modeling of Hydraulic Fracture Network Propagation in a Naturally Fractured Formation.” *SPE Hydraulic Fracturing Technology Conference*: 18. https://doi.org/10.2118/140253-MS.

Weng, Xiaowei, and Eduard Siebrits. 2007. “Effect of Production Induced Stress Field on Refracture Propagation And\nPressure Response.” *Proceedings of SPE Hydraulic Fracturing Technology Conference*: 1–9. http://www.spe.org/elibrary/servlet/spepreview?id=SPE-106043-MS.

Wilson, Zachary A, and Chad M Landis. 2016. “Phase-Field Modeling of Hydraulic Fracture.” *Journal of the Mechanics and Physics of Solids* 96: 264–90. http://www.sciencedirect.com/science/article/pii/S002250961630285X.

Wright, Ca, Ra Conant, Dw Stewart, and Pm Byerly. 1994. “Reorientation of Propped Refracture Treatments.” *Rock Mechanics in Petroleum Engineering Conference*: 417–24. http://www.onepetro.org/mslib/servlet/onepetropreview?id=00028078.

Wu, Kan, and Jon E Olson. 2014. “Mechanics Analysis of Interaction Between Hydraulic and Natural Fractures in Shale Reservoirs.” *Proceedings of the 2nd Unconventional Resources Technology Conference*: 1824–41. http://search.datapages.com/data/doi/10.15530/urtec-2014-1922946.

Wu, Kan, and Jon E Olson. 2015. “Simultaneous Multifracture Treatments: Fully Coupled Fluid Flow and Fracture Mechanics for Horizontal Wells.” *SPE Journal* 20(02): 337–46. https://doi.org/10.2118/167626-PA.

Wu, Y. S., K. Pruess, and P. A. Witherspoon. 1991. “Displacement of a Newtonian Fluid by a Non-Newtonian Fluid in a Porous Medium.” *Transport in Porous Media* 6(2): 115–42.

Yadav, Himanshu, and Siyavash Motealleh. 2017. “Improving Quantitative Analysis of Frac-Hits and Refracs in Unconventional Plays Using RTA.” *SPE Hydraulic*

Fracturing Technology Conference and Exhibition. http://www.onepetro.org/doi/10.2118/184812-MS.

Yao, Yao, Shekhar V Gosavi, Kevin H Searles, and Tim K Ellison. 2010. "Cohesive Fracture Mechanics Based Analysis to Model Ductile Rock Fracture." *44th U.S. Rock Mechanics Symposium and 5th U.S.-Canada Rock Mechanics Symposium*: 8. https://doi.org/.

Yew, Ching H, and Xiaowei Weng. 2015. "Chapter 2 - Three-Dimensional Fracture Modeling." In eds. Ching H Yew and Xiaowei B T - Mechanics of Hydraulic Fracturing (Second Edition) Weng. Boston: Gulf Professional Publishing, 23–48.

York, J. R. 2018. PhD Dissertation "Advanced Hydraulic Fracture Modeling : Peridynamics , Inelasticity , and Coupling to FEM." The University of Texas at Austin. http://pge.utexas.edu/images/pdfs/theses18/York18.pdf.

Zang, Arno, and Ove Stephansson. 2010. "Rock Fracture Criteria BT - Stress Field of the Earth's Crust." In eds. Arno Zang and Ove Stephansson. Dordrecht: Springer Netherlands, 37–62. https://doi.org/10.1007/978-1-4020-8444-7_3.

Zhao, X P, and R P Young. 2009. "Numerical Simulation of Seismicity Induced by Hydraulic Fracturing in Naturally Fractured Reservoirs." *SPE Annual Technical Conference and Exhibition*: 17. https://doi.org/10.2118/124690-MS.

Zheng, Shuang, Ripudaman Manchanda, and Mukul M. Sharma. 2019. "Development of a Fully Implicit 3-D Geomechanical Fracture Simulator." *Journal of Petroleum Science and Engineering* 179(October 2018): 758–75. https://doi.org/10.1016/j.petrol.2019.04.065.

Zhou, Jian, Mian Chen, Yan Jin, and Guang qing Zhang. 2008. "Analysis of Fracture Propagation Behavior and Fracture Geometry Using a Tri-Axial Fracturing System in Naturally Fractured Reservoirs." *International Journal of Rock Mechanics and Mining Sciences* 45(7): 1143–52.

Vita

Shivam Agrawal registered in the doctoral program in the Department of Petroleum and Geosystems Engineering at The University of Texas at Austin in 2014. Agrawal completed his B.Tech and M.Tech degrees in Chemical Engineering in 2013 from the Indian Institute of Technology Kharagpur. His research interests include geomechanics, hydraulic fracturing, reservoir engineering, computational modeling, and data-driven modeling.

Permanent email: shivamagrawal2006@gmail.com

This dissertation was typed by the author.